

**UNIVERSIDAD DE GRANADA**

**FACULTAD DE CIENCIAS**

**Departamento de Física Aplicada**



**Fernando Martínez Pedrero**

**TESIS DOCTORAL**

Editor: Editorial de la Universidad de Granada  
Autor: Fernando Martínez Pedrero  
D.L.: GR.1720-2008  
ISBN: 978-84-691-5189-1



# Colloidal Aggregation Induced by an Uniaxial Magnetic Field

por

Fernando Martínez Pedrero

DIRECTORES DEL TRABAJO

Dr. D. José Callejas Fernández  
Prof. Titular de Física Aplicada

Dr. D. Artur Schmitt  
Prof. Titular de Física Aplicada

Dra. D. María Tirado Miranda  
Contratada Doctor de Física Aplicada

Trabajo presentado para aspirar al grado de  
DOCTOR POR LA UNIVERSIDAD DE  
GRANADA

Fernando Martínez Pedrero  
Granada, Junio de 2008



*A mis padres*



# Agradecimientos

La lectura de la Tesis cierra una etapa no sólo académica en la vida del becario. Es un buen momento para mirar atrás, hacer recuento, y es también una buena ocasión para darles las gracias a todos con los que uno se siente en deuda. A ellos están dedicadas estas líneas.

En primer lugar quisiera agradecerle al Dr. José Callejas la oportunidad que me brindó de participar en el proyecto que lidera, y el haberme sugerido esta bonita línea de investigación. Gracias por su confianza en mí, que se mantuvo firme aún en los momentos difíciles. Gracias a su empuje, su tenacidad, y a su ayuda continua durante toda la Tesis. También quiero agradecerles a mis otros dos directores, a los Doctores Artur Schmitt y María Tirado, la ayuda, el perfeccionismo, las exhaustivas revisiones, y las discusiones que con ellos he mantenido durante estos años, que han ayudado a mejorar mucho el trabajo que aquí se presenta. Gracias a los tres por su gran humanidad y su amistad.

Gracias al grupo de Física de Fluidos y Biocoloides, en el que he desarrollado esta Tesis. El esfuerzo de los que lo componen nos ha permitido ya a muchos iniciarnos en el tortuoso camino de la investigación. Gracias a los profesores del grupo, por el buen trato con el que dispensa a todos los que comenzamos, por la ayuda que me han prestado en muchos momentos, por las sugerencias, por haber acudido con interés a mis seminarios... y por los ratos de esparcimiento.

Gracias a los becarios de la vieja guardia. A Migue, por su buen recibimiento y por su ánimo constante (si lo piensas bien Migue, no hay ni pizca de ironía en mis palabras). A Alberto y a Julia, por sus buenos consejos, su ayuda y su amistad. A Catalina, quien fue mi "severa" maestra en los primeros pasos del laboratorio, amiga, y ejemplo en muchos aspectos de la vida. A Cecilia y a Jaime, porque son los dos muy "apaños". A Juan Carlos, mi hermanillo de Granada, con quien empecé la carrera, con quien llevo viviendo ya mucho desde hace mucho, y a quien quiero y conozco ya más que a las partículas



magnéticas. Y al resto de compañeros con el que he compartido muy buenos momentos: Juanjo, Teresa, Pedro, José Manuel, Roberto, Joaquín, Manolo y Javier. Perdonad que no os dedique las líneas que os merecáis, pero es que somos muchos.

A los que fueron llegando. Al Moro y a su compañera Sabina, por su genuina forma de verlo todo, a Sándalo, por sus discusiones científico-filosóficas, por su búsqueda y por su cariño. Al "otro" Fernando y a Christine, que en no mucho tiempo se han convertido en dos buenos amigos. A Miguel Alberto, digno relevo como "hijo de la luz", y a la nueva remesa de becarios, muy prometedores todos tanto en lo científico como en lo humano.

A "los vascos", el grupo de San Sebastián de Jacqueline Forcada con el que este grupo mantiene un tradicional hermanamiento. A Josetxo, a Ainara y a Álvaro, con quienes espero seguir encontrándome aunque sea de congreso en congreso.

A los amigos que conocí durante mi estancia en el Colegio de España. En especial a mi compañero de cuarto Pedro, y a nuestra vecina Rosa.

Al Laboratoire de Colloïdes et Matériaux Divisés, dirigido por el Profesor Bibette, y en especial a Abdeslam El-Harrak y a Jean Baudry con quienes trabajé muy a gusto durante mis meses de estancia en París.

Y a los que poco tienen que ver con los coloides, pero que de algún modo están entre estas letras y numerajos. A mi profesora Evangelia, quien inútilmente se esfuerza en que chapurree algo de inglés, y que es ya también una buena amiga. A mi gran amiga Cristina, por el cariño que me ha dado siempre y que a sabido mantener a pesar de la distancia. A la Magdi, compañera de aventuras, de penas y alegrías, quién sabe si también en los próximos años. A "las rubias", a Ángeles y a Álvaro, por haber confiado siempre en el congresista que hay en mí. Y cómo no, a Rafa, mi otro hermano granadino a quien tanto aprecio, por animarme y cuidarme en los momentos de tristeza o de cansancio. Espero que disculpes el que al final, por problemas en la edición, no te haya dedicado los tres tomos de agradecimiento que te prometí.

A mi hermanilla, de quien ya de niño aprendí a valorar las cosas buenas, y quien, junto a mis padres, me ha sabido inculcar su amor a la ciencia.

A Mamen. Por hacerme feliz, por estar siempre ahí, y porque lo sigas estando.

# Contents

<b>1</b>	<b>Introduction</b>	<b>1</b>
<b>2</b>	<b>Physical Phenomena in Magnetic Colloids</b>	<b>7</b>
2.1	Colloids . . . . .	7
2.2	Magnetic Colloids . . . . .	9
2.3	Brownian Motion . . . . .	15
2.4	Diffusion Equations . . . . .	18
2.5	Diffusion Coefficients . . . . .	22
2.5.1	Spheres . . . . .	23
2.5.2	Rods . . . . .	24
2.6	Interactions in Magnetic Colloids . . . . .	27
2.6.1	DLVO Theory . . . . .	28
2.6.2	Magnetic Dipolar Interaction . . . . .	31
2.7	Aggregate Stability . . . . .	37
2.8	Sedimentation . . . . .	39
<b>3</b>	<b>Micro-Structural Evolution</b>	<b>41</b>
3.1	Introduction . . . . .	42
3.2	Smoluchowski's Equation . . . . .	43
3.3	Kernel Classification . . . . .	46
3.4	The Brownian Kernel . . . . .	47
3.5	Field Induced Aggregation . . . . .	49
3.5.1	Miyazima's Kernel . . . . .	50
3.5.2	Field induced aggregation Kernel . . . . .	51
3.5.3	Coupled Sedimentation and Field Induced Aggregation Kernel . . . . .	55
3.5.4	Mutual Induction Kernel . . . . .	56
3.6	An Alternative Scenario . . . . .	57

3.7	Aggregate Morphology . . . . .	58
3.7.1	Fractal Dimension . . . . .	59
3.7.2	Morphology of Field Induced Aggregates . . . . .	61
<b>4</b>	<b>Light Scattering</b>	<b>67</b>
4.1	Introduction . . . . .	67
4.2	Electromagnetic Light Scattering Theory . . . . .	70
4.3	Scattering from Small Particles . . . . .	72
4.3.1	Spherical Particles . . . . .	76
4.3.2	Linear Particles . . . . .	79
4.4	Scattering from Large Particles . . . . .	86
4.4.1	Form Factor . . . . .	87
4.4.2	Time Correlation Function . . . . .	92
4.5	Scattering from Aggregates . . . . .	99
4.5.1	Structure Factor . . . . .	99
4.5.2	Time Correlation Function . . . . .	101
4.5.3	Linear Magnetic Aggregates in Uniaxial Fields . . . . .	102
<b>5</b>	<b>Materials and Methods</b>	<b>105</b>
5.1	Experimental Systems . . . . .	105
5.1.1	Magnetic Polystyrene Particles . . . . .	105
5.1.2	Silica Particles . . . . .	108
5.2	Experimental Devices . . . . .	110
5.2.1	Light Scattering . . . . .	110
5.2.2	Video Microscopy . . . . .	114
5.2.3	Machine de Force . . . . .	116
5.3	Methods . . . . .	117
5.3.1	Light Scattering Techniques . . . . .	117
5.3.2	Image Analysis . . . . .	122
5.3.3	Solving Smoluchowski's Equation . . . . .	125
<b>6</b>	<b>Kinetics of Field Induced Aggregation</b>	<b>127</b>
6.1	Field Induced Aggregation . . . . .	127
6.2	Magnetic Field Effects . . . . .	129
6.3	Electrolyte Effects . . . . .	137
6.3.1	Light Scattering Experiments: Polystyrene Particles . . . . .	138
6.3.2	Video Microscopy Experiments: Silica Particles . . . . .	146
6.4	Sedimentation Effects . . . . .	151
6.5	Mutual Induction Effects . . . . .	156

<b>7</b>	<b>Stability and Structure of Magnetic Filaments</b>	<b>159</b>
7.1	Magnetic Filaments . . . . .	159
7.2	Formation of Permanent Magnetic Chains . . . . .	160
7.2.1	Changes in the Mean Diffusion Coefficient . . . . .	161
7.2.2	Maeda's Model . . . . .	164
7.2.3	Magnetic Chain Rupture . . . . .	167
7.2.4	Magnetic Chain Stability . . . . .	171
7.3	Aggregate Morphology . . . . .	178
7.3.1	Particle Form Factor . . . . .	179
7.3.2	Structure of Electrolyte Induced Aggregates . . . . .	181
7.3.3	TEM Micrographs . . . . .	182
7.3.4	Structure of Field Induced Aggregates . . . . .	188
<b>8</b>	<b>Summary and Conclusions</b>	<b>193</b>
8.1	Conclusions . . . . .	194
8.1.1	Light Scattering . . . . .	194
8.1.2	Kinetics of Field Induced Aggregation . . . . .	195
8.1.3	Stability of Magnetic Chains . . . . .	197
8.1.4	Structure of Magnetic Chains . . . . .	197
<b>9</b>	<b>Resumen y Conclusiones</b>	<b>199</b>
9.1	Conclusiones . . . . .	200
9.1.1	Dispersión de Luz . . . . .	200
9.1.2	Cinética de Agregación Inducida por un Campo . . . . .	201
9.1.3	Estabilidad de Cadenas Magnéticas . . . . .	204
9.1.4	Estructura de Cadenas Magnéticas . . . . .	205
<b>A</b>	<b>Table of Magnetic Units</b>	<b>207</b>
<b>B</b>	<b>INSPACE</b>	<b>209</b>
<b>C</b>	<b>Magnetotactic Bacteria</b>	<b>211</b>



# Chapter 1

## Introduction

*There is plenty of room at the bottom.*

Richard Feynman.

Magnetorheological fluids are colloidal dispersions of micron sized magnetic particles suspended in a nonmagnetic fluid. Due to their magnetic character the particles present an anisotropic interaction that is tuneable through the strength of an applied magnetic field. When the field is present, the particles experience an attractive force along the field direction and a repulsive force normal to it. If the particles are allowed to aggregate, linear particle aggregates or filaments form due to the anisotropic character of the magnetic interaction. The final aggregate structure depends mainly on the particle volume fraction and the magnetic field strength. At high field strength and low particle concentrations, regular one particle-thick chainlike aggregates are formed. At higher particle concentrations, the chains experience additional lateral attractions and assemble in column like structures [1].

Formation of magnetic particle filaments is not only of great interest for pure science but also very important for the assembly of new materials. Dispersions of magnetic particles and chainlike aggregates immersed in different fluids have special physicochemical properties that make them very suitable for a growing number of applications in different fields such as microfluids, liquid crystals, DNA separation, rheology, biomedical applications, magnetic

colloidal crystals, etc. [2, 3, 4, 5, 6].

The microstructure of magnetorheological fluids plays a significant role for their physicochemical properties, and evidently, an adequate modelling of chain formation processes is of practical importance for the control of technological applications. So far, however, only a relatively small number of experimental and simulation studies address this topic, i.e. the formation of linear aggregates through field-induced aggregation processes in dipolar colloidal dispersions. In their pioneer work, Promislow and Gast determined the *mean cluster size*  $S(t)$  as a function of the exposure time to the magnetic field by means of optical microscopy [7]. They found a power-law time dependency  $S \propto t^z$  that was in good agreement with the theoretical predictions made by Miyazima et al. for aggregation of oriented anisotropic particles [8]. The values of the *kinetic exponents*  $z$  measured by Promislow and Gast, however, differ noticeably from the ones reported by Miyazima et al.

Several papers published from then on report a variety of values for the kinetic exponent at different experimental conditions. Even alternative theoretical dependencies have been proposed [9, 10]. However, only Miyazima et al. proposed an analytical aggregation kernel capable to predict the observed power-law dependency for the time evolution of the average cluster size. Their kernel assumes that the cross section of a chain-like aggregate should not depend on its total length. Nevertheless, it does not consider other important parameters such as the diffusion coefficient of the chains, or the range of the interactions. On the other hand, most of these works focus on structural and scaling aspects. The kinetic information given is commonly limited to the asymptotic behaviour of the average cluster size that usually shows a power law dependency at long aggregation times. However, a detailed study of the aggregation kinetics and the time evolution of the cluster size distribution is usually not performed. The influence of different phenomena and parameters are still quite unclear. Some of the particular weak points of the experimental and theoretical description established so far are sedimentation effects, electrostatic inter-particle interactions, or the degree of magnetic saturation of the particles:

- Repulsive electrostatic interactions are usually not considered for magnetic filament formation since they are, in general, much weaker than dipolar magnetic attractions. Nevertheless, this is not necessarily true for charged magnetic particles [11, 12, 13]. Especially at low electrolyte concentrations, the strength of electrostatic repulsions may be at least of the order of the magnetic interactions. Thus, the growth processes and

the structure of the aggregates formed are expected to depend mainly on the relative strength of the electrostatic and magnetic interactions.

- The magnetic rheological fluids are suspension of small particles containing different quantities of iron oxides. This increases the relative density of the particles with respect to the surrounding fluid. Hence, particle sedimentation can not be avoided by the Brownian motion in a effective way [14]. Since particles and linear aggregates are usually settling as they aggregate, the effect of the differential settling must also be considered in order to describe field induced aggregation processes.
- A further effect that should not be neglected a priori is the mutual induction of the chain forming particles. At weak field strengths, the degree of magnetization of the particles is proportional to the local field strength and so, the net magnetization of the particles contained within a chain is enhanced by the presence of neighbouring particles [15]. This effect leads to an increased range of the magnetic interaction between the aggregates as they gain in size.

Hence, the kinetics of magnetic chain formation processes is still not completely understood and remains an open question. One of the steps to go would be to improve the theoretical description proposing an aggregation kernel that includes those physical parameters explicitly. The corresponding solutions of Smoluchowski's aggregation equation would then allow the time evolution of the cluster size distribution to be predicted more reliably. The main aim of this work has been to deepen our knowledge about chain formation processes and to improve the theoretical description of field-induced aggregation phenomena. For that purpose, we measured the time evolution of the cluster size distribution and the average cluster size arising in aggregating magnetic particle dispersions. We propose theoretical models based on Smoluchowski's approach and use the experimental results to test and validate them. Therefore, it was essential to determine an aggregation kernel that included all the effects mentioned above.

On the other hand, magnetic filaments able to survive in the absence of an applied magnetic field have been observed by several authors over the latter years [16, 17]. Such permanent chains are formed due to field induced aggregation in a deep primary energy minimum that is mainly determined by attractive short-range interactions. The chain-like aggregates that are able to survive in absence of the applied field have led to new applications like "artificial swimmers", microfluidic mixers, etc [18, 19, 20, 21]. The stiffness



and magnetorheological properties of these chains have been the subject of several works during the last years [22, 23, 24, 25]. In this work, we tried to deepen our knowledge in this field and studied the influence of isotropic electric and anisotropic magnetic particle interactions on the formation and growth of permanent magnetic particle filaments. We focused our attention on the role of the electrolyte concentration on the stability of the chains. Therefore, we designed an accurate experimental protocol that allowed the final length of the linear aggregates to be controlled by tuning the exposure time to the magnetic field and the relative strength of the different interparticle interactions.

An additional purpose of this work has been to demonstrate that light scattering techniques, widely used for the study of the structure and the kinetics of colloidal aggregation, can be also employed to obtain valuable data regarding magnetic colloidal aggregation. Throughout the Thesis, we will always focus our attention on the magnetic character of the colloidal particles employed and the effect of an uniaxial magnetic field on the light scattering experiments. We will show that the final filament size as well as the chain structure may be reliably monitored by light scattering techniques, when the filaments are either aligned due to the action of the magnetic field, or freely diffusing once the magnetic field has been removed. Large diffusing rods are complicated to describe because the coupling of translational and rotational diffusion modes has to be taken into account. This point requires a rather sophisticated theoretical background. Nevertheless, light scattering techniques give rise to much better statistics, and shorter measuring times if compared with most of the well established imaging methods. We will show that these advantages can make light scattering a highly valuable tool for the development and standardization of materials made of magnetic filaments. An improved understanding of the complex properties of magnetorheological fluids and the interactions of the particles contained therein, will undoubtedly help scientists to improve industrial processes and devices that are based on such fluids.

The outline of this Thesis is as follows:

- Chapter II gives a brief overview of magnetic fluids, focusing on their magnetic characteristics, the diffusive motion of the particles, and the particle-particle interactions.
- Chapter III presents the main theoretical tools that are required for an adequate description of field induced aggregation processes and the morphology of the aggregates formed.

- Chapter IV deals with the light scattering techniques that were used to determine the average size and the fractal geometry of the field induced aggregates.
- The materials and methods are presented in Chapter V.
- The main results are detailed in Chapters VI and VII. Chapter VI studies the kinetics of field induced aggregation processes. Chapter VII deals with the stability and the morphology of the aggregates formed.
- This Thesis ends with a brief summary and a list detailing the main conclusions.



## Chapter 2

# Physical Phenomena in Magnetic Colloids

*...eso es lo que se llama movimiento browniano, ¿ahora entendés?, un ángulo recto, una línea que sube, de aquí para allá, del fondo al frente, hacia arriba, hacia abajo, espasmódicamente, frenando en seco y arrancando en el mismo instante en otra dirección, y todo eso va tejiendo un dibujo, una figura, algo inexistente como vos y como yo...*

Julio Cortázar, de Rayuela.

## 2.1 Colloids

Colloidal systems are mixtures of at least two phases: a dispersed phase made of micro-sized particles distributed throughout a continuous phase or dispersion medium. Both, the colloidal particles as well as the continuous medium may be solid, liquid, or gaseous, forming different materials like foams (gas dispersed in liquid), emulsions (liquid in liquid), aerosols (solid in gas), dispersions<sup>1</sup> (solid in liquid), etc. However, all these colloidal systems present one common characteristic: a large surface area with respect to the volume.

---

<sup>1</sup>The colloidal dispersions are so-called colloidal suspensions, since the colloidal material is dispersed or suspended in a liquid phase.

Indeed, it is better to define a colloid as a system in which surface effects are predominant, rather than simply in terms of particle size. The range of size of the colloidal particles is more or less defined by the importance of *Brownian motion*, i.e., the endless translational diffusion of the particles resulting from the random impacts of the molecules of the medium. In broad terms, colloidal particles can be considered as effective large molecules, and be treated according to the theories of Statistical Mechanics [26].

Colloidal systems have applications in many industrial areas. In fact, colloidal particles are the major components of familiar products such as foods, inks, paints, coatings, papers, cosmetics, photographic films, etc. They are also frequently studied in materials science, pharmacy, nanotechnology, chemistry, or biotechnology. Notable examples include silica colloids, polymer latexes, magnetic colloids, clays, minerals, macromolecules, aggregates of surfactant molecules, proteins, viruses, bacteria, cells, etc. Biological cells are typically  $10\ \mu\text{m}$  across, which is approximately the size of biggest colloidal particles. On the other hand, their components are in the sub-micron size domain. The proteins, for example, have a typical size of just 5 nm, which is comparable with the dimensions of smallest nanoparticles. Colloidal systems have already found a broad range of amazing applications in fields such as drug delivery, biodiagnostics, and combinatorial synthesis, and they allow experimenting at the cellular scale [27].

Colloidal systems present particular optical, rheological, or statistical properties (among others). These properties are determined not only by their specific chemical composition, but also by the nature and strength of the interactions among the constituent particles. One characteristic property of colloid systems that distinguishes them from true solutions is that colloidal particles scatter light (as we will see in Chapter 4).

When two colloidal particles collide there are chances that particles will attach to each other, if it is energetically favourable. There are three major physical mechanisms to bring the particles together: Brownian motion, fluid shear and differential settling. Furthermore, aggregation processes can be induced by the attractive interactions between the particles. Both, the colloidal stability as well as the growth mechanism depend on the interaction between the particles and their motion. The structure of the resulting aggregates as well as the kinetics of the aggregation processes are usually determined by them. Aggregation processes are very important for understanding many industrial and natural phenomena. Aggregation and gelation processes are of paramount importance in many applications when aggregates of desired size and structure are to be produced [28].

Colloids are of considerable interest also from a fundamental point of view because in physics colloids are an interesting model system for atoms. Many of the forces that govern the structure and behaviour of matter, such as excluded volume interactions or long range electrostatic forces, also govern the structure and behaviour of colloidal suspensions. For example, the same theoretical techniques used to model ideal gases can also be used to model the behaviour of a hard sphere colloidal suspension. These systems take advantage of the colloidal particle scales. Colloidal particles, though microscopic, are still very large from an atomic point of view, and the phase transitions in colloidal suspensions, which are analogous to atomic phase transitions, can be studied in real time using optical or light scattering techniques [29].

## 2.2 Magnetic Colloids

Magnetic colloids are colloidal dispersions of small magnetic particles that present a dipolar interaction when an external magnetic field is applied. When the field is present, the particles experience an attractive force along the field direction and a repulsive force normal to it. The magnetic interaction is tunable through the strength of an external magnetic field. If the particles are allowed to aggregate then linear aggregates, aligned along the field direction, are formed due to the anisotropic character of the dipolar interaction. At relatively high particle concentrations, even more complex structures may arise [1].

Analogous behaviour can be observed in a suspension of dielectric spheres in a dielectric medium, so called *electrorheological fluids* (ER). In fact, most of the concepts and fundamental ideas developed in magnetic colloid research can be directly applied to ER suspensions [10, 30]. However, there are some complicating factors, such as surface charge or electrode polarization, which have limited the range of their applications up to now. Unlike electric manipulation, the magnetic interactions are generally not affected by surface pH, surface charges, or ionic concentrations. For a brief discussion regarding the limitations of ER fluids see the paper of Promislow et al. [7].

Magnetic colloidal dispersion are usually classified as *Ferrofluids* and *Magnetorheological Fluids*, mainly depending on the particle size:

- Ferrofluids (FF) are composed of nanoscale magnetic particles of a diameter of 10 nanometers or less suspended in a carrier fluid, usually an organic solvent or water. In these systems, the fluid magnetization is limited by the domain magnetization of the magnetic grains. FF are at-

tracted by the external magnetic fields adopting its shape to the applied magnetic field, and forming regular patterns of corrugations on the surface of the medium. FF, however, remain liquid even in the presence of strong magnetic fields. Steric repulsions prevent the nanoparticles from aggregation, ensuring that the magnetic domains do not form clusters that become too heavy to be held in suspension by Brownian motion. Therefore, FF can be stable for years: they do not settle with time, not even when a magnetic field is applied [31].

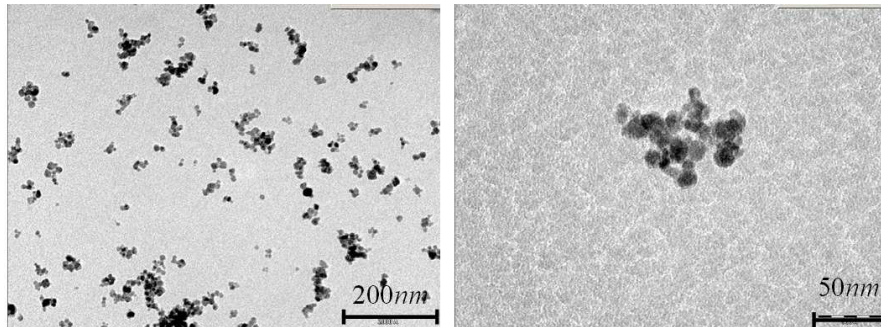


Figure 2.1: TEM images of a diluted ferrofluid synthesized by Vereda et al. [32]. Small magnetic grains roughly 10 *nm* in size appear as dark spots in both images.

- Magnetorheological Fluids (MR) are similar to ferrofluids. However, magnetorheological fluids contain micrometre scale magnetic particles that are one to three orders of magnitude larger than those of ferrofluids. These micron-size magnetic particles are usually composite materials. The small magnetic grains are often contained within microscopic colloids like emulsions, latexes, or liposomes (please, see Figure 2.2) [2, 33, 34, 35]. When MR are subject to a magnetic field, linear aggregates of particles form and restrict the movement of the fluid perpendicular to the direction of the magnetic field, increasing its viscosity to the point of becoming a viscoelastic solid. Therefore, reversible changes in the medium viscosity can be achieved very quickly. Although these smart fluids are rightly seen as having many potential applications, they are of limited commercial use. High density, due to presence of magnetic grains, makes them heavy, and favours the sedimentation.

Due to their response to external fields, dispersions of dipolar particles and linear aggregates thereof have special physicochemical properties that make

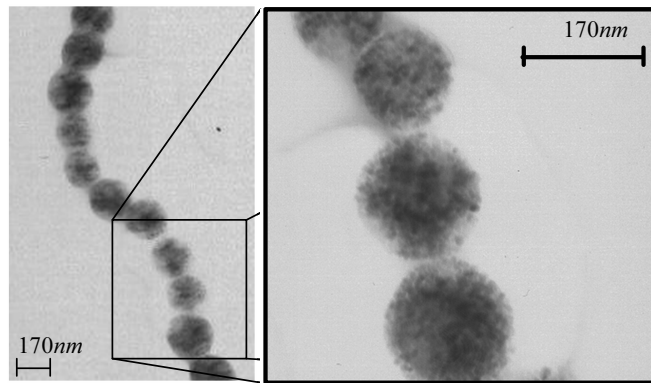


Figure 2.2: TEM pictures of magnetic polystyrene particles (R0039, Merck). The small magnetic grains randomly distributed within polystyrene spheres appear as dark spots in the images. Linear aggregates have been previously formed under the presence of a uniaxial magnetic field. In this particular case, the linear aggregates formed are stable enough to withstand the absence of the magnetic field.

them very suitable for a growing number of applications in different fields such as rheology, micro-fluids, light transmission devices, etc. These applications take advantage of the magnetic response, the optical response (the dispersion becomes birefringent) [36], or the rheological response (the medium becomes structured) [37].

Magnetic colloidal particles are also used in medicine, both in diagnostic as well as in therapeutic biomedical applications like:

- Hyperthermia, where the magnetic particles are heated selectively by application of an high frequency magnetic field. Hyperthermia may be used as a cancer treatment to kill or weaken tumor cells, with negligible effects on healthy cells [6, 27, 38].
- Magnetic carriers for drug vectorization, where the particles are directed by means of a magnetic field gradient towards a certain location [6, 27].
- Magnetic contrast agents in magnetic resonance imaging (MRI) [6, 39].

On the other hand, different applications like isolation and purification of biomolecules, separation of biochemical products, or cell labelling and sorting, have been performed with magnetic microparticles [40].



Magnetic particles have also been employed to directly determine the force-distance profile between tiny colloidal particles [41]. Other authors have prepared stabilized pickering emulsions using magnetic colloids that undergo phase separation under the action of an external magnetic field [42]. Paramagnetic colloidal particles dispersed in water and deposited above magnetic bubble domains of a uniaxial ferrimagnetic garnet film are used as microscopic stirrer when subjected to external rotating magnetic fields [43].

”*Bottom up techniques*”, where nanomaterials are fabricated from atoms or molecules in a controlled manner, are investigated to obtain more and more complex colloidal architectures. Within this framework, the preparation of particles arrays is very interesting for the design of novel nanostructured devices. These linear nano-structures can be easily obtained by applying an external magnetic field to a colloidal suspension of magnetic nanoparticles. Therefore, over the last years magnetic filaments have been built using colloidal magnetic particles, and chain-like aggregates able to survive in absence of the applied field have given rise to new applications like ”artificial swimmers”, microfluidic mixers, or instruments for proving the kinetics of adhesive processes [18, 19, 20].

Nature also has taken advantage of these systems. Cluster of superparamagnetic magnetite particles have been found in the beak skin of homing pigeons [44, 45], where the particles could work as magnetic field receptors. Single-domain magnetic colloids are also synthesized by magnetotactic bacteria (see the Appendix C for further information). The magnetic domains allow the bacterias to orient themselves along the lines of the Earth’s magnetic field.

### Magnetic Properties of Fine Particles

In ferro-ferrimagnetic materials, the atomic magnetic dipoles tend to align spontaneously, without any applied field. However, the order of the oriented atomic dipoles leads to a high magnetostatic energy. Hence, the bulk material is splited in different volumes, known as *magnetic domains*, in order to reduce this energy. These domains are small (several hundred nanometer), but much larger than atomic distances. The transition between two domains, where the magnetization flips, is called a *domain wall*. In zero field, the dipoles of each domain have the magnetic moments orientated along their *easy axis of magnetization* in order to minimize the magnetostatic energy, and the dipoles in the whole material are on average not aligned. Hence, the ferromagnetic materials have little or no net magnetic moment at zero field. On the other hand, if a strong enough external magnetic field is applied, the numbers of the

domains oriented along the field direction will increase at the expense of the others. This configuration will partially remain once the field is turned off, thus creating a permanent magnet<sup>2</sup>. Hence, the magnetization as a function of the external field is described by a magnetization curve with a hysteresis loop.

The magnetic character of ferrofluids and magnetorheological fluids is usually due to the presence of small magnetic grains of roughly 10 *nm* in size. Since the size of the magnetic grains is often smaller than a magnetic domain, each one can be considered as a magnetic monodomain. Hence, each grain has a magnetic moment having an intensity that depends on the grain's size and the magnetic material. Because more magnetic materials are easily oxidized, most of the magnetic grains employed consist of iron oxides. For small enough nano-grains, the magnetic moment fluctuates around the easy axis of magnetization when no external magnetic field is applied. This magnetic behaviour is known as *superparamagnetism* [2].

### Superparamagnetism

Moving the dipoles away from an easy axis of magnetization costs a given amount of energy called *energy of anisotropy*. This energy, however, decreases when the grain size decreases. If the magnetic grain size reaches a minimum value then the energy of anisotropy becomes of the same order of magnitude as the thermal energy  $k_B T$ . Consequently, even when the temperature drops below the *Curie temperature*<sup>3</sup>, the thermal energy is sufficient to change the direction of magnetization of the entire grain, and the magnetization vector fluctuates around the easy axis of magnetization with a characteristic relaxation time [2]. Hence, in zero field the magnetic moment direction fluctuates around the easy axis of magnetization, so that each grain's time averaged magnetization is zero. When the field is switched on, in average, the dipole moment of each grain still align along a direction parallel to the easy axis of magnetization, although it will point for a longer time in the direction that maximizes the dipole's projection on the external field direction. As a result, a net magnetization will be induced in the magnetic grain [46]. The size below which these fluctuations are observed depends on the material and the

---

<sup>2</sup>Although this state is not a minimal-energy configuration, it is extremely stable and has been observed to persist for millions of years.

<sup>3</sup>At temperatures above the Curie temperature, the thermal energy is sufficient to overcome the coupling forces, causing the atomic magnetic moments to fluctuate randomly. Because there is no longer any magnetic order, the internal magnetic field no longer exists and the magnetic materials exhibit paramagnetic behaviour.

temperature.

The superparamagnetic behaviour of the magnetic grains can be transmitted to more complex systems in which the iron oxides grains are dispersed. In composite particles the easy axis of magnetization of the grains are often randomly oriented in the absence of an external magnetic field, and their dipoles fluctuate around their easy axes of magnetization. Consequently the randomly distributed oscillating dipoles do not contribute to a net moment of the entire particle. By applying a magnetic field, however, one of the two easy axis directions is favoured in each magnetic grain, and the particles acquire a net magnetic moment  $\vec{m}$  (see Figure 2.3). The magnetization processes are usually completely reversible. The dipoles oscillate again on the easy axis of magnetization as soon as the magnetic field is turned off. Macroscopically the material behaves in a manner similar to paramagnetism, and the magnetization curve does not present any hysteresis.

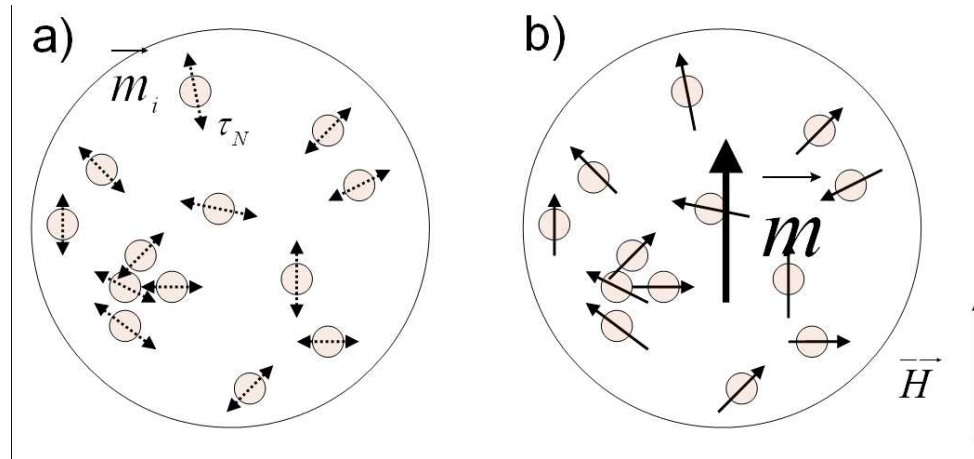


Figure 2.3: In the absence of an external magnetic field, the easy axis of magnetization are randomly oriented within the polystyrene matrix, and the magnetic moment of the grains  $\vec{m}_i$  fluctuate between the two possible orientations with a characteristic relaxation time  $\tau_N$  (Figure a). Once the magnetic field is applied one of the two directions is favoured in each magnetic grain, and the particle acquires a net moment  $\vec{m}$  (Figure b).

## 2.3 Brownian Motion

Small particles suspended in a thermally equilibrated fluid present a perpetual random movement. The botanist Robert Brown was the first person to detect this erratic movement in 1827, while he observed the irregular motion of pollen grains immersed in a fluid. However, it wasn't until 1905 that Albert Einstein's described the physics behind this erratic motion. Einstein showed that the so called *Brownian motion*, in honor of Robert Brown, is due to the thermal collision with solvent molecules [47]. During a short period of time a random number of solvent molecules collide with the colloidal particles. These impacts of random strength and from random directions cause a sufficiently small particle to move in exactly the way described by Brown. The new theoretical frame described the experiments observed, representing an additional validation of the *Molecular Theory*.

Brownian motion is only relevant when the thermal displacements are comparable with the particle dimension. Hence, the maximum size of a colloidal particle is usually defined as  $10 \mu m$  approximately. For these sufficiently small particles, the upward diffusion produced by the Brownian movement overcomes the gravitational fall, and an equilibrium is reached. On the other hand, the size of a colloidal particle has to be big enough if compared with the solvent molecules<sup>4</sup>, i.e., approximately  $1 nm$  in at least one dimension. The large difference in relevant length and time scales between the fluid and the assembly of Brownian particles allows as a continuous phase the fluid to be considered.

In the study of the diffusive motion of the magnetic particles we will mainly follow the formulation given in the book of Dhont [26]. For further details about light scattering topics the interested reader should consult this excellent book.

### Langevin Equation

The separation between the molecular and atomic time scales allows the random motion of the colloidal particles to be described on the basis of Newton's equations

$$\frac{d\vec{p}}{dt} = -\hat{\gamma} \frac{\vec{p}(t)}{m} + \vec{f}(t), \quad (2.1)$$

---

<sup>4</sup>The pollen particles observed by Brown were roughly 10,000 times larger than a water molecule.

where  $\vec{p}$  is the momentum of the particle,  $m$  its mass, and the constant matrix  $\hat{\gamma}$  is the *friction coefficient* or the *Stoke's friction coefficient*. In the previous Equation, the interaction of the Brownian particles with the solvent is separated into two terms. A friction force, directly proportional to the velocity of the particles, and a random force which arises from the random impacts of solvent molecules (the first and the second term on the right-hand side of Equation 2.1 respectively). The random force  $\vec{f}(t)$  accelerate and decelerate the colloidal particles in random directions. Therefore, the ensemble average of the fluctuating force is equal to zero

$$\langle \vec{f}(t) \rangle = \vec{0}. \quad (2.2)$$

On the other hand, each impact is practically instantaneous, and the successive collisions are uncorrelated, so

$$\langle \vec{f}(t)f(t') \rangle = 2\hat{I}\hat{\gamma}k_B T\delta(t-t'), \quad (2.3)$$

where  $\delta$  is the delta distribution, and  $\hat{I}$  is the unit matrix. The strength of the fluctuating force is given by  $2\hat{I}\hat{\gamma}k_B T$ . Here, the *Equipartition Theorem* was implicitly used. The Equipartition Theorem states that the total kinetic energy of a system is shared equally among all the independent components of motion once the system has reached thermal equilibrium<sup>5</sup>.

Equation 2.1, together with the properties described by Equations 2.2 and 2.3, are referred as *Langevin's Equation*. This Equation is a stochastic differential equation in the sense that the position of the particles as well as their velocity are now stochastic variables.

Successive integrations of Equation 2.1 yield [26]

$$\begin{aligned} \vec{p}(t) &= \vec{p}(0) \exp\left(-\frac{\hat{\gamma}t}{m}\right) \\ &+ \int_0^t dt' \vec{f}(t') \exp\left(-\frac{\hat{\gamma}(t-t')}{m}\right), \end{aligned} \quad (2.4)$$

and

$$\begin{aligned} \vec{r}(t) &= \vec{r}(0) + \vec{p}(0)\hat{\gamma}^{-1} \left[ 1 - \exp\left(-\frac{\hat{\gamma}t}{m}\right) \right] \\ &+ \hat{\gamma}^{-1} \int_0^t dt' \vec{f}(t') \left[ 1 - \exp\left(-\frac{\hat{\gamma}(t-t')}{m}\right) \right]. \end{aligned} \quad (2.5)$$

---

<sup>5</sup>Further information can be found in [26].

### Mean Squared Displacement

Using Equations 2.2, 2.3, and 2.5 the mean squared displacement is determined to be

$$\begin{aligned} \langle (\vec{r}(t) - \vec{r}(0))(\vec{r}(t) - \vec{r}(0)) \rangle &= \vec{p}(0)\vec{p}(0)\hat{\gamma}^{-2} \left[ \exp\left(-\frac{\hat{\gamma}}{m}t\right) - 1 \right]^2 \\ &+ \hat{I}2mk_B T \hat{\gamma}^{-2} \left( \frac{\hat{\gamma}t}{m} - \frac{1}{2} \left[ \exp\left(-\frac{2\hat{\gamma}t}{m}\right) - 1 \right] - 2 \left[ 1 - \exp\left(-\frac{\hat{\gamma}t}{m}\right) \right] \right). \end{aligned} \quad (2.6)$$

For times  $t \gg m\hat{\gamma}^{-1}$ , the previous equation becomes

$$\langle (\vec{r}(t) - \vec{r}(0))(\vec{r}(t) - \vec{r}(0)) \rangle = 2\hat{I}k_B T \hat{\gamma}^{-1}t, \quad (2.7)$$

and the mean squared displacement varies linearly with time. The non-linear evolution of Equation 2.7 can reflect such effects as caging in dense colloidal suspensions, non-Newtonian behaviour in the suspending fluid, or two-dimensional corrections for geometrically confined suspensions [48]. On a time scale longer than the *Brownian time*  $\tau_B = m\hat{\gamma}^{-1}$ , the particles move diffusively. Notice the difference for ballistic motion where the mean squared displacement is proportional to  $t^2$ . The reason is that the particles suffer many random impacts with the solvent molecules in their motion, decreasing their mean squared displacement with time. The quantity that determines the extension of the Brownian motion in Equation 2.7 is its *self-diffusion coefficient*

$$\hat{D}_0 \equiv k_B T \hat{\gamma}^{-1}. \quad (2.8)$$

Here, we describe the phenomenon of self-diffusion, assuming the particle movement to be independent at "infinite dilution". Equation 2.8, commonly referred to as *Einstein Relation*, relates the diffusion coefficient with the friction coefficient, and clarifies the physical meaning of the self-diffusion constant  $\hat{D}_0$ : it sets the time required for significant displacements of the Brownian particles. The above-mentioned mechanism connects the macroscopic magnitude  $\hat{D}_0$  with the microscopic jumps of the particle.

It takes, however, a finite amount of time for the molecules to alter the motion of a particle. Indeed, for times  $t \ll m\hat{\gamma}^{-1}$  Equation 2.6 becomes

$$\langle (\vec{r}(t) - \vec{r}(0))(\vec{r}(t) - \vec{r}(0)) \rangle = \frac{\vec{p}(0)\vec{p}(0)}{m}t^2, \quad (2.9)$$

and a ballistic behaviour is observed.

### Rotational Langevin Equation

Thermal collisions of solvent molecules with the particles also lead to rotational random motions. In this case, the Langevin equation can be generalized by replacing the lineal moment  $\vec{p}$  by the angular momentum vector  $\vec{L}$ , the linear velocity  $\vec{v}$  by the angular velocity  $\vec{\Omega}$ , the friction matrix  $\hat{\gamma}$  by the rotational friction coefficient  $\hat{\gamma}_r$ , and the random force  $\vec{f}$  by the fluctuating torque  $\vec{\tau}$

$$\frac{d\vec{L}}{dt} = -\hat{\gamma}_r \vec{\Omega}(t) + \vec{\tau}(t). \quad (2.10)$$

Analogous to the stochastic force  $\vec{f}$ , the ensemble average of the random torque is equal to zero

$$\langle \vec{\tau}(t) \rangle = \vec{0}, \quad (2.11)$$

while

$$\langle \vec{\tau}(t) \vec{\tau}(t') \rangle = 2\hat{I} \hat{\gamma}_r k_B T \delta(t - t'). \quad (2.12)$$

The rotational Brownian motion may be visualized as the random motion of the tip of a unit vector  $\hat{u}$  on the surface of a unit sphere<sup>6</sup>. Hence, the mean squared rotational displacement on a time scale  $t \gg \hat{M} \hat{\gamma}_r^{-1}$  is equal to

$$\langle |\hat{u}(t) - \hat{u}(0)|^2 \rangle = 2(1 - \exp(-2k_B T \hat{\gamma}_r^{-1} t)). \quad (2.13)$$

where  $\hat{M}$  is the *inertia matrix*. Analogously to translation, the *rotational diffusion coefficient*  $\hat{D}_r$  is given by

$$\hat{D}_r \equiv k_B T \hat{\gamma}_r^{-1} \quad (2.14)$$

## 2.4 Diffusion Equations

In Section 2.3 we have seen that Brownian particles have a range of different velocities, orientations, and displacements during their random motion. These quantities constantly change due to collisions with solvent molecules. Therefore, a deterministic description of the Brownian motion is impracticable due to the great number of particles as well as to their stochastic behaviour. The fraction of a large number of particles within a particular velocity range,

---

<sup>6</sup>Here the caret indicates that the vector is a unit vector.

however, is nearly constant. Hence, it is quite useful to have probabilistic equations to describe the particle motion.

The *probability density function*  $G_s(\vec{R}, t)d^3R$  can be regarded as the probability of finding a particle in the neighborhood  $d^3R$  of the position  $\vec{R}$  at time  $t$ , given that its position at time  $t = 0$  was in the neighborhood of the origin. Since the system is assumed to be spatially homogeneous, the probability density depends only on  $\vec{R} = \vec{r}_j(t) - \vec{r}_j(0)$ , and since the net displacement of the Brownian particles is the sum of many independent stochastic displacements, the probability density should be a Gaussian distribution function. The *Central Limit Theorem* states that the sum of many stochastic variables is a stochastic variable with a Gaussian probability distribution [49]. Indeed, on the diffusive time scale the probabilistic density function yields [26]

$$G_s(\vec{R}, t) = \frac{1}{(4\pi\hat{D}_0t)^{3/2}} \exp \left[ -\frac{|\vec{r}(t) - \vec{r}(0)|^2}{4\hat{D}_0t} \right], \quad (2.15)$$

where  $\hat{D}_0$  is the coefficient of self-diffusion previously defined.

This probability density function can also be regarded as the solution to the diffusion equation

$$\frac{\partial}{\partial t} G_s(\vec{R}, t) = \hat{D}_0 \nabla^2 G_s(\vec{R}, t), \quad (2.16)$$

subject to the initial condition  $G_s(\vec{R}, 0) = \delta(\vec{R})$ . Similar arguments are suitable for the angular displacements. Throughout this Thesis we are interested in the diffusive motion of spherical particles and the motion of relatively stiff chains made of individual beads. When a chain moves there is not only a translational and rotational displacement of the entity as a whole. There may also be small internal vibrational modes that may affect the dynamics of the system. Hence, an accurate description of this diffusive motion is not straightforward. Hereafter, we will simplify the problem by assessing the diffusion of the linear aggregates as the diffusion of a simple but important model: the rigid rod.

## Spherical Particles

In the following, we are going to study the diffusive behaviour of spherical particles.

- Translational Diffusion Equation



Due to spherical symmetry, the translational diffusion tensor is given by [50]

$$\hat{D}_0 = D_0 \hat{I}, \quad (2.17)$$

where  $D_0$  is the isotropic translational diffusion coefficient. Hence, the diffusion Equation 2.16 becomes

$$\frac{\partial}{\partial t} G_s(\vec{R}, t) = D_0 \nabla^2 G_s(\vec{R}, t). \quad (2.18)$$

- Rotational Diffusion Equation

In addition to the translational diffusive motion, spherical colloidal particle also present a rotational motion due to fluctuating forces exerted on the particle by the medium. If  $c(\hat{u}, t) d^2 \hat{u}$  is the number of particles found with orientation  $\hat{u}$  in  $d^2 \hat{u}$  at time  $t$ , then the diffusion equation is given by

$$\frac{\partial}{\partial t} c(\hat{u}, t) = \left( \vec{L} \cdot \hat{D}_r \cdot \vec{L} \right) c(\hat{u}, t). \quad (2.19)$$

Due to spherical symmetry, the rotational diffusion tensor can also be considered as a scalar  $D_r$ .

- Combined Rotational-Translational Diffusion Equation

If now  $c(\hat{u}, \vec{R}, t) d^3 \vec{R}, d^2 \hat{u}$  represents the number of particles found at  $\vec{R}$  in  $d^3 \vec{R}$  with orientation  $\hat{u}$  in  $d^2 \hat{u}$  at time  $t$ , then the diffusion equation is given by

$$\frac{\partial}{\partial t} c(\hat{u}, \vec{R}, t) = D_0 \nabla^2 c - D_r \vec{L}^2 c(\hat{u}, \vec{R}, t), \quad (2.20)$$

which is separable in a rotation and translational part.

### Rigid Rod Particles

In the following, we are going to study the diffusive behaviour of long and thin rods.

- Translational Diffusion Equation

If  $\hat{u}$  is redefined as a unit vector aligned along the rod axis, then translational diffusion tensor is given by [50]

$$\hat{D}_0 = \bar{D}\hat{I} + (D_{\parallel} - D_{\perp}) \left[ \hat{u}\hat{u} - \frac{1}{3}\hat{I} \right], \quad (2.21)$$

where  $D_{\parallel}$  is the diffusion coefficient for motion *parallel to the principal axis*,  $D_{\perp}$  is the diffusion coefficient *perpendicular to this axis*, and  $\bar{D} = 1/3(D_{\parallel} + 2D_{\perp})$  is the *isotropic translational diffusion coefficient*. Hence, translational diffusion of a linear particle is described by the two diffusion coefficients  $D_{\parallel}$  and  $D_{\perp}$ . According to Equation 2.21 the diffusion equation 2.16 becomes

$$\frac{\partial}{\partial t} G_s(\vec{R}, t) = \bar{D}\nabla^2 G_s(\vec{R}, t) + (D_{\parallel} - D_{\perp}) [(\hat{u} \cdot \nabla)^2 - \frac{1}{3}\nabla^2] G_s(\vec{R}, t). \quad (2.22)$$

- Rotational Diffusion Equation

If  $c(\hat{u}, t)d^2\hat{u}$  is the number of rods found with orientation  $\hat{u}$  in  $d^2\hat{u}$  at time  $t$ , then the diffusion equation is given by

$$\frac{\partial}{\partial t} c(\hat{u}, t) = \left( \vec{L} \cdot \hat{D}_r \cdot \vec{L} \right) c(\hat{u}, t). \quad (2.23)$$

Hereafter, we will ignore the rotation around the rod axis. Hence,  $\hat{D}_r$  only assesses the rotational around the direction perpendicular to the rod axis.

- Combined Rotational-Translational Diffusion Equation

If  $c(\hat{u}, \vec{R}, t)d^3\vec{R}, d^2\hat{u}$  represent the number of particles found at  $\vec{R}$  in  $d^3\vec{R}$  with orientation  $\hat{u}$  in  $d^2\hat{u}$  at time  $t$ , the diffusion equation is given by

$$\begin{aligned} \frac{\partial}{\partial t} c(\hat{u}, \vec{R}, t) &= \bar{D}\nabla^2 c(\hat{u}, \vec{R}, t) - \hat{D}_r \vec{L}^2 c(\hat{u}, \vec{R}, t) \\ &+ (D_{\parallel} - D_{\perp}) [(\hat{u} \cdot \nabla)^2 - \frac{1}{3}\nabla^2] c(\hat{u}, \vec{R}, t). \end{aligned} \quad (2.24)$$

If the particle suffers a translational displacement, the rotational diffusion will be harder in a plane perpendicular than in a plane parallel to its displacement. That means that the rotational diffusion should depend on the relative orientation between  $\vec{R}$  and  $\vec{u}$  [26]. Hereafter, however, we

will ignore a possible anisotropy in the rotational diffusion coefficient, and  $D_r$  will be assumed to be a scalar.

If the difference ( $D_{\parallel} - D_{\perp}$ ) is small, as would be the case for short rods or spherical particles, the last term in Equation 2.24 can be ignored, and the previous Equation would be separable in the rotation and translational contributions. However, if ( $D_{\parallel} - D_{\perp}$ ) is sufficiently large, the full Equation 2.24 must be apply, and there would be coupling between translational and rotational diffusive modes.

As we will see in Section 2.5, all the diffusion coefficients described throughout this Section can be related to the size of brownian particles by solving the corresponding hydrodynamic equations.

## 2.5 Diffusion Coefficients

The diffusion coefficient of a Brownian particle is given by the Einstein relation  $\hat{D}_0 = k_B T \hat{\gamma}^{-1}$  (Equation 2.8), where the friction coefficient  $\hat{\gamma}$  has been introduced as the ratio between the force that the fluid exerts on the particle and the particle's velocity. In the case of finite dilution, the friction coefficient of each particle depends on the positions and velocities of the others. Since the fluid flow velocity induced by the motion of a brownian particle affects the motion of the remaining particles, the friction coefficient  $\hat{\gamma}$  is a matrix which depends on the positions of the Brownian particles. In the case of infinite dilution, however, the particles are independent, and the friction coefficient of each particle only depends on its geometry.

As we have seen in Section 2.3, the time scale on which colloidal particles move is much larger than those of the solvent. Hence, it is sufficient to consider the interaction of the solvent molecules with the colloidal particle only in an averaged way. Consequently, Brownian motion can be described through macroscopic equations and macroscopic properties of the solvent, i.e. its temperature and viscosity. For the calculation of the friction coefficients we have to resolve the *Navier-Stokes equation*<sup>7</sup>. It allows us to assess the fluid flow as a result of traslation or rotation of the Brownian particles. For incompressible fluids, and assuming constant temperature and mass density, the Navier-Stokes equation reduces to

$$\rho_0 \frac{\partial \vec{u}(\vec{r}, t)}{\partial t} + \rho_0 \vec{u}(\vec{r}, t) \cdot \nabla \vec{u}(\vec{r}, t) = \eta \nabla^2 \vec{u}(\vec{r}, t) - \nabla p(\vec{r}, t), \quad (2.25)$$

---

<sup>7</sup>The Navier-Stoke equation is Newton's equation of motion for the fluid flow.

where  $\rho_0$  is the constant mass density of the fluid,  $\vec{u}(\vec{r}, t)$  is the fluid flow velocity, and  $p(\vec{r}, t)$  the pressure. The constant  $\eta$ , which is a scalar quantity for isotropic fluids, is the *shear viscosity*. Together with the *Continuity Equation*<sup>8</sup>, Equation 2.25 determines the fluid flow once the boundary conditions are specified.

In this work, however, only an outline of the derivation is provided. A detailed discussion about this complicated hydrodynamic problem, however, falls outside the scope of this work.

### 2.5.1 Spheres

For the calculation of the friction coefficient of spherical brownian particles we have to solve the Navier-Stokes equation and to assess the fluid flow as a result of their traslation or rotational movement. The boundary conditions employed, so called *Stick Boundary Conditions*, assume that the velocity of the fluid on the surface of the Brownian particles is equal to the velocity of the particle's surface.

#### Translational Diffusion Coefficients

If we consider a spherical particle moving with a constant velocity  $\vec{v}$  in a fluid, then the stick boundary conditions reads [26]

$$\vec{u}(\vec{r}) = \vec{v}, \quad \forall \vec{r} \in \textit{particle surface}. \quad (2.26)$$

On the other hand

$$\vec{u}(\vec{r}) \rightarrow 0, \quad r \rightarrow \infty, \quad (2.27)$$

Once the velocity of the Brownian particles is determinated, forces which the particles exert on the fluid can be calculated from Equation 2.25, together with the previous boundary contitions. Finally, the relation between the force and the particle velocity is given by [26]:

$$\vec{f} = \hat{\gamma}\vec{v} = 6\pi\eta a\vec{v}. \quad (2.28)$$

This is the *Stokes friction law* for translational motion of a sphere. According to Equations 2.8, 2.17, and 2.28 the translational diffusion coefficient of a sphere is given by

---

<sup>8</sup>The continuity equation expresses the conservation of mass.

$$D_0 = \frac{k_B T}{6\pi\eta a}, \quad (2.29)$$

which is known as *Stokes-Einstein* equation. For colloidal monomeric particles in water at laboratory temperatures,  $D_0 \approx 10^{13} - 10^{12} m^2 s^{-1}$ .

### Rotational Diffusion Coefficient

Analogous to the calculation of the translational friction coefficient described in the previous Subsection, we now consider a spherical particle rotating with a constant angular velocity  $\vec{\Omega}$  in a fluid. In this case, the stick boundary conditions read [26]

$$\vec{u}(\vec{r}) = \vec{\Omega} \times \vec{r}, \quad \forall \vec{r} \in \text{particle surface}, \quad (2.30)$$

and

$$\vec{u}(\vec{r}) \rightarrow 0, \quad r \rightarrow \infty. \quad (2.31)$$

Once the angular velocity of the Brownian particles is determined, torques which the particles exert on the fluid can be calculated from Equation 2.25, together with the previous boundary conditions. Hence, the relation between the torque and the angular velocity is given by [26]:

$$\vec{\tau} = \hat{\gamma}_r \vec{\Omega} = 8\pi\eta a^3 \vec{\Omega}. \quad (2.32)$$

This is the *Stokes friction law* for rotational motion of a sphere. According to Equations 2.8 and 2.32 the rotational diffusion coefficient of a sphere is given by

$$D_r = \frac{k_B T}{8\pi\eta a^3}. \quad (2.33)$$

### 2.5.2 Rods

For the calculation of the friction coefficients of a rodlike Brownian particle we have to assess the fluid flow as a result of translation and rotation. This treatment, however, is by far more complicated than that of a brownian sphere. Since there are no analytical expression for the friction coefficient of a rod with arbitrary length  $L$  and radius  $a$ , a general method have been developed by several authors [51, 52]. In this method, the rod is modeled as a rigid array of  $N$  connected spherical particles. This array model allows us to resolve

the Navier-Stokes equation, applying the results previously obtained for the spherical objects.

### Translational Diffusion Coefficients

Hydrodynamic interactions play a significant role for a single rod even at infinite dilution. The reason is that a moving rod segment induces a flow at the position of a neighbouring segment. In case of rigid arrays of  $N$  connected spherical particles, the hydrodynamic forces are approximately equal for each bead. Only the beads near the ends of the rod experience differing hydrodynamic forces. Hence, for very long rods the end effects can be neglected, and the Navier-Stokes equation has an analytical solution given by [26]

$$\begin{aligned}\vec{f}_{\perp}^h &= \hat{\gamma}_{\perp} \vec{v}_{\perp} = \frac{8\pi\eta Na}{\ln N} \vec{v}_{\perp} \\ \vec{f}_{\parallel}^h &= \hat{\gamma}_{\parallel} \vec{v}_{\parallel} = \frac{4\pi\eta Na}{\ln N} \vec{v}_{\parallel},\end{aligned}\tag{2.34}$$

where the forces  $\vec{f}_{\parallel,\perp}^h$  parallel and perpendicular to the rod axis include hydrodynamics effects, and  $N = L/(2a)$  is the number of particles per rod. As we have seen in Section 2.4, the translational diffusion of a linear particle is described by the diffusion coefficients  $D_{\parallel}$  and  $D_{\perp}$ . As a result of the hydrodynamic interactions, the diffusion coefficient  $D_{\parallel}$  in the direction parallel to the rod axis is about twice as large as the one for perpendicular diffusion  $D_{\perp}$ .

M. Tirado et al. included end effects to assess the friction coefficient of finite rigid cylinders [51, 52]. These authors solved the hydrodynamic equations in cylindrical coordinates, and found that the translational friction coefficients are given by

$$\begin{aligned}\gamma_{\perp}(N) &= \frac{8\pi\eta Na}{\ln N + \gamma_{\perp}^{end}(N)} \\ \gamma_{\parallel}(N) &= \frac{4\pi\eta Na}{\ln N + \gamma_{\parallel}^{end}(N)},\end{aligned}\tag{2.35}$$

where the cylinder length function  $\gamma^{end}(N)$  accounts for the so-called end of chain effects. In their theoretical approach, these authors modeled the circular cylinder as a stack of  $N_r$  rings, each composed of  $s$  touching spheres of radius  $\sigma$ . Hence, for a perfectly smooth cylinder, the ratio of the number of frictional

elements  $sN_r$  to the area of the cylindrical surface approaching infinity, the end functions are given by

$$\begin{aligned}\gamma_{\perp}^{end}(N) &= 0.84 + \frac{0.18}{N} + \frac{0.24}{N^2} \\ \gamma_{\parallel}^{end}(N) &= -0.21 + \frac{0.90}{N},\end{aligned}\tag{2.36}$$

and the diffusion coefficients are finally given by

$$\begin{aligned}D_{\perp}(L) &= \frac{k_B T}{4\pi\eta L} \left( \ln\left(\frac{L}{2a}\right) + \gamma_{\perp}^{end}(L) \right) \\ D_{\parallel}(L) &= \frac{k_B T}{2\pi\eta L} \left( \ln\left(\frac{L}{2a}\right) + \gamma_{\parallel}^{end}(L) \right).\end{aligned}\tag{2.37}$$

So far, other treatments have been proposed in order to assess the friction coefficients of finite rigid cylinders. However, all embody certain degrees of approximation, and lead to a variety of values for the end-effects corrections [53, 54].

### Rotational Diffusion Coefficients

As translational diffusion, the rotational diffusion coefficient of finite rods can be obtained by solving the Navier-Stokes equations

$$D_r(L) = \frac{3k_B T}{\pi\eta L^3} \left( \ln\left(\frac{L}{2a}\right) + \gamma_r^{end}(L) \right).\tag{2.38}$$

M. Tirado et al. have also included end effects to describe the rotational friction coefficient of finite rigid cylinders. According to these authors the chain end effect functions may be written as

$$\gamma_r^{end}(L) = -0.66 + \frac{0.92}{N} - \frac{0.05}{N^2}.\tag{2.39}$$

Figure 2.4 shows the size dependence of the different diffusion coefficients defined so far.

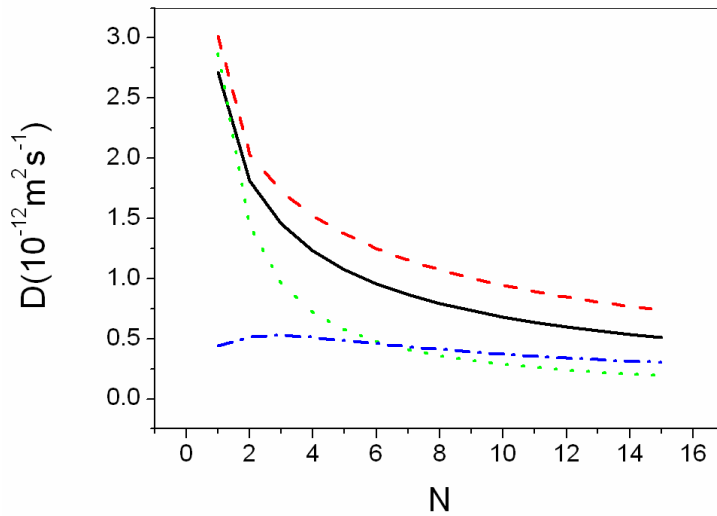


Figure 2.4: Perpendicular (continuous line  $-$ ) and parallel (dashed line  $-$ ) translational diffusion coefficients of rod-like particles as function of  $N$ , ratio between the length  $L$  and the width of the cylinders  $2a$ . The rotational diffusion coefficient multiplied by the factor  $Na^2/3$  is also represented (dotted-dashed line  $- \cdot -$ ). On the other hand, the translational diffusion coefficient of a sphere is given by the dotted line ( $\cdot \cdot$ ). In the latter case  $N$  represent the ratio between the sphere diameter and the cylinder width. All the calculations were performed for  $d = 170 \text{ nm}$ , and  $T = 298 \text{ K}$ .

## 2.6 Interactions in Magnetic Colloids

The stability and the aggregation kinetics of a colloidal suspension are controlled by the total particle–particle interaction energy. According to the classical DLVO<sup>9</sup> approach the total interaction energy  $E_T$  of charged particles dispersed in water may be expressed as the sum of a repulsive electrostatic term  $E_{El}$  and an attractive London-van der Waals interaction  $E_{LvdW}$ . In the case of magnetic fluids, magnetic additional dipole-dipole  $E_{DD}$  interaction has to be added as soon as an external magnetic field is applied [57].

There are interactions which are special for colloidal systems. As a particle

<sup>9</sup>DLVO stands for Derjaguin-Landau, and Verwey-Overbeek, the scientists who established the theory concerning these kind of interactions [55, 56].



translates or rotates it induces a fluid flow in the solvent which indirectly affects other particles in their motion. Brownian particles thus exhibit hydrodynamic interactions. In dilute colloidal suspensions, however, the movements of the particles do not affect the rest of particles significantly in their motion. Since in the experiments we always have worked at very diluted conditions, hereafter we will neglect the effects of hydrodynamic interactions on the stability of colloidal suspensions.

### 2.6.1 DLVO Theory

A considerable advance in the quantitative understanding of colloidal stability was achieved when the DLVO theory of the interaction of two colloidal particles was developed [55, 56]. Using this theory, colloid stability could be explained as a consequence of the balance of two interactions: an attractive London-van der Waals interaction,  $E_{LvdW}$ , and an electrostatic repulsive interaction,  $E_{El}$ . Assuming that these two components are independent, the total potential energy  $E_T$  could be expressed as

$$E_T = E_{El} + E_{LvdW}. \quad (2.40)$$

In the next subsections, the results of what is commonly referred as DLVO theory will be briefly reviewed.

#### London-van der Waals Interaction

The destabilizing attractive London-van der Waals interaction arises from molecular interactions between the particles. London-van der Waals interactions are of a relatively short range and can lead to irreversible aggregation of the colloidal particles. These attractive forces, however, may be masked by long range repulsive interactions arising from charges adhered on the surface of the particles, polymer chains grafted on the surface, or solvation layers.

For what follows, we consider two spherical particles of radius  $a$  whose centers are separated by a distance  $r$ . Even when we assume that the spheres are neutral, the particles suffer a mutual attraction<sup>10</sup>. The molecules which make up the particles are attracted to one another by London-van der Waals interactions. The interaction arises from the attractive force for transient dipoles in molecules without permanent multipole moments. By adding up all the pairs of interactions between the molecules in one particle, with those in

---

<sup>10</sup>In some unusual cases the London-van der Waals interaction can be repulsive [58].

the other particle, one can calculate the total attractive potential between the two spheres. This interaction is isotropic, and for two equally sized spherical particles of radius  $a$  given by

$$E_{LvdW}(r) = -\frac{A}{6} \left[ \frac{2a^2}{r^2 - 4a^2} + \frac{2a^2}{r^2} + \ln \left( 1 + \frac{4a^2}{r^2} \right) \right], \quad (2.41)$$

where  $A$  is the *Hamaker constant* of the particles within a given medium. The concentration of colloidal particles is assumed to be sufficiently diluted to consider only the interaction between pairs of particles. In this work, a typical value of  $A = 10^{-20} J$  for the Hamaker constant of aqueous suspensions of polystyrene particles has been used. For metallic oxides, the Hamaker constant is of the order of  $A = 10^{-19} J$  [2]. Since for large distances  $E_{LvdW} \propto r^{-6}$ , the London-van der Waals interaction is relatively unimportant except at very small particle-particle distances.

### Electrostatic Interaction

The surface of a colloidal particles may carry ionized chemical groups, or charged polymers can be chemically attached to the surface of the particles. The charged surfaces of such colloidal particles repel each other. However, in a polar solvent the pair repulsion is not a Coulomb repulsion proportional to  $1/r$ , where  $r$  is the distance between the centres of the particles. The electrostatic repulsion is screened to some extent by the free ions in the solvent. Since the particles are immersed in an electrolyte solution, there will be on average an excess of ions of the opposite charge around the colloidal particles which tend to screen the charges on the particles. On the other hand, the charged surface of a colloidal particle expels the free ions whose charge is of the same sign from the region around the particle. Therefore, a charge distribution referred as *double layer* is formed around the particles, partly screening the surface charge. The asymptotic form of the pair interaction potential for large distances, where the potential energy is not too large, is a screened Coulomb potential, or equivalently, a Yukawa type potential proportional to  $(\exp -(\kappa r))/r$ . The electrostatic interaction arises from the overlapping of the electrical double layers. For like-charged particles this interaction gives rise to a repulsion between the particles.

If the colloidal suspension is considered to consist of spheres of radius  $a$  in a monovalent aqueous electrolyte solution, the ions are approximated as point charges  $\pm e$ , and the electrostatic potential on the surface of the particles is taken to be  $\psi_0$  with respect to the bulk electrolyte, the electrostatic potential

is given by the *Poisson-Boltzmann equation* which reads

$$\nabla^2\psi(\vec{r}) = -\frac{e}{\epsilon k_B T} \sum_i^N z_i n_i \exp\left(\frac{z_i e \psi(\vec{r})}{k_B T}\right), \quad (2.42)$$

where  $\epsilon = \epsilon_r \epsilon_0$  is the dielectric constant of the solvent. The dielectric constant of the vacuum is  $\epsilon_0 = 8.85 \times 10^{-12} C^2 J^{-1} m^{-1}$ , and the solvent is usually approximated as a uniform dielectric medium with a relative dielectric constant  $\epsilon_r$ <sup>11</sup>. In Equation 2.42,  $N$  ionic species are considered, whose bulk concentrations and electric charges are  $n_i$  and  $z_i e$ , respectively.

In order to determine  $E_{El}$ , it is necessary to solve Equation 2.42 numerically for a two-sphere geometry. Using a moderate potential ( $\psi \leq k_B T/e \approx 25.4$  mV), the Poisson-Boltzmann equation 2.42 can be linearized

$$\nabla^2\psi(\vec{r}) = \kappa^2\psi(\vec{r}). \quad (2.43)$$

The screening parameter  $\kappa$  is defined as

$$\kappa = \sqrt{\frac{e^2}{\epsilon k_B T} \sum_i^N z_i^2 n_i}, \quad (2.44)$$

and the length scale of the electric double layer interaction is given by the *Debye length*  $\kappa^{-1}$ , which depends on the ionic strength of the suspension medium. If we assume the surface potential remains constant when the particle approach each other, a reasonable expression for the repulsive electrostatic term  $E_{El}(H)$  is given by

$$E_{El}(H) = 2\pi a \epsilon_r \epsilon_0 \psi_0^2 \ln(1 + \exp(-\kappa H)), \quad (2.45)$$

where  $H = r - 2a$  is the distance between the particle surfaces. Equation 2.45 was derived by applying the Derjaguin approach of infinitesimally small, parallel rings in each particle that contribute to the net electrostatic potential of particles with thin double layers [28]. The *Stern potential*  $\psi_\delta$  is the effective potential in the thin region, or *Stern layer*, where the counter-ions, i.e. the electrolyte ions whose charge is opposite in sign to the particle charge, are strongly bound to the particle surface. The absorbed ions neutralize part of the particle surface charge, giving rise to  $|\psi_\delta| < |\psi_0|$ . Unfortunately, the Stern potential is non trivially related to the surface potential  $\psi_0$ . As frequently found in colloid stability, the Stern potential is identified with the

---

<sup>11</sup> $\epsilon_r = 78.5$  for water at 25°C.

experimental available zeta potential, which can be obtained directly from electrophoretic mobility measurements. When surface potentials are not low enough to allow the linear approximation of the Poisson-Boltzmann equation to be used, the electrostatic interaction is usually given by the linear superposition approximation

$$E_{El}(H) = 2\pi a \epsilon_r \epsilon_0 \psi_0^2 \exp(-\kappa H). \quad (2.46)$$

In practice, the net interaction between charged colloidal particles suspended in aqueous media can be easily controlled by changing the electrolyte concentration. The electrolyte compresses the electric double layers around the particles and so varies the electrostatic interaction due to electric double layers overlap.

### 2.6.2 Magnetic Dipolar Interaction

For the specific case of magnetic colloids, the DLVO theory of colloidal stability has to be extended in order to include magnetic dipole-dipole interactions and the corresponding interaction potential  $E_{DD}$ . In the presence of induced or permanent magnetic dipoles, the total interaction potential energy is assumed to be

$$E_T = E_{El} + E_{LvdW} + E_{DD}. \quad (2.47)$$

In order to estimate the long-range magnetic interactions, the magnetized spheres are usually approximated as point dipoles of a well-defined magnetic moment. The *magnetic moment*  $\vec{m}$  may be estimated using the relationship

$$\vec{m} = \frac{4}{3}\pi a^3 \vec{M}, \quad (2.48)$$

where  $\vec{M} = \chi \vec{H}$  is the *magnetization*,  $\vec{H}$  is the strength of the external magnetic field, and  $\chi$  is the *magnetic susceptibility* of the particles.

#### Dipole-Dipole Interaction

For a given dipole orientation, the magnetic dipolar interaction between two identical dipoles  $\vec{m}$  is given by<sup>12</sup>

$$E_{DD}(\vec{r}) = \frac{\mu_0 \mu_s}{4\pi r^3} [(\vec{m}_i \cdot \vec{m}_j) - 3(\vec{m}_i \cdot \hat{r})(\vec{m}_i \cdot \hat{r})], \quad (2.49)$$

---

<sup>12</sup>Neglecting higher order dipolar interactions.

where  $r$  is the distance between the dipoles,  $\mu_0$  is the magnetic permeability of the vacuum, and  $\mu_s$  is the relative magnetic permeability of the medium. The dipole-dipole interaction is anisotropic, and depends on the relative orientation between the magnetic moments  $\vec{m}$  and the position vector  $\vec{r}$ .

Under the presence of an external magnetic field the magnetic moments are aligned by a torque that is given by

$$\vec{\tau} \propto \vec{m} \times \vec{H}. \quad (2.50)$$

For two identical magnetic moments aligned along the field direction the potential energy becomes

$$E_{DD}(r, \varphi) = \frac{\mu_0 \mu_s m^2}{4\pi r^3} (1 - 3 \cos^2 \varphi), \quad (2.51)$$

where  $\varphi$  is the angle between the field direction and the center-to-center vector.

The interaction may be either attractive or repulsive and its range depends on the angle  $\varphi$ . The interaction is attractive when the dipoles are head-to-tail and repulsive when they are side-by-side. According to magnetic theory, the interaction range  $h(\varphi)$  is proportional to  $\sqrt[3]{|3 \cos^2 \varphi - 1|}$ , and the attractive region has a dumbbell like shape and fits in a symmetric double cone with an aperture angle of  $\varphi_c \approx 55^\circ$  with respect to the field direction (please, see Figures 2.5 and 2.6). Hence, the magnetic interaction is cylindrically symmetric, while London van der Waals and electrostatic interactions are spherically symmetric.

When the maximum attraction energy, at  $r = 2a$  and  $\varphi = 0 \text{ rad}$ , is gauged with respect to the thermal energy, we obtain the dimensionless dipole strength  $\lambda$

$$\lambda = -\frac{E_{DD}(r = 2a, \varphi = 0 \text{ rad})}{k_B T} = \frac{\pi \mu_0 \mu_s a^3 \chi^2 H^2}{9 k_B T}. \quad (2.52)$$

For  $\lambda < 1$  the thermal fluctuations overcome the dipole-dipole interactions, preventing the aggregation process. For  $\lambda > 1$  the aggregation is irreversible as long as the magnetic field is present.

### Mutual Induction

When two magnetic particles are under the influence of an external magnetic field, each generates an additional magnetic field at the position of the other particle. If the particles are modeled as identical dipoles  $\vec{m}$  placed at the

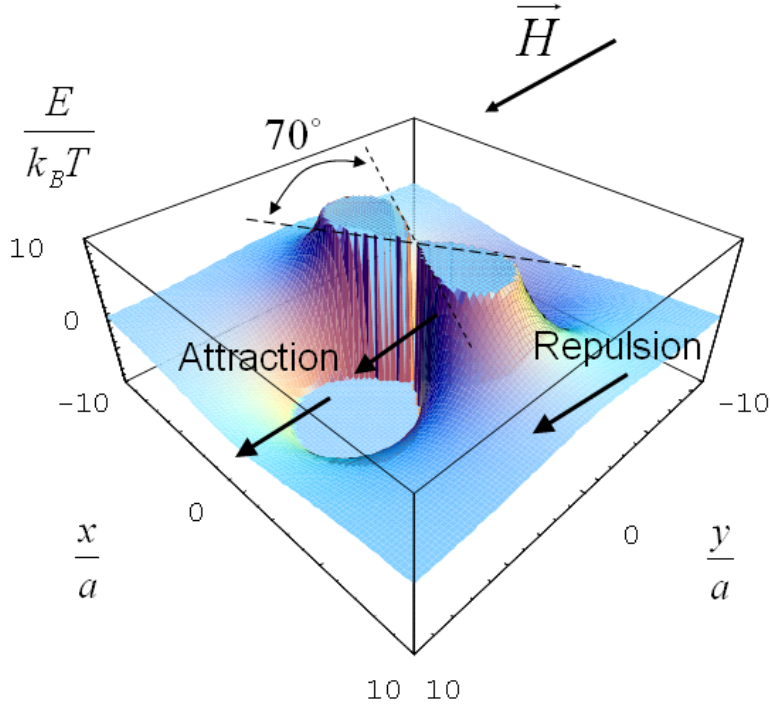


Figure 2.5: Schematic picture for the total potential energy between two magnetic spheres of radius  $a$ . The magnetic particles are approximated as point dipoles, symbolized by the arrows in the image. For two aligned dipoles the potential energy is attractive when the dipoles are head-to-tail, and repulsive when they are side-by-side.

center of the spheres, and separated a distance  $r$ , then the total external field acting on each particle is given by

$$\vec{H}_{tot} = \vec{H}_{ext} + \vec{H}_1, \quad (2.53)$$

where

$$\vec{H}_1 = \frac{3(\vec{m}\hat{r})\hat{r} - \vec{m}}{4\pi r^3} \quad (2.54)$$

is the field generated by each magnetic moment at the center of the other. If the magnetic moments are aligned parallel to the external field, then  $\vec{H}_1 = \vec{m}/2\pi r^3$  [59].

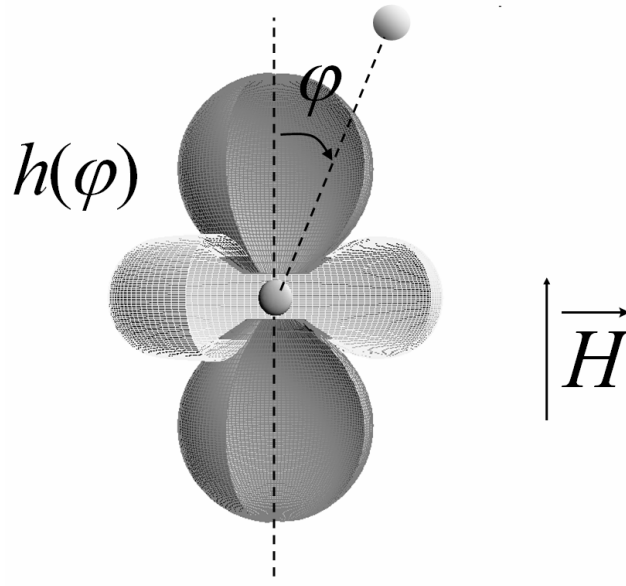


Figure 2.6: For two dipoles aligned along the field direction the interaction range  $h(\varphi)$  depends on the angle  $\varphi$  between the external magnetic field and the line joining the particle centers.

Zhang and Widom studied the magnetic forces acting within a field induced linear aggregate as a function of the external applied field  $\vec{H}_{ext}$  and the particle separation  $r$  [15]. Combining Equation 2.48 with Equations 2.53 and 2.54, the magnetic moment  $\vec{m}$  in terms of the external applied field is

$$\vec{m} = \frac{\frac{4\pi}{3}a^3\chi}{1 - \frac{2\pi}{3}\left(\frac{a}{r}\right)^3\chi} \vec{H}_{ext}, \quad (2.55)$$

when the two dipole moments are aligned parallel to the field direction. For a particle within an infinitely long chain of particles with equal spacing  $r$ , the total field from all other particles is

$$\vec{H}_1 = 2 \sum_{n=1}^{\infty} \frac{\vec{m}}{2\pi(nr)^3} = \zeta(3) \frac{\vec{m}}{2\pi r^3}, \quad (2.56)$$

where  $\zeta(3) = \sum_{n=1}^{\infty} \frac{1}{(n)^3} = 1.202$  is the *Riemann function*. Hence, according to the Equation 2.56, the magnetic moment is given by

$$\vec{m} = \frac{\frac{4\pi}{3}a^3\chi}{1 - \frac{4\zeta(3)}{3}\left(\frac{a}{r}\right)^3\chi} \vec{H}_{ext}, \quad (2.57)$$

and the mutual induction increases dramatically the magnetic moment of the particles. If the particles are in contact and  $\chi \sim 1$ , then a particle in an infinite linear aggregate is about 20% more magnetized than an isolated particle. On the other hand, mutual induction also increases the aperture angle of the attractive zone  $\varphi_c$ . Considering  $\chi \sim 1$ , the aperture angle  $\varphi_c$  increases by 8% [46]. The finite size of the linear aggregates reduces the  $\zeta(3)$  function, as we will see in the Section 3.5.4.

### Grain-Grain Interaction

Suspensions of composite magnetic nano-particles are frequently employed. The magnetic character of these particles often is due to the presence of small grains of iron oxide distributed within the organic matrix. Since the magnetic grains embedded within the polystyrene are very small (1-20 nm), these magnetized spheres are usually treated as point dipoles of a well-defined magnetic moment for which the dipole model is applicable. However, due to the  $r^{-3}$  dependence of the magnetic interaction neighbouring grains will contribute more on the total energy than the grains which are more separated, and a dependence on the spatial distribution of the grains could be expected. Trying to describe the influence of the grain size, the number of grains, or the spatial distribution of the grains on the total magnetic interaction, we have calculated  $E_{DD}$  as the sum of all the interactions between pairs of embedded grains.

### Lateral Interactions between Chains

In this Subsection we will briefly summarize several theories about the lateral interaction of dipolar chains, including the interaction of rigid chains and the effects of thermal fluctuations and chain defects:

- Rigid Chains

The total dipolar potential energy can be determined as the sum of all the interactions between pairs of dipoles. Hence, aligned chains of rigid dipoles exhibits short range interactions perpendicular to their axis. Furst and Gast derived a model in which the dipoles form two parallel chains of 50 particles [1]. The authors take into account the mutual



induction between particles due to the induced field from all other particles, and calculate the interaction energy as function of the lateral separation between the chains. The sum of all the interaction between the pairs dipoles give rise to either attractive or repulsive configurations depending on the lateral separation, and the relative position of the neighbouring chains along the chain axis direction.

- Thermal Fluctuations

According to the previously mentioned authors, two straight chains do not attract unless they are almost in contact. In a real system, however, the chains present thermal fluctuations (as we will see in Section 4.5.3, and in Chapter 6). These effects cause variations in the field around the dipoles, and thus in the lateral interaction that the chains experience. In order to explain this, Halsey and Toor (HT) determined that these fluctuations may give rise to a long-range attraction between the chains (Landau-Peierls interactions)<sup>13</sup> [1, 61]. This long-range interaction was predicted to be independent of the applied field strength. Later, Martin et al. proposed an extension of the HT model that takes into account the field strength dependency [62].

- Chain defects

In a real system the chains also may present configurational defects (as we will see in Section 3.7.2). Likewise, chain defects also create local variations in the dipole moment density and variations in the field around the dipoles. Martin et al. used computer simulations to study this defect-driven lateral aggregation [63].

### Field divergence

A net magnetic force on a dipole exists only in the presence of a field divergence. It is given by

$$\vec{F}(\vec{r}) = -\vec{\nabla}U = \mu_s\mu_0\vec{\nabla}\left(\vec{m}\cdot\vec{H}_{ext}(\vec{r})\right) = \mu_s\mu_0\left(\vec{m}\cdot\vec{\nabla}\right)\vec{H}_{ext}(\vec{r}). \quad (2.58)$$

Hence, the spatial field homogeneity will be crucial for the experiments since it avoids particle migration and, consequently, particle concentration heterogeneities.

---

<sup>13</sup>This kind of interactions are not new in Colloidal Science. London-van der Waals interactions are also due to the thermal fluctuations of molecular dipoles [60].

## 2.7 Aggregate Stability

In addition to the magnetic content, most of the magnetic particles bear electric surface charge. The corresponding electrostatic repulsion helps to ensure the stability of the system with regard to aggregation when no magnetic field is applied. However, when a uniaxial magnetic field is applied to a suspension of magnetic particles, a magnetic moment is induced in each bead and an anisotropic dipolar interaction arises. Consequently the particles self-organize due to the action of the field, and aggregates of particles aligned along the field direction are formed.

The potential energy corresponding to two approaching particles presents in general a secondary minimum due to the interplay between the electrostatic repulsion and the dipolar magnetic attraction [57, 64, 65]. A schematic plot of the total potential energy (Equation 2.47, which includes van der Waals, electrostatic and magnetic dipole interactions), versus the separation distance between two particles is shown in Figure 2.7. In the scheme, we represented a representative attractive configuration, where the angle between the external magnetic field direction and the line joining the particle centres is smaller than  $\varphi_c \approx 55^\circ$ .

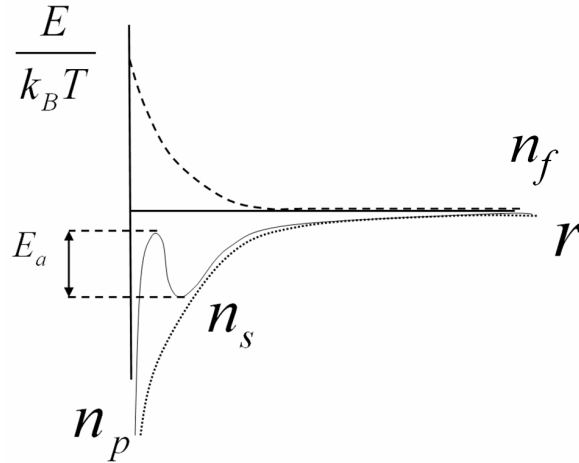


Figure 2.7: Scheme of a typical potential energy curve (solid line) which includes van der Waals, electrostatic (dashed line) and magnetic dipole interactions (dotted line). In the Figure  $n_s$ ,  $n_p$  and  $n_f$  denote the number of secondary bonds, primary bonds, and not yet established bonds, respectively.

The total energy curve shows a deep primary minimum at short distance and a shallower secondary minimum separated by an energy barrier. Therefore, particle aggregation may occur in the primary minimum, where the particles are in contact with each other, or in the secondary minimum, where the neighbouring particles within the linear aggregates are a short distance apart from each other. The height of the energy barrier is mainly determined by the electrostatic repulsion between the particles.

Secondary minimum aggregation is reversible, since the secondary minima disappear when the magnetic field is turned off. Then, the electrostatic repulsion controls the stability of the system and pushes the particles away from each other, giving rise to a complete break up of the linear aggregates [64, 65, 66]. On the other hand, primary minimum aggregation is irreversible. At close contact, the short range attractive London van der Waals interaction is capable to keep the particles together even when the external field is removed [21, 67, 68]<sup>14</sup>. The linear aggregates formed in this way have an almost infinite lifetime. The bonds in these chains are strong enough to withstand not only the absence of the magnetic field but also the drying process that is necessary for taking TEM images, as we observed in Figure 2.2. Hence, the magnetic particles can be found in three different configurations when the magnetic field is applied:

1. Aggregated in the primary-minimum (close contact).
2. Aggregated in the secondary-minimum (short distance).
3. Unlinked (large distance).

In Figure 2.7,  $n_p$ ,  $n_s$  and  $n_f$  denote the number of primary bonds, secondary bonds, and open bonds (not yet established bonds), respectively.  $n = n_s + n_p$  is the total number of links. The neighbouring particles within the linear aggregates must overcome the energy barrier in order to go from a metastable secondary bond to a stable primary bond. Therefore, we propose the following rate equations for field induced reactions<sup>15</sup>:

$$\begin{aligned} \frac{dn_s}{dt} &= -\frac{dn_f}{dt} - k_{sp}n_s(t) \\ \frac{dn_p}{dt} &= k_{sp}n_s(t). \end{aligned} \tag{2.59}$$

---

<sup>14</sup>Permanent chains have also been obtained using absorbing polymers as particle linkers [20, 21, 22, 69]

<sup>15</sup>We thank Dr. José Manuel López López for the useful discussions.

Secondary bonds may turn into primary bonds when the corresponding particles overcome the potential barrier. The *rate constant*  $k_{sp}$  parametrizes the probability per unit time that a secondary bond turns into a primary bond. The rate coefficient includes all the factors that affect the reaction rate, except for number of secondary bonds, which is explicitly accounted for. The primary bonds, formed due to short range van der Waals interactions, are stable enough so that the back rate constant  $k_{ps}$  may be neglected completely. The equations proposed also assume that the bond formation between particles can be considered as independent events. Moreover, all the particles initially heading from the free unbounded state towards the primary minimum will indeed pass through a secondary bond for at least a short time. This assumption is only correct when the energy barrier between the primary and the secondary minimums is high enough, i.e. at not too high electrolyte concentration. Since the rupture of the linear aggregates is forbidden in these equations, it adequately describes the experimental observations only as long as the magnetic field is applied.

The primary bonds formed are found to be thermally activated, and so, the corresponding rate constant should be given by an Arrhenius law [21]

$$k_{sp} = \tau_0^{-1} \exp\left(-\frac{E_a}{k_B T}\right). \quad (2.60)$$

The Arrhenius equation determines the dependence of the rate constant  $k_{sp}$  on the temperature  $T$  and the *activation energy*  $E_a$ , i.e. the height of the energy barrier. The rate constant  $k_{sp}$  depends on temperature and also on the ionic strength [21]. The particles are supposed to stick when they collide along their line-of-centers with a relative kinetic energy that exceeds  $E_a$ . At an absolute temperature  $T$ , the fraction of particles that have a kinetic energy greater than  $E_a$  can be calculated from the Maxwell-Boltzmann distribution, and turns out to be proportional to  $\exp\left(-\frac{E_a}{k_B T}\right)$ . The units of the pre-exponential factor  $\tau_0^{-1}$  are identical to those of the rate constant ( $s^{-1}$ ). Hence, it is referred to as an *attempt frequency* of the reaction [70].

## 2.8 Sedimentation

Sedimentation of colloidal particles is a topic that has been studied extensively. Efforts have been made to address coupled aggregation and sedimentation processes, at moderate particle concentrations and taking into account different interparticle interactions such as van der Waals attraction, electrostatic re-

pulsion, steric repulsion, etc. [26, 71, 72]. However, only a few studies on sedimentation of magnetic particles have been reported so far [14, 73, 74, 75]. Repulsive interactions decelerate the sedimentation processes, since the brownian particles tend to keep a maximum distance [26]. The magnetic interaction, on the contrary, accelerates the settling of the magnetic particles. As we will see, linear aggregates sediment more quickly than monomeric particles, so sedimentation is even enhanced when an external magnetic field is applied.

Usually, the sedimentation processes are characterized with the help of the so-called *Péclet number*  $Pe = \frac{v_1^s a}{D_0}$  that quantifies the relative strength of sedimentation and diffusion effects. Here,  $v_1^s$  is the monomer sedimentation velocity, and  $D_0$  is the monomer diffusion coefficient.

During sedimentation, the gravitational force is balanced by the drag force. Hence, at low Reynolds number the sedimentation velocity of a chain of length  $2aN$  that is settling with its main axes oriented parallel to the ground, is given by

$$v_N^s = \frac{N^{\frac{4}{3}} \pi a^3 \Delta \rho g}{\gamma_{\perp}(N)}, \quad (2.61)$$

where  $\Delta \rho = \rho_p - \rho_m$  is the density mismatch between the chain forming particles and the continuous medium [59]. Including the friction coefficient  $\gamma_{\perp}(N)$  given by the Equation 2.35, the sedimentation velocity can be expressed as

$$v_N^s = \frac{\ln(N) + \gamma_{\perp}^{end}(N)}{6\eta} a^2 \Delta \rho g. \quad (2.62)$$

The sedimentation velocity of linear aggregates, however, can be affected significantly by convection and back flow effects. Furthermore, the fluid flow pattern may suffer a distortion due to the limited container size. The container walls that may also affect the sedimentation of the particles placed close to them [14, 76].

## Chapter 3

# Micro-Structural Evolution

*... estos átomos se mueven en el vacío infinito, separados unos de otros y diferentes entre sí en figuras, tamaños, posición y orden; al sorprenderse unos a otros colisionan y algunos son expulsados mediante sacudidas al azar en cualquier dirección, mientras que otros, entrelazándose mutuamente en consonancia con la congruencia de sus figuras, tamaños, posiciones y ordenamientos, se mantienen unidos y así originan el nacimiento de los cuerpos compuestos.*

Simplicio de Cilicia, comentando a Demócrito. S VI d.J.C.

.

The formation of complex structures from small subunits like atoms or colloidal particles have been investigated for decades [28, 77, 78]. In these processes the sub-units diffuse due to Brownian motion and eventually encounter each other. Bonding reactions may then lead to monomer-monomer, monomer-cluster, and cluster-cluster aggregation. Unlike equilibrium states in which a partition function may be determined, aggregation is a kinetic process far from equilibrium, in which the states of the system are intricately entangled in their history. Therefore, the familiar theorems of Statistical Mechanics are not applicable here, and the corresponding processes are difficult to describe theoretically.

Several theoretical and simulations approach have been developed to describe the behaviour of aggregating systems: Smoluchowski's coagulation equation, and the numerical simulations [77, 79]. Furthermore, scaling concepts and fractal geometry have shown to be useful tools for an adequate understanding of those processes. Based on these methods, the relationship between structural and kinetic aspects of aggregate formation and the underlying aggregation mechanism has been studied quite in detail [77], and the well-known *Diffusion* and *Reaction Limited Aggregation* regimes have been established.

- *Diffusion Limited Colloid Aggregation* (DLCA) occurs when long range interactions between the freely diffusing sticky particles are negligible, and the predominant term in the total interaction energy is an attractive short range interaction. Hence, two approaching particles will adhere upon contact, as soon as they are sufficiently close to feel this attractive force. In these processes, every collision between particles results in the formation of an aggregate. The aggregation rate is then limited by the time the clusters need to encounter each other by diffusion. This explains why relatively open and ramified structures, characterized by a fractal dimension<sup>1</sup> close to 1.75, have been found experimentally.
- *Reaction Limited Colloid Aggregation* (RLCA) occurs when there is a substantial, but not insurmountable, repulsive energy barrier between the particles. Thus the aggregation rate is limited by the diffusion time and the time taken for two clusters to overcome this repulsive barrier by thermal activation. In these processes only a very small fraction of cluster collision leads to the formation of an aggregate. This situation gives rise to more densely packed clusters and explains why the experimentally observed cluster fractal dimensions are close to 2.10.

These regimes correspond to the limiting cases of rapid and slow colloid aggregation that are well-known in Colloid Science.

### 3.1 Introduction

Although systems with isotropic interactions are fairly well understood, our knowledge of aggregation processes dominated by dipolar interactions is far from complete. When a field is present, the particles experience an attractive force along the field direction and a repulsive force normal to it. On the other

---

<sup>1</sup>Fractal dimension concept will be described in the Section 3.7.1.

hand, cluster diffusion ceases to be isotropic due to the linear geometry of the formed aggregates. The breakdown of the spherical symmetry gives rise to a rather complicated theoretical description of field induced aggregation process.

Thus far, the principal approach to these processes has been done within the framework of Smoluchowski's equation. In the case of aggregation of dipolar particles that are aligned under the influence of an external field, Miyazima et al. proposed a theoretical description based on the DLCA model, assuming that during field induced aggregation the cluster cross section must be independent of the cluster size [8]. However, these authors neglect not only the anisotropic character of chain diffusion but also the long range of magnetic interactions (Section 3.5.1). An alternative procedure, including logarithmic corrections to the diffusion coefficient of the linear aggregates, has been proposed by Miguel et al. [9] (see Section 3.6).

The aim of this Chapter is twofold: (a) to deepen our knowledge about chain formation processes deriving an aggregation kernel for a improved theoretical description of the experimental results; (b) to study the influence of different phenomena such as electrostatic interactions between the particles, or differential settling on field-induced aggregation. The proposed aggregation kernel will consider an effective aggregation cross section and will depend explicitly on the average range of the interactions. It will allow us to understand the influence of sedimentation, electrostatic interactions, or the strength of the magnetic field on field induced aggregation processes. On the other hand, the theoretical background that is necessary to deal with the geometry of the aggregates is briefly provided towards the end of this Chapter in order to achieve that this Thesis is selfcontained. In writing this Chapter, we tried to balance mathematical rigor with intuitive arguments.

## 3.2 Smoluchowski's Equation

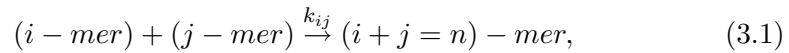
The most frequently used theoretical description of irreversible aggregation is the set of Smoluchowski's rate equations which describe the time evolution of the average number of clusters<sup>2</sup> made of  $n$  identical monomers per unit volume of solution  $c_n(t)$ . Within the framework of this theory, the cluster number concentration  $c_n(t)$  changes in time when two clusters coagulate and form a single cluster. Hence, the irreversible aggregation of two clusters forming a

---

<sup>2</sup>Throughout this Thesis the set of adjacent particles that keep approximately constant their relative positions will be referred indistinctly as "cluster" or "aggregate".



larger cluster can be written in terms of the following reaction scheme:



where  $i - mer$  denotes a cluster of mass  $i$ , and  $k_{ij} = k_{ji} \geq 0$  is a set of concentration independent coefficients named *kernel* that parametrizes the probability per unit time for aggregation of  $i$  cluster and  $j$  cluster. The assumption that there are only binary collisions limits the applicability of this deterministic description to dilute systems<sup>3</sup>. At low volume fraction the probability of three or more cluster collisions is small.

All the physics of these processes is entirely contained in  $k_{ij}$ . The aggregation rate constants contain information regarding the transport mechanisms that give rise to cluster-cluster contact, and the interactions that determine the probability of cluster-cluster attachment. Thus, the aggregation kernel will depend on the physical and chemical conditions of the aggregating system and, in general, on the size of the reacting clusters  $i$  and  $j$ . However, since there are no spatial variables in the Equation 3.1, neither the aggregation kernel  $k_{ij}$  nor the cluster size distribution  $c_n(t)$  take into account the spatial arrangement of the monomers within of the aggregates. Hence, the aggregation kernel is necessarily a mean-field approach, and the kernel itself has to be understood as an orientational and configurational average of the exact aggregation rates for two specific clusters of size  $i$  and  $j$  that collide under a particular orientation. Since the kernel has dimensions of volume per unit of time it can be understood as a flux. In fact, throughout Section 3.4 we will see that the aggregation kernel  $k_{ij}$  can be calculated as the flux of clusters of size  $i$  colliding with a sink cluster of size  $j$ .

In order to formulate an equation which describes the temporal evolution of the entire distribution of clusters-sizes  $(c_1, c_2, \dots, c_\infty)$ , one must account for all the pairs of collisions which generate or deplete a given cluster size. Hence, the clusters of size  $n$  appear as a product of the reaction between  $i - mers$  and  $j - mers$ , but may also disappear when they are involved in the formation of  $n + m$  species, by reacting with a  $m - mer$ . Since in diluted suspension we are only dealing with binary reactions, we can assume that the reaction rate is proportional to the concentration of the reacting clusters. For instance, the changes in the concentration of monomers are due to collisions with other monomers and aggregates (dimers, trimers, etc.), and the total change in monomer concentration can be expressed as

---

<sup>3</sup>Volume fraction less than 1% [78].

$$\frac{dc_1}{dt} = -c_1 \sum_{i=1}^{\infty} k_{1i} c_i. \quad (3.2)$$

The changes of the concentration of dimers is given by

$$\frac{dc_2}{dt} = \frac{1}{2} k_{11} c_1 c_1 - c_2 \sum_{i=1}^{\infty} k_{2i} c_i, \quad (3.3)$$

and in general, the change of the concentration of aggregates of kind  $n$  is given by

$$\frac{dc_n}{dt} = \frac{1}{2} \sum_{i+j=n} k_{ij} c_i c_j - c_n \sum_{i=1}^{\infty} k_{ni} c_i, \quad (3.4)$$

where  $n = 1, 2, \dots, \infty$ . This equation is the sum of two terms. The first term, or *gain term*, represents the rate at which  $n$ -mers are generated due to the aggregation of  $i$ -mers and  $j$ -mers for which  $i + j = n$ . The second term, or *loss term*, represents the rate at which  $n$ -mers are depleted when they themselves aggregate with any other  $i$ -mer. This infinite set of coupled deterministic differential equations was developed by von Smoluchowski at the beginning of the last century [79]. It has a unique solution  $c_n(t)$  that is determined by the initial conditions,  $c_n(0)$ . Thus, if we consider the matrix elements  $k_{ij}$  to be known quantities we may predict how the cluster size distribution  $c_n(t)$  evolves in time. The time evolution of the cluster size distribution characterizes the kinetic properties of a coagulating system.

The time evolution of the aggregation process is usually featured in global terms using the *number average cluster size* given by

$$N(t) = \frac{\sum_{i=1}^{\infty} i c_i(t)}{\sum_{i=1}^{\infty} c_i(t)}, \quad (3.5)$$

and the *weight-average cluster size* defined as

$$S(t) = \frac{\sum_{i=1}^{\infty} i^2 c_i(t)}{\sum_{i=1}^{\infty} i c_i(t)}. \quad (3.6)$$

Since the Smoluchowski's equation does not allow for cluster fragmentation, the average cluster size must grow monotonously in time. Therefore, as  $t \rightarrow \infty$ , this unrestrained growth results in the formation of a single huge cluster which contains all the sub-units.

It is useful to rewrite this equation in a dimensionless form

$$\frac{dX_n}{dT} = \frac{1}{2} \sum_{i+j=n} K_{ij} X_i X_j - X_n \sum_{i=1}^{\infty} K_{ni} X_i, \quad (3.7)$$

where  $X_n$  is the concentration of clusters  $c_n$  containing  $n$  primary particles normalized by the initial monomer concentration  $c_0$ , and the aggregation kernel  $K_{ij} = k_{ij}/k_s$ . The normalized aggregation time  $T = t/t_{agg}$  is scaled by the characteristic aggregation time  $t_{agg} = \frac{2}{c_0 k_{11}}$  for pure diffusion controlled aggregation where  $k_s$  is the dimer formation rate constant. In aqueous media at 298 K,  $k_s = 12.3 \times 10^{-18} m^3 s^{-1}$ .

### 3.3 Kernel Classification

Smoluchowski's equation is quadratic in  $c_i$ . Thus, the techniques used to solve linear equations are not applicable, and not surprisingly, a closed form solution for arbitrary  $k_{ij}$  is not always possible<sup>4</sup>. Despite of the mathematical complexity of the Smoluchowski's equation, some general conclusions concerning the behaviour of the solutions can be established from a much coarser knowledge of the kernel. According to van Dongen and Ernst [80, 81],  $k_{ij}$  can be analyzed in terms of two exponents  $\lambda_{hom}$  and  $\mu_{hom}$ :

$$\begin{aligned} k_{aiaj} &\approx C^{\lambda_{hom}} k_{ij} && (\lambda_{hom} \leq 2) \\ k_{i<j} &\approx k_0 i^{\mu_{hom}} j^{(\lambda_{hom} - \mu_{hom})} && (\lambda_{hom} - \mu_{hom} \leq 1), \end{aligned} \quad (3.8)$$

Here  $C$  is some positive constant, and  $k_0$  is a scale factor. The restrictions imposed in Equation 3.8 are required due to physical grounds and guarantee that clusters can never be more reactive than if they fully interpenetrate [28]. The *homogeneity exponent*  $\lambda_{hom}$  indicates whether the reactivity between aggregates of the same size increases or decreases with aggregate size:

$$\begin{aligned} k_{big-big} &> k_{small-small} && \text{for } \lambda_{hom} > 0 \\ k_{big-big} &= k_{small-small} && \text{for } \lambda_{hom} = 0 \\ k_{big-big} &< k_{small-small} && \text{for } \lambda_{hom} < 0. \end{aligned} \quad (3.9)$$

The exponent  $\mu_{hom}$  parametrizes whether large aggregates preferentially react with small aggregates or coagulation among large aggregates predominates.

<sup>4</sup>Only certain mathematical forms for  $k_{ij}$  allow Equation 3.4 to be solved exactly [28].

$$\begin{aligned}
k_{big-big} &> k_{big-small} && \text{for } \mu_{hom} > 0 \\
k_{big-big} &= k_{big-small} && \text{for } \mu_{hom} = 0 \\
k_{big-big} &< k_{big-small} && \text{for } \mu_{hom} < 0.
\end{aligned} \tag{3.10}$$

Though few real kernels obey Equations 3.8 exactly, many kernels can be well approximated by these equations for large  $i$  and  $j$ .

### 3.4 The Brownian Kernel

For pure diffusion-limited aggregation processes, the so called *Brownian kernel* (hereafter referred to as BK)

$$k_{ij}^{BK} = 4\pi(D_i + D_j)(a_i + a_j) \tag{3.11}$$

is known to describe the corresponding aggregation kinetics quite satisfactorily [28, 78, 79]. The BK is strictly valid only for solid spheres of radius  $a_i$  and  $a_j$  that undergo isotropic Brownian motion and aggregate as soon as they come into contact, i.e. when the distance between their centers becomes  $a_i + a_j$ .  $D_i$  is the diffusion coefficient, which for spherical particles of radius  $a_i$  is given by the Stokes-Einstein relation (Equation 2.29)

$$D_i = \frac{k_B T}{6\pi\eta a_i}.$$

The BK was derived considering a particle of size  $j$ , placed at the origin of the coordinate system, that is surrounded by initialing uniform field of freely diffusing spheres of radius  $a_i$  (please, see the Figure 3.1). The density of diffusing spheres  $c_i(\vec{r}, t)$  obeys the diffusion equation (see Equation 2.18)

$$\frac{\partial c_i(\vec{r}, t)}{\partial t} = D_i \nabla^2 c_i(\vec{r}, t).$$

Under spherical symmetry, Equation 3.12 is given by

$$\frac{\partial c_i(r, t)}{\partial t} = D_i \left( \frac{\partial^2 c_i(r, t)}{\partial r^2} + \frac{2}{r} \frac{\partial c_i(r, t)}{\partial r} \right). \tag{3.12}$$

The  $a_j$  particle is acting as a perfect sink when all the particles of radius  $a_i$  that come into contact with it will form aggregates of size  $i + j$ . Hence,

there are no individual particles of radius  $a_i$  at the contact surface and the corresponding boundary condition becomes  $c_i(r = a_i + a_j, t) = 0$ , where the distance  $r$  points from the center of the sink particle to the centers of the diffusing spheres. Far from the origin,  $c_i(\vec{r}, t)$  becomes spatially uniform and  $c_i(r = \infty, t) = c_{i0}$ , where  $c_{i0}$  is the initial density of diffusing spheres of size  $i$ . Solving the diffusion equation for this initial configuration, the radial particle flux density  $j_r(t)$  may be determined. The total flux of diffusing  $i$  spheres is given by

$$j_i(r, t) = -D_i \frac{\partial c_i(r, t)}{\partial r}. \quad (3.13)$$

Using the solution of the Equation 3.12, subject to the previously defined boundary conditions, Equation 3.13 yields [28]

$$j_i(a_i + a_j, t) = -D_i \left[ \frac{1}{a_i + a_j} + \frac{1}{\sqrt{\pi D_i t}} \right] c_{i0}. \quad (3.14)$$

As stated above, the hypothesis of isotropic diffusion and spherical symmetry is implicitly contained in Equation 3.14. Assuming that the motions of the diffusing spheres are totally uncorrelated, and allowing sphere  $j$  also to diffuse, then  $D_i \mapsto (D_i + D_j)$ , and so

$$j_i(a_i + a_j, t) = -(D_i + D_j) \left[ \frac{1}{a_i + a_j} + \frac{1}{\sqrt{\pi(D_i + D_j)t}} \right] c_{i0}. \quad (3.15)$$

The number of particles of radius  $a_i$  that aggregate with the sink particle per unit time is simply the number of particles that diffuse towards the sink particle and get in contact with it. Evidently, this number can be obtained by multiplying the radial flux density with the area of the contact surface, i.e. with  $4\pi(a_i + a_j)^2$ . This yields

$$\begin{aligned} J_r(t) &= 4\pi(a_i + a_j)^2 j_i(a_i + a_j, t) = \\ &4\pi(D_i + D_j)(a_i + a_j) \left( 1 + \frac{a_i + a_j}{\sqrt{\pi(D_i + D_j)t}} \right) c_{i0}. \end{aligned} \quad (3.16)$$

Apparently the flux is time dependent. However, for colloidal aggregation in three dimensions the steady state is usually reached very fast

$$t \gg \frac{(a_i + a_j)^2}{\pi(D_i + D_j)} \equiv t_{relax}, \quad (3.17)$$

and the time dependent term is usually neglected [28, 78].

Finally, if the sphere of size  $j$  are presenting with an average density  $c_{j0}$ , the rates of spheres of radius  $a_j$  colliding with spheres of radius  $a_i$  is achieved by multiplying the net particle flux  $J_r(t)$  for one central particle by the concentration of sink particles  $c_{j0}$ . The result obtained reads:

$$\begin{aligned} \frac{dc_j}{dt} &= J_r(t)c_{j0} = & (3.18) \\ -4\pi(D_i + D_j)(a_i + a_j)c_{i0}c_{j0} &= -k_{ij}c_{i0}(t)c_{j0}(t). \end{aligned}$$

This expression has the typical form of a kinetic rate equation with an aggregation rate constant  $k_{ij}$  given by the BK (see Equation 3.11).

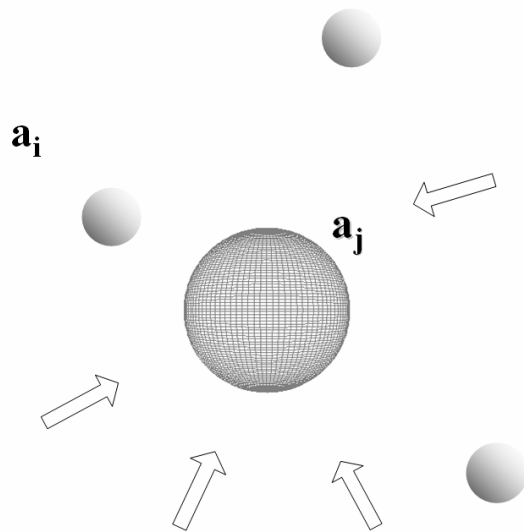


Figure 3.1: Schematic illustration of the space around a sink particle considered for deriving a diffusion induced aggregation kernel. The arrows symbolize the radial flux  $J_r$  of  $a_i$  size particles towards the sink particle  $a_j$ .

### 3.5 Field Induced Aggregation

Several authors suggested that a kernel for aggregation of magnetic particle dispersions should be based on the BK. At low concentrations, chain-like ag-

gregates of dipolar magnetic particles also undergo free diffusive motion until they reach the area of influence of another aggregate. If the interaction is attractive, the particle motion becomes ballistic and the linear aggregate snaps into position at the end of the other chain. Otherwise, the chains repel each other and diffuse away, or eventually reach the attractive zone.

### 3.5.1 Miyazima's Kernel

Miyazima et al. used the BK for describing the time evolution of the average cluster size arising in aggregating dispersions of dipolar particles aligned under the influence of an external field [8]. They assumed the linear aggregates of dipolar particles at not too high concentrations to behave as rod-like clusters that aggregate tip to tip. Supposing the chain ends to be the only active aggregation sites, they conclude that the collision cross section and the corresponding term in the BK should be constant. On the other hand, the cluster diffusion coefficients, were considered to depend on the cluster size as a power law, i.e. as  $D_i \propto i^\gamma$ , where  $\gamma$  is a positive constant in the range from 0 to 1. Based on these assumptions, they proposed the following power-law type aggregation kernel that can be written in terms of  $i$  and  $j$

$$k_{ij} = C(i^\gamma + j^\gamma). \quad (3.19)$$

where  $C$  is an arbitrary positive constant. This kernel is a homogeneous function of the cluster size  $i$  and  $j$ , being  $\gamma = \lambda_{hom} = \mu_{hom}$  the corresponding homogeneity exponents. Hence, Miyazima's kernel can be analyzed in terms of the two previously mentioned parameters  $\lambda_{hom}$ , and  $\mu_{hom}$  (Section 3.3).

For these kernels, dynamic scaling theory predicts the average cluster size to diverge as a power of time, i.e. as  $\langle S(t) \rangle \propto t^z$ . The kinetic exponent  $z$  is directly related to the homogeneity exponent through the expression [8]

$$z = \frac{1}{1 - \gamma}. \quad (3.20)$$

Based on the analogy with the Stokes-Einstein approximation relation for a single spherical particle where  $D_1 \propto a^{-1}$ , Miyazima et al. proposed a particular value of  $\gamma = -1$ , which according to Equation 3.20 corresponds to  $z = 1/2$ . Montecarlo simulations incorporating these assumptions predicted a crossover from two or three dimensions to one-dimensional behaviour, for high enough particle concentrations.

### 3.5.2 Field induced aggregation Kernel

It should be noted that the kernel proposed by Miyazima et al. implicitly includes the hypothesis of isotropic diffusion and spherical symmetry that was used for deriving the BK. During field induced aggregation processes, however, spherical symmetry is lost and cluster diffusion ceases to be isotropic. Moreover, the net interaction between two approaching chains becomes long range. All these effects are not accounted for in the Miyazima kernel. Hence, it is not clear at all why this kernel should be employed for describing the aggregation behaviour of magnetic chains. In what follows, we will use physical yet somewhat heuristic arguments for deriving a kernel for field induced aggregation, that considers not only the long-range character but also the anisotropic nature of the magnetic dipole-dipole interactions among the particles.

For this purpose, we consider the same configuration that was used for deriving the BK, i.e., freely diffusing particles of radius  $a_i$  that aggregate as soon as they come into contact with a sink particle of radius  $a_j$ . In order to include the long range character of the net interaction among the approaching particles, we define an effective interaction range  $h$  such that the particles will, on average, aggregate as soon as the distance between the particle surfaces becomes smaller than  $h$ . This means that the sink particle behaves as if it were a sphere with an effective radius of  $a_j + h$  (please, see Figure 3.2).

Modifying the BK accordingly yields

$$k_{ij}^{BK} = 4\pi(D_i + D_j)(a_i + a_j + h). \quad (3.21)$$

For interacting magnetic particles, however, the interaction may be either attractive or repulsive and its range depends on the angle  $\varphi$  between the external magnetic field and the line joining the particle centers. Figure 3.3 shows a 3-dimensional plot of the interaction range  $h(\varphi)$ , which is proportional to  $\sqrt[3]{|3\cos^2\varphi - 1|}$ , according to magnetic theory (Section 2.6.2). The attractive and repulsive regions are indicated as zone *I* and *II*, respectively. As can be seen, the attractive region has a dumbbell like shape and fits in a symmetric double cone with an aperture angle of  $\varphi_c \approx 55^\circ$  with respect to the field direction. Evidently, all the particles flowing into the dumbbell shaped attractive region will aggregate while those trying to enter zone *II* will be repelled. The corresponding aggregation kernel could, in principle, be derived by solving the diffusion equation for this configuration. Due to the missing spherical symmetry, however, this is not straight forward. Hence, we propose to simplify the problem somewhat further and to consider an angle independent effective interaction range  $\bar{h}$  maintaining the aperture angle of the attractive zone



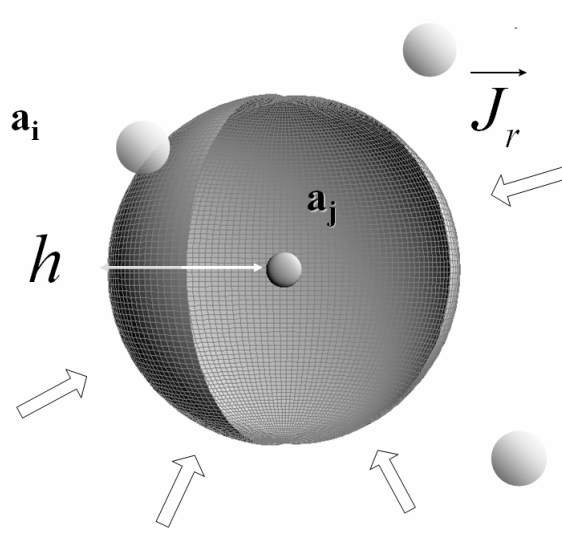


Figure 3.2: Schematic illustration of the space around a sink particle considered for deriving an aggregation kernel for field induced aggregation. In order to include the long range character of the net interaction among the approaching particles, we define an effective interaction range  $h$ . The arrows symbolize the radial flux of  $i$  size particles towards the sink particle.

(please, see Figure 3.4). This means that the particles of radius  $a_i$  will be diffusing freely until the center to center distance to the sink particle becomes  $a_i + \bar{h} + a_j$ . Hence, the spherical shape of the contact surface is recovered and the sink particle will again behave as a sphere with an effective radius of  $a_j + \bar{h}$ . Evidently, only the particles diffusing through the attractive pole caps of the effective spherical contact surface will aggregate while the particles approaching the lateral regions will be repelled. Hence, only the fraction  $A_{pc}/A_0 = (1 - \cos\varphi_c)$  of the total flux of particles towards the sink particle will be effective. Here,  $A_{pc}$  is the total area of the pole caps while  $A_0$  is the area of the entire sphere. Based on these approximations, the corresponding aggregation kernel becomes

$$k_{ij}^{Bdip} = 4\pi(1 - \cos\varphi_c)(D_i + D_j)(a_i + a_j + \bar{h}). \quad (3.22)$$

This aggregation kernel should provide a reasonable description for the aggregation behaviour of spherical particles of radii  $a_i$  and  $a_j$  that interact like aligned magnetic dipoles.

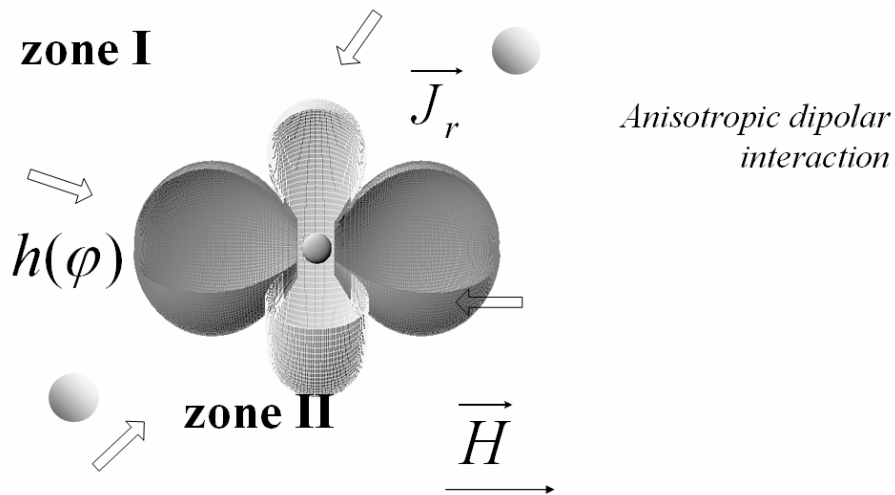


Figure 3.3: Schematic illustration of the space around a sink particle considered for deriving an aggregation kernel for field induced aggregation. In the plots, the attractive and repulsive regions are indicated as zone *I* and *II*, respectively.

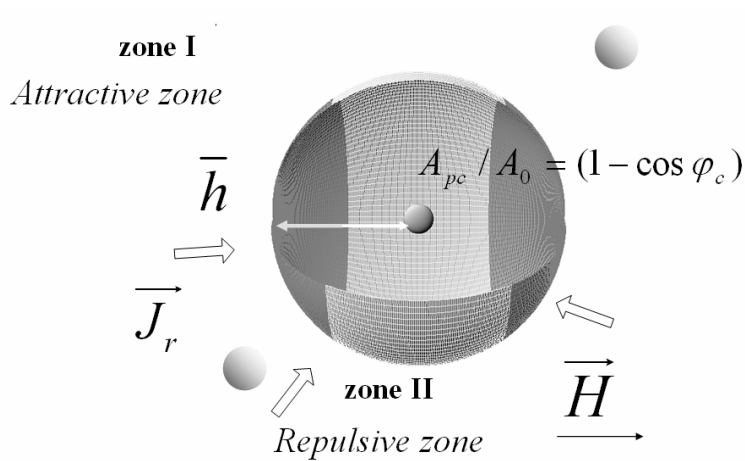


Figure 3.4: Schematic illustration of the space around a sink particle considered for deriving an aggregation kernel for field induced aggregation. In the plots, the attractive and repulsive regions are indicated as zone *I* and *II*, respectively.

The final step to go is to extend the validity of the kernel given by Equation 3.22 to field induced aggregation process where chain-like clusters are formed. Figure 3.5 shows a schematic view of a chain-like aggregate consisting of aligned magnetic particles of identical radius  $a$ . At not too high concentrations laterally approaching particles or chain-like clusters are repelled while those arriving at the chain ends will be attracted. In other words, there is an attractive zone at the chain tips and a repulsive region at the lateral chain side. If one accepts that the effective range  $\bar{h}$  of the net magnetic interaction and the aperture angle of the attractive zone are not affected too much by the presence of further chain forming particles, the area of the attractive zone at the chain tips will be approximately the same as the one of individual particles<sup>5</sup>. Consequently, the net flux of clusters that diffuse through that surface and aggregate with the cluster must also be very similar. This means that the kernel derived for individual particles, Equation 3.22, should also be able to describe the aggregation behaviour of chain-like aggregates if the diffusion behaviour of the chains were not affected by the presence of further particles in the chain. The latter is, of course, not the case and so, we propose to replace the diffusion coefficients in the aggregation kernel by the average translational diffusion coefficient  $\bar{D}$  of rods mentioned in Section 2.4. This expression describes rod diffusion quite exactly when the difference  $(D_{\parallel} - D_{\perp})$  is small (Equation 2.24), as would be the case for short rods. Based on these assumptions, the kernel for field induced aggregation processes arising in magnetic particle dispersions becomes

$$k_{ij}^{Bdip} = 4\pi(1 - \cos\varphi_c)(\bar{D}_i + \bar{D}_j)(a_i + a_j + \bar{h}). \quad (3.23)$$

This aggregation kernel should be understood as a mean field approximation using effective quantities such as the effective interaction range  $\bar{h}$  and the effective diffusion coefficients  $\bar{D}_i$  and  $\bar{D}_j$ .

It should be noted that the only one freely adjustable parameter is the effective interaction range  $\bar{h}$ . To the best of our knowledge, Equation 3.23 is the first analytical expression for an aggregation kernel for field induced aggregation process that is explicitly expressed in terms of physically meaningful quantities [82].

---

<sup>5</sup>As we have seen in Section 2.6.2, the angle of the attractive cone will increase somewhat due to mutual induction between the particles making up the linear aggregates.

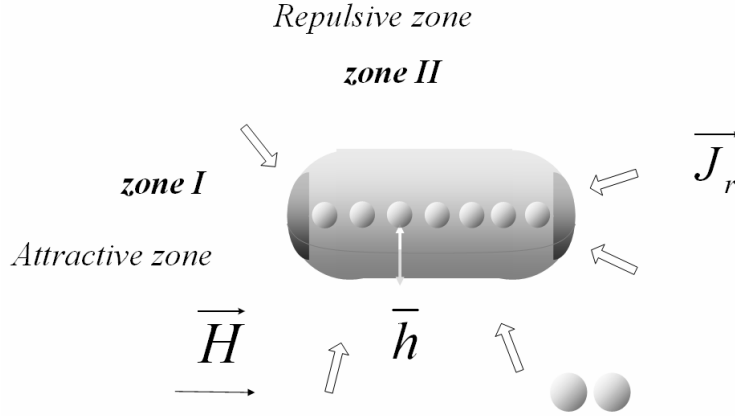


Figure 3.5: Schematic illustration of the space around a linear aggregate considered for deriving an aggregation kernel for field induced aggregation. In the plots, the attractive and repulsive regions are indicated as zone *I* and *II*, respectively.

### 3.5.3 Coupled Sedimentation and Field Induced Aggregation Kernel

For the additional contribution to the aggregation kernel due to differential sedimentation, the following kernel has been proposed in the literature [83]:

$$k_{ij}^s = A_{ij}|(v_i^s + v_j^s)|. \quad (3.24)$$

Here,  $A_{ij}$  is the combined cross section for aggregates of size  $i$  and  $j$  that settle with an average velocity of  $v_i^s$  and  $v_j^s$ , respectively. For two spherical particles of radii  $a_i$  and  $a_j$ , the combined cross section  $A_{ij}$  is given by  $A_{ij} = \pi(a_i + a_j)^2$ . For linear magnetic clusters, however, the cross section does not depend on the cluster size since the chains essentially aggregate end to end. Considering the previously defined effective attractive zone of range  $\bar{h}$  and aperture angle  $\varphi_c$ , the combined cross section becomes approximately (please, see Figure 3.6)

$$A_{ij} = 2\varphi_c(a + \bar{h} + a)^2. \quad (3.25)$$

The sum kernel  $k_{ij}^{Bdip-s} = k_{ij}^{Bdip} + k_{ij}^s$  allows coupled aggregation-sedimentation processes to be described theoretically within the framework of Smoluchowski's equation [84].

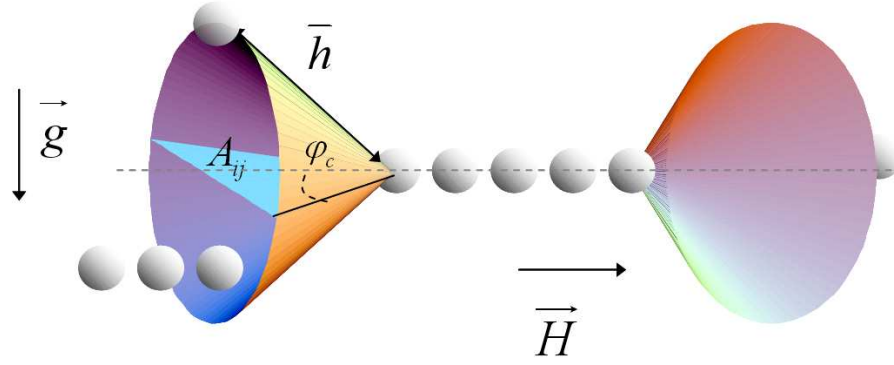


Figure 3.6: Schematic view of the attractive zone around a linear aggregate. Only clusters that are swept by the shaded circular sectors will aggregate due to differential settling.

### 3.5.4 Mutual Induction Kernel

For a particle contained within an infinite chain of identical particles, we have seen that the magnetic moment normalized by the magnetic moment of an isolated particle  $m_0$  becomes (please, see Section 2.6.2)

$$m/m_0 = \frac{1}{1 - \frac{16\pi\zeta(3)}{3} \left(\frac{a}{r}\right)^3 \chi_{sphere}}, \quad (3.26)$$

where  $\zeta(3) = \sum_{n=1}^{\infty} 1/n^3 = 1.202$  is the Riemann function,  $r$  is the distance between the particle centers, and  $\chi_{sphere}$  is the magnetic susceptibility.

However, Equation 3.26 must be adapted to finite chains before it may be applied in aggregation theory. The magnetic moment of the particles placed at the chain ends may be assessed imposing the following three approximations:

1. The chain forming particles are in close contact, i.e.  $r = 2a$ .
2. All the chain forming particles have an identical magnetic moment.
3. The infinite sum in the Riemann function  $\zeta_i$  may be truncated at  $n = N - 1$ .

Since the range of the magnetic dipole interaction scales as  $h \propto m^{\frac{2}{3}}$ , it is straight forward to deduce the following approximation for  $\bar{h}$

$$\frac{\bar{h}_{ij}}{\bar{h}_{11}} = \frac{1}{(1 - \frac{\pi\zeta_j(3)}{3})^{2/3}} \quad j > i, \quad (3.27)$$

where  $\zeta_j(3) = \sum_{n=1}^{j-1} 1/n^3$ . This means that the effective range  $\bar{h}$  of the net interaction between the particles depends on the aggregate size (see Figure 3.7)[84].

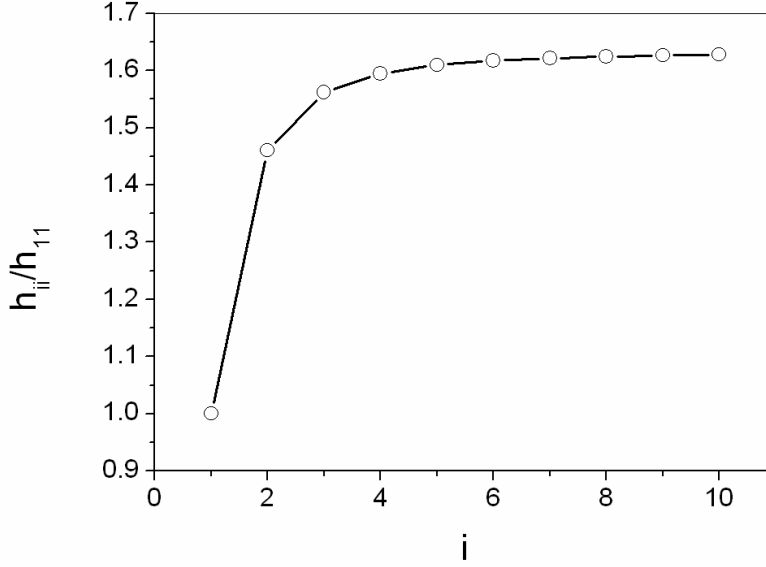


Figure 3.7: Dependence of the effective range  $\bar{h}_{ii}$  of the net interaction, normalized by the effective range  $\bar{h}_{11}$ , on the aggregate size  $i$ . See Equation 3.27.

### 3.6 An Alternative Scenario

The hydrodynamic interactions increase the effective mobility of a cluster of mass  $s$ , making it larger than the mobility of a collection of  $s$  independent particles. The translational motion of field induced aggregates is anisotropic, and the drag coefficients depend on the orientation of the linear aggregate (please, see Section 2.5.2). Hence, the approximation made by Miyazima et al.,  $D_i \propto i^\gamma$ , is a too strong assumption in the case of linear aggregates. Miguel and Pastor-Satorras proposed an alternative approach, based on heuristic arguments, which includes logarithmic corrections to the standard power-law behaviour [9].

Firstly, they assume that the linear aggregates have the average length  $S$ . Thus, the averaged distance  $\bar{R}$  between closer aggregates is given by

$$\bar{R} \approx \left(\frac{S}{\phi}\right)^{1/Dim}, \quad (3.28)$$

where  $\phi$  is the initial density, and  $Dim$  is the spatial dimension. Since the movement of the cluster is essentially diffusive, in three dimensions, the characteristic time  $T$  required by the aggregates to cover a unitary distance such that the clusters will encounter  $n(t)$  aggregates is

$$T \propto \frac{1}{n} \frac{1}{D_S} \propto \frac{1}{\phi} \frac{S^2}{\ln(S)}, \quad (3.29)$$

where the diffusion coefficient  $D_S \propto \frac{\ln(S)}{S}$  takes into account the logarithmic correction due to hydrodynamic interactions. Using similar arguments these authors propose a different characteristic time for low-dimensional systems ( $Dim = 1, 2$ )

$$T \propto \frac{\bar{R}^2}{D_S} \propto \frac{1}{\phi^{2/Dim}} \frac{S^{2+Dim}}{\ln(S)}. \quad (3.30)$$

Therefore, the functional dependence of the mean cluster size  $S$  with time can be expressed as

$$\begin{aligned} \frac{S}{[\ln(S)]^{\frac{Dim}{2+Dim}}} &\propto t^{\frac{Dim}{2+Dim}} & Dim \leq 2 \\ \frac{S}{[\ln(S)]^{\frac{1}{2}}} &\propto t^{\frac{1}{2}} & Dim \geq 2. \end{aligned} \quad (3.31)$$

Within this approach, the authors obtained logarithmic corrections to the power-law dependence proposed by Miyazima et al. for  $\gamma = -1$ . Monte Carlo simulations making use of this assumption provide a different kinetic exponent  $z = 0.6$ , and predict a crossover to a quasi-one dimensional regime for high particle concentrations [9]. These simulations have been confirmed by experimental results [36, 85].

### 3.7 Aggregate Morphology

A detailed analysis of colloidal aggregation involves two main aspects: the cluster morphology and the kinetics of aggregate formation. The cluster mor-

phology is usually characterized by means of the *fractal dimension*,  $d_f$ , that is understood as a measure on how the particles fill the three-dimensional space.

### 3.7.1 Fractal Dimension

The fractal dimension was introduced in the seventies by B. Mandelbrot. It allows for a quantitative description of the structure of the aggregates that was generally considered as too complicated in the past [86, 87]. The more general definition of the fractal dimension is due to Hausdorff [88]. If we define the *embedding dimension*  $d$  as the smallest Euclidean dimension of the space an object can be embedded in, the "volume" of such object  $V(r)$  can be measured by covering it with  $d$  dimensional balls or boxes of length  $r_0$

$$V(r) = N(r)r_0^d, \quad (3.32)$$

where  $N(r)$  is the smallest number of balls of radius  $r_0$  with which the object can be covered completely. For usual geometrical objects (line, sphere, triangle, etc.)  $V(r)$  attains a constant value as  $r_0$  decreases<sup>6</sup>. However, there are some objects which  $V(r) \mapsto 0$  as  $r_0 \mapsto 0$ . For instance, the measured "area" of the shore goes to zero if we determine it by using squares of decreasing width. On the other hand, if we measure the "volume"  $V(r)$  of this kind of objects by covering it with  $d - 1$  boxes of length  $r_0$  we will find that  $V(r) \mapsto \infty$  as the unit of length  $r_0$  decreases. If we want to measure a section of coastline with a ruler, we would get a different result depending on the ruler length. The measured length will increase as the length of the ruler decreases. This is due to the fact that with the smaller ruler we would be laying it along a more curvilinear route than that followed by the longer one (see Figure 3.8). This empirical evidence suggests that the measured length increases without limit as the measurement scale decreases towards zero. Therefore, the coastline is neither a one- nor a two-dimensional object. It seems to be "wider" than a line but having an infinitely small surface. Hence, there are objects that have no integer dimension. Such objects have a *fractal dimension*, that does not have special reason to be an integer.

If we suppose an aggregate to be a set of a characteristic fractal dimension  $d_f$ , the density  $\rho$  in a  $d_f$ -dimensional space of such an aggregate is

$$\rho(r) \propto \frac{M(r)}{r^{d_f}}, \quad (3.33)$$

---

<sup>6</sup>That is the method generally employed to measure a distance, an area or a volume.



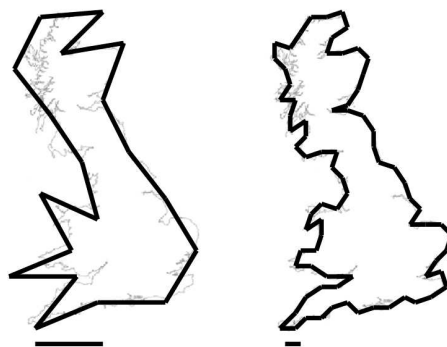


Figure 3.8: How long is the coast of Great Britain? If we want to measure a section of coastline with a ruler, we would get a different result depending on the ruler length. This means that the coast line of Great Britain is not a linear object of 1 dimension. It must rather have a non integer dimension. Mandelbrot found a fractal dimension of 1.25 for the West coast of Britain, using empirical dates measured by Lewis Fry Richardson [86].

where  $M(r)$  is the mass contained in a sphere of radius  $r$  centered at some point within the cluster [86]. If the spheres density of radius  $r_0$  is normalized, the mass contained in a sphere of radius  $r$  is given by  $N(r) \times r_0^{d_f} \times 1$ . Hence, the density is

$$\rho(r) \propto \frac{M(r)}{r^{d_f}} \propto N(r) \left(\frac{r_0}{r}\right)^{d_f}. \quad (3.34)$$

For  $r \gg r_0$ ,  $N(r)$  has to be proportional to  $r^{d_f}$ . Hence, the fractal dimension  $d_f$  is given by

$$d_f \equiv \lim_{r \rightarrow \infty} \frac{\ln N(r)}{\ln r}. \quad (3.35)$$

On the other hand, the spatial correlations between particles of a structure are usually accounted in terms of a *spatial correlation function*  $c(r)$

$$c(r) \equiv \frac{1}{V} \sum_{r'} [\rho(r+r')\rho(r')], \quad (3.36)$$

where  $V$  is the structure volume and  $\rho(r)$  the local particle density. The structure of some fractal objects are invariant under change of scale. Such fractals are called *self-similar fractals*. In this case, the previously defined spatial cor-

relation function remains unchanged when the length scale is changed by an arbitrary factor  $b$

$$c(br) \approx b^{-\alpha}c(r), \quad (3.37)$$

where  $\alpha$  is a positive number smaller than the embedding dimension  $d$ . It can be shown that

$$c(r) \approx r^{-\alpha} \quad (3.38)$$

is the only function which satisfies the Equation 3.37 [28]. The number of boxes within a sphere of radius  $r$  from the 3 D correlation function, according to Equation 3.38, is given by

$$N(r) \sim \int_0^r c(r)d^3r \sim L^{3-\alpha}. \quad (3.39)$$

In a fractal object,  $N(r)$  grows asymptotically as  $r^{d_f}$ . Hence, the parameter  $\alpha = 3 - d_f$  is related to the fractal dimension, and Equation 3.38 becomes

$$c(r) \sim r^{d_f-3}. \quad (3.40)$$

When we consider real physical objects, the objects can be described as a fractal only between two well defined length scales. In particular the natural lower cut off size of colloidal aggregates is the diameter of the particles, whereas the higher cut off is the mean size of the aggregates. For instance, the reader can observe the aggregates depicted in Figure 3.9. Therefore, we have to introduce a cut-off function  $f(r/R)$  to take care of the finite character of the aggregate. This function is such that  $f(x) \sim 0$  for  $x > 1$ , and  $f(x) \sim \text{constant}$  for  $x < 1$ .

### 3.7.2 Morphology of Field Induced Aggregates

When the magnetic particles are allowed to aggregate<sup>7</sup>, linear particle aggregates or filaments are formed. The final aggregate structure depends mainly on the particle volume fraction.

---

<sup>7</sup>Supposing that the dipolar magnetic potential is sufficiently larger than the thermal energy and the possible repulsive interactions between the particles.

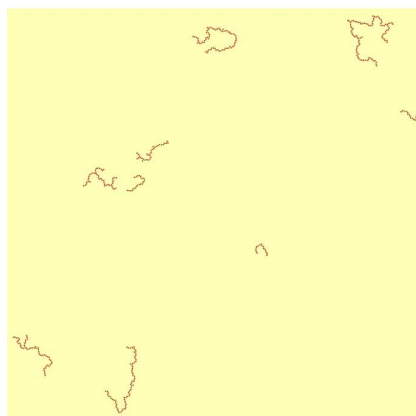


Figure 3.9: Aggregates obtained by Molecular Dynamics simulation. Their fractal dimension is  $d_f \approx 1.2$ . The particles aggregate under the action of a long range repulsive Yukawa potential that is small enough to be overcome by thermal activation. This plot has been taken from Fernández-Toledano et al. [89].

### Pearl-Chain Like Clusters

At low particle concentrations, regular one-particle-thick chainlike aggregates are formed aligned along the field direction. Electrostatic repulsion helps to ensure the stability of the magnetic colloidal particles with regard to aggregation when no magnetic field is applied. However, once the magnetic field is applied, a deep primary minimum appears at short distances, and a shallower secondary minimum at further distances. As we have shown in the Section 2.7, both energy minimum are separated by an energy barrier. Hence, particle aggregation may occur either in the primary minimum where the particles are in contact, or in the secondary minimum where the neighbouring particles within the linear aggregates are separated by a short distance. In that latter case, relative positional particle fluctuations inside the linear aggregates may take place due the competition between Brownian motion and magnetic dipole-dipole interactions, as we will see in Section 6.2.

When the chain-forming particles aggregate in the primary minimum, the filaments or at least parts of them will remain assembled even in absence of the magnetic field (see Figure 3.10) [64, 65, 66]. The deformation and magnetorheological properties of these "permanent" chains have been the subject of

several works during the last years [22, 23, 24, 25]. As we will see in Chapter 4, light scattering allows the fractal dimension  $d_f$  to be measured using the known theoretical relationship between the mean scattered light intensity  $I(q)$  and the scattering wave vector  $q$ . Therefore, the light scattering data will be employed to confirm the linear character of the permanent filaments and to assess chain deformation due to the interaction with the surrounding medium.

### **Columns and networks**

At higher particle concentrations, long chains experience additional lateral attractions and aggregate, forming columns or networks that are also aligned in the direction of the magnetic field. The lateral aggregation is due to a short range attraction between the chains (Section 2.6.2). Furthermore, thermal fluctuations and topological defects due to polydispersity can also be responsible for lateral aggregation at lower volume fractions (see Figure 3.11).

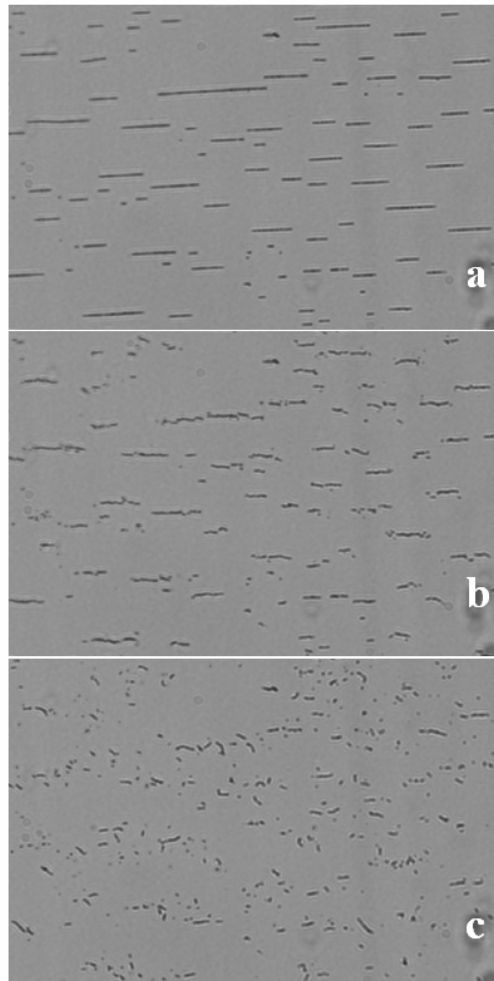


Figure 3.10: Transmission electron microscopy images of magnetic particles aggregated in an electrolyte solution under the presence of a constant magnetic field (Figure a). The added electrolyte allows the particles to come close so that van der Waals interactions dominate and "permanent" aggregates are formed. Once the magnetic field is turned off these aggregates rotate freely, and the linear aggregates lose part of their linear character. (Figures *b* and *c*).

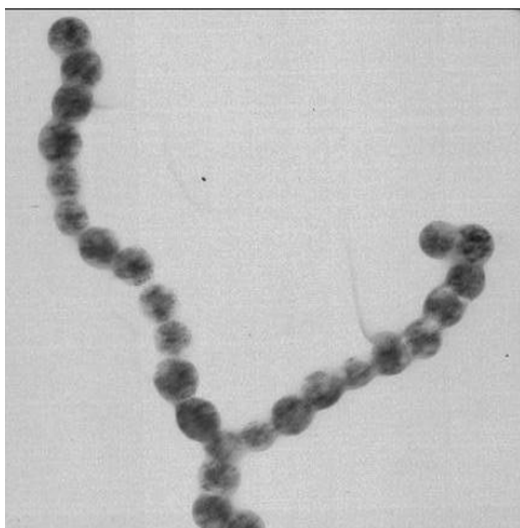


Figure 3.11: Branching defect observed at low volume fraction. Thermal fluctuations, polydispersity, or chain defects create local variations in the dipole moment density along a chain.



## Chapter 4

# Light Scattering

*La luz es sepultada por cadenas y ruidos  
en impúdico reto de ciencia sin raíces.*

Federico García Lorca, de Poeta en Nueva York.

### 4.1 Introduction

Light is electromagnetic radiation of a wavelength of approximately 400–700  $nm$  that is visible to the human eye. In light waves the electric and magnetic fields oscillate in perpendicular directions, and in directions perpendicular to the direction of propagation of the wave. In general, absorption and scattering are the two ways in which electromagnetic radiation can interact with colloidal particles. Scattering is a general physical process whereby some forms of radiation, such as light, sound, or subatomic particles, for example, are forced to deviate from a straight trajectory by one or more localized non-uniformities in the medium through which it passes. The types of non-uniformities that can cause scattering, sometimes known as scatterers or scattering centers, are too numerous to list, but a small sample includes colloidal particles, density fluctuations in fluids, bubbles, surface roughness, droplets, defects in crystalline



solids, cells in organisms, etc. The effects of such objects on the path of a propagating wave are described in the framework of scattering theory.

When light impinges on matter, the electric field of the light induces an oscillating polarization in the molecules. The incident light beam then is said to polarize the medium. The charges in the illuminated volume subject to this electric field experience a force and are accelerated. According to classical electromagnetic theory an accelerating charge radiates light, and consequently the charges serve as secondary sources and scatter light.

All the charges in a subregion that is small if compared with the incident light wavelength, see almost the same incident electric field. If the incident light illuminates many small subregions, then the total electric field that is scattered in a certain direction is the sum of the electric fields scattered in the same direction by the individual subregions. The phase difference of the scattered light from two different subregions depends on their relative positions, as well as on the direction in which the scattered light is detected. If all these subregions have the same refractive index, there will no scattered light in other than the forward direction. This is because the waves scattered from each subregions are identical except for this phase difference, and a complete cancellation will then take place. However, in colloidal suspensions where the particles have a refractive index different to the medium, the amplitudes of the field scattered from the different subregions are not identical, and there will be scattered light in other than the forward direction. Thus, in this semi-macroscopic view, light scattering is a result of local fluctuations in the refractive index of the medium [90]. When a beam of light passes through a solution there is so little scattering of the light that the path of the light cannot be seen. However, if a beam of light passes through a colloidal suspension then the colloidal particles, which size is comparable to the light wavelength, reflect or scatter the light and its path can therefore be observed. This particular property of the colloidal suspensions is known as the *Tyndall effect* (see Figure 4.1).

The particles in colloidal suspensions are perpetually moving due to the Brownian motion. As the particles change their positions, the phase difference of the scattered field from the particles changes, so that the total scattered electric field measured at the detector will fluctuate in time. The scattered light by the particles then undergoes either constructive or destructive interference, and the intensity fluctuation contains information about the time scale of the particle movement. In other words, there is implicit important statistical information about the positions and orientations of the scatters. The angular distribution of the scattered light intensity, the fluctuation of the scattered

electric field, or the polarization are determined by the size, shape, and motion of the particles within the scattering volume. From the light scattering characteristics of a given system it is possible, with the aid of electrodynamics and the theory of time-dependent statistical mechanics, to obtain information about the structure and dynamics of the scattering medium. In summary, light scattering is a useful experimental tool in order for studying the structural and dynamical properties of colloidal systems.

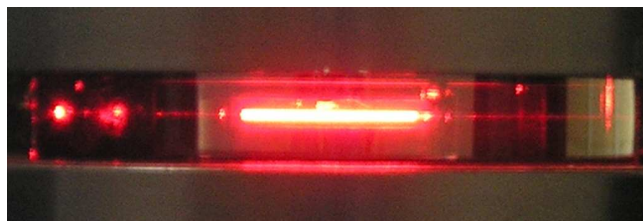


Figure 4.1: He-Ne laser passing through a colloidal suspension during a typical light scattering experiment. The colloidal particles, which size is comparable to the light wavelength, scatter the light and the path of the light can therefore be observed (Tyndall effect).

The dynamics of a dilute colloidal suspension of spherical particles is well-understood; physics or chemistry students, during their practical training, sometimes perform light scattering experiments which determines the diameter of monodisperse charged polystyrene spheres through the fluctuation of the scattered electric field. However, there are few studies on the dynamics of rodlike particles<sup>1</sup>. This is due to the fact that their dynamics is more complex. When a chain or rod moves, there is not only a translational and rotational displacement of the entity as a whole; there may also be small internal vibrational modes that may affect the dynamics of the system. On the other hand, if the incident light is linearly polarized, the scattered light will also be linearly polarized. However, if the scatters are nonspherical or if they have anisotropic polarizabilities along different directions, there will be a component of the scattered light with a polarization perpendicular to the direction defined by the incident electric field. Hence, an accurate description of this diffusive motion is not straightforward.

---

<sup>1</sup>Among them are works dealing with tobacco mosaic viruses [91, 92], gold particles [93], or carbon nanotubes [94].

Scattering experiments also give access to the position correlations between particles. For aggregating particles light scattering is a useful tool to measure their fractal dimension, which quantitatively determines the degree of compactness of the clusters.

In this Chapter we develop the theoretical background for describing the experiment in which the light is scattered by spherical particles, anisotropic particles, or linear aggregates. Moreover, we will focus our attention on the magnetic character of the colloidal particles and on the effect that an uniaxial magnetic field might have on the light scattering experiments. We mainly follow the molecular formulation given in the book of Berne and Pecora [50]. For further details about light scattering topics the interested reader should consult this excellent book.

## 4.2 Electromagnetic Light Scattering Theory

If the wavelength of the light is comparable to the principal dimensions of the system, and if the photon energies are small compared with the characteristic energy of the system, a very useful approximation is to disregard Quantum Mechanics effects. This method is based on the *Classical Theory of Electromagnetic Radiation*, which will be discussed throughout this Chapter.

Let the incident electric field  $\vec{E}_i(r, t)$  at point  $\vec{r}$  and time  $t$  be given by a plane electromagnetic wave

$$\vec{E}_i(\vec{r}, t) = \vec{n}_i E_0 \exp i[\vec{k}_i \cdot \vec{r} - \omega_i t] \quad (4.1)$$

of wavelength  $\lambda$ , frequency  $\omega_i$ , and amplitude  $E_0$ . Here,  $\vec{n}_i$  is a unit vector pointing in the polarization direction of the incident electric field. The *incident wave vector*  $\vec{k}_i$  is

$$\vec{k}_i = \left(\frac{2\pi}{\lambda}\right) \hat{k}_i, \quad (4.2)$$

where  $\hat{k}_i$  is a unit vector pointing in the propagation direction of the incident wave.

The surrounding medium is assumed to behave as a nonmagnetic, nonconducting, and nonabsorbing medium with average dielectric constant  $\varepsilon$  and a magnetic permeability equal to that of vacuum  $\mu_0$ . Fluctuations of the refractive index  $\sqrt{\varepsilon\mu_0}$  of the medium, resulting from density fluctuations, are neglected here.

When this incident electric field impinges on a single molecule, which has a polarizability given by a polarizability tensor  $\hat{\alpha}$ , it induces an electric dipole moment which varies with time

$$\vec{\mu}(t) = \hat{\alpha} \cdot \vec{E}(t). \quad (4.3)$$

According to Electro-Magnetic theory, a time varying dipole emits electromagnetic radiation [60]. The radiated electric field  $\vec{E}_s$  is proportional to the acceleration of the dipole moment  $\ddot{\vec{\mu}}(t')$ , where the *retarded time*  $t'$  is the time it takes, at speed of light  $c$ , to get from the dipole to the detector [95, 96]. Therefore, the scattered light from a molecule can be considered as the radiation from an induced dipole. Maxwell's equations may be used to show that the component of the scattered electric field at a large distance  $r$  from the scattering volume with polarization  $\vec{n}_f$ , propagation vector  $\vec{k}_f$ , and frequency  $\omega_i$ , is proportional to [50]

$$\vec{E}_s(\vec{r}, t) \propto \alpha_{if}(t) \exp(i\vec{q} \cdot \vec{r}(t)), \quad (4.4)$$

where

$$\alpha_{if}(t) = \vec{n}_f \cdot \hat{\alpha}(t) \cdot \vec{n}_i \quad (4.5)$$

is the component of the molecular polarizability tensor along  $\vec{n}_i$  and  $\vec{n}_f$ . Here,  $\vec{r}(t)$  is the position of the center of mass of the molecule at time  $t$ . The *multiple scattering*, i.e. when light is scattered many times within the molecule or between distinct molecules, was entirely neglected during the operations. In literature on scattering such an approximation is usually referred to as a *first Born approximation*. The molecules are supposed not to exhibit magnetic properties which affect the scattering process. Although the light scattering by colloidal particles of different optical properties is a well-documented topic, little attention has been paid to the case of light scattering by magnetic particles. Some remarks about light scattering by magnetic particles will be given in Section 4.4.1 on the basis of the Mie theory.

The vector  $\vec{q}$ , shown in Equation 4.4, is defined as

$$\vec{q} = \vec{k}_i - \vec{k}_f, \quad (4.6)$$

where  $\vec{k}_i$  and  $\vec{k}_f$  are in the directions of propagation of the incident wave and the wave that reaches the detector, respectively. The angle between  $\vec{k}_i$  and  $\vec{k}_f$  is called the *scattering angle*  $\theta$ . All the geometry is illustrated in the Figure 4.2. The magnitudes of  $\vec{k}_i$  and  $\vec{k}_f$  are respectively  $\frac{2\pi n}{\lambda_i}$  and  $\frac{2\pi n}{\lambda_f}$ , where  $\lambda_i$  and  $\lambda_f$  are the wavelengths in vacuo of the incident and the scattered light, and  $n$

is the refractive index of the scattering medium. Usually the interaction of the electric field with the material of the molecules is such that the wavelength is not affected and so

$$|\vec{k}_i| \cong |\vec{k}_f|. \quad (4.7)$$

Thus, the triangle shown in Figure 4.2 is an isosceles triangle and the magnitude of  $\vec{q}$  can be found from the law of cosines

$$q = 2k_i \sin \frac{\theta}{2} = \frac{4\pi n}{\lambda_i} \sin \frac{\theta}{2}. \quad (4.8)$$

Since the wavelength (and therefore the energy) of the incident photon is conserved and only its direction is changed, such a scattering event is called *elastic light scattering*. The photon is bounced off the scattering material without any transfer of energy to the material. The scattering vector  $\vec{q}$  has the units of  $1/\text{length}$ . Thus, essentially,  $q^{-1}$  gives the "spatial resolution" of a scattering experiment.

### 4.3 Scattering from Small Particles

The polarizability of the colloidal particles (or macromolecules) is enormous by comparison to the polarizability of the solvent molecules. Therefore the colloidal particles will be far more efficient scatterers of light than individual molecules, and only the scattered field due to the presence of the colloidal particles will be considered. If the charges of the particles are not perturbed too much by the presence of their neighbours, we can assume that the field scattered from the assembly of particles will be the superposition of amplitudes scattered from each of the particles in the illuminated volume. In fact, many of the scattered light properties are easily explained using the rule that when two or more light beams impinge on the same surface, the resulting intensity is obtained by first adding the electric fields due to the individual beams and then squaring the sum to obtain the average light intensity. This is an example of what is called the *Principle of Superposition* for linear systems. This principle states that the total field due to all the sources is the sum of the fields due to each source. As far as we know today, for the electricity this is an absolutely guaranteed law, which is true even when the force law is complicated because the motions of the charges. According to Equation 4.4, the total scattered field will be proportional to

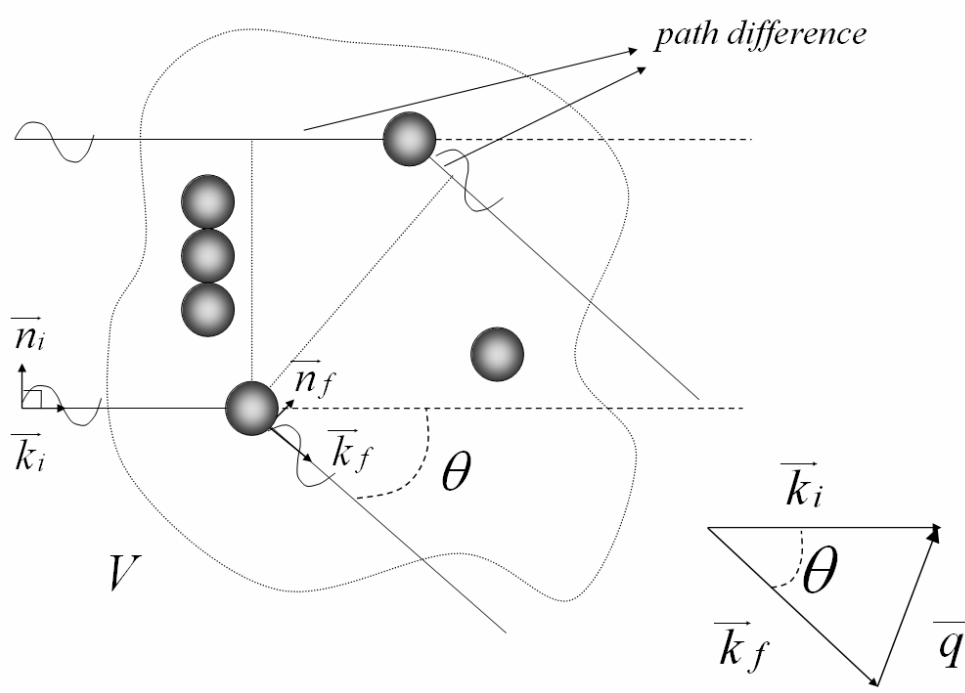


Figure 4.2: Light of polarization  $\vec{n}_i$  and wave vector  $\vec{k}_i$  is scattered in all directions. Only scattered light of wave vector  $\vec{k}_f$  and polarization  $\vec{n}_f$  arrives at detector. The scattering vector  $\vec{q}$  is defined by the wavelength, as well as by the direction in which the scattered light is detected.

$$\vec{E}_s(\vec{R}, t) \propto \sum_{j=1}^N \alpha_{if}(t) \exp(i\vec{q} \cdot \vec{r}_j(t)), \quad (4.9)$$

where the vector  $\vec{r}_j(t)$  is the centre of mass position of particle  $j$  at time  $t$ , and the prime on the sum indicates that the sum is only over particles within the scattering volume. The phase difference of the scattered electric field under a scattering angle  $\theta$  by two particles is equal to  $\frac{2\pi\Delta}{\lambda}$ , where  $\Delta$  is the path difference between two light beams (Figure 4.2). It is straight forward to show that this phase difference is equal to  $\vec{q} \cdot (\vec{r}_i - \vec{r}_j)$  [26]. Therefore, we can associate a phase equal to  $\vec{q} \cdot \vec{r}_j$  to every particle  $j$ , and the total scattered electric field is the sum of  $\exp(i\vec{q} \cdot \vec{r}_j(t))$  over all particles of the scattering volume.

According to Equation 4.9,  $\vec{E}_s$  depends on time via the position (through the exponential contains the positions) and the orientation of the Brownian particles (through the polarization tensors). A change in the configuration of the brownian particles (reorientation or translation) changes the interference pattern of the scattered electric field. The electric field thus fluctuates randomly around a mean value, as depicted in Figure 4.3. The time required for a fluctuation between extremes will depend on the scattering angle as well as the size of the particle<sup>2</sup>.

The simplest way to characterize the fluctuations of the electric field is by means of a *field autocorrelation function*, defined as

$$g_E(t) \equiv \langle E_s^*(R, 0)E_s(R, t) \rangle \equiv \lim_{T \rightarrow \infty} \frac{1}{T} \int_0^T E_s^*(R, 0)E_s(R, t)dt, \quad (4.10)$$

where \* denotes complex conjugation, and  $T$  is the time over which the electric field is averaged. The average becomes meaningful only if  $T$  is large compared to the period of fluctuation. If the random process is stationary, then the autocorrelation function depends only on the time difference and not on the particular values 0 and  $t$ .

Time-dependent *correlation functions* have been used for a long time in the theory of noise and stochastic processes, and nowadays they are easily measured using digital techniques, as we will see in the Chapter 5. However, the time-correlation functions measured in light scattering experiments are time averages, whereas in most theoretical calculations what is calculated is the ensemble-averaged correlation function. According to *Birkhoff's ergodic theorem*, these two correlation functions will be identical if the system is ergodic. The idea that we observe the ensemble average arises from the view in which measurements are performed over a long time, and that due to the flow of the system through state space, the time average is the same as the ensemble average. The equivalence of a time average and an ensemble average, while sounding reasonable, is not at all trivial [49]. This assumption seems reasonable if the observation is carried out over a very long time<sup>3</sup> or if the observation is the average over many independent observations.

---

<sup>2</sup>Typical values range from a few  $\mu s$  for small molecules to many  $ms$  for objects as large as a cell. Brownian motion is slow enough, so that many photons are scattered in a time interval during which the configuration of the particles did not change to an extent that the phases of the scattered fields are seriously affected.

<sup>3</sup>"Long time" refers to a duration much longer than any *relaxation time* for the system. After this relaxation time the system will lose all memory of its initial conditions.

Correlation functions provide concise method for expressing the degree to which dynamical properties are correlated over a period of time. At short times the correlation will be high because the particles do not have a chance to move to a great extent from the initial state that they were in. Thus, the signal is essentially unchanged when compared after only a very short time interval. Then

$$g_E(t) \rightarrow \langle |E(0)|^2 \rangle \quad \text{for } t \rightarrow 0. \quad (4.11)$$

As the time delays become longer, the correlation starts to exponentially fall off. This means that there is no correlation between the scattered intensities by the initial and the final states after a long time period<sup>4</sup> has elapsed (please, see the Figure 4.3). Then,

$$g_E(t) \rightarrow \langle |E(t)|^2 \rangle \quad \text{for } t \rightarrow \infty. \quad (4.12)$$

The exponential decay will then be obviously related to the motion and the size of the scatter particles. The time-correlation function of  $E_s$  can be evaluated from Equation 4.9

$$g_E(t) \propto \langle \delta\alpha_{if}^*(\vec{q}, 0) \delta\alpha_{if}(\vec{q}, t) \rangle, \quad (4.13)$$

where

$$\delta\alpha_{if}(\vec{q}, t) \equiv \sum_{j=1}^N \alpha_{if}^j(t) \exp(i\vec{q} \cdot \vec{r}_j(t)) \quad (4.14)$$

is the spatial Fourier component of the polarizability density

$$\delta\alpha_{if}(\vec{r}, t) = \sum_{j=1}^N \alpha_{if}^j(t) \delta(\vec{r} - \vec{r}_j(t)). \quad (4.15)$$

The time dependence of the polarizability component  $\alpha_{if}^j$  can be regarded as the product of two contributions: the movement of the rigid molecular polarizability, and the internal vibrational displacements, which gives rise to the *vibration-rotation Raman spectrum*. In this study we are concerned only with the part of the scattered light that depends on pure rotations and translations of particles. No further discussion of the vibrational Raman scattering is given. This scattering is referred as "*Rayleigh-Brillouin*" scattering.

---

<sup>4</sup>Relative to the motion of the particles.



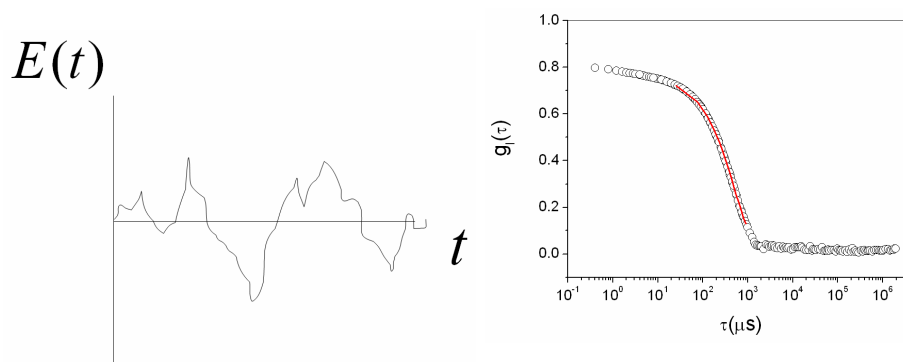


Figure 4.3: Typical fluctuating scattered electric field as function of time in arbitrary units (left), and a normalized autocorrelation function of the scattered light intensity (right). Here, the continuous line represents a second order cumulant fit (see Section 4.4.2).

As can be seen in Equation 4.15, the scattered electric field is proportional to a certain Fourier component of the instantaneous density  $\sum_{j=1}^N \delta(\vec{r} - \vec{r}_j(t))$ . This makes light scattering such an important experimental tool because it allows studying of density fluctuations. These fluctuations are determined by the Brownian motion of the colloidal particles. Different Fourier components of the density can be set by the wavelength of the light and the scattering angle.

#### 4.3.1 Spherical Particles

The simplest case to treat in light scattering is that of optically spherical particles. In this case  $\hat{\alpha}$  is proportional to the unit matrix  $\hat{I}$  and the induced dipole moment is always parallel to the applied field so that

$$\vec{\mu}(t) = \alpha(t)\vec{E}(t). \quad (4.16)$$

The dipoles induced in the scattering particles oscillate with the same polarization as the incident light beam, and the oscillating dipoles then radiate light with the same polarization.

#### Spatial Distribution of Scattered Light Intensity

According to the Electromagnetic theory, the intensity of a beam of light is proportional to the square of the electric field amplitude. This theory allows

us to predict quite easily the intensity of the scattered light at any angle for the spherical particles. As we have mentioned before, small spherical particles behave like oscillating dipoles, since the polarization direction of the incident field is in the same direction as the induced dipoles for optically isotropic particles. If the detector is looking "right on top of the heads of the dipoles", the amplitude of the reradiated light is at a maximum in any direction perpendicular to the dipole axis, and the mean intensity collected by a detector in the plane perpendicular to the dipole axis will be almost constant [60]. Such small spherical scatters are frequently referred to as *Rayleigh Scatters*.

### Time Correlation Function

The time-correlation function arising in light scattering involves the molecular polarizability through the quantity given by the Equations 4.13 and 4.14. For spherical particles, this reads (see Equation 4.5)

$$\alpha_{if}(t) = (\vec{n}_i \cdot \vec{n}_f)\alpha(t). \quad (4.17)$$

It immediately follows from Equations 4.9 and 4.17 that for identical spherical particles the scattered field is proportional to

$$\vec{E}_s \propto (\vec{n}_i \cdot \vec{n}_f)\alpha(t) \sum_{j=1}^N \exp(i\vec{q} \cdot \vec{r}_j(t)), \quad (4.18)$$

and the time-correlation function of  $\vec{E}_s$  is proportional to

$$g_E(t) \propto F_1(\vec{q}, t) \equiv \langle \psi^*(\vec{q}, 0)\psi(\vec{q}, t) \rangle, \quad (4.19)$$

where  $\psi$  is simply

$$\psi(\vec{q}, t) \equiv \sum_{j=1}^N \exp(i\vec{q} \cdot \vec{r}_j(t)). \quad (4.20)$$

If all the particles are identical the contributions to the scattered electric field due to the individual particles have the same magnitude. The phases, however, are different.

### Diluted Solutions

In sufficiently diluted solutions the distance between the particles is much larger than their own dimensions, and the interactions among them can be

neglected. Hence, we can assume their positions to be statistically independent. Therefore, the cross terms  $i \neq j$  vanish for non-interacting particles, and Equation 4.19 becomes

$$F_1(\vec{q}, t) = \left\langle \sum_{j=1}^N \exp[i\vec{q} \cdot (\vec{r}_j(t) - \vec{r}_j(0))] \right\rangle. \quad (4.21)$$

This is an example of a self-correlation function where only properties of the same particle are correlated. We only treat the self part of the intermediate scattering function, as a consequence of not having included the interactions between the particles. The quantity

$$F_s(\vec{q}, t) \equiv \langle \exp[i\vec{q} \cdot (\vec{r}_j(t) - \vec{r}_j(0))] \rangle \quad (4.22)$$

should be identical for each particle  $j$ , because it represents an ensemble average.  $F_s(\vec{q}, t)$  can therefore be factored out of the above sum, so that  $F_1(\vec{q}, t)$  becomes

$$F_1(\vec{q}, t) = \langle N \rangle F_s(\vec{q}, t). \quad (4.23)$$

The quantity  $F_s(\vec{q}, t)$  is called the *self-intermediate scattering function*.  $F_s(\vec{q}, t)$  is the Fourier transform of the probability distribution  $G_s(\vec{r}, t)$  for a particle to suffer a displacement  $\vec{R}$  in the time  $t$

$$G_s(\vec{R}, t) = \left\langle \delta \left( \vec{R} - (\vec{r}_j(t) - \vec{r}_j(0)) \right) \right\rangle. \quad (4.24)$$

This function was described in Section 2.4. Since particle  $j$  is not unique, any particle could have been chosen, and the same  $G_s(\vec{R}, t)$  would result.

### Brownian Particles

As we defined in the Section 2.4, for non-interacting Brownian particles  $G_s(\vec{R}, t)$  denotes the probability density for the Brownian particle position  $\vec{R}$  at time  $t$ , given that the particle was initially at the origin. In the approximation of infinite dilution,  $G_s(\vec{R}, t)$  can be regarded as the solution of the diffusion equation (Equation 2.18)

$$\frac{\partial}{\partial t} G_s(\vec{R}, t) = D_0 \nabla^2 G_s(\vec{R}, t), \quad (4.25)$$

subject to the initial condition  $G_s(\vec{R}, 0) = \delta \vec{R}$ , where  $D_0$  is the self-diffusion coefficient.

Since  $F_s(\vec{q}, t)$  is the Fourier transform of the probability distribution  $G_s(\vec{r}, t)$ , the spatial Fourier transform of Equation 4.25 is

$$\frac{\partial}{\partial t} F_s(\vec{q}, t) = -q^2 D_0 F_s(\vec{q}, t), \quad (4.26)$$

and the solution of this equation, subject to the boundary condition  $F_s(\vec{q}, 0) = 1$ , is easily obtained

$$F_s(\vec{q}, t) = \exp(-q^2 D_0 t). \quad (4.27)$$

According to Equations 4.19, 4.23 and 4.27, we obtain for the field autocorrelation function

$$g_E(t) \propto \exp(-q^2 D_0 t). \quad (4.28)$$

This allows a characteristic relaxation time to be defined as  $\tau_q \equiv (q^2 D_0)^{-1}$ .

In order to determine the average sphere diameter from the self-diffusion coefficient, a hydrodynamic relation has to be known which describes the reaction force of the viscous medium to the movement of the particle. For an isolated sphere, this is the well known Stokes-Einstein equation (Equation 2.29)

$$D_0 = \frac{k_B T}{6\pi\eta a},$$

Hence, the autocorrelation function can be used to measure the diffusion coefficient of a spherical particle and to determine the particle radius therefrom. The DLS measured radius, by definition, is the radius of a hypothetical hard sphere that diffuses with the same speed as the scatters under examination. This definition is somewhat problematic since hypothetical hard spheres are non-existent. In practice, macromolecules in solution are non-spherical, polydisperse, and solvated. Hence, the radius calculated from the diffusional properties of the particle is indicative of the apparent size of the dynamic hydrated/solvated particle. A radius determined in this way is commonly referred to as the *hydrodynamic radius*. For charged particles it is important to note that electroviscous effects are usually neglected [97].

### 4.3.2 Linear Particles

In the previous Section we have discussed the general features of the scattered light by spherical Brownian particles. In a more general case, however, particles could be anisotropic. In this case the magnitude and direction of the

induced dipole moment depend on the orientation of the particle with respect to the electric field vector of the incident light.

The previously defined component of the molecular polarizability tensor  $\alpha_{if}(t)$  (Equation 4.5) is the projection of the polarizability tensor  $\alpha^j$  of molecule  $j$  onto the initial and final polarization directions of the light wave. Due to the optical anisotropy of the particles, the polarizability tensor generally has off-diagonal elements. This means that the components of the dipole moment induced by the field  $\vec{\mu}_f(t) = \hat{\alpha}_{if}(t)\vec{E}_i(t)$ , will generally not be parallel to the applied field  $\vec{E}_i$ . Since the particles continuously reorient, the magnitude and direction of its induced moment fluctuates. This leads to a change in the polarization and the electric field strength of the light emitted by the fluctuating induced dipole moment. Therefore, diffusive rods are more complicated to describe than diffusing spheres. The light scattered from an assembly of particles contains information about molecular tumbling. For linear particles the orientational variables play a fundamental role.

### Time Correlation Function of Diluted Suspension of Linear Particles

According to Equation 4.13 the time-correlation function of  $E_s$  is determined by the autocorrelation of  $\delta\alpha_{if}(\vec{q}, t) = \sum_{j=1}^N \alpha_{if}^j(t) \exp[i\vec{q} \cdot \vec{r}(t)]$ . In this Section the experimental system is assumed to be diluted, and so again only self-correlations need be considered. According to Equation 4.19, the autocorrelation function becomes

$$g_E(t) \propto \sum_{j=1}^N \left\langle \alpha_{if}^j(0) \alpha_{if}^j(t) \exp[i\vec{q} \cdot (\vec{r}_j(t) - \vec{r}_j(0))] \right\rangle, \quad (4.29)$$

where the  $\alpha_{if}^j(t)$  changes with time due to translational and rotational particle movement.

In what follows we will assume that the center of mass position and the orientation of the particles are statistically independent. This means that translational diffusion is isotropic and not coupled with rotational diffusive modes. Furthermore, the diffusion coefficient for translational motion should be a scalar quantity. This is, however, not a good assumption for highly anisotropic or long rods. In these cases, a strong coupling between translational and rotational modes is expected and, as we will see in the Section 4.4.2, a non-trivial coupled diffusion equation has to be solved.

According to the assumption of statistical independence of particle translation and rotation, the previous Equation 4.29 becomes

$$g_E(t) \propto \sum_{j=1}^N \left\langle \alpha_{if}^j(0) \alpha_{if}^j(t) \right\rangle F_s(\vec{q}, t). \quad (4.30)$$

The only  $\vec{q}$  dependence on the right-hand side of Equation 4.30 is in the translational factor  $F_s(\vec{q}, t)$ . The rods reorient many times while diffusing a distance comparable to  $q^{-1}$ , and the expression  $\left\langle \alpha_{if}^j(0) \alpha_{if}^j(t) \right\rangle$  can be considered as purely local in character, and consequently does not depend on  $\vec{q}$ .

The linear particles are assumed to be identical, so that the correlation function  $\left\langle \alpha_{if}^j(0) \alpha_{if}^j(t) \right\rangle$  is the same for every equivalent particle in the system. Moreover, the autocorrelation function involves an ensemble average. Consequently, Equation 4.29 becomes

$$g_E(t) \propto \langle N \rangle \langle \alpha_{if}(0) \alpha_{if}(t) \rangle F_s(\vec{q}, t). \quad (4.31)$$

Until now, all the equations have been written in general tensor notation and hence are independent of any specific coordinate system employed. However, in order to calculate the autocorrelation function according to the Equation 4.31, the components of the molecular polarizability tensor must be defined with regard to the scattering geometry. The geometry used in our experiments is indicated in Figure 4.4. In this geometry the  $XY$  plane is the *scattering plane*, which is the plane defined by the incident and scattered wave vectors.  $\theta$  is the scattering angle. The subscripts  $V$  and  $H$  correspond to directions that are vertical and horizontal with respect to the scattering plane. In typical light scattering experiments, laser light passes through a polarizer in order to set the polarization of the incident beam. In our geometry, the incident electric field is polarized along the  $z$  axis, and so,  $\vec{n}_i = \hat{z}$ .

This means that the dipole moment is  $\vec{\mu}(t) = E(t)(\hat{\alpha}(t) \cdot \hat{z})$  and  $\vec{\mu}_z(t) = \hat{z} \cdot \vec{\mu} = E(t)(\hat{z} \cdot \hat{\alpha} \cdot \hat{z})$ . Thus, the laboratory-fixed quantity  $\alpha_{zz}$  may be considered as the  $z$  component of the dipole moment induced in the particles by a unit field in the  $z$  direction. A similar interpretation holds for  $\alpha_{yz}(t)$ . The vertical component of the initially vertically polarized scattered electric field, is known as the *polarized* component  $\vec{E}_{VV}$ , and the horizontal component  $\vec{E}_{VH}$  as the *depolarized* component. Thus, using the definition of  $\alpha_{if}$  and the polarization directions, we obtain

$$g_E(t)_{VV} \propto \langle N \rangle \langle \alpha_{zz}^j(0) \alpha_{zz}^j(t) \rangle F_s(\vec{q}, t), \quad (4.32)$$

and

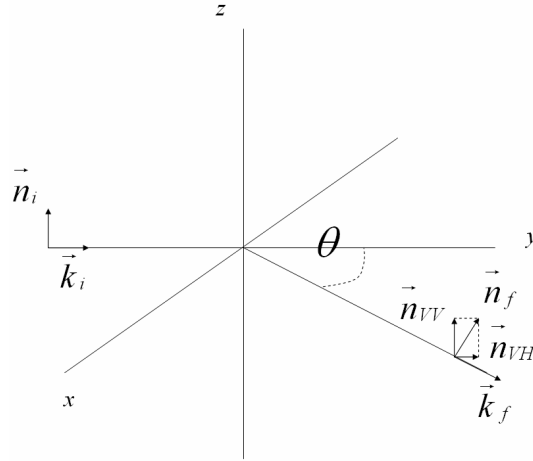


Figure 4.4: Schematic plot of the scattering geometry. The incident electric field is polarized along the  $z$  axis, and the  $XY$  plane is the *scattering plane*.  $\theta$  is the scattering angle. Due to the anisotropy of the non-spherical scatters, the scattered electric field may have two different polarization directions,  $\vec{n}_{VV}$  and  $\vec{n}_{VH}$ .

$$g_E(t)_{VH} \propto \langle N \rangle \langle \alpha_{yz}^j(0) \alpha_{yz}^j(t) \rangle F_s(\vec{q}, t). \quad (4.33)$$

The elements  $\alpha_{if}$  of the molecular polarizability tensor have been defined with regard to the laboratory coordinate system. The induced dipole moment, however, depends on the orientation of the linear particles and so, the molecular polarizability tensor must be expressed in terms of the coordinate system fixed in the molecules. Let the particle have particle-fixed polarizability component  $\alpha_{\parallel}$  parallel to its symmetry axis, and  $\alpha_{\perp}$  in a direction perpendicular to this axis. The polar coordinates specifying the orientation of the molecular symmetry axis in the laboratory-fixed coordinate system are  $(\varphi, \phi)$ , as defined in Figure 4.5. In this new coordinate system, the polarizability may be expressed as

$$\alpha_{zz} = \alpha + \left(\frac{16\pi}{45}\right)^{\frac{1}{2}} \beta Y_{2,0}(\varphi, \phi), \quad (4.34)$$

and

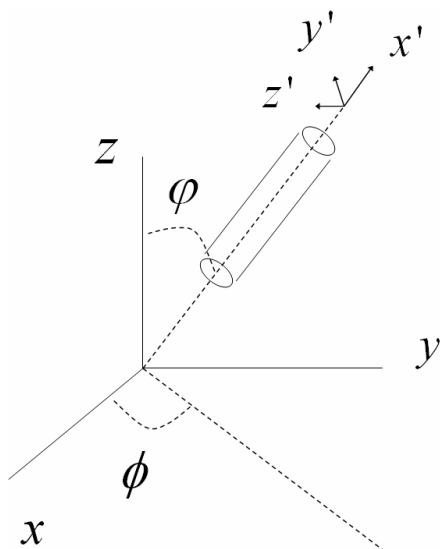


Figure 4.5: The laboratory-fixed axes are  $XYZ$  and the particle-fixed axes are  $X'Y'Z'$ . The orientation angles of the symmetry axis of the cylindrical particle are given by  $\varphi$  and  $\phi$ .

$$\alpha_{yz} = i\left(\frac{2\pi}{15}\right)^{\frac{1}{2}}\beta(Y_{2,1}(\varphi, \phi) + Y_{2,-1}(\varphi, \phi)), \quad (4.35)$$

where  $Y_{2,m}(\varphi, \phi)$  are the second order spherical harmonics [50]. The only molecular parameters that appear in the laboratory-fixed polarizabilities given in Equations 4.34 and 4.35 are

$$\alpha \equiv \frac{1}{3}(\alpha_{\parallel} + 2\alpha_{\perp}), \quad (4.36)$$

and

$$\beta \equiv (\alpha_{\parallel} - \alpha_{\perp}), \quad (4.37)$$

where  $\alpha$  is called the *isotropic part* of the polarizability tensor. This is independent of the molecular orientation. The parameter  $\beta$  is related to the optical anisotropy of the particle, and it is known as the *anisotropic part* of the polarizability. For optically spherical particles  $\alpha_{\perp} = \alpha_{\parallel}$  and consequently



$\beta = 0$ . The parameters  $\alpha$  and  $\beta$  determine the intensities of the different components of the scattered light.

Substituting Equations 4.34 and 4.35 in Equations 4.32 and 4.33, we obtain

$$g_E(t)_{VV} \propto \langle N \rangle [\alpha^2 F_s(\vec{q}, t) + (\frac{16\pi}{45})\beta^2 F_{2,0}^2(t) F_s(\vec{q}, t)], \quad (4.38)$$

and

$$g_E(t)_{VH} \propto \langle N \rangle (\frac{2\pi}{15})\beta^2 [F_{1,1}^2(t) + F_{1,-1}^2(t) + F_{-1,-1}^2(t) + F_{-1,-1}^2(t)] F_s(\vec{q}, t), \quad (4.39)$$

where

$$F_{m,m'}^l(t) \equiv \langle Y_{l,m'}^*(\varphi(0), \phi(0)) Y_{l,m}(\varphi(t), \phi(t)) \rangle \quad (4.40)$$

are orientational correlation functions which reflect how the angles  $\varphi(t)$  and  $\phi(t)$  change in time. The first term on the right-hand side of the Equation 4.38 is independent of rotations since it involves only the isotropic part of the polarizability tensor.

### Linear Brownian Particles

During all the Section 4.3 we have assumed that the center of the mass position and the orientation of the linear aggregates are statistically independent. Hence, the diffusion equation given in Section 2.4 for short rods would be separable in rotational and translational parts. Hence, the motion of the linear particles is described by the diffusion equation (see Equation 2.24)

$$\frac{\partial}{\partial t} c = D_t \nabla^2 c - D_r \hat{\mathbf{L}}^2 c,$$

This theory assumes that translational diffusion is isotropic. In other words, the diffusion constant parallel and perpendicular to the long molecular axis are the same in a molecular fixed frame.

Keeping constant the spatial position of the cylinder  $R = 1$ , Equation 2.24 becomes the *rotational diffusion equation*

$$\frac{\partial}{\partial t} c = -D_r \hat{\mathbf{L}}^2 c.$$

The particular solution of this diffusion equation can be interpreted as the probability density for a rod to have orientation  $\hat{u}$  at time  $t$  given that it

had orientation  $\hat{u}_0$  at time 0. As is well known, the spherical harmonics  $Y_{l,m}(\theta, \phi) \equiv Y_{l,m}(\hat{u})$  are eigenfunctions of  $\hat{\mathbf{L}}^2$  and  $\hat{\mathbf{L}}_z$  corresponding to the eigenvalues  $l(l+1)$  and  $m_l$  respectively, and form a complete orthonormal set spanning the space of functions of  $\hat{u}$ . The particular solution of Equation 4.41 subject to the initial condition

$$c(\hat{u}, 0) = \delta(\hat{u} - \hat{u}_0) = \sum_{lm} Y_{l,m}(\hat{u}_0) Y_{l,m}^*(\hat{u}) \quad (4.41)$$

is therefore

$$c(\hat{u}, t) = \sum_{lm} \exp(-l(l+1)D_r \hat{\mathbf{I}}^2) Y_{l,m}^*(\hat{u}) Y_{l,m}(\hat{u}_0). \quad (4.42)$$

According to the previous definition, the solution of the diffusion equation can be interpreted as the transition probability of finding a cylinder pointing at the direction  $\hat{u}$ , given that the orientation of its mean axis at time  $t = 0$  was aligned along  $\hat{u}_0$

$$K_s(\hat{u}, t | \hat{u}_0, 0) = \sum_{lm} \exp(-l(l+1)D_r \hat{\mathbf{I}}^2) Y_{l,m}^*(\hat{u}) Y_{l,m}(\hat{u}_0). \quad (4.43)$$

The correlation functions required in light scattering (please, see Equations from 4.32 to 4.35) are of the form  $\langle Y_{l',m'}^*(\hat{u}(0)) Y_{l,m}(\hat{u}(t)) \rangle$ . These may be written as

$$\langle Y_{l',m'}^*(\hat{u}(0)) Y_{l,m}(\hat{u}(t)) \rangle = \int d^2 u_0 \int d^2 u Y_{l,m}(\hat{u}) G_s(\hat{u}, t; \hat{u}_0, 0) Y_{l',m'}^*(\hat{u}_0), \quad (4.44)$$

where

$$G_s(\hat{u}, t | \hat{u}_0, 0) = K_s(\hat{u}, t | \hat{u}_0, 0) p(\hat{u}_0) \quad (4.45)$$

is the probability of finding a rod in the neighborhood  $d^2 u$  of the orientation  $\hat{u}$  at time  $t$  given that the particle was initially in the neighborhood of the origin. In an equilibrium ensemble of rods, we expected a uniform distribution of molecular orientations, so that the probability distribution function  $p(\hat{u}_0)$  of the initial orientation  $p(\hat{u}_0) = \frac{1}{4\pi}$ . Combining Equations from 4.43 to 4.45, and returning to the Equation 4.40, it is observed that the correlation required orientation functions become

$$F_{mm'}^2 = \frac{1}{4\pi} \exp(-6D_r t) \delta_{mm'} \quad (4.46)$$

In Section 4.3.1, we found for the spatial Fourier component  $F_s(\vec{q}, t) = \exp(-q^2 D t)$  for translational diffusion. Combining this result with Equations 4.38, 4.39 and 4.46 gives for rotational and translational diffusion

$$g_E(t)_{VV} \propto \langle N \rangle \left[ \alpha^2 + \left( \frac{4}{45} \right) \beta^2 \exp(-6D_r t) \right] \exp(-q^2 D t), \quad (4.47)$$

and

$$g_E(t)_{VH} \propto \frac{1}{15} \langle N \rangle \beta^2 \exp(-6D_r t) \exp(-q^2 D t). \quad (4.48)$$

Equations 4.47 and 4.48 are valid for very diluted solutions of symmetric cylindrically particles, when the particles satisfy the following assumptions: molecular rotation and translation are independent, the translational motions are described by the translational diffusion equation, and the rotational motions are described by the rotational diffusion equation.

Depolarized scattered light can provide dynamic and structural information that is often not obtained by other techniques [98, 91]. Despite these advantages, depolarized scattering has so far played a relatively minor role in the study of particles in solution. The difficulties stem from the fact that macromolecular optical anisotropies are usually small relative to the average molecular polarizabilities. Thus, unless the polarizers in the experiment are extremely good, the experiment results are for the most part unrealizable. The polarized scattering (very large) usually "leak through" the polarizers and is measured as part of the depolarized component. Another difficulty is that since the depolarized intensity is very weak, the solution must be relatively concentrated to obtain measurable depolarized signal. Moreover, these high concentrations results in multiple scattering of the isotropic signal. Since polarizations change in multiple scattering (even for optically isotropic particles), this multiply scattered light could easily be mistaken for the single scattered depolarized signal<sup>5</sup>.

## 4.4 Scattering from Large Particles

So far, we have considered only light scattering from small particles. When particles are very large, however, the wavelets scattered from different subre-

---

<sup>5</sup>On the other hand, at high particle concentrations the linear aggregates formed by magnetic particles experience additional lateral attractions and aggregate, forming columns.

gions of the same particle are not always in phase and hence do not necessarily interfere constructively at the detector. Therefore, intraparticle interference must be taken into account in the calculations of the scattered intensity. The latter depends entirely on the optical properties of the particles and, for non spherical particles, on their orientation. Hence, the scattered light intensity contains information about particle translation and rotation, particle shape, and internal particle fluctuations. We present here a short discussion of these effects for large particles in diluted solutions.

In the optically isotropic case the polarizability  $\alpha_l^i$  is a scalar quantity  $\alpha$ , and the induced dipole moment is always parallel to the applied field. Most of the work on intramolecular interference has been concerned with isotropic scattering, because the depolarized signal is usually much weaker to the polarized signal, and is hence relatively more hard to measure. Thus, throughout this Section we will focus on the isotropic scattering.

#### 4.4.1 Form Factor

First, we will divide the particle in different subregions, such that its maximum size  $l$  is small compared to  $q^{-1}$ . This ensures that each subregion can be considered as a point scatter, that is, that there is no significant intrasubregion interference. Each large particle contains  $n$  subregions and the scattering volume contains  $N$  particles. Then, according to Equation 4.18, the *scattered field zero-time correlation function* is

$$g_E(q, 0) \propto (\vec{n}_i \cdot \vec{n}_f)^2 \left\langle \sum_{i,j,l,m} \alpha_l^i(0) \alpha_m^j(0) \exp(i\vec{q} \cdot (\vec{r}_l^i(0) - \vec{r}_m^j(0))) \right\rangle, \quad (4.49)$$

where  $\vec{r}_l^i$  is the position and  $\alpha_l^i(0)$  the polarizability of the  $l^{th}$  subregion of the  $i^{th}$  particle.

If the solution is dilute enough, the subregions on different particles are uncorrelated so that the  $i \neq j$  sum gives zero<sup>6</sup>. Moreover, if all the subregions and particles have identical optical properties the zero autocorrelation function may be written as

$$g_E(q, 0) \propto (\vec{n}_i \cdot \vec{n}_f)^2 \langle N \rangle \alpha_M^2 P(q), \quad (4.50)$$

where  $\alpha_M \equiv n\alpha$  is the particle polarizability, and

---

<sup>6</sup>Assuming that there are no correlations between the particles. The spatial interparticles correlations will be discussed in Section 4.5.1.

$$P(q) \equiv \frac{1}{n^2} \left\langle \sum_{l,m} \exp(i\vec{q} \cdot (\vec{r}_l(0) - \vec{r}_m(0))) \right\rangle \quad (4.51)$$

is the *form factor*, or *interparticle structure factor*. In Equation 4.51, the double sum is only over pairs of segments belonging to the same particle.

On the other hand, the scattered field zero-time correlation function given by Equation 4.50 can be expressed as

$$g_E(q, 0) \equiv \langle E_s^*(q, 0) E_s(q, 0) \rangle \propto \langle I(q) \rangle, \quad (4.52)$$

where  $\langle I(q) \rangle$  is the average scattered intensity<sup>7</sup>. Combining Equations 4.50 and 4.52, yields

$$\langle I(q) \rangle \propto P(q). \quad (4.53)$$

### Form Factor of Large Rigid Spheres

In this case,  $P(q)$  is easily evaluated. For calculations it is convenient to express the positions of the different subregions  $\vec{r}_i^j$  in terms of the position of the particle's center of mass  $\vec{R}(t)$  and a vector giving the position of the subregion relative to the center of mass  $\vec{b}_j(t)$

$$\vec{r}_j(t) = \vec{R}(t) + \vec{b}_j(t). \quad (4.54)$$

Thus, the form factor for a spherical particle becomes

$$P(q) \equiv \frac{1}{n^2} \left\langle \sum_{l,m} \exp(i\vec{q} \cdot (\vec{b}_l(0) - \vec{b}_m(0))) \right\rangle. \quad (4.55)$$

Equation 4.55 may be written as

$$P(q) = \frac{1}{n^2} \left| \sum_{i=1}^n \exp(i\vec{q} \cdot \vec{b}_i) \right|^2, \quad (4.56)$$

and the sum may then be replaced by an integral

$$P(q) = \left| \frac{3}{4\pi r^3} \int_0^a \exp(i\vec{q} \cdot \vec{b}) 4\pi b^2 db \right|^2, \quad (4.57)$$

<sup>7</sup>The equivalence between the ensemble-averaged correlation function and the time-correlation functions was discussed in Section 4.3.

where  $a$  is the radius of the spherical particle. Now, the integral in Equation 4.57 is easily performed, and the result becomes [26]

$$P(q) = \left[ \frac{3}{(qa)^3} (\sin qa - qa \cos qa) \right]^2. \quad (4.58)$$

### Form Factor

Let us consider a long thin rod, i.e. a particle with a diameter that is small if compared to its length. If the rod diameter is small enough, the light scattered from two points contained in the same cross section does not have any significant phase difference. Thus, as far as light scattering is concerned, the rod is a distribution of polarizable segments along a straight line. We may then apply Equation 4.51 written in the form

$$P(q) = \left\langle \left| \sum_l \frac{1}{n^2} \exp(i\vec{q} \cdot \hat{u}r_l) \right|^2 \right\rangle, \quad (4.59)$$

where  $\hat{u}$  is a unit vector aligned along the cylindrical axis of the rod. The sum is, as before, over all rod segments and the brackets denote an average over all  $\hat{u}$ . By making  $n$  very large while keeping the length  $L$  of the rod constant, the sum in Equation 4.59 may be replaced by an integral

$$\lim_{n \rightarrow \infty} \sum_l \frac{1}{n^2} \exp(i\vec{q} \cdot (\hat{u}r_l)) = \frac{1}{L} \int_{-L/2}^{L/2} \exp(i\vec{q} \cdot \hat{u}r) dr = j_0(\vec{q} \cdot \hat{u} \frac{L}{2}), \quad (4.60)$$

where  $j_0(w)$  is the spherical Bessel function of order zero. Choosing a coordinate system such that  $\vec{q}$  is aligned along the  $z$  axis, and expressing  $\hat{u}$  in spherical coordinates we find that  $\vec{q} \cdot \hat{u} = q \cos \theta$  and so,

$$P(q) = \left\langle \left| j_0\left(\frac{x}{2} \cos \theta\right) \right|^2 \right\rangle, \quad (4.61)$$

where  $x \equiv qL$ . In an equilibrium ensemble, all possible rod orientations are equally probable so that the orientation distribution function becomes  $p(\theta, \phi) = \frac{1}{4\pi}$ . The brackets in Equation 4.61 denote an average over all possible rod orientation. Therefore,

$$P(q) = \frac{1}{4\pi} \int_0^{2\pi} d\phi \int_0^\pi d\theta \sin \theta \left| j_0\left(\frac{x}{2} \cos \theta\right) \right|^2. \quad (4.62)$$

This formula can be evaluated numerically in order to determine how  $P(q)$  depends on  $q$ .

### Mie Solution of Maxwell's equations

All the theories previously described in this chapter are valid only in what is called *Rayleigh-Gans-Debye* approximation (RGD). This approximation assumes that each segment of scattering particles "sees" the same (or nearly the same) incident light wave. However, since part of the incident light passes through the particles and part traverses through the fluid there are phase differences in the incident field. The phase difference is equal to is  $\frac{4\pi}{\lambda}a|m - 1|$  [26], and therefore a rough criterion of the validity of the RGD approximation is

$$\frac{4\pi}{\lambda}a|m - 1| \ll 1, \quad (4.63)$$

where  $a$  is the radius of the colloidal particle and  $m$  is the ratio of the refractive index inside the particle to that outside. The RGD approximation breaks down when the particles become very large and have a size that is of the order of the wavelength of the incident light. Now, the particle interior is optically very different from the surrounding medium. The problem of electromagnetic scattering by large spheres was first solved by Gustav Mie (1869-1957). Mie theory is a complete analytical solution of Maxwell's equations for the scattering of electromagnetic radiation by spherical particles of any size (see Figure 4.6). A detailed discussion about this complicated optic problem, however, surpasses the scope of this work. For further details, the interested reader is referred to the excellent book written by Kerker [99]<sup>8</sup>.

Considering the configuration described in Figure 4.4, where  $XY$  is the horizontal plane and the incident field is vertically polarized, we obtain

$$P(q) \propto |S_1|^2, \quad (4.64)$$

where the *amplitude function*  $S_1$  is

$$S_1 \equiv \sum_{n=1}^{\infty} \frac{2n+1}{n(n+1)} [a_n \pi_n(\cos\theta) + b_n \tau_n(\cos\theta)] (-1)^{n+1}, \quad (4.65)$$

and the angular functions are

$$\pi_n(\cos\theta) \equiv \frac{P_n^1(\cos\theta)}{\sin\theta} \quad (4.66)$$

---

<sup>8</sup>Different programs to compute the Mie solution for a sphere can be found in <http://www.iwt-bremen.de/vt/laser/wriedt/> in several programming languages.

$$\tau_n(\cos\theta) \equiv \frac{d}{d\theta} P_n^1(\cos\theta). \quad (4.67)$$

Here, the function  $P_n^m(\cos\theta)$  are the associated Legendre polynomials. The *scattering coefficients*,  $a_n$  and  $b_n$ , contain all the physical parameters that describe the particle. They are given by

$$\begin{aligned} a_n &\equiv \frac{\psi_n(\alpha)\psi_n'(\beta) - m\psi_n(\beta)\psi_n'(\alpha)}{\zeta_n(\alpha)\psi_n'(\beta) - m\psi_n(\beta)\zeta_n'(\alpha)} \\ b_n &\equiv \frac{m\psi_n(\alpha)\psi_n'(\beta) - \psi_n(\beta)\psi_n'(\alpha)}{m\zeta_n(\alpha)\psi_n'(\beta) - \psi_n(\beta)\zeta_n'(\alpha)}, \end{aligned} \quad (4.68)$$

where  $\alpha \equiv 2\pi a/\lambda$ , and  $\beta \equiv m\alpha$ . The radial functions  $\psi_n(x)$  and  $\zeta_n(x)$  are the Ricatti-Bessel and Hankel functions.

In the Mie regime, the shape of the scattering center becomes much more significant and the theory only works well for spheres. Applying reasonable modifications, infinitely long cylinders and ellipsoidal particles may also be approximated [99, 100, 101]. These theories, however, are not applicable for finite cylinders. To account for scattering that arises from inhomogeneous objects of arbitrary shape, a more complicated model is needed<sup>9</sup>.

Until now, we have studied non-magnetic materials. However, for magnetic particles the relative magnetic permeability  $\mu \neq 1$ ,  $m = \sqrt{\epsilon\mu}$ , and

$$\begin{aligned} a_n &\equiv \frac{\mu\psi_n(\alpha)\psi_n'(\beta) - m\psi_n(\beta)\psi_n'(\alpha)}{\mu\zeta_n(\alpha)\psi_n'(\beta) - m\psi_n(\beta)\zeta_n'(\alpha)} \\ b_n &\equiv \frac{m\psi_n(\alpha)\psi_n'(\beta) - \mu\psi_n(\beta)\psi_n'(\alpha)}{m\zeta_n(\alpha)\psi_n'(\beta) - \mu\psi_n(\beta)\zeta_n'(\alpha)}. \end{aligned} \quad (4.69)$$

Some unusual electromagnetic scattering effects have been theoretically described for spheres composed of magnetic materials (please, see Figure 4.7 and the references [103, 104]). Moreover,  $\mu$  and  $\epsilon$  are usually complex. The imaginary part is called the *extinction coefficient*. It determined the amount of light that is absorbed when the electromagnetic wave propagates through the material. Indeed, even reversible light-induced cluster formation of magnetic colloids has been observed, when kerosene-based magnetite ferrofluids were illuminated with visible light within their optical absorption band [105, 106].

---

<sup>9</sup>For instance, the finite-difference-time-domain (FDTD) technique is a powerful computational method that provides a full solution of Maxwell's equations. Complex objects of any dielectric structure can be modeled using this method [102].



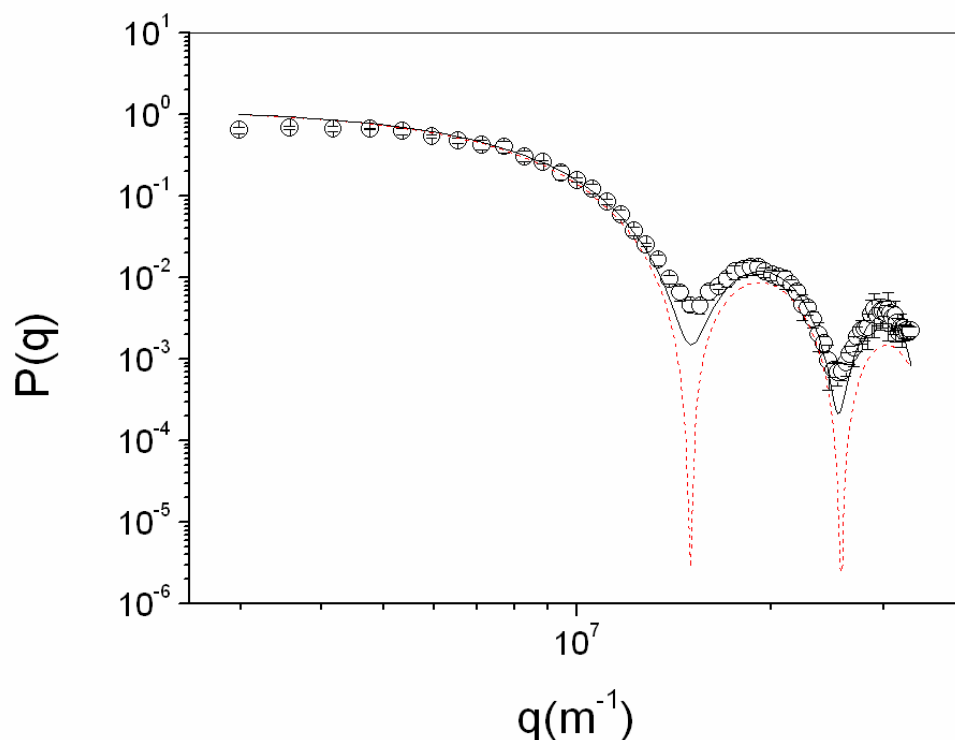


Figure 4.6: Experimental normalized Form Factor for a stable sample of polystyrene particles. The particles are highly monodisperse spheres with an average diameter of  $(540 \pm 10)$  nm (AS1). The experimental data are shown as points  $\circ$ . The continuous curve was calculated according to Mie's theory for spheres with an average diameter of 540 nm and a refractive index of  $n = 1.49$ . The dashed curve was calculated according to the RGD theory for spheres with an average diameter of 600 nm and with a refractive index  $n = 1.49$ . In both cases the particle radius was chosen as fitting parameter.

#### 4.4.2 Time Correlation Function

The measurement of the diffusion coefficients of spherical and linear particles through the autocorrelation function has already been described in Section 4.3. When particles are very large, however, other dynamic properties may also affect the correlation function of the scattered light.

Let us consider a dilute solution of identical particles which may be subdivided into identical segments. Similarly to Equation 4.50, the scattered field

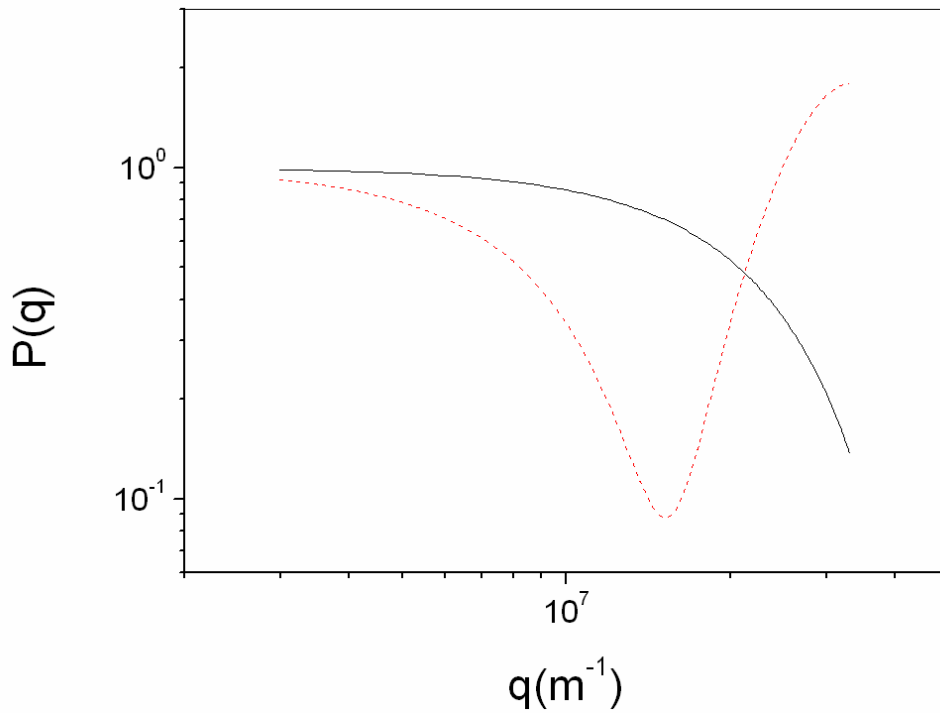


Figure 4.7: Form factor of spherical particles calculated according to Mie's theory for spheres with an average diameter of  $85 \text{ nm}$ , a refractive index  $n = 1.49$ . Solid and dashed lines correspond to particles with a relative magnetic permeability of  $\mu_r = 1$  and  $\mu_r = 2$ , respectively.

time correlation function is proportional to

$$g_E(\vec{q}, t) \propto (\vec{n}_i \cdot \vec{n}_f)^2 \langle N \rangle \alpha_M^2 S(\vec{q}, t), \quad (4.70)$$

where

$$S(\vec{q}, t) \equiv \frac{1}{n^2} \left\langle \sum_{l,m} \exp(i\vec{q} \cdot (\vec{r}_l(t) - \vec{r}_m(0))) \right\rangle \quad (4.71)$$

is the *dynamic structure factor* for a single particle. The sum in Equation 4.71 is only over segments belonging to a single particle.

### Uniform Large Spherical Particles

If we express the positions of the different subregions  $\vec{r}_l^z$  in terms of the position of the particle center of mass  $\vec{R}(t)$  and a vector  $b_j(t)$  pointing from there to the position of the subregion, Equation 4.71 may be written as

$$S(\vec{q}, t) \equiv \frac{1}{n^2} \left\langle \exp(i\vec{q} \cdot \vec{R}_t) \sum_{l,m} \exp(i\vec{q} \cdot (\vec{b}_l(t) - \vec{b}_m(0))) \right\rangle. \quad (4.72)$$

Here the sum over segments is not time dependent since the only relative segmental motion allowed is rotation, and the sum is invariant to any rotation of the sphere [50]. Thus, Equation 4.72 becomes

$$S(\vec{q}, t) = \left\langle \exp(i\vec{q} \cdot \vec{R}_t) \right\rangle S(\vec{q}), \quad (4.73)$$

where

$$S(\vec{q}) \equiv \frac{1}{n^2} \left\langle \sum_{l,m} \exp(i\vec{q} \cdot (\vec{b}_l(t) - \vec{b}_m(0))) \right\rangle \quad (4.74)$$

If we further assume that the particles move due to translational diffusion, it was already shown in Subsection 4.3.1 that

$$g_E(\vec{q}, t) \propto S(\vec{q}, t) \propto \exp(-q^2 D_0 t). \quad (4.75)$$

Thus, only the translational diffusion coefficient may be measured under these conditions.

### Polydispersity

For monodisperse samples the decay of the correlation function is given by a single exponential. For polydisperse systems, however, the autocorrelation function can no longer be represented as a single exponential and the equation 4.28 must be represented as a sum over a distribution of decay rates. This yields

$$g_E(t) \propto \sum_n a_n(q) \exp(-q^2 D_n t), \quad (4.76)$$

where  $a_n$  contains the relative number frequency of spherical particles with translational diffusion coefficient  $D_n$ . Once the autocorrelation curve has been generated, different mathematical approaches can be employed to fit the curve

and thus to determine the average translational diffusion coefficient. One of the most common fitting methods is the *cumulant method*, in which the experimental autocorrelation function is treated as an expansion in powers of  $t$  (please, see the right-hand side of the Figure 4.3) [107]. The expression for its logarithm gives

$$\ln[g_E(t)] \propto -\mu_1 t + \frac{1}{2}\mu_2 t^2 + \dots \quad (4.77)$$

where the numbers  $\mu_i$ , known as the  $i$ th-order cumulant, are interpreted in terms of the average diffusion coefficient, the width of the distribution of diffusion coefficients, skewness of the distribution, etc. The relationship between the cumulants and the moments of the distribution of decay rates  $\Gamma$  is

$$\begin{aligned} \mu_1 &= \langle \Gamma \rangle \\ \mu_2 &= \langle (\Gamma - \langle \Gamma \rangle)^2 \rangle \\ \mu_3 &= \langle (\Gamma - \langle \Gamma \rangle)^3 \rangle - 3 \langle (\Gamma - \langle \Gamma \rangle)^2 \rangle \langle \Gamma - \langle \Gamma \rangle \rangle. \end{aligned} \quad (4.78)$$

Thus, the first cumulant describes the average decay rate of the distribution. It is directly related to the mean diffusion coefficient of the aggregates, and according to  $\mu_1 = q^2 D_{eff}$ , also to the mean particle size. On the other hand, the mean diffusion coefficient is given by [108]

$$\frac{\mu_1}{q^2} = D_{eff} = \sum_n \frac{a_n(q) D_n}{a_n(q)}. \quad (4.79)$$

Depending on the anisotropy and polydispersity of the system, a resulting plot of  $D_{eff}$  vs.  $q$  may or may not show an angular dependence. Monodisperse spherical particles will show no anisotropy, hence no angular dependence is expected and a plot of  $\frac{\mu_1}{q^2}$  vs.  $q$  will result in a horizontal line. Particles with a shape other than a sphere will show anisotropy and thus may present an angular dependence when plotting of  $\frac{\mu_1}{q^2}$  vs.  $q$ .

The second cumulant  $\mu_2$  contains the standard deviation. It is directly related to the second order *polydispersity index*

$$p.i. \equiv \frac{\mu_2}{\mu_1^2} \quad (4.80)$$

and gives an indication of the variance [109].

### Long Rigid Rods

In this section, we treat the rigid rod model. This model illustrates the conditions under which rotational motions of rigid, nonspherical particles affect the field autocorrelation function. The rods are considered to consist of  $n$  identical, optically isotropic segments that are arranged along a line of length  $L$ .

As stated above, the previous theories assume that translational diffusion is isotropic. Hence, the diffusion Equation described in the Equation 2.24 is separable in rotation and translational contributions. In fact, the vast majority of experimental results exclude the coupling effects. However, if one wants to study very long rods this is probably not a good assumption, and one has to take the coupling effect into account. Large diffusing rods are complicated to describe, because a rod will have two independent components in the translational diffusion tensor. One component stands for translations parallel to the long rod axis ( $D_{\parallel}$ ) and one perpendicular to it ( $D_{\perp}$ ). Furthermore, the coupling of translational and rotational diffusion modes has also to be taken into account. This general case yields rather complicated results.

Since all segments are arranged along a line, all  $\vec{b}_j$  are either parallel or antiparallel to a given vector pointing along the rod. All we have to determine to describe the segmental motion is the joint probability distribution function  $c(\vec{R}, \vec{\Omega}, t | \vec{0}, \vec{\Omega}_0, 0)$  of the cylinder to be at position  $\vec{R} = \vec{0}$  with an orientation  $\vec{\Omega} = \vec{\Omega}_0$  at time  $t = 0$ , and at position  $\vec{R}$  and orientation  $\vec{\Omega}$  at time  $t$ . In Section 4.3.2 (Equation 4.45) we showed that this probability distribution is given by

$$c(\vec{R}, \vec{\Omega}, t | \vec{0}, \vec{\Omega}_0, 0) = \frac{1}{4\pi} K_s(\vec{R}, \vec{\Omega}, t | \vec{0}, \vec{\Omega}_0, 0). \quad (4.81)$$

The suspension is again assumed to be homogeneous with respect to the center of gravity of the rods, but also concerning their orientation with respect to the reference frame. The following probability distribution satisfies the translation-rotation diffusion Equation 2.24

$$\frac{\partial}{\partial t} c(\vec{R}, \vec{\Omega}, t | \vec{0}, \vec{\Omega}_0, 0) = \overline{D} \nabla^2 - D_r \hat{\mathbf{I}}^2 + (D_{\parallel} - D_{\perp}) [(\hat{u} \cdot \nabla)^2 - \frac{1}{3} \nabla^2] c(\vec{R}, \vec{\Omega}, t | \vec{0}, \vec{\Omega}_0, 0).$$

Maeda and Fujime included in their calculations the coupling of translational and rotational motion implicitly [97, 110]. However, their calculations

are rather complex, and will not be described here. These authors showed that a complete expression for the autocorrelation function is only numerically possible. However, without solving the diffusion equation, Maeda and Fujime derive an analytical expression for the first cumulant of the field autocorrelation function. They obtained

$$\frac{\mu_1}{q^2} = [\bar{D} - \frac{1}{3}(D_{\parallel} - D_{\perp})] + (\frac{L^2}{12})D_r f_1(K) + (D_{\parallel} - D_{\perp})f_2(K), \quad (4.82)$$

where  $f_1(K)$  and  $f_2(K)$  are functions that depend only on  $K \equiv qL/2$  (please, see the Figure 4.8)

$$f_1(K) = \frac{3}{K^2} \frac{\sum_n n(n+1)(2n+1)b_n(K)^2}{\sum_n (2n+1)b_n(K)^2} \quad (4.83)$$

$$f_2(K) = \frac{\sum_{\text{even } n} (2n+3)(\frac{j_{n+1}(K)}{K})^2}{\sum_n (2n+1)b_n(K)^2},$$

$$b_n(K) = \frac{1}{K} \int_0^{\infty} j_n(z) dz \quad (\text{even } n) \quad (4.84)$$

$$b_n(K) = 0 \quad (\text{odd } n),$$

and  $j_n(z)$  is the  $n$ -th order spherical Bessel function.

Since  $f_1(K) \rightarrow 0$  and  $f_2(K) \rightarrow 1/3$  as  $K \rightarrow 0$ , and  $f_1(K) \rightarrow 1$  and  $f_2(K) \rightarrow 0$  as  $K \rightarrow \infty$ , we have the limiting values of

$$\frac{\mu_1}{q^2} \rightarrow \bar{D} \quad (K \ll 1) \quad (4.85)$$

$$\frac{\mu_1}{q^2} \rightarrow [\bar{D} - \frac{1}{3}(D_{\parallel} - D_{\perp})] + (\frac{L^2}{12})D_r \quad (K \gg 1)$$

All these parameters can be used together with hydrodynamic theories to access information about the size and shape of the cylinders in solution [97].

The theoretical model proposed by Maeda and Fujime takes into account the effect of the anisotropic translational diffusion on the polarized field correlation function. However, this model is only quantitatively correct for the case of large  $qL$  [110]. Moreover, the RGD condition is assumed to be valid by

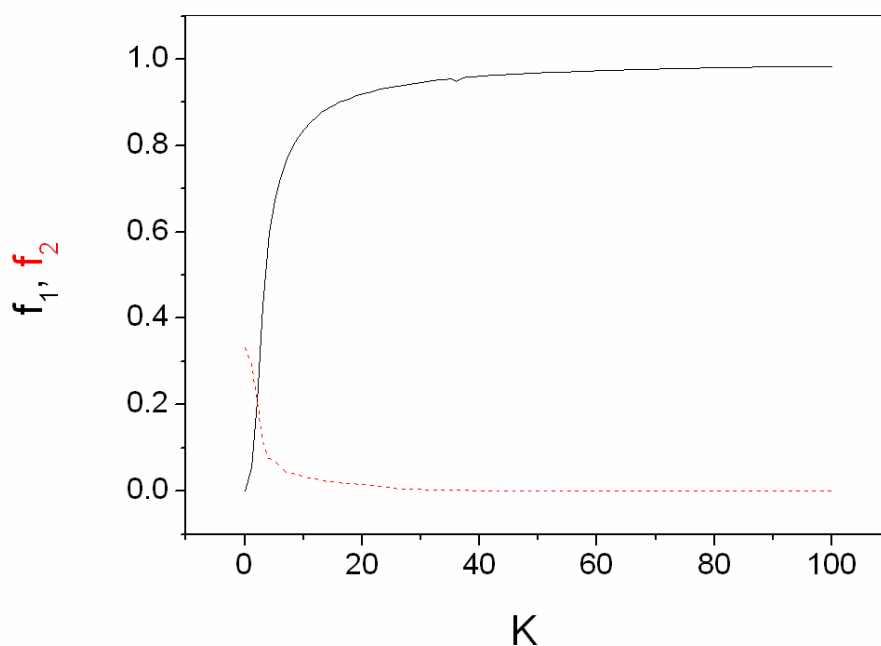


Figure 4.8: Functions  $f_1(K)$  (continuous line) and  $f_2(K)$  (dotted line) vs  $K$ .

assuming small beads, which restrict the theory to thin rods<sup>10</sup>. Even if linear aggregates formed by magnetic particles seems to be rigid, they might still be somewhat flexible, as we will see in Chapter 7, when they become very long. Thus, one would have to take account also the effect of filament flexibility on the correlation function [112, 113]. In this work, however, the flexibility effect was not considered. All these assumptions were assumed in the derivation of the previous equations and so the dynamics might be influenced if one of these did not hold. The characteristic features of their model may serve as a guide for the analysis of experimental data for any pair of  $L$  and  $q$  values.

<sup>10</sup>Several authors have studied the range of validity of the RGD approximation for the light scattered by cylindrical particles [111].

## 4.5 Scattering from Aggregates

Fractal colloid aggregates are frequently studied with light scattering techniques. Light scattering is used to measure the average diffusion coefficient and the fractal dimension,  $d_f$ , which gives information about the average cluster size and the internal structure of the aggregates, respectively.

### 4.5.1 Structure Factor

Aggregate structure information may be obtained using standard fractal analysis techniques. If we assume the particles to be optically identical spheres, the instantaneous intensity impinging on the detector is (see Equation 4.18)

$$I(t) \propto E_s^*(t)E_s(t) \propto \sum_{i=1}^N \sum_{j=1}^N \exp(i\vec{q} \cdot (\vec{r}_i(t) - \vec{r}_j(t))). \quad (4.86)$$

The experimentally accessible quantity is, however, the intensity averaged over a great number of cluster configurations, i.e.

$$I_{mean} \propto \langle E_s^*(t)E_s(t) \rangle \propto \left\langle \sum_{i=1}^N \sum_{j=1}^N \exp(i\vec{q} \cdot (\vec{r}_i(t) - \vec{r}_j(t))) \right\rangle. \quad (4.87)$$

In this expression, it is useful to distinguish between the contribution for  $i = j$  and  $i \neq j$ . The first contribution is due to all individual particles of the cluster, and the second contribution is the intensity variation due to the interference of waves scattered by all pairs of particles. Both effects can be factorized, so that the scattered intensity  $I(q)$  can be written as [99]

$$I(q) = KP(q)S(q), \quad (4.88)$$

where  $K$  is a scattering constant related to the measuring device and the optical properties of the particles,  $P(q)$  is the previously defined form factor (please, see the Subsection 4.4.1), and  $S(q)$  is the *interparticle structure factor* which describes the spatial correlations between the centers of the individual particles.

Let us now study the structure factor in the case of fractal aggregates of a characteristic mean size  $R$ . As we have already mentioned in Section 4.2, the scattering vector  $\vec{q}$  has the units of  $1/\text{length}$ . Therefore, when  $a \gg q^{-1}$  we will observe interference patterns from the primary particles. For



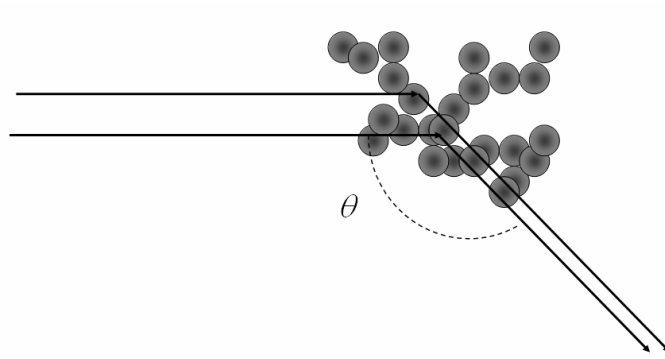


Figure 4.9: The structure factor  $S(q)$  describes the spatial correlations between the centers of the individual particles contained within the aggregates.

$a \ll q^{-1}$  the scattering pattern will mainly come from the interference deriving from different particles. When  $qa \gg 1$ ,  $S(q) \sim 1$  and the observed scattering essentially comes from the individual particles only, i.e.  $I(q) \sim KP(q)$ . However, within the range  $1/R \ll q \ll 1/a$  we see that  $I(q) \sim KP(q)S(q)$ . Finally, if  $qR \ll 1$ , the aggregates essentially behave as point particles and thus scatter isotropically, independent of  $q$ , and  $S(q) \sim 1$ <sup>11</sup>.

The structure factor can be defined as

$$S(q) = \frac{1}{N} \left\langle \sum_{i,j}^N \exp(i\vec{q} \cdot (\vec{r}_i(t) - \vec{r}_j(t))) \right\rangle \quad i \neq j, \quad (4.89)$$

where  $\vec{r}_i(t)$  and  $\vec{r}_j(t)$  are the center of mass position of particles  $i$  and  $j$  at time  $t$ . This function is the Fourier transform of the correlation function  $c(r)$  between the centers of the particles. Assuming a spherical symmetry<sup>12</sup>, the structure factor can be written as

$$S(q) \propto \int_0^\infty \frac{\sin(qr)}{qr} c(r) r^2 dr. \quad (4.90)$$

As we have described previously, it is possible to probe structural correlations at increasing separations within the aggregate by observing a certain range of

<sup>11</sup>Assuming that there are no spatial correlations between the aggregates

<sup>12</sup>This is true if one deals with a collection of randomly oriented aggregates. Since the magnetic field impose a privileged direction for the linear aggregates formed by magnetic particles, the fractal dimension can be only measured in absence of any applied magnetic field.

$q$ . In the intermediate  $q$  regime,  $1/R \ll q \ll 1/a$ , the fractal character of the structure must show up in the scattered intensity.

For colloidal aggregates, self-similarity occurs only over a limited range of length scales. The upper limit for the scaling form of  $c(r)$  is reached when  $r$  come close to the characteristic mean size  $R$ . The lower limit of the scaling is given by the primary particle radius  $a$ . Hence, we have to introduce a cut-off function  $f(r/R)$  in order to take care of the finite character of the aggregate. This function is such that  $f(x) \sim 0$  for  $x > 1$ , and  $f(x) \sim \text{const.}$  for  $x < 1$ . Finally, by introducing the expression for  $c(r)$  given by Equation 3.40 in Equation 4.90, one finds

$$S(q) \propto \int_0^\infty \frac{\sin(qr)}{qr} r^{d_f-1} f\left(\frac{r}{R}\right) dr. \quad (4.91)$$

In the intermediate  $q$ -regime, the cut-off function  $f(x)$  remains almost constant. Thus, the integral in Equation 4.91 converges [114], and one finally finds

$$I(q) \propto S(q) \propto q^{-d_f}. \quad (4.92)$$

Hence, by recording the scattered intensity as function of scattering vector  $q$  we are able to determine the aggregate fractal dimension.

#### 4.5.2 Time Correlation Function

The first cumulant of the measured field autocorrelation function divided by  $q^2$  yields an average effective diffusion coefficient (see Section 4.4.2, and Equation 4.79). According to the current light scattering theory, the average diffusion coefficient  $D_{eff}$  is related to the diffusion coefficients of the different clusters of size  $N$  through the expression [115]

$$D_{eff} = \frac{\sum_{N=1}^{N_c} n_N(t) N^2 S(qR_g) D(N)}{\sum_{N=1}^{N_c} n_N(t) N^2 S(qR_g)}, \quad (4.93)$$

where  $n_N(t)$  is the cluster size distribution,  $S(qR_g)$  is the structure factor that accounts for the spatial distribution of the individual particles within the aggregates, and  $D(N)$  is the diffusion coefficient of a cluster formed by  $N$  monomeric particles. Hence, the effective diffusion coefficients are weighted by the scattering intensity and the number of cluster of each mass. The cut-off size  $N_c$  is the size of the largest aggregate in the system.  $R_g$  is the aggregate radius of gyration. The geometry of the aggregates only is included in Equation 4.93 through  $D(N)$  and  $S(qR_g)$ .

### 4.5.3 Linear Magnetic Aggregates in Uniaxial Fields

The presence of an external magnetic field introduces a preferential orientation in space and impedes the rotational diffusion of the linear aggregates formed by magnetic particles.

#### Bragg Diffraction

William Lawrence Bragg and William Henry Bragg found intense peaks of reflected radiation reflected from crystalline solids at certain wavelengths and incident angles. W. L. Bragg explained this result by modeling the crystal as a set of discrete parallel planes separated by a constant parameter  $d$ . They proposed that the incident X-ray radiation would produce a Bragg peak if the reflections from the different planes interfered constructively. For constructive interference, the separately reflected waves must remain in phase and the difference in the path length of each wave must be equal to an integer multiple of the wavelength [116]. The concept of Bragg diffraction may be applied equally to light diffraction processes.

As we have seen in Section 2.7, field induced aggregation may occur in a primary minimum of energy, where the particles are in contact with each other or in a secondary energy minimum, where the neighbouring particles within the linear aggregates are a short distance apart from each other. Hence, for perfectly aligned particles with a separation  $d$ , illuminated by a white light source, the first order *Bragg condition* reduces to

$$d = \frac{\lambda}{n(1 - \cos\theta)}, \quad (4.94)$$

where  $n$  is the refractive index of the suspension medium,  $\lambda$  is the wavelength of the light, and  $\theta$  is the angle between the incident and the scattered light beams (see Figure 4.10). Because field induced aggregates formed by magnetic particles give rise to a strong Bragg diffraction, the interparticle spacing is accurately measurable. Since repulsive forces between the colloidal particles are balanced by attractive forces (magnetic dipole-dipole and van der Waals interactions), the interparticle force profile between colloidal particles may be obtained as a function of the interparticle spacing  $d$  (see the work of Leal-Calderon et al. [41]).

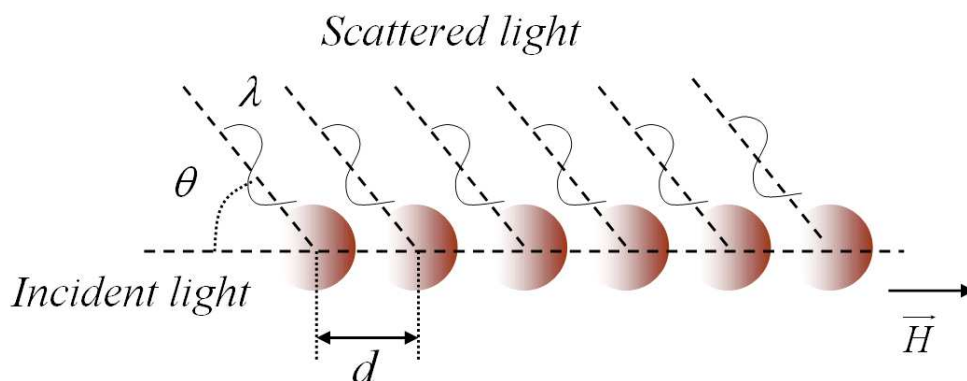


Figure 4.10: The scheme represents the Bragg diffraction of the light scattered by a field induced aggregate of magnetic particles. The incident light direction is parallel to the applied magnetic field.

### Internal Fluctuations

Linear aggregates of magnetic particles may bend and twist slightly due to Brownian motion. Such internal fluctuations may give rise to an additional contribution to the measured average diffusion coefficient. Dynamic light scattering is sensitive to movement at different spatial scales, as we have shown in the Subsection 4.5.1. When the characteristic length  $q^{-1}$  is higher than the particle radius  $a$ , then the centre of mass diffusion of the filaments is detected. For  $q^{-1}$  values close to the particle radius  $a$ , however, dynamic light scattering reflects mainly the internal movement of the particles contained within the aggregates. Using surfactant coated kerosene-based ferrofluid droplet particles, Cutillas et al. have shown experimentally that such positional fluctuations of the particles within the chains cause a linear dependency of the mean diffusion coefficient measured by light scattering on  $q$  [117]. Their experiments also verified that the chains become more rigid and the fluctuations disappear as the field strength increases.

### Birefringency and Dichroism

Since the linear aggregates have a preferential orientation once the constant magnetic field is applied, the colloidal suspensions of magnetic particles present optical anisotropy by means of a complex refractive index. The optical anisotropy leads to *birefringence effects* (different phase velocity for each polarization component of the scattered wave) and *dichroism effects* (different attenuation for

each polarization component of the scattered wave). These optical effects can be described in terms of anisotropies in the real and imaginary part, respectively, of the refractive index [100]. Several authors have taken advantage of these optical effects to study the aggregation kinetics in magnetorheological fluids subject to a constant magnetic field [118]. In these works the scattering dichroism was larger than the scattering birefringence<sup>13</sup>. On the other hand, both dichroism and birefringence effects are negligible as the ratio between the radius and the wavelength becomes smaller [46].

Other authors have been analyzed the birefringence effect on the measurements of the autocorrelation function [119]. These authors suggest that birefringency effects are negligible if the difference between the refractive index of the cylinder and the refractive index of the solvent is small, which is also a requirement for the accuracy of the RGD approximation.

---

<sup>13</sup>In general, if the radius of the linear aggregates is comparable or bigger than the wavelength, then the dichroism is larger than the birefringence.

# Chapter 5

## Materials and Methods

*La técnica es el esfuerzo para ahorrar esfuerzo.*

José Ortega y Gasset

One of the aim of this work has been to demonstrate that some light scattering techniques widely used on the study of the structure and the kinetics of colloidal aggregates, can be used to get valuable data on magnetic colloidal aggregation. With respect to imaging techniques, the statistics is better and the measurements are performed much faster. We believe that these advantages can make light scattering a highly valuable technique for the development and standardization of materials made of magnetic filaments.

### 5.1 Experimental Systems

Various strategies have been developed for synthesizing composite magnetic nanoparticles. These particles must fulfil different requeriments, such as stability in different media, a uniform size distribution, superparamagnetism, a certain iron oxide content, etc<sup>1</sup>.

#### 5.1.1 Magnetic Polystyrene Particles

Magnetic polystyrene particles are known for their almost monodisperse size distribution and perfect spherical shape. Polymer stabilizes the magnetic par-

---

<sup>1</sup>Different suppliers of magnetic particles and related materials can be found in <http://www.magneticmicrosphere.com>

ticles and decreases the particle mass density. In some applications the polymer coating is required in order to provide selective functionality and interaction with target solutes. More detailed information about the synthesis and properties of magnetic polymer microspheres of the size ranging from 50 *nm* to several microns can be found in the literature [35, 120, 121].

The superparamagnetic latex particles used for the light scattering experiments were purchased from Merck Laboratories S.A. (Ref:R0039) The particles are roughly monodisperse polystyrene spheres with an average diameter of  $(165 \pm 5)$  *nm*.

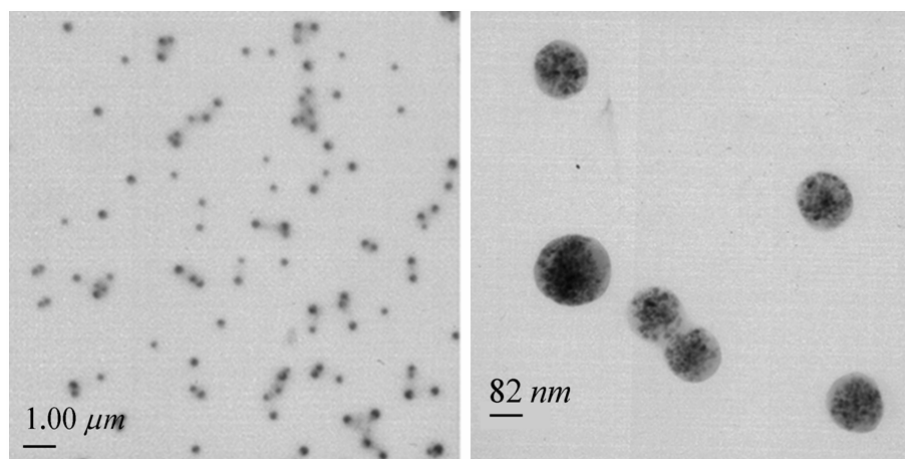


Figure 5.1: Transmission Electron Microscopy images of several individual magnetic polystyrene particles R0039 observed with different magnifications. Magnetic grains appear as dark spots in transmission electron micrographs and do appear to be randomly distributed within the polystyrene matrix.

Their magnetic character derives from magnetite grains of approximately 10 *nm* in size. The magnetic grains appear as dark spots in transmission electron micrographs (TEM) (see Figure 5.1). They seem to be quite randomly distributed within the polystyrene matrix. However, the TEM images also reveal that the iron oxide distribution within particles is not always homogeneous. Sometimes, the magnetic grains show significant clustering within the polystyrene matrix<sup>2</sup>.

---

<sup>2</sup>Unusual rotational effects have been observed by other authors when the magnetic grains

According to the manufacturer, the magnetic polystyrene particles have a ferrite mass content of approximately 53.2% and a saturation magnetization  $M_s$  of approximately  $36 \text{ kA/m}$ . The sample was dried, and the magnetization of the resulting powder was measured at  $298\text{K}$ . The particles reach the saturation magnetization for external magnetic field above  $200 \text{ kA/m}$ . The magnetization curve shown in Figure 5.2 reveals the super-paramagnetic character of the EDLMP. Consequently, the dipolar magnetic interactions between the particles only appear in presence of an applied magnetic field. At the field strengths employed, we are in the linear regime of the magnetization curve, where the magnetization  $M$  is proportional to the external magnetic field  $H$ , i.e.  $M = \chi H$ . From the curve, the magnetic susceptibility of our particles was estimated to be  $\chi = 0.6$ .

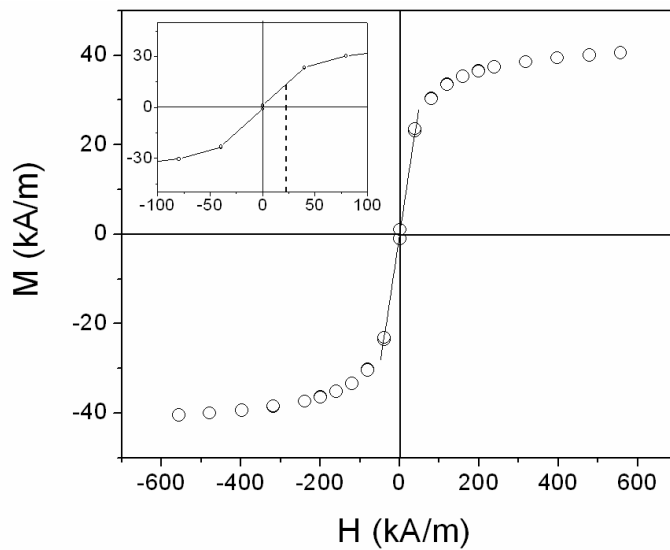


Figure 5.2: Magnetization curve of the polystyrene particles employed for the experiments acquired at room temperature. The measurements were obtained using a MPMS-XL magnetometer (Quantum Design). A detailed view of the low field region is given in the inset. The field strength employed for the aggregation experiments is indicated by a dashed line.

The particles are dispersed in water. The stability of the system is en-  


---

present a nonsymmetric distribution within the polystyrene matrix. Since mass density of magnetite greatly exceeds that of polystyrene, the rotation of these magnetic particles resembles more a "wobble" than a "spin" like behaviour [98].



sured by repulsive forces due to charged carboxylic surface groups and anionic sodium dodecyl sulphate (SDS) surfactant molecules adsorbed on the particle surface. The particle surface potential of approximately  $-50\text{ mV}$  was determined by means of electrophoretic mobility measurements. Due to their relatively low density of  $1.2\text{ g/cm}^3$ , particle sedimentation was found to be negligible during the experiments. Indeed, the light intensity scattered by the sample remains almost constant for 2 days. Prior to the aggregation experiments, the diluted samples were filtered through a  $450\text{ nm}$  pore size membrane filter in order to eliminate primary clusters.

### 5.1.2 Silica Particles

Inorganic magnetic silica spheres are highly stable, even in organic solvent. The nonmagnetic silica serves as a steric barrier which reduces magnetic attraction between particles. Up to now, however, magnetic silica particles are not available with a small size distribution nor a perfect spherical shape.

The samples used for the video-microscopy experiments were aqueous suspensions of core shell particles. The particles were synthesized by the Dr. Abdeslam El-Harrak of the Laboratoire de Colloides et Materiaux Divises (ESPCI, Paris). The particles were produced starting from an octane-based ferrofluid containing 80% by weight of oleic acid covered  $Fe_2O_3$  nanoparticles. To this, tetraethylortosilicate (TEOS) was added (8% by weight). In the next step, 80 g of ferrofluid/TEOS mixture was added dropwise to 15 g of an aqueous solution of sodium alginate (2% by weight) and SDS (2% by weight). The pre-mix was scanty sheared during its preparation. The resulting brownish paste was transferred to a Couette cell where it was sheared at 600 rpm in a  $100\text{ }\mu\text{m}$  gap with a maximum injection rate of  $7\text{ mm/min}$ . The solution obtained was then placed in a rota-vapor at  $50\text{ }^\circ\text{C}$  under vacuum conditions in order to eliminate the octane content from the emulsion droplets. Afterwards, 50 ml of a 50/50 mixture of ammoniac and isopropanol were added dropwise in order to hydrolyze the TEOS. After 3 hours of mechanical stirring, the particles were separated from the suspension medium by means of a magnet and washed several times with pure water. Finally, the particle surface was reinforced by increasing the thickness of the silica shell. This was achieved using Stoeber's method.

Image analysis revealed that the particles are polydisperse in size (ranging from  $300\text{ nm}$  to  $2\text{ }\mu\text{m}$ ) with an average diameter of approximately  $500\text{ nm}$  (Figure 5.3). Prior to the aggregation experiments, the samples were passed through a sucrose density gradient column in order to obtain more monodis-

perse spheres. The average hydrodynamic particle size was determined by means of dynamic light scattering, using a ALV-5000/E correlator. The measurements showed a final size distribution with an average diameter of  $0.58 \mu\text{m}$  and a polydispersity index of 0.12. The particle mass density was measured by equilibrium centrifugation in sucrose obtaining approximately  $\rho \approx 3.6 \text{ g/cm}^3$ . Charged surface silanol groups prevent particle aggregation through repulsive electrostatic interactions. The particle surface potential of approximately  $-10 \text{ mV}$  was obtained by means of electrophoretic mobility measurements.

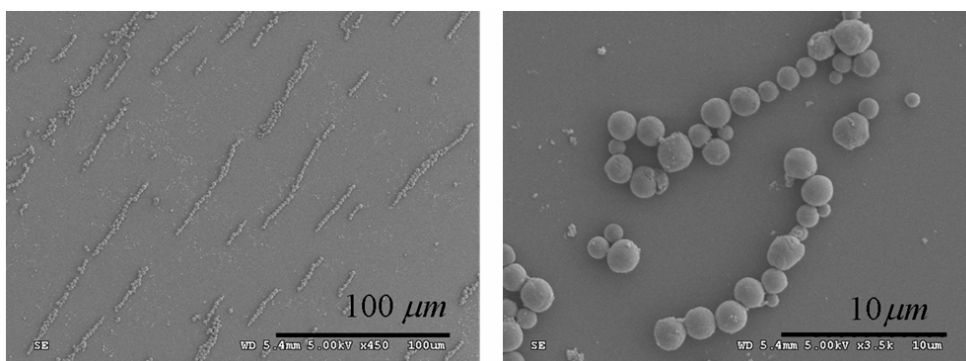


Figure 5.3: Scanning Electron Microscopy images of the magnetic silica sample exposed to a magnetic field. The particles assemble in field-orientated chains. Please, note that the images were taken at different magnifications.

The resulting particles may be considered as a nano-composite material: the inner components, roughly  $10 \text{ nm}$  in size maghemite particles, are extremely confined inside the silica spheres (almost close-packed). The magnetic character of the particles arises from iron oxide content of 65% in weight. The sample was dried, and the magnetization of the resulting powder was measured at  $298\text{K}$ . The particles reached a saturation magnetization  $M_s$  of approximately  $125 \text{ kA/m}$  for applied magnetic fields stronger than  $200 \text{ kA/m}$ . In the linear regime of the magnetization curve, where the magnetization  $M$  is proportional to the external magnetic field  $H$ , the magnetic susceptibility of our particles was estimated to be  $\chi \approx 2.6$ . The magnetization measurements confirm that the particles are superparamagnetic (Figure 5.4).

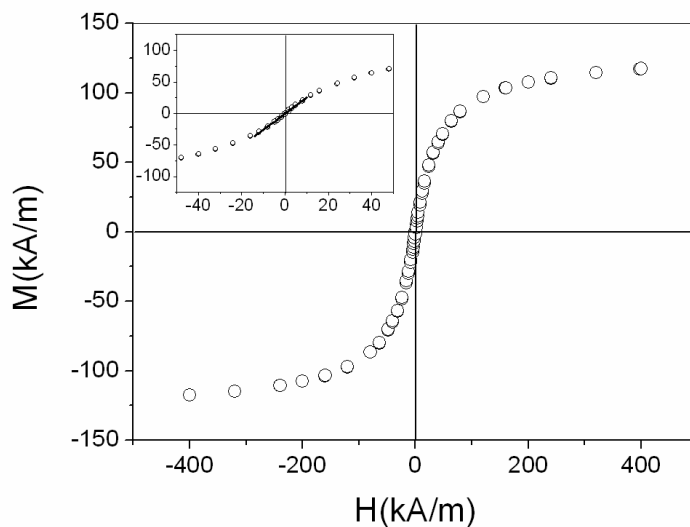


Figure 5.4: Magnetization curves of the silica particles. The sample was dried, and the magnetization of the resulting powder was measured at 298 K. A detailed view of the low field region is given in the inset.

## 5.2 Experimental Devices

### 5.2.1 Light Scattering

The light scattering experiments were performed using a commercial Malvern 4700C System (UK) (Figure 5.5). In general terms, all light scattering devices contain the same basic components. In our light-scattering device, a *laser light source* generates a beam of electromagnetic radiation. The monochromatic *laser beam* passes through a *polarizer* in order to define the polarization plane of the incident beam. Then the beam is focused on the *sample*. The scattered light enters a *detector*. The position of the detector defines the *scattering angle*. The intersection of the incident beam and the field of view of the detector defines the *scattering volume*. The detected signal is analyzed by a *correlator* and finally, a *computer* is used to recover information from the correlation function obtained by the signal analyzer [122]. The main components of the light scattering devices are:

**A** Light source: The main difficulties in performing light-scattering exper-

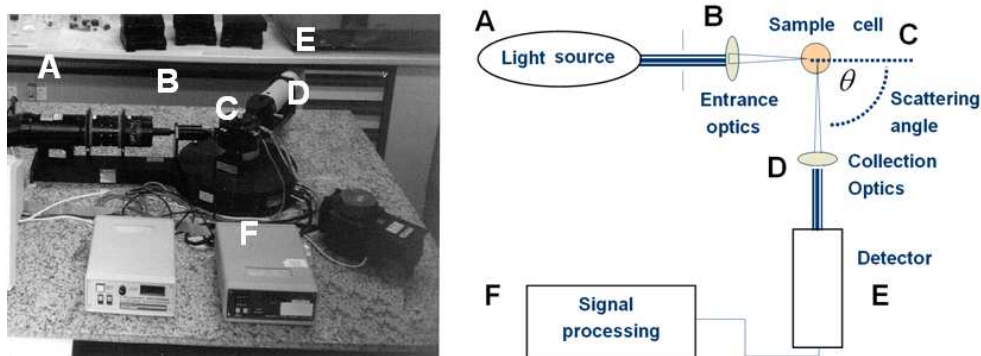


Figure 5.5: Scheme of the major components of a photon spectroscopy set-up.

iments encountered in the past were eliminated when laser are used. For this work two different vertically polarized laseres, a 488 *nm* wavelength Argon and a 632.8 *nm* wavelength Helium-Neon laser, have been employed. The wavelength of the impinging electromagnetic radiation should be of the order of the typical size of the studied object. This means that sructures ranging from 1 *nm* to 1  $\mu\text{m}$  can be studied. The lasers may have up to 200 *mW*, and they have a life time of more than 10000 hours. The laser beams were approximately vertically polarized.

- B** Entrance Optics: Standard entrance optics consists of filters, some focusing lenses, and a set of pinholes that eliminate stray light. It focuses the laser beam and bundles as much intensity as possible in a single coherence area within the sample.
- C** Sample Cell: Sample cells may have a wide variety of shapes and sizes. For angle-dependent measurements, however, cylindrical cells are used. The sample cell is immersed in a thermostated bath, in order to control the temperature during the experiment.
- D** Detection Optics: Just like the entrance optics, the detection optics is made of a system of pinholes and lenses, which define the scattering volume and the number of coherence areas seen by the detector. Its task is to focus the scattered light on the detector.
- E** Detector: Detection systems usually consist of a photomultiplier tube with a pulse amplifier-discriminator. The photomultiplier contains a alkali metal cathode which emit an electron when a photon is absorbed. The

electron is accelerated by an electric field and collides with a sheet of metal knocking out several electrons. The group of electrons is again accelerated, collides with a second dynode, and so forth until after 9 to 14 dynodes the single electron has been multiplied into  $10^5$  to  $10^7$  or more electrons. This group of electrons originating from the capture of a single photon forms the output of a photomultiplier.

The thermostated sample cell is placed on a motor-driven precision goniometer ( $\pm 0, 1^\circ$ ) which enables the photomultiplier detector to be moved accurately from  $10^\circ$  to  $150^\circ$  in steps of  $1^\circ$ .

**F Signal Processing Unit:** Correlators are instruments that determine the correlation function of an electrical signal. Mathematically the auto-correlation function is defined in the Section 4.3 (Equation 4.10). The timing and operation of the correlator is controlled by the *sample time* generator, which divides time into intervals of equal duration  $\Delta\tau$ . At the end of each sample time the number of counts is entered into the first register counter of the correlator, the number that was in the first counter is shifted to the second, the number that was in the second stage is shifted to the third, etc. Hence, the first counter contains  $n(t - \Delta\tau)$ , the second  $n(t - 2\Delta\tau)$ , the third  $n(t - 3\Delta\tau)$ , and the  $k$ th counter contains  $n(t - k\Delta\tau)$  counts. Thus, the correlator will accumulate in the  $k$ th channel

$$G(k\tau) = \sum_{i=0}^{N-1} n_k \tilde{n}_{i+k}, \quad (5.1)$$

where the number  $n_i$  represents the number of times the content of each stage of the register is added to its respective correlation function memory channel and the number  $\tilde{n}_{i+k}$  is the number stored in the register. That is a good approximation to the true correlation function whenever the change in the value of the correlation function during the time  $\Delta\tau$  is small [123].

As we have seen in Section 4.3.1, small optically spherical scatters reradiate light with a maximum and constant intensity in any direction perpendicular to the light polarization. Hence, the calibration of the light scattering instrument can be done using toluene (refractive index  $n = 1.496$ ) as a reference sample. Before the measurements, toluene is passed through a  $0.2 \mu\text{m}$  membrane filter in order to remove dust particles. The filtered toluene was also centrifuged to remove any other contaminants. Figure 5.6 shows the angular dependence of

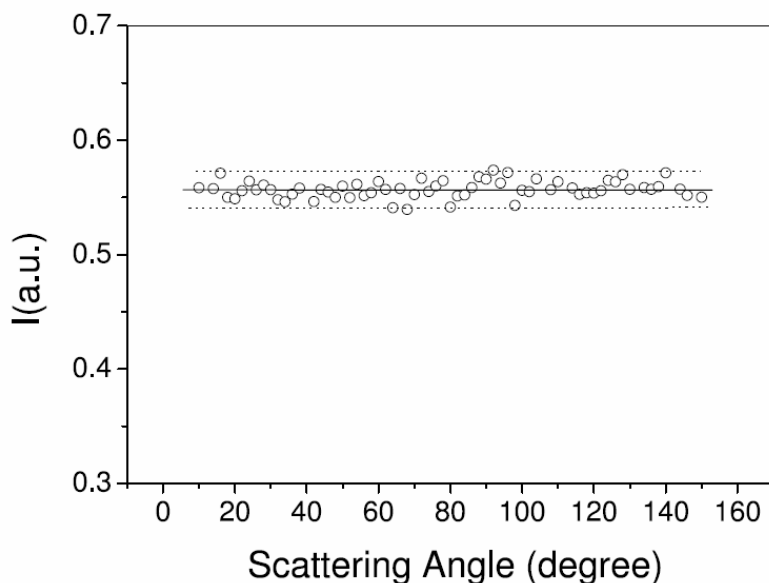


Figure 5.6: Scattering intensity profile for toluene.

the scattered intensity from toluene. It can be seen that the scattering profile is very flat with a deviation of less than 5% from the mean value over the angular range from 10 to 150 degrees.

### Magnetic Field

A non-uniform magnetic field gives rise to a magnetic force (see Equation 2.58). This means that the clusters tend to move out of the scattering volume in direction towards the magnet, where the field strength and its divergence are strongest. The spatial field homogeneity, hence, is crucial for the experiments since it avoids particle migration and, consequently, concentration heterogeneities within the reaction vessel.

The magnetic field needed to achieve field-induced aggregation was applied to the sample by placing different number of neodymium disk magnets (Halde Gac, Barcelona, Spain)<sup>3</sup> on top of the sample cell. The magnetic flux was led to the scattering volume by an iron cylinder. If a magnetic material, such as soft iron, is placed in a magnetic field, the magnetic lines are redirected through the material, taking advantage of its greater permeability. Another

---

<sup>3</sup><http://www.halde-gac.com/>

iron disc was placed at the bottom of the cell in order to collect the magnetic flux and reduce the magnetic field divergence (please, see Figure 5.7 b)).

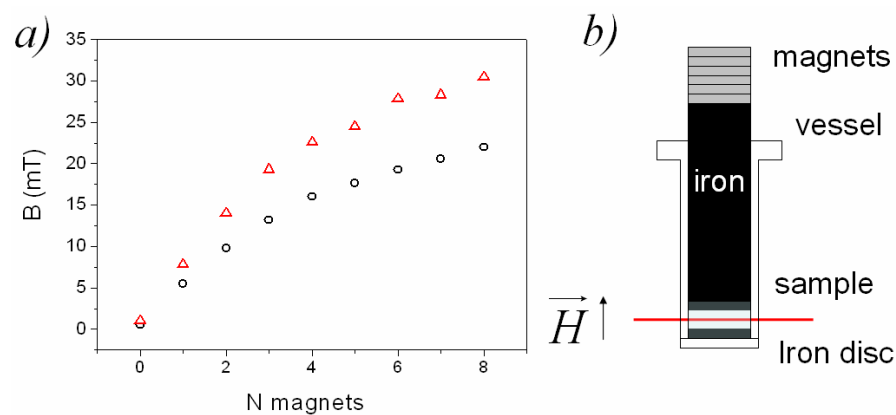


Figure 5.7: a) Magnetic field achieved in the scattering volume by means of  $N$  neodymium disk magnets (o). The magnetic field increases when an extra iron disc is placed at the bottom of the cell. The iron disc collects the magnetic flux and reduces the magnetic field divergence ( $\Delta$ ). b) Scheme that shows how the magnets were placed on the measurement cell. The laser passes through the colloidal suspension, between the two iron pieces. Hence, the applied magnetic field is perpendicular to the scattering plane.

The magnetic field is controlled by changing the number of magnets placed on top of the cell. At the field strength range  $0 - 23.9 \text{ kA/m}$  employed in our work, we are in the linear regime of the magnetization curve of the magnetic polystyrene particles (R0039), where the magnetization  $M$  is proportional to the external magnetic field  $H$ . The magnetic field was always perpendicular to the scattering plane.

### 5.2.2 Video Microscopy

Optical microscopy has been widely used for monitoring the structure and the time evolution of the mean cluster size through a detailed analysis of sequences of photographs [7, 124]. In our work, the aggregation processes have been monitored directly with an inverted microscope (Leica DM IL) equipped with a Scion CCD video camera and a set of lenses for magnifications of



Figure 5.8: Inverted microscope (Leica DM IL) equipped with a Scion CCD video camera and a set of lenses for magnifications of 10, 20, 40 and 100.

10, 20, 40 and 100 (Figure 5.8). The particle suspensions were contained in sealed rectangular capillars with a cross section of  $1.0 \text{ mm} \times 0.1 \text{ mm}$ . At  $10x$  magnification, the field of view of the microscope was  $768 \times 512$  pixels, corresponding to an area of  $620 \times 420 \mu\text{m}^2$  and an observed sample volume of  $2.64 \times 10^{-5} \text{ cm}^3$  (see Figure 5.9). The relatively large depth of field available at low magnification ( $10x$ ) helped to keep the particles in focus despite of their random Brownian motion.

### Magnetic Field

Aggregation was induced applying an uniaxial magnetic field of approximately  $5 \text{ mT}$ . The magnetic field vector was oriented parallel to the ground. The field divergence was small enough so that significant particle migration was not observed during the experiments. In this configuration, the aggregates settle with their longer axis orientated perpendicular to the gravitational field. Typical examples of what could be seen in the microscope are shown in the Figures 5.11 and 5.12. As expected, the video camera images reveal tip-to-tip



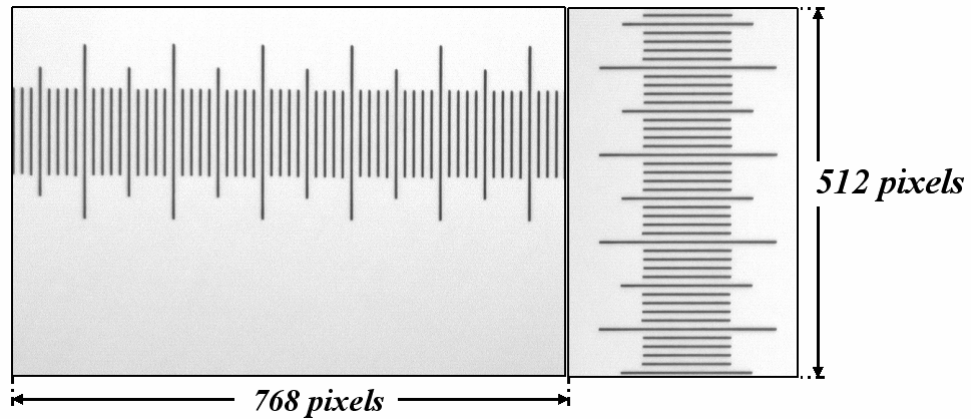


Figure 5.9: The field of view of the microscope was  $768 \times 512$  pixels. A ruler was used to calibrate the microscope image resolution. Each subdivision corresponds to  $10 \mu\text{m}$ .

aggregation when the field is applied.

Due to the mass density mismatch, the particles used for our experiments settle due to gravity. If we had monitored the aggregation processes from above, the particles and linear aggregates might have reached the bottom of the sample chamber where they could have continued to aggregate but essentially in two dimensions. In order to study the pure three-dimensional case, we used the same experimental set-up previously employed by Promislow et al. [7] who placed the microscope with its optical axes parallel to the ground. The longer axis of the sample tube is orientated parallel to the gravitational field vector. In this configuration, the aggregates can diffuse in all directions long before they can reach the bottom surface. Hence, aggregation takes place in the bulk where the diffusive particle motion is not restricted in any direction.

### 5.2.3 Machine de Force

As we have seen in Section 4.5.3, the distance between neighbouring particles aligned along the field direction can be assessed by the spectral distribution of the scattered light intensity at a constant angle. For this purpose, the sample was introduced by capillarity in a cell formed by two parallel squared glass sheets. The sheets were separated by fishing lines of  $100 \mu\text{m}$  in size, which allow us to control the distance between the walls (see Figure 5.10). Then, the cell was sealed by means of ultraviolet glue. The final sample volume

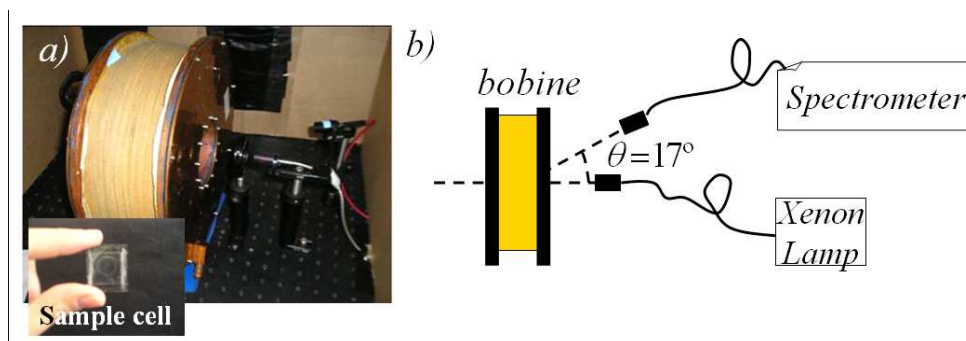


Figure 5.10: a) Photograph of the Machine de Force and the sample cell constituted by two parallel squared glass sheets. b) Scheme of the major components of the Machine de Force.

was approximately  $40 \mu L$ . The sample was illuminated using a Xenon gas-discharge lamp. The emergent light was led by an optical fiber. The incident beam was perpendicular to the cell walls containing the colloidal suspension. The scattered light was collected by a second optical fiber which was connected to a spectrometer. This optical fiber was placed at  $\theta = 17^\circ$ . A sufficiently large scattering angle is necessary in order to avoid detection of the light reflected by the cell walls. However, if the angle were too large then the spatial resolution measured would worsen. Further information about the device and its characteristics as well as the calibration procedure can be found in [59].

## Magnetic Field

The magnetic field was applied by means of a coil. The inner and outer diameter of the coil was  $9 \text{ cm}$  and  $28 \text{ cm}$  respectively. The coil is made of a compactly coiled, of  $2 \text{ mm}$  diameter wire of  $1000 \text{ m}$  in length. The applied magnetic field was directly proportional to the supplied electric current, that was provided by a  $1 \text{ kW}$  power source. The achieved uniaxial magnetic field was between  $0 \text{ mT}$  and  $100 \text{ mT}$ .

## 5.3 Methods

### 5.3.1 Light Scattering Techniques

The aggregation behaviour of our experimental system has been monitored using non intrusive light scattering (LS) techniques, that are quite suitable for

studying of the structure and kinetics of colloidal aggregates [28]. In the literature, however, there are only a few papers that describe how light scattering techniques may be used for studying aggregation phenomena in magnetic fluids [36, 125, 126, 127, 128]. To employ these techniques for an experimental study of aggregation processes arising in magnetic colloids is not straight forward due to light adsorption, anisotropy, multiple scattering effects, relatively high particle concentrations etc. Mainly, the high volume fractions used in most studies give rise to adsorption and multiple scattering that impede light scattering experiments be performed reliably. Furthermore, the large polydispersity of the employed samples make the interpretation of light scattering data a difficult task.

### Static Light Scattering

When the average scattered intensity  $I(q)$  is measured as function of the scattering wave vector  $q$ , the experiment is usually called *Static Light Scattering* (SLS). The collected light intensity  $I(q)$  depends mainly on the particle form factor  $P(q)$  and the aggregate structure factor  $S(q)$  (please, see Section 4.5.1). In these terms,  $I(q)$  reads (Equation 4.88)

$$I(q) = KP(q)S(q).$$

The particle form factor  $P(q)$  contains information on the optical properties of the individual particles, whereas the structure factor  $S(q)$  quantifies mass correlations within the aggregates. The proportionality constant  $K$  depends on the optical properties of the light scattering device. In stable systems without any spatial correlation between the monomer positions, the structure factor becomes  $S(q) \approx 1$ . In this case, the particle form factor can be determined easily from direct measurements of the scattered light intensity, since  $I(q) \propto P(q)$ . For an aggregated system, however, the structure factor  $S(q)$  is directly related to the fractal dimension of the clusters formed. SLS characterizes the aggregate morphology in terms of the cluster fractal dimension. Therefore, the SLS data will be employed to confirm the linear character of filaments and to study chain deformation due to the interaction with the surrounding medium. For structures having a fractal dimension  $d_f$ ,  $S(q)$  becomes (Equation 4.92)

$$S(q) \propto q^{-d_f}.$$

This relationship is valid for  $R_h^{-1} < q < a^{-1}$ , where  $a$  is the particle radius and  $R_h$  is the average hydrodynamic radius of the aggregates. Equation 4.92 implies that the scattered intensity has reached an asymptotic time-independent behaviour once the fractal structure of the clusters is fully developed. The cluster fractal dimension can then be easily determined from the slope of these asymptotic curves in a logarithmic plot of  $I(q)$ . According to its definition,  $d_f$  quantifies how mass varies with length scale. It provides a convincing measure for the compactness of fractal aggregates. After a sufficiently long aggregation time, the structure factor  $S(q)$  showed the theoretically predicted time independent behaviour for fully developed fractal clusters. From the slope of these asymptotic curves, the fractal dimensions were determined according to Equations 4.88 and 4.92.

After removing the field, linear aggregates may or not remain in the sample. Partial cluster break-up also may take place. In any case, SLS will confirm the chainlike cluster morphology. All the fractal dimension measurements reported in this work have been performed in the absence of any applied external magnetic field. This avoids the optical anisotropy that could bias the SLS measurements when the polarized light beam passes through a dispersion of aggregates aligned in the field direction [36].

### Dynamic Light Scattering

There are several ways to determine dynamic information about the particle movement in solution by Brownian motion. One of such methods is Dynamic Light Scattering (DLS). In DLS, the fluctuations of scattered light intensity are analyzed at a fixed scattering angle, and the dynamic information of the particles is derived from an autocorrelation of the intensity trace recorded during the experiment. DLS assesses the scattered intensity autocorrelation function as the product of the photon counts at times  $t$  and  $t + \tau$  such that  $G(\tau) = \langle I(t)I(t + \tau) \rangle$ . Then, from the normalized intensity autocorrelation function

$$\hat{g}_I(\tau) = \frac{\langle I(t)I(t + \tau) \rangle}{\langle I(t)I(t) \rangle} \quad (5.2)$$

was calculated and converted into the scattered field autocorrelation function by the aid of the Siegert relationship. The Siegert equation, relates the field autocorrelation function with the intensity autocorrelation function as follows

$$g_I(\tau) = 1 + C e^{-2D_{eff}q^2\tau}, \quad (5.3)$$

where  $C$  is a constant which depends on the optics of the instrument [28]. For deriving the Siegert relation, no assumption was made concerning the nature of the Brownian particles. Hence, the Siegert relation is equally valid for spherical and for rigid rod like Brownian particles.

Once the autocorrelation curve has been measured, different mathematical approaches can be employed to fit the curve and thus determine the averaged diffusion coefficient. For this purpose, the well-established *cumulant method* was used for expanding the logarithm of the field autocorrelation function as a power series in  $\tau$  (see Section 4.4.2). Linear fits were done between the correlation times that minimized the regression coefficients. DLS gives direct access to an effective mean diffusion coefficient  $D_{eff}$  of the scatters within the scattering volume. The averaged diffusion coefficient depends on the different diffusive modes that the aggregates may undergo. Since this quantity is related to the average aggregate size, it will allow the state of aggregation to be monitored. DLS studies about aggregation of isotropically interacting particles that lead to more or less compact fractal clusters are profuse. Nevertheless, DLS studies on linear aggregates are scarce [125, 126]. The main reason for this lies in the difficulty to extract the mean filament size from the average diffusion coefficient. The difficulties found in the description of the chain diffusive motion were discussed in the previous Chapter 4.

### Linear Aggregates Under Uniaxial Constant Magnetic Field

In our work the external magnetic field was always applied perpendicularly to the scattering plane forcing the filaments to align in the same direction. Hence, the measurements were only sensitive to transversal motion perpendicular to the chains axis. These facts have two important consequences:

- The structure factor  $S(q)$  may be approximated by the form factor of cylindrical rods with their axis aligned perpendicular to the scattering plane. Hence, it is sufficient to consider  $\theta = \pi/2$  in Equation 4.62.
- Rotational chain diffusion is not possible when the field is applied. Due to this geometry, the measurements are only sensitive to the transversal motion of the linear aggregates, and the parallel diffusion coefficient  $D_{\parallel}(N)$  may also be neglected. Consequently, only the mean translational diffusion coefficient perpendicular to the rod axis  $D_{\perp}(N)$  must be considered when equation 4.93 is used.

Moreover, linear aggregates of magnetic particles may also bend and twist slightly due to Brownian motion. In an experimental study, Cutillas and

Liu confirmed that the dependency of  $D_{eff}$  on  $q$  increases when the magnetic interaction decreases, i.e. the chains become more rigid for higher values of  $\lambda$ , which represents the ratio between the maximum attractive magnetic dipole-dipole energy and the thermal energy (see Section 2.6.2). If the magnetic field are strong enough then significant relative motion within the filaments are avoided, and the filament diffusion coefficient should not depend on  $q$ . In this case, Liu et al. were able to describe the  $q$ -dependency of the mean diffusion coefficient  $D_{eff}$  for their experimental system by the following empiric linear approximation [117, 126].

$$D_{eff}(q) \propto \left(\frac{2}{\sqrt{\lambda}}\right)qaD_{\perp}, \quad (5.4)$$

where  $a$  is the particle radius. The slope in this relationship depends on the magnetic field strength through the dimensionless parameter  $\lambda$ . Therefore, when the magnetic field is strong enough to avoid significant relative motion within the filaments, then the filament diffusion coefficient should not depend on  $q$ .

### Linear Aggregates in Absence of Magnetic Field

In presence of an external magnetic field, the filaments are forced to align in the field direction and so, rotational chain diffusion is forbidden. However, rotational Brownian motion becomes possible when the magnetic field is removed. At first sight, depolarized dynamic light scattering (DDLS) seems to be the technique of choice for measuring translational and rotational diffusion coefficients since a system of freely diffusing monodisperse non-flexible cylinders is characterized by a depolarized decay rate of  $\mu_1 = 2(D_t q^2 + 6D_r)$ . DDLS, however, presents some drawbacks. The depolarized VH signal is weak and blended with the polarized VV component. Furthermore, the solution must be relatively concentrated and high laser power is required in order to achieve a measurable depolarized signal [50]. In our experiments, however, DDLS could not be employed since the available laser power was only about  $20mW$  and the samples were so dilute, that no VH component could be detected.

The previously light scattering theory assumes that translational diffusion is isotropic and not coupled with rotational diffusive modes. This means that the diffusion coefficients for motion parallel and perpendicular to the rod axis should be similar and the rods must reorient many times while diffusing a distance comparable to  $q^{-1}$ . For long rods, however a strong coupling between translational and rotational modes is expected and a no-trivial coupled

diffusion equation has to be solved. Neglecting relative motion of the particles inside the linear aggregates, Maeda and Fujime [110] derived the effective diffusion coefficient given by the Equation 4.82.

### 5.3.2 Image Analysis

When the aggregation processes were monitored by videomicroscopy, digital images were taken in regular time intervals. As can be seen in Figures 5.11 and 5.12, the individual silica particles and chain-like aggregates appear as dark spots and thin lines on a clear background. The length of individual clusters was analyzed using the public domain software Image-J<sup>4</sup>. After subtracting the smooth continuous background (Figure 5.11 b), the images were thresholded in order to identify the particles and aggregates (Figure 5.11 c). The threshold level was automatically set by the Image-J program based on an analysis of the gray level histogram of the image. Then, the program determined the Feret's length of all the clusters detected on the image. Feret's length, also known as the capillary length, is the longest distance between any two points along the aggregate boundaries, and it is directly related to the length of the linear aggregates. ImageJ offers also other parameters that are directly related with the length of the linear aggregates: the perimeter, the primary or secondary axis of the best fitting ellipse, the area, etc. There were no special reasons to choose the Feret's length in order to assess the length of the linear aggregates. For the case of long linear clusters, Feret's length corresponds to the length of the aggregate axes. The program ignored aggregates touching the edge of the image since their total length is unknowable. Evidently, this effect introduced some extra but unavoidable noise in the cluster length histogram.

In order to correlate the Feret's length with the number of chain-forming particles, we compared different images obtained just before and after turning off the magnetic field. When the field is present, the clusters remain aligned along the field direction and the Feret's length of the clusters can be determined (Figure 5.12). Once the field is removed, the magnetic interaction vanishes due to the super-paramagnetic character of our magnetic colloids. If aggregation has taken place in a secondary energy minimum the particles redisperse immediately, i.e. a complete rupture of the chains is observed (please, see Section 2.7). Since the clusters disassemble completely, the number of chain-forming particles can be counted quite easily (Figure 5.13).

Figure 5.14 plots the Feret's length measured in pixels as a function of the number of particles per chain. For not too short chain lengths, a clear linear

---

<sup>4</sup>"Image-J" is available on the Internet at <http://rsb.info.nih.gov/ij/index.html>

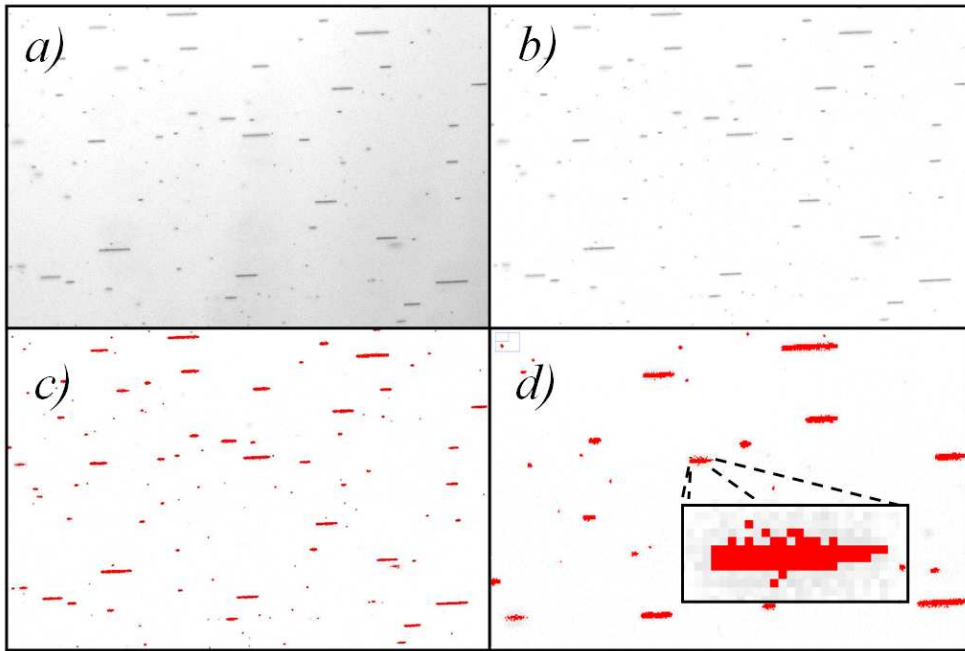


Figure 5.11: a) The individual particles and chain-like aggregates appear as dark spots and thin lines on a continuous background. b) After subtracting the smooth continuous background, c) the images were thresholded in order to identify the particles and aggregates. d) The particles are clearly visible, but also some tiny spots appear on the images that may be caused by dust particles or noise.

relationship was found. The best linear fit was obtained for

$$L_{Fer} = 1.84N + 0.01, \quad (5.5)$$

where  $L_{Fer}$  is the Feret's length expressed in number of pixels and  $N$  is the number of particles in the corresponding chain. For aggregates smaller than  $N = 4$ , the linear relationship is lost and the Feret's length is somewhat larger than what would be expected from the fit. This effect is probably due to the slightly blurred and consequently, so not clearly detectable border of the particles. In addition, digitalization effects may also play an important role. Evidently, these uncertainties are most pronounced for smaller chains when the cluster length comes close to the pixel size. We fitted this part of the curve



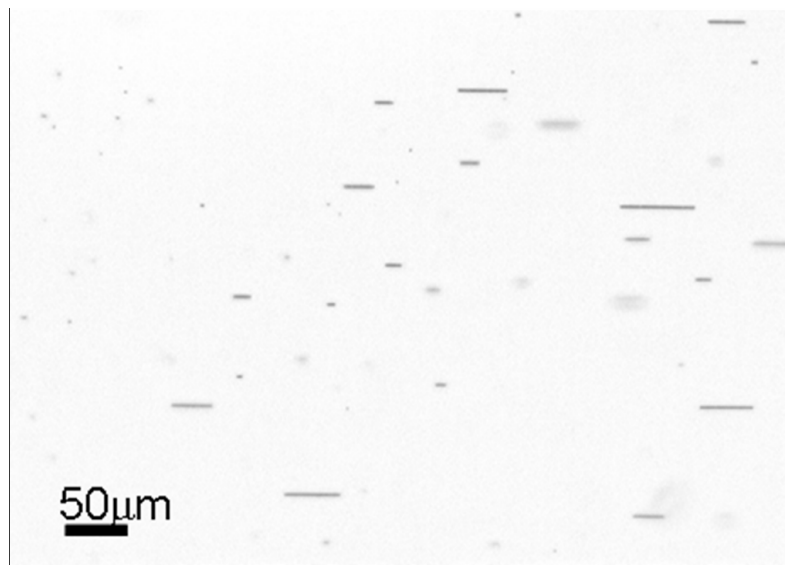


Figure 5.12: Low magnification (10x) images taken at 495 s after having turned on the magnetic field. The linear aggregates of different length aligned along the field direction are clearly visible.

by a second order polynomial. The best fit was obtained for

$$L_{Fer} = 0.09N^2 + 0.98N + 2.01 \quad (5.6)$$

Using both fitting equations, the cluster size distribution and the average cluster size could be calculated for each image.

It should be noted that sometimes tiny spots appear on the image that may be caused by dust particles or noise (see Figure 5.11 d). Since these spots are too small for being individual monomeric particles, they had to be deleted from the cluster size distribution. Therefore, we established a minimum Feret's length below which a detected particle was not taken into account. After a manual examination of the images, we established this level at 2.85 pixels or  $N = 0.8$ , and kept it constant throughout the experiments. Nevertheless, particles and clusters that are about to drift out of the focal plane, e.g., may either not be detected or counted as smaller clusters. This effect introduces an extra error that makes an exact and univocal determination of the cluster size even more difficult.

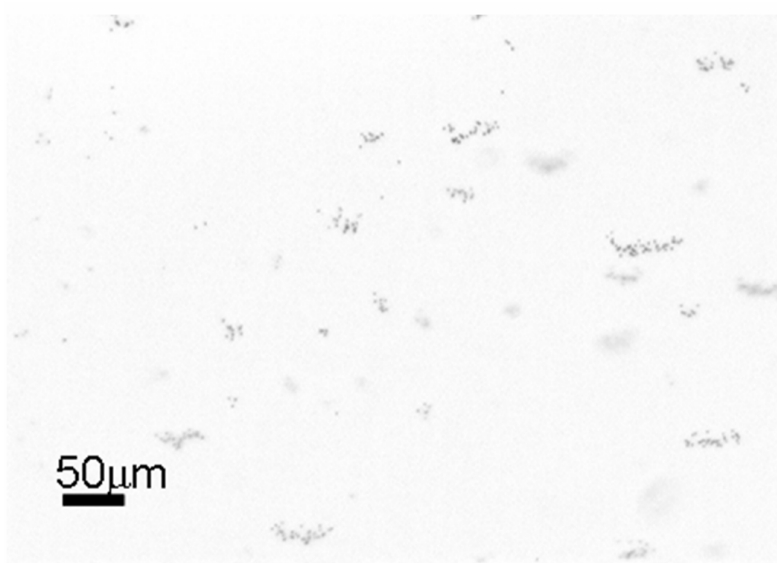


Figure 5.13: Low magnification image (10x) of the situation shown in Figure 5.12 at 5 s after turning the field off. The chains disassemble into individual monomers.

### 5.3.3 Solving Smoluchowski's Equation

The theoretical time evolution of the cluster size distributions  $X_n(t)$  was always obtained solving Smoluchowski's equation. For this purpose, a fast and reliable *Stochastic Algorithm* was employed<sup>5</sup>. The algorithm solves the master equation equivalent of Smoluchowski's equation for a given aggregation kernel. It involves the calculation of the reaction probability density function. The stochastic description of the aggregation process takes into account the finite size of the system. Further information regarding this method can be found in references [129, 130].

---

<sup>5</sup>We express our gratitude to Dr. Gerardo Odriozola for kindly providing the code of the corresponding computer programme.

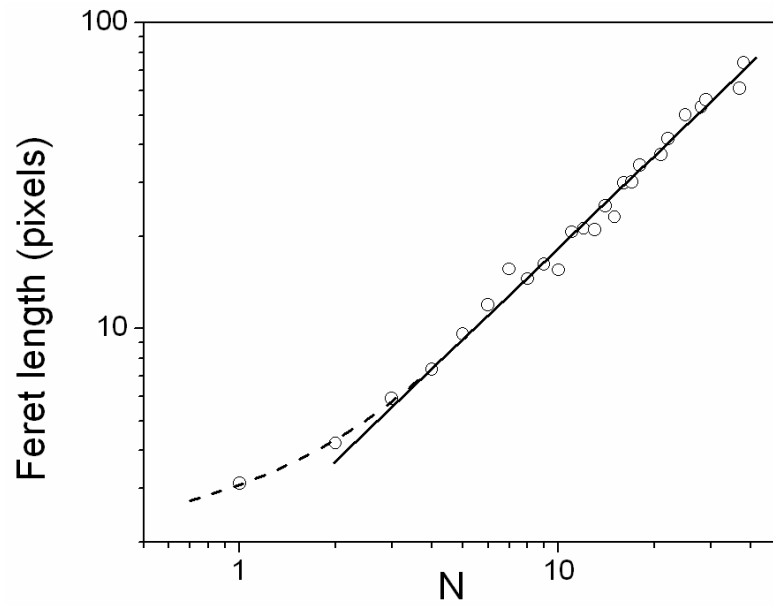


Figure 5.14: Average Feret's length of the clusters as a function of the chain size (data points). The continuous line shows linear fit for clusters larger than  $N = 3$ . The quadratic fit for the shorter clusters is indicated by the broken line.

## Chapter 6

# Kinetics of Field Induced Aggregation

A detailed analysis of colloidal aggregation involves two main aspects: the cluster morphology and the kinetics of aggregate formation. The kinetics of the processes is frequently studied by means of the temporal evolution of the concentration of aggregates  $c_n(t)$  containing  $n$  monomers, and several statistical variables that can be calculated from  $c_n(t)$ , such as the mean number of particles per aggregate  $N(t)$ , or the average aggregate size  $S(t)$ .

In this Chapter, the kinetics of field induced aggregation processes arising in magnetic fluids has been studied. Experimental results will be compared with the theoretical predictions obtained using the proposed kernel described throughout Chapter 3.

### 6.1 Field Induced Aggregation

Studies concerning aggregation phenomena in magnetic fluids have attracted great interest of the the scientific community over the past decades. So far, most of the experimental and numerical studies that focus on field-induced aggregation processes seem to indicate the same type of power law for the asymptotic behaviour of the mean cluster size  $S(t) \propto t^z$ , and for the average length of the linear aggregates  $N(t) \propto t^{z'}$ . Both scaling exponents  $z$  and  $z'$  are parameters that classify the growth process, and both depend on the dimension of space.

Experiments have shown that under specific conditions the scaling exponents are significantly different than the value of  $z = 0.5$  predicted theoretically

by Miyazima et al. [8]. Fermigier and Gast, reported a  $z$  of approximately 0.5, for diluted suspensions of micron-diameter superparamagnetic spheres aggregating due to a constant magnetic field [131]. Promislow and Gast, however, reported a  $z$  values between 0.5 and 0.75 under similar experimental conditions. Furthermore, these authors suggest a dependence of the  $z$  value to depend on the volume fraction and the field strength [7]. More recently a  $z$  value close to unity was observed by Shon for field induced magnetic latex aggregation [98]. S. Relle et al. reported  $z$  values between 0.54 and 0.32 for superparamagnetic particles aggregating under the action of a external magnetic field [132]. In the latter work, however, the magnet was placed directly above the measuring cell containing the colloidal dispersion, which implies that the field strength was not uniform. The field divergence may give rise to particle migration, affecting seriously the field induced aggregation process.

Two dimensional field induced aggregation processes have also been studied. Fraden et al. reported a kinetic exponent of  $z' = 0.6$  for a diluted suspension of micron-diameter dielectric spheres confined in two dimensions when a constant electric field was applied [30]. On the other hand, Helgesen et al. measured a kinetic exponent of  $z = 1.7$  for two dimension field induced aggregation processes [133]. In this work, the experimental system was also a diluted suspension of superparamagnetic micron-diameter spheres. Also Dominguez-García et al. studied field induced aggregation using superparamagnetic latex particles, working in a wide range of experimental conditions [124]. However, they did not find a direct dependence of the kinetic exponents with the strength of the external field or the particle concentration. They obtained  $z = 0.57$  and  $z' = 0.47$  as the average values of the kinetic parameters. These authors corroborated the predictions of the anisotropic diffusion model of Miguel et al. described in Section 3.6. Experimental studies of field induced aggregation processes have also been carried out by Cernak et al. using a two dimensional magnetic hole system, i.e. nonmagnetic microspheres dispersed in a thin layer of ferrofluid. Values of  $z = 0.40$  and  $z' = 0.43$  were reported for microspheres with a diameter of  $d = 1.9 \mu m$ . For larger particles with diameter  $d = 4.0 \mu m$  these authors observed a broader range of  $z$  values, and for particles with a diameter of  $d = 14 \mu m$  described a strong dependence between  $z$  and the strength of the applied magnetic field [85]. In their experiments the predictions of the anisotropic diffusion model of Miguel et al. were confirmed once more.

All the results summarized so far were obtained by videomicroscopy. A detailed description of the image analysis, however, was only given in the studies of Dominguez-Garcia et al. [124] and Fermigier et al. [131]. Other techniques

have been used for studying field induced aggregation processes. Light scattering methods, for instance, have been used in order to study three dimensional aggregation processes [126]. Cutillas et al. monitored the aggregation kinetic by means of DLS, obtaining for the kinetic parameter a value of  $z' = 0.47$ . Scattering dichroism studies have also been performed [36].

Irreversible aggregation of particles has been the subject of computer simulations using scaling concepts. Miguel et al. [9] developed a model using the Monte Carlo method in order to simulate two and three dimensional aggregation of magnetic particles. They obtained an exponent of  $z = 0.61$  for two dimensional process in accordance with the experimental results reported in reference [30]. Later, Dominguez-García et al. [124] compared their experimental results with 2D Brownian dynamics simulations. They found that the kinetic exponents obtained from simulations do not depend on the external field or the surface fraction. They determined  $z = 0.62$  and  $z' = 0.59$ . These values differ slightly from the average values obtained in their video microscopy experiments.

In spite of the large number of studies addressing field induced aggregation processes, the influence of phenomena and parameters such as sedimentation effects, electrostatic inter-particle interactions, the strength of the applied field, or the degree of magnetic saturation of the particles, are still not understood. The main aim of this Thesis has been to deepen our knowledge about chain formation processes and to improve the theoretical description of field-induced aggregation phenomena when the electrolyte concentration or sedimentation play a significant role. Therefore, we determined the time evolution of the cluster size distribution and the average cluster size arising in aggregating magnetic particle dispersions. We used the experimental data to test several theoretical models based on Smoluchowski's approach. For this purpose, it was essential to determine an aggregation kernel that includes all the effects mentioned above.

## 6.2 Magnetic Field Effects

As we have seen so far, there is not consensus about the influence of the field strength on the aggregation kinetics. Dominguez-Garcia et al. [124] did not find a direct dependency of the kinetic parameters  $z$  and  $z'$  on the dimensionless parameter  $\lambda$  (Equation 2.52). Cernak et al. [85] studied the field induced aggregation arising in a two dimensional magnetic hole system. They reported on the relationship between the strength parameter  $\lambda$  and the scaling exponent

$z$ . For  $\lambda < 50$ , the  $z$  parameter does not depend on the field strength. For  $\lambda > 50$ , however, these authors found an apparent weak increase of  $z$ , which is just the opposite of what observed by Promislow et al. [7], who reported a decrease of  $z$  for larger  $\lambda$ . On the other hand, the latter authors proposed a characteristic time scale that is proportional to  $1/\lambda$ , and so, seems to suggest that the aggregation mechanism as well as the kinetic parameters do not depend on the field strength. In fact, a time scale is usually used to normalize time so that all plots of  $S(t)$  as function of the reduced time collapse together, regardless of the experimental conditions.

In order to study the influence of the field strength on the aggregation behaviour, light scattering experiments were performed using a Malvern 4700C instrument working with a vertically polarized 632.8 nm wavelength argon laser. The DLS mode was used for monitoring the average diffusion coefficient of the magnetic filaments formed. The light scattering experiments were performed using small magnetic polystyrene particles of 165 nm in size. Hence, sedimentation was found to be negligible during the experiments due to the relatively small size and low mass density of the chosen particles. The particle number concentration was adjusted to  $\approx 1.0 \times 10^{10} \text{ cm}^{-3}$ , corresponding to a volume fraction  $\phi = 2.6 \times 10^{-5}$ . The relative low particle concentration avoids multiple light scattering and lateral chain-chain aggregation. The DLS measurements were always performed at a scattering angle of  $\theta = 60^\circ$  corresponding to  $q^{-1} = 75.7 \text{ nm}$ .

Aggregation was not observed for the electrolyte free sample. Hence, the experiments were performed at 5 mM of *KBr*. Electrolyte addition screens the electrostatic repulsion between the particles, allowing for field induced aggregation of the particles. The added electrolyte, however, was too low to affect the stability of the samples when the magnetic field is absent. The effect of the electrolyte concentration on the field induced aggregation kinetics will be described later on in more detail.

The strength of the magnetic field applied to the sample was controlled by changing the number of neodymium disk magnets placed on top of the sample cell, as we described in the Section 5.2.1. The spatial divergence of the applied magnetic field was small enough so that significant particle migration was not observed during the experiments. Since the external magnetic field was applied perpendicularly to the scattering plane, the linear aggregates were forced to align in the same direction. Hence, the measurements were mainly sensitive to transversal diffusion perpendicular to the chains axis.

Figure 6.1 shows the time evolution of the effective aggregate diffusion coefficient  $D_{eff}$  for several applied magnetic field strengths. The data are the

average of at least five measurements that were carried out. The corresponding errors bars are not shown for the sake of clarity. A decrease of  $D_{eff}$  as time proceeds is observed in all cases. This means that the length of the linear aggregates grows with exposure time to the magnetic field under all the experimental conditions reported.

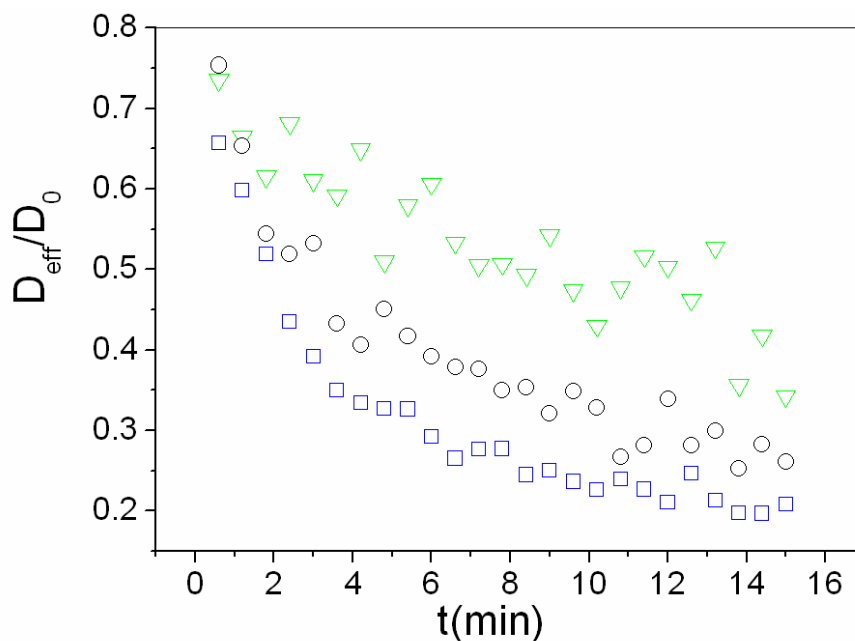


Figure 6.1: Effective diffusion coefficient  $D_{eff}$  normalized by the single particle diffusion coefficient  $D_0$  versus the exposure time to the external magnetic field for different interaction parameters: ( $\nabla$ )  $\lambda = 2.9$ , ( $\circ$ )  $\lambda = 5.5$ , and ( $\square$ )  $\lambda = 11.6$ .

As was mentioned previously (please, see Sections 4.5.3 and 5.3.1), the linear aggregates formed may be treated as rigid cylinders when the magnetic field is present. However, at low magnetic field strengths relative positional particle fluctuations inside the linear aggregates may take place due the competition between Brownian motion and magnetic dipole-dipole interactions. DLS measurements are sensitive to brownian movement of the particles contained within the linear aggregates, since the internal spatial fluctuations of the particles give rise to a dependency of the measured diffusion coefficient with the scattering vector  $q$ . In Figure 6.2 the diffusion coefficient of the lin-



ear aggregates is depicted as function of  $q$ . At low magnetic field strengths, the effective diffusion coefficient measured by DLS depends linearly on  $q$ , according to the Equation 5.4 which reads

$$D_{eff} \propto \left(\frac{2}{\sqrt{\lambda}}\right)qaD_{\perp}.$$

However, when the magnetic field is strong enough to avoid significant relative motion within the filaments, the diffusion coefficient does not depend on  $q$ . This is just what we observed when we applied higher magnetic fields. As can be seen in Figure 6.2, for  $\lambda = 5.5$  the magnetic filaments behave as rigid rods.

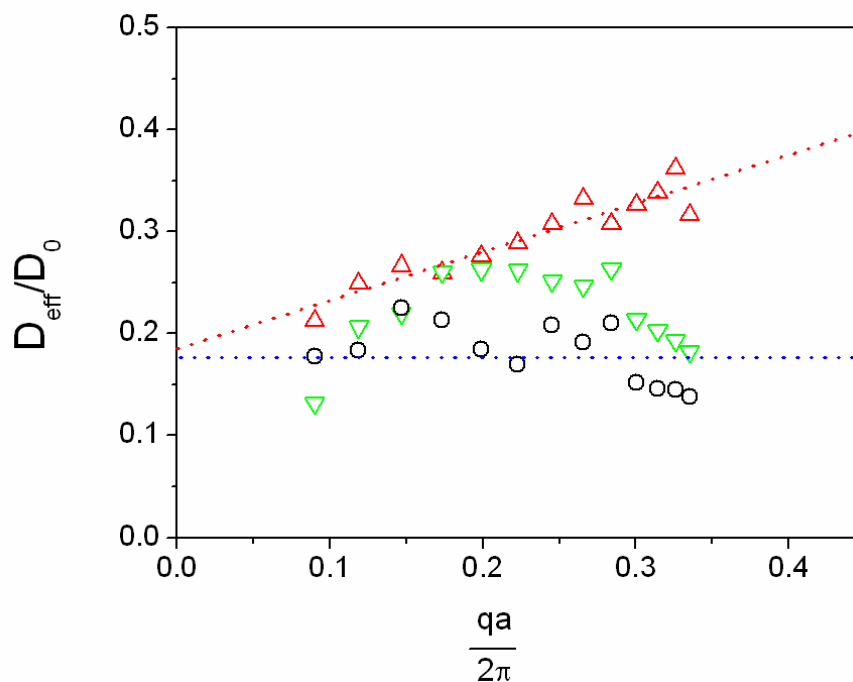


Figure 6.2: Effective diffusion coefficient  $D_{eff}$  normalized by the single particle diffusion coefficient  $D_0$  versus the normalized scattering vector  $q$  at an advanced stage of aggregation in presence of the external magnetic field. The values of the interaction parameter were ( $\triangle$ )  $\lambda = 0.9$ , ( $\nabla$ )  $\lambda = 2.9$ , and ( $\circ$ )  $\lambda = 5.5$ . The dashed lines are drawn as a guide to the eye.

From the data for the perpendicular diffusion coefficient, the average chain

length expressed in number of particles per aggregate  $N$  was extracted, according to the hydrodynamic Equation 2.37 proposed by Tirado et al. :

$$D_{\perp}(L) = \frac{k_B T}{4\pi\eta L} \left( \ln\left(\frac{L}{2a}\right) + \gamma_{\perp}^{end}(L) \right).$$

Hence, the mean number of particles per chain could be obtained from the mean diffusion coefficient for all the applied magnetic fields. However, only for  $\lambda > 2.9$  we may safely assume that the effective diffusion coefficient measured by DLS contains a single contribution due to perpendicular translational chain diffusion. Figure 6.3 shows the mean number of particles per aggregate  $N$  as a function of the exposure time to the magnetic field.

According to Figure 6.3 the data show a similar asymptotic behaviour with a slope of  $z' = 0.69 \pm 0.61$  for all the experimental conditions. Linear fits were done between the experimental points that minimized the regression coefficient. Such a power law dependence has been reported by most of the experimental and numerical studies. The values obtained for the slope  $z'$  are again given in Table 6.1. As can be seen, we do not find a direct dependence of the kinetic exponents with the interaction parameter  $\lambda$ .

$\lambda$	0.9	2.9	5.5	11.6
$z'$	0.74	0.61	0.71	0.69
$\bar{h}/a$	-0.8	1.0	3.5	

Table 6.1: The kinetic parameter  $z'$  and the average range  $\bar{h}$  as function of the dimensionless parameter  $\lambda$ .

The similarity in shape, and the almost identical kinetic exponents obtained from the slope of the curves shown in the previous figure seem to indicate that the underlying aggregation mechanism does not depend on the magnetic field strength. Gast et al. studied the influence of the magnetic field strength on aggregation kinetics. In their experiments, they found that the time evolution of the average cluster size  $S(t)$  collapsed on a single master curve when the time axis was rescaled using the characteristic time [7, 131]:

$$\tau_{Br}^* = \frac{a^2}{D_0\phi_{eff}}. \quad (6.1)$$

From a physical point of view, this characteristic time may be interpreted as a modified Brownian time scale that accounts for the attractive nature of

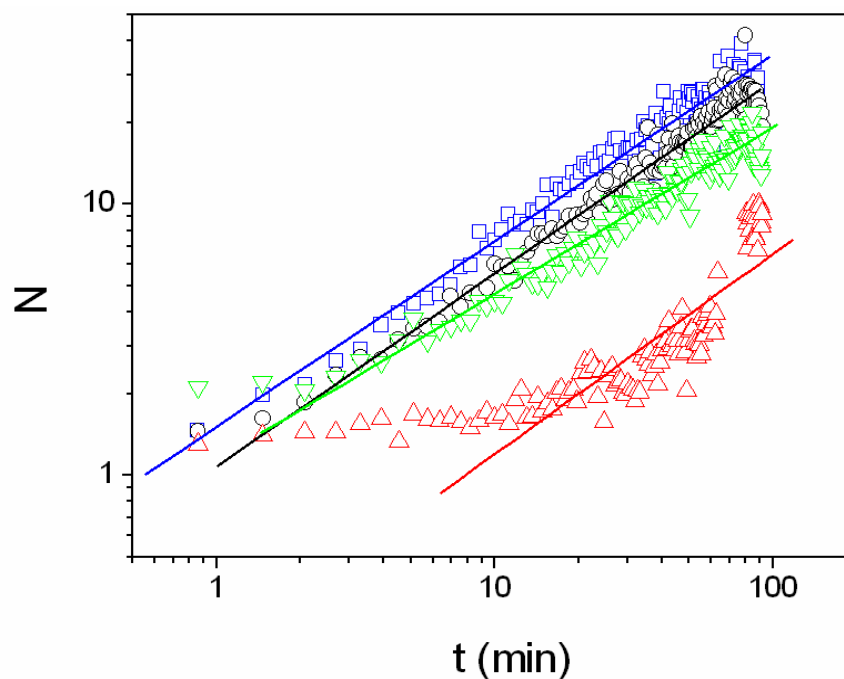


Figure 6.3: Average number of constituent particles per aggregate  $N$  as function of the exposure time to the external magnetic field. The values of the dimensionless parameter  $\lambda$  were  $(\triangle)$   $\lambda = 0.9$ ,  $(\nabla)$   $\lambda = 2.9$ , and  $(\circ)$   $\lambda = 5.5$ , and  $(\square)$   $\lambda = 11.6$ . Straight lines show asymptotic behaviour according to  $N \propto t^{z'}$ .

the magnetic interaction in terms of an effective particle volume fraction given by

$$\phi_{eff} = 24[(1/3)^{1/2} - (1/3)^{3/2}]\lambda\phi. \quad (6.2)$$

In other words, the capture volume of the aggregates scales as  $a^3\lambda$  due to the long range character of the magnetic interaction. We will now confirm their experimental results by means of our own Dynamic Light Scattering (DLS) experiments.

As is shown in Figure 6.4, the time evolution of the mean number of

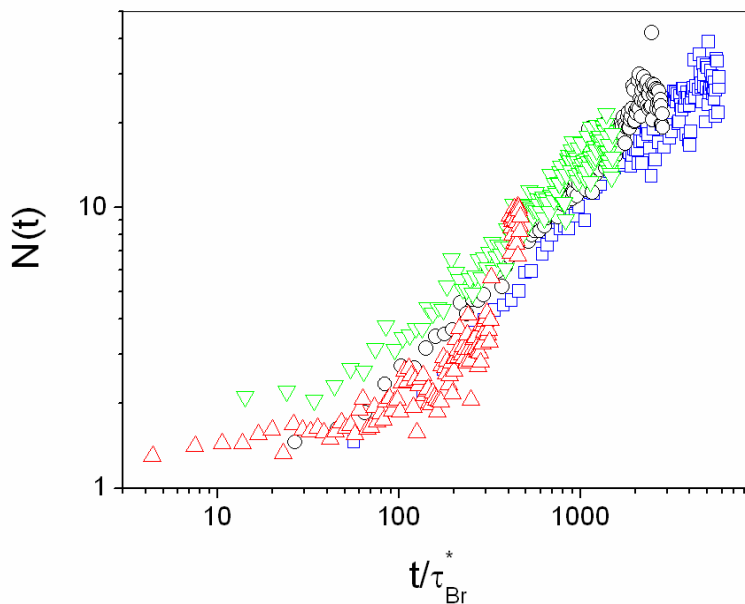


Figure 6.4: Average number of constituent particles per aggregate  $N$  as function of the scaled time  $t/\tau_{Br}^*$ . The values of the dimensionless parameter  $\lambda$  were ( $\triangle$ )  $\lambda = 0.9$ , ( $\nabla$ )  $\lambda = 2.9$ , and ( $\circ$ )  $\lambda = 5.5$ , and ( $\square$ )  $\lambda = 11.6$ .

particles per chain  $N$  align along a single master curve and so, follows the scaling behaviour described by Promislow et al. for the average cluster size  $S(t)$ . The alignment is observed even for the lowest applied field of  $\lambda = 0.9$ , where the mean number of particles per chain has been directly determined from the Equation 6.1, neglecting the contribution of the internal fluctuations on the assessed diffusion.

The increase of the external field gives rise to an enhanced filament growth rate. Nevertheless, the kinetic exponent seems to no depend on the magnetic field strength. This seems to indicate that the aggregation mechanism may be described by the same aggregation kernel. Figure 6.5 shows the time evolution of the measured effective diffusion coefficients in presence of the applied magnetic field together with the theoretical predictions. The continuous lines show the fits that were obtained using the proposed kernel for field induced aggregation (Equation 3.23)

$$k_{ij}^{Bdip} = 4\pi(1 - \cos\varphi_c)(\bar{D}_i + \bar{D}_j)(a_i + a_j + \bar{h}),$$

for the numerical solutions of Smoluchowski's aggregation equation.

According to light scattering theory, the average diffusion coefficient  $D_{eff}$  measured by DLS is related to the diffusion coefficients of the different clusters of size  $N$  through Equation 4.93:

$$D_{eff} = \frac{\sum_{N=1}^{N_c} n_N(t) N^2 S(qR_g) D(N)}{\sum_{N=1}^{N_c} n_N(t) N^2 S(qR_g)}$$

In our case, the structure factor  $S(qR_g)$  may be approximated by the form factor of cylindrical rods with their axis aligned perpendicular to the scattering plane. Hence, it is sufficient to consider  $\theta = \pi/2$  in Equation 4.62. On the other hand, only the mean translational diffusion coefficient perpendicular to the rod axis  $D_{\perp}(N)$  must be considered when Equation 4.93 is used.

The effective interaction range  $\bar{h}$  defined by Equation 3.23 was the only adjustable parameter. The agreement between experiments and theory can be considered satisfactory. This means that the time evolution of the mean diffusion coefficient of the linear aggregates can be described using the same aggregation kernel at different magnetic field strengths. The proposed aggregation kernel explicitly includes the range of the effective inter-particle interaction as a control parameter. The higher the magnetic field is, the longer the effective range of the total interaction becomes. As stated in the theory section, the fitting parameter  $\bar{h}$  has to be understood as an effective range of the net interaction between the aggregates. The real interaction range, however, depends on the angle between the magnetic field direction and the vector indicating the relative position of the interacting species. Moreover, the electrostatic repulsion also modifies the effective interaction range especially at low electrolyte concentrations. The average character of the fitting parameter  $\bar{h}$  may explain the negative value obtained for the lowest value of the applied magnetic field. At this field strength, most of the angular configurations are in fact repulsive due to the remaining electrostatic repulsion between the particles, even within the theoretically attractive zone  $I$  defined in Section 3.5.2. In addition, the reversibility of the field induced aggregation process may also play an important role. The values obtained for the fitting parameter  $\bar{h}$  are included in Table 6.1.

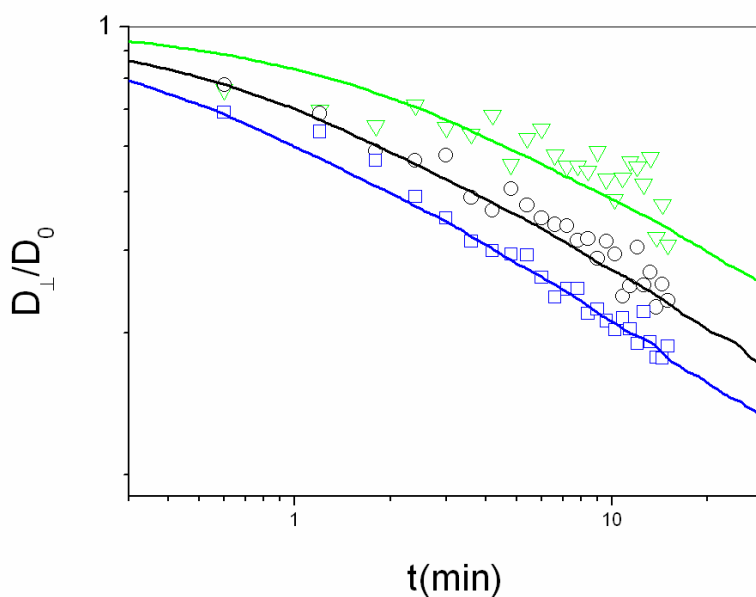


Figure 6.5: Effective diffusion coefficient  $D_{\perp}$  normalized by the single particle diffusion coefficient  $D_0$  versus the exposure time to the external magnetic field. The applied magnetic field strength was ( $\nabla$ )  $11.1 \text{ kA/m}$  ( $\lambda = 2.9$ ), ( $\circ$ )  $15.3 \text{ kA/m}$  ( $\lambda = 5.5$ ), and ( $\square$ )  $22.2 \text{ kA/m}$  ( $\lambda = 11.6$ ). The continuous lines show the best fits using to the proposed kernel (Equation 3.23) for the numerical solutions of Smoluchowski's aggregation equation.

### 6.3 Electrolyte Effects

When the magnetic particles are suspended in aqueous media they usually bear a non vanishing net surface charge that gives rise to isotropic electrostatic interactions. The interplay between these isotropic electrostatic and the anisotropic magnetic interactions is of interest not only from an applied but also from a theoretical point of view. So far, most of the research works dealing with magnetic colloidal particles only consider magnetic forces. Nevertheless, electrostatic forces play also an important role and should, as we will show, not be neglected.

### 6.3.1 Light Scattering Experiments: Polystyrene Particles

Figure 6.6 shows the measured effective aggregate diffusion coefficient  $D_{eff}$  as a function of the exposure time to the applied magnetic field for all electrolyte concentrations used in this study. The data are the average of at least five measurements that were carried out. The corresponding error bars are not shown for the sake of clarity. The magnetic field strength was measured to be  $23.9 \text{ kA/m}$ , corresponding to  $\lambda = 13.5$ , throughout the scattering volume. At the field strength employed, the absence of significant internal fluctuations within the linear aggregates is guaranteed. Excluding the electrolyte free sample, a decrease of  $D_{eff}(t)$  is observed in all cases. This means that the average filament size increases with the exposure time to the magnetic field. It should be noted that chain formation takes place even at relatively low electrolyte concentrations. Although such electrolyte concentrations are too low to affect the stability of the samples when the magnetic field is absent, linear aggregates start to grow once the field is applied. The growth behaviour depends strongly on small variations of the electrolyte concentration. For increasing electrolyte concentrations, the growth rate rises and reaches a limiting value already at about  $50 \text{ mM KBr}$ . This shows clearly that the electrostatic repulsion between the particles at lower electrolyte concentrations is strong enough to slow down aggregation at least partially. At high electrolyte concentration, however, the electrostatic repulsion is overcome completely by the magnetic interaction. For higher electrolyte concentrations, the results superimpose and follow the curve observed at  $50 \text{ mM}$ .

From the data obtained for the perpendicular diffusion coefficient, the average chain length, expressed in number of particles per aggregate  $N$ , was extracted according to Equation 2.37. The obtained results are shown in Figure 6.7 in logarithmic scale only for the most representative cases, i.e. at electrolyte concentrations of 0.10, 0.25, 1.0 and  $50 \text{ mM}$ . According to Figures 6.7 and 6.8, the data show a similar asymptotic behaviour and follow well-defined straight lines with a slope of  $z = (0.67 \pm 0.40)$  at all the electrolyte concentrations used. The similarity in shape and the almost identical kinetic exponents of the curves shown seem to indicate that the underlying aggregation mechanism does not depend on the electrolyte concentration. Electrolyte addition screens the electrostatic repulsion and so, increases the effective range of the total interaction. This gives rise to an increased aggregation rate. Nevertheless, the kinetic exponent does not depend on the electrolyte concentration, and is very similar to the value  $z = 0.69 \pm 0.61$  obtained in the previous Section. This indicates that the aggregation mechanism is controlled by the

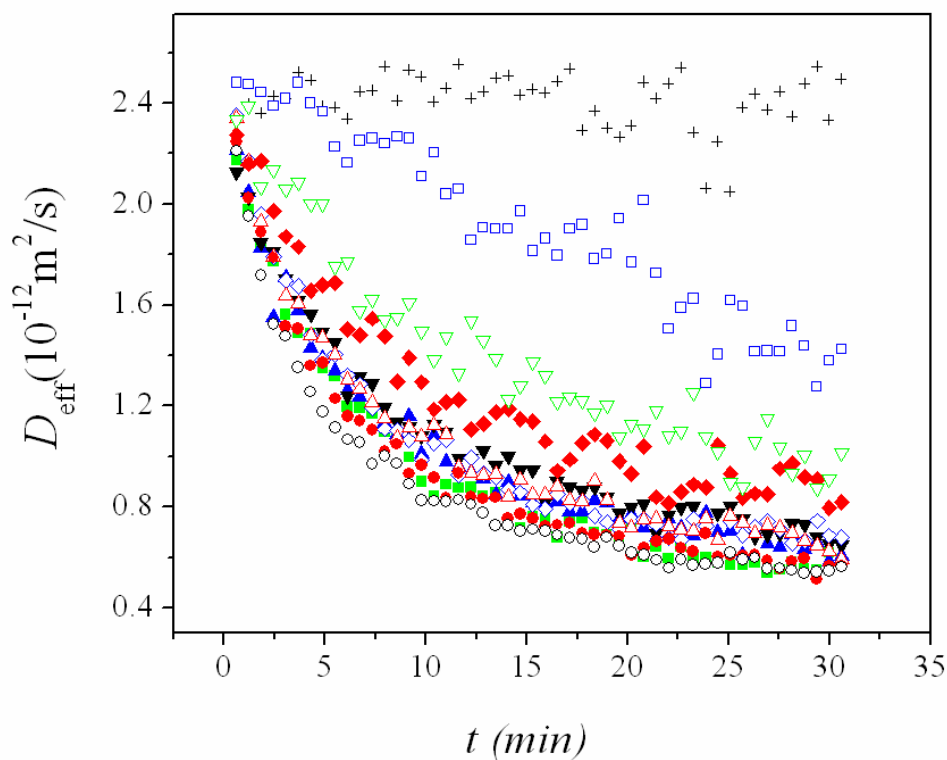


Figure 6.6: Effective diffusion coefficient of the aggregated samples versus exposure time to the applied magnetic field. The electrolyte concentrations in the samples were: (+) 0.0 *mM*, (□) 0.10 *mM*, (▽) 0.25 *mM*, (◆) 0.50 *mM*, (△) 1.0 *mM*, (◇) 2.0 *mM*, (▼) 5.0 *mM*, (▲) 10 *mM*, (■) 20 *mM*, (●) 25 *mM* and (○) 50 *mM*.

dipolar magnetic interaction rather than the electrostatic interactions.

Neglecting electrostatic interactions, Promislow et al. found the time evolution of the average chain length in pure field induced aggregation processes to collapse on a single master curve when the time axis is rescaled using the previously defined characteristic time (Equation 6.1). In our experimental systems, however, electrostatic interactions are present at almost all the electrolyte concentrations employed while the strength of the external magnetic field and consequently  $\lambda$  remains constant. Since similar kinetic exponents were obtained for all the curves shown in Figure 6.7, it should be possible to use scaling methods also in our case. Therefore, a characteristic scaling



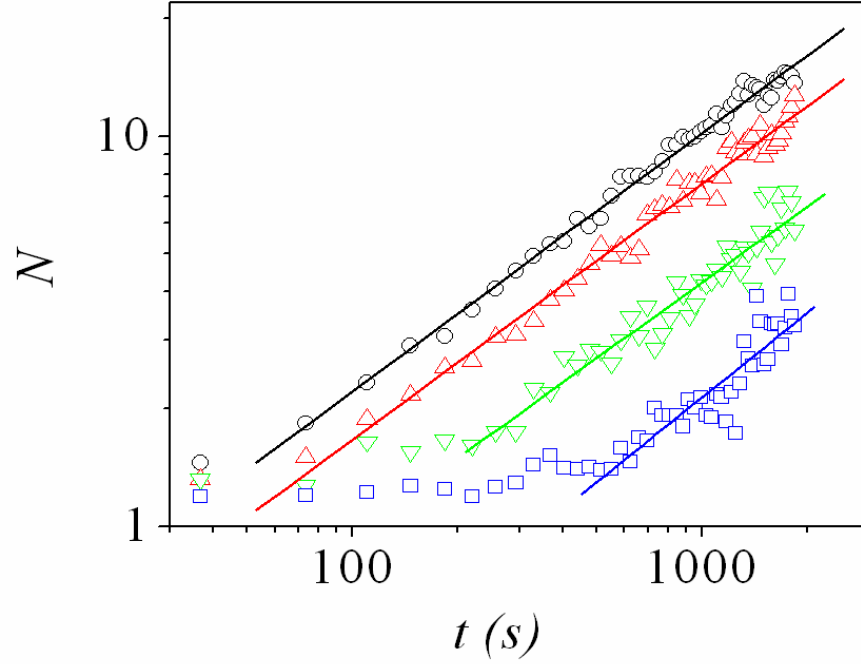


Figure 6.7: Average number of constituent particles per aggregate  $N$  as function of the exposure time to the external magnetic field at electrolyte concentrations of ( $\square$ )  $0.10 \text{ mM}$ , ( $\nabla$ )  $0.25 \text{ mM}$ , ( $\triangle$ )  $1.0 \text{ mM}$  and ( $\circ$ )  $50 \text{ mM}$ . Straight lines show asymptotic behaviour according to  $N \propto t^{z'}$ .

time for the average cluster size has to be found. This scaling time should take into account that the effective capture volume is sensitive to both, the electrostatic and the magnetic interactions. Hence, we redefine the effective volume of Equation 6.2

$$\phi_{eff} = 24[(1/3)^{1/2} - (1/3)^{3/2}]\Gamma_{el}\lambda\phi, \quad (6.3)$$

so that it accounts for the effect of the electrostatic interactions through a dimensionless parameter  $\Gamma_{el}$ . This coefficient reflects the influence of the electrolyte concentration on the range of the total interaction and is used here as a freely adjustable fitting parameter for making the data superimpose. In our experimental systems, the repulsive electrostatic interaction is already sufficiently screened and negligible with respect to the magnetic forces at  $50 \text{ mM}$ . Therefore we assume  $\Gamma_{el} = 1$  at this electrolyte concentration and take the

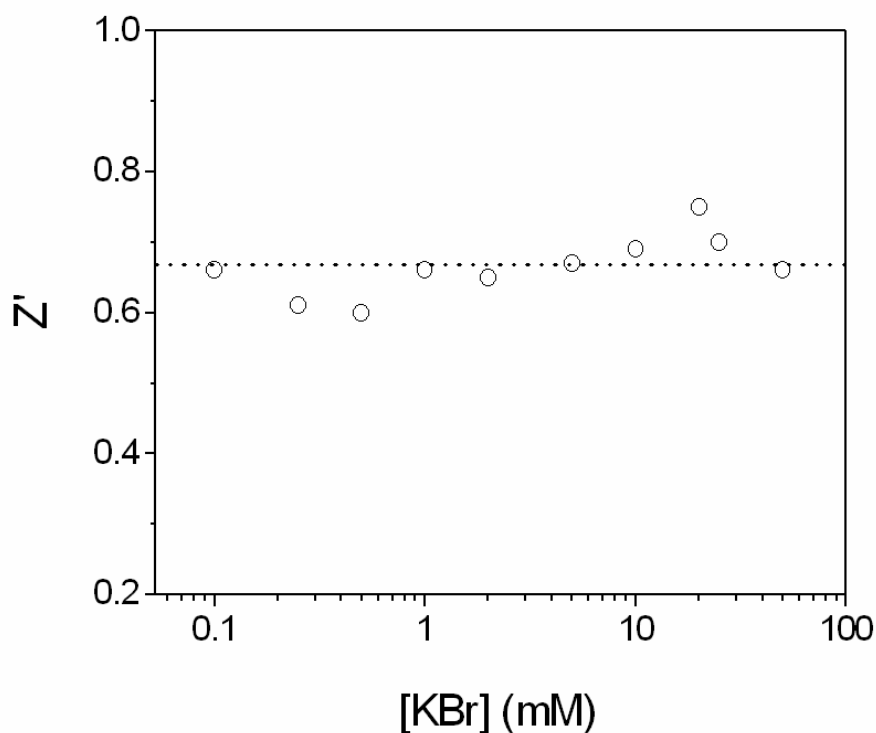


Figure 6.8: Kinetic exponents obtained for all the curves shown in Figure 6.6 as a function of the electrolyte concentration.

50 *mM* curve as reference curve onto which the rest of the curves should collapse. Figure 6.9 shows the average chain length as a function of the scaled time  $t/\tau_{Br}^*$  at all the electrolyte concentrations employed.

As can be seen, the experimental data align almost perfectly along a single master curve. The values obtained for  $\Gamma_{el}$  are shown in Figure 6.10 as a function of the electrolyte concentration. As expected,  $\Gamma_{el}$  decreases for decreasing electrolyte concentration, i.e. it is the smaller the stronger the electrostatic repulsions become. A fit to a linear relationship between  $\Gamma_{el}$  and the electrolyte concentration for  $[KBr] < 50 \text{ mM}$  gives  $\Gamma_{el} = 0.3 \log[KBr] + 0.48$ .

Figure 6.11 shows once more the time evolution of the measured effective diffusion coefficients in presence of the applied magnetic field. The time is scaled by the characteristic aggregation time for purely diffusion controlled aggregation  $t_{agg} = 2/(n_0 k_s)$ , where  $k_s = 12.3 \times 10^{-18} \text{ m}^3 \text{ s}^{-1}$  is Smoluchowski's kinetic rate constant (Equation 3.7). The continuous lines show the fits that

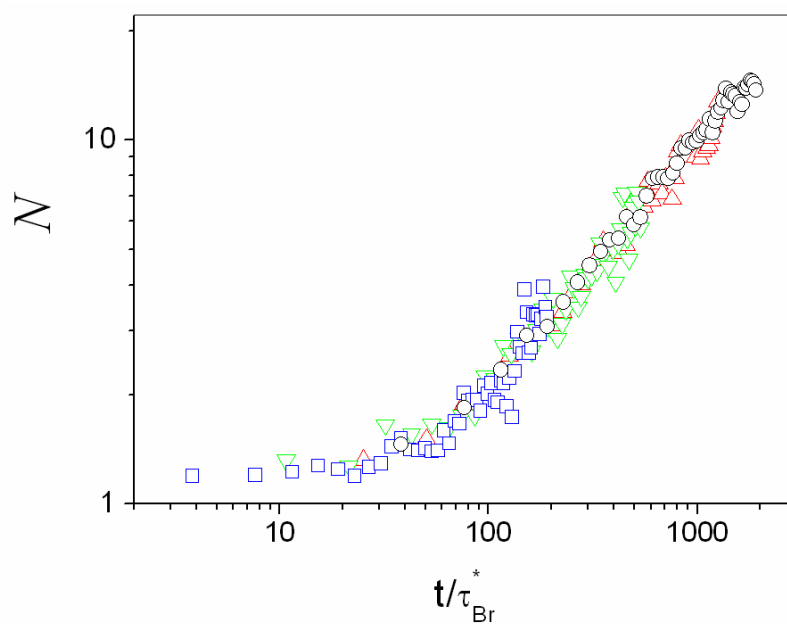


Figure 6.9: Average number of constituent particles per aggregate as function of the scaled exposure time at electrolyte concentrations of ( $\square$ ) 0.10 mM, ( $\nabla$ ) 0.25 mM, ( $\triangle$ ) 1.0 mM and ( $\circ$ ) 50 mM.

were obtained using again the proposed kernel (Equation 3.23)

$$k_{ij}^{Bdip} = 4\pi(1 - \cos\varphi_c)(\bar{D}_i + \bar{D}_j)(a_i + a_j + \bar{h}),$$

for the numerical solutions of Smoluchowski's aggregation equation. The effective interaction range  $\bar{h}$  was the only adjustable parameter again. The agreement between experiment and theory can again be considered as very satisfactorily. The values obtained for the fitting parameter  $\bar{h}$  are included in Table 6.2.

The effective interaction range and the effective particle volume fraction increase for increasing electrolyte concentration. These observations may be understood in terms of the enhanced shielding of the repulsive electrostatic interaction caused by the added electrolyte. Since the total interaction potential

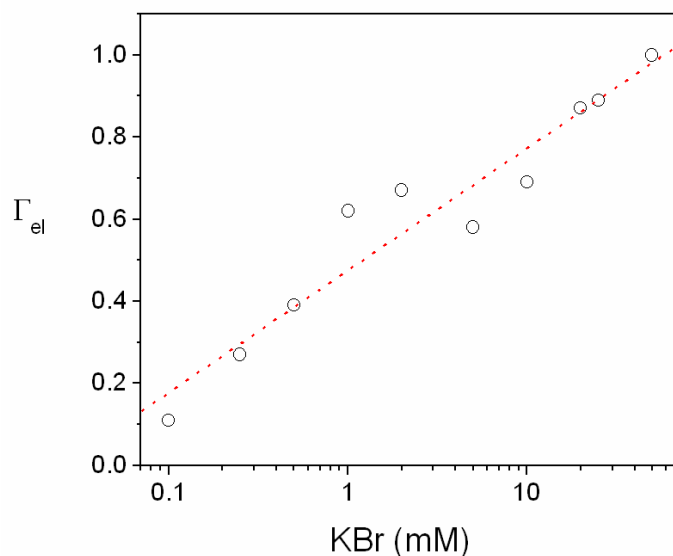


Figure 6.10:  $\Gamma_{el}$  values obtained for all the curves shown in Figure 6.6 as a function of the electrolyte concentration. The straight line is a fit to a linear relationship between  $\Gamma_{el}$  and the electrolyte concentration for  $[KBr] < 50$   $mM$ .

between double layered magnetic particles usually shows a primary minimum due to strong short range attractive interactions and a shallow secondary minimum that is mainly due to the long range magnetic interactions, electrolyte addition plays two important roles for linear aggregate formation. Firstly, it increases the effective range of the total interaction and secondly, it lowers the height of the energy barrier between both minima [64]. The latter will eventually allow the particles to aggregate in the primary minimum. Only particle-particle bonds in the primary energy minimum are able to persist when the magnetic field is removed. As we will see in the next Chapter, the relative strength of the electrostatic and magnetic interactions is a fundamental parameter which controls not only the kinetics of chain growth but also their stability once the magnetic field is turned off. Once again, the average character of the fitting parameter  $\bar{h}$  explains the negative value obtained for the lowest electrolyte concentration of 0.10  $mM$ .

For the sake of completeness, we would like to compare the fits reported so far using the proposed kernel (Equation 3.23) with fits that could be achieved employing the Miyazima kernel given by  $k_{ij} = C(i^\gamma + j^\gamma)$ . The latter kernel

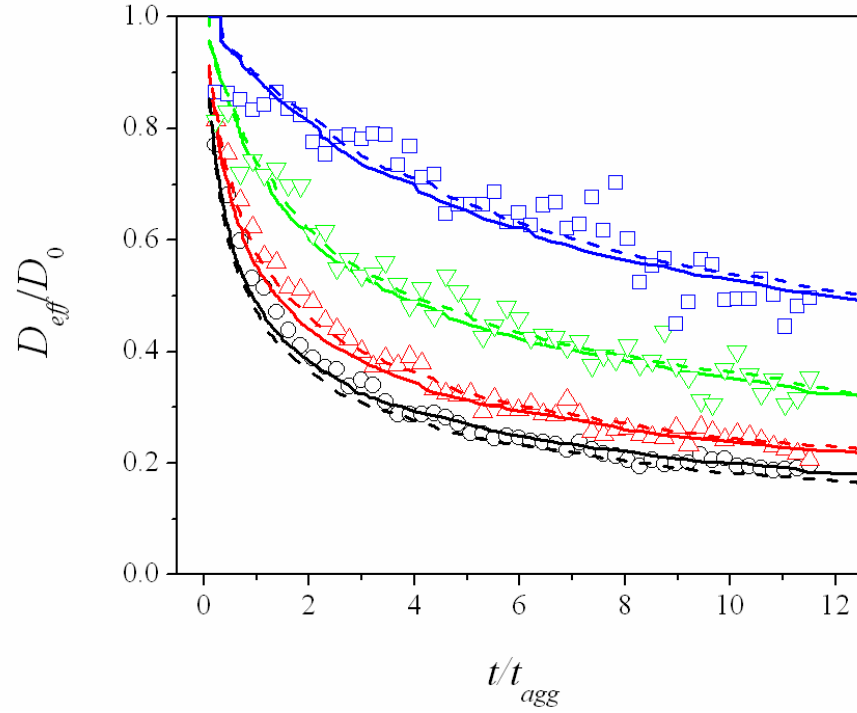


Figure 6.11: Time dependence of the normalized average diffusion coefficient  $D_{eff}/D_0$ , obtained for electrolyte concentrations of ( $\square$ ) 0.10  $mM$ , ( $\nabla$ ) 0.25  $mM$ , ( $\triangle$ ) 1.0  $mM$  and ( $\circ$ ) 50  $mM$ . The continuous and dotted lines show the best fits using to the proposed kernel (Equation 3.23) and the Miyazima kernel (Equation 3.19) for the numerical solutions of Smoluchowski's aggregation equation, respectively.

has

$$\lambda_{hom} = \mu_{hom} = \gamma \quad (6.4)$$

and

$$z = \frac{1}{1 - \gamma} \quad (6.5)$$

Hence, if we determined the homogeneity exponent from the experimental kinetic exponent  $z' = 0.67$ <sup>1</sup> then we obtain  $\gamma = \lambda_{hom} = \mu_{hom} = -0.5$ . A

<sup>1</sup>Here, we have assumed that  $z = z'$ . However, some differences between  $z$  and  $z'$  have been observed by other authors [85, 124].

$[KBr](mM)$	50	1.0	0.25	0.10
$\Gamma_{el}$	1.00	0.66	0.28	0.10
$\frac{\bar{h}}{a}$	3.78	2.72	0.85	-0.42
$C(10^{-17}m^3s^{-1})$	2.34	1.23	0.49	0.15

Table 6.2: The dimensionless parameter  $\Gamma_{el}$ , the effective interaction range  $\bar{h}$ , and the cross sectional parameter  $C$  assessed for different electrolyte concentrations.

negative value of  $\lambda_{hom}$  indicates that the reactivity between linear aggregates of the same length declines with chain length. On the other hand, a negative value of  $\mu_{hom}$  indicates that large aggregates preferentially react with small aggregates. The above-mentioned is qualitatively consistent with the theoretical frame that states: As aggregates grow in size, their mobility decreases whereas their cross section remains constant [134].

For the Miyazima kernel, we have used the proportionality constant  $C$  as fitting parameter. The fitting constants obtained are shown in Table 6.2 and the corresponding fits are included in Figure 6.11. At first sight, the comparable quality of both fits is quite striking. In order to understand the reason thereof, we plotted the normalized rate constants  $k_{ii}/k_{11}$  for both kernels versus the aggregate size in Figure 6.12. For cluster sizes smaller than  $i \cong 10$ , both kernels are virtually identical. For larger aggregates, however, the Miyazima kernel starts to overestimate the aggregation rate constants with respect to the proposed kernel. Since the largest average chain lengths reported in this paper do not surpass the value of  $i \cong 15$  (see Figure 6.12), it is not surprising that both kernels lead to similar fits. According to the size dependence of both kernels, we expect the fits based on the Miyazima kernel to worsen for larger aggregates and longer aggregation times. Unfortunately, our experimental data do not reach out so far and so, we cannot unequivocally state that the Miyazima kernel cannot predict the long time behaviour of field induced aggregation processes. Hence, further investigation in this direction is needed before this question could be solved.

Finally, we would like to point out that the parameters in the Miyazima kernel have no clearly defined physical meaning. Especially, the meaning of the cross sectional parameter  $C$  remains unclear. For the proposed kernel, however, the anisotropy of magnetic interaction as well as the long range character of the net particle interaction are explicitly taken into account. Both characteristics are included on average in terms of the distinction between the

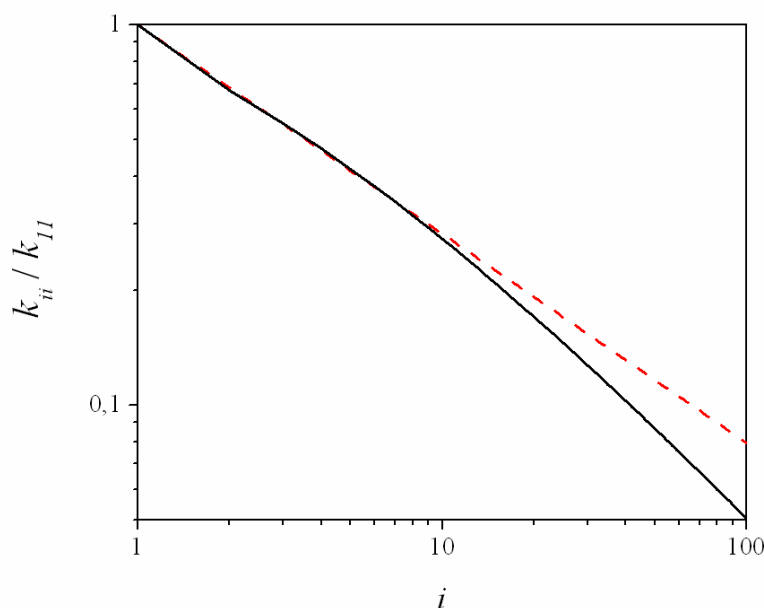


Figure 6.12: Size dependence of the normalized aggregation rate constant  $k_{ii}/k_{11}$  for the proposed kernel (solid line  $-$ ) and the Miyazima kernel with  $\gamma = -0.5$  (dashed line  $--$ ).

attractive zone I and the repulsive zone II defined in Section 3.5.2, and the effective interaction range  $\bar{h}$ . In this sense, the proposed kernel helps to achieve a deeper insight in the kinetics of aggregating magnetic filaments in presence of magnetic and electrostatic interactions [82].

### 6.3.2 Video Microscopy Experiments: Silica Particles

In the previous Section we have observed that the growth behaviour of small polystyrene particles depended even on small variations of the electrolyte concentration. In the present Section we will study the field induced aggregation of larger silica particles. Since the magnetic moment of the particles is proportional to their volume, larger particles allow us to study processes where the electrostatic repulsion between the particles may be completely overcome by magnetic dipolar interactions.

We have used direct visualization via video microscopy and digital image processing to study the kinetics of the field induced aggregation. Video-

microscopy experiments allows not only the time evolution of the mean cluster size but also the time evolution of the cluster size distribution to be assessed. Solving the corresponding Smoluchowski equation, the experimental cluster size distributions may be compared with theoretical predictions. Such a comparison is essential in order to test the quality of the proposed aggregation kernel, since different aggregation kernels may give rise to the same time evolution of the mean cluster size. To the best of our knowledge, there are no previous studies that contrast experimental cluster size distribution with theoretical predictions for magnetorheological fluids.

The silica particles used were synthesized by Dr. Abdeslam El-Harrak (see Section 5.1.2). Charged surface silanol groups prevented particle aggregation through repulsive electrostatic interactions. A particle surface potential of  $\sim -10mV$  was obtained by means of electrophoretic mobility measurements, as was stated in the Section 5.1.2. Several series of experiments have been performed at different salt concentrations using  $KBr$  as indifferent 1:1 electrolyte. The electrolyte was always added to the colloidal dispersion before exposing the samples to the magnetic field. The electrolyte concentrations used for reducing the repulsive electrostatic interactions were  $0.0 mM$ ,  $0.5 mM$ , and  $1.0 mM$ . Under these electrolyte concentrations the systems remained stable when they were not exposed to the magnetic field. For higher electrolyte concentrations the particles started to aggregate to the glass interface. This is not surprising since reported surface charge densities for glass interfaces in aqueous solutions are usually smaller than the charge density of colloidal particles [135]. In fact, the particle concentration was determined adding  $KBr$  electrolyte at  $20 mM$  to the samples. At this salt concentration, the electrolyte screens the electrostatic repulsion between the particles and the glass walls. In this way, all the particles appear stuck to the walls and monomer counting becomes quite straight forward.

Some exploratory experiments were performed at different particle concentrations. However, high concentrations made the images difficult to analyse during the first stages of aggregation, and low concentrations worsed the statistics of the cluster size distribution. Therefore, the employed concentration was finally chosen such that image analysis process was optimized. Prior the measurements, the particles were diluted in water to a final concentration of  $2.65 \times 10^7 particles/cm^3$ , corresponding to a volume fraction of  $\phi = 2.74 \times 10^{-6}$ . According to the theoretical background the aggregation kernel does not depend on the particle concentration as long as the particle concentration is within the range where the Smoluchowski's equation is applicable, and the lateral chain-chain aggregation is avoided [9].



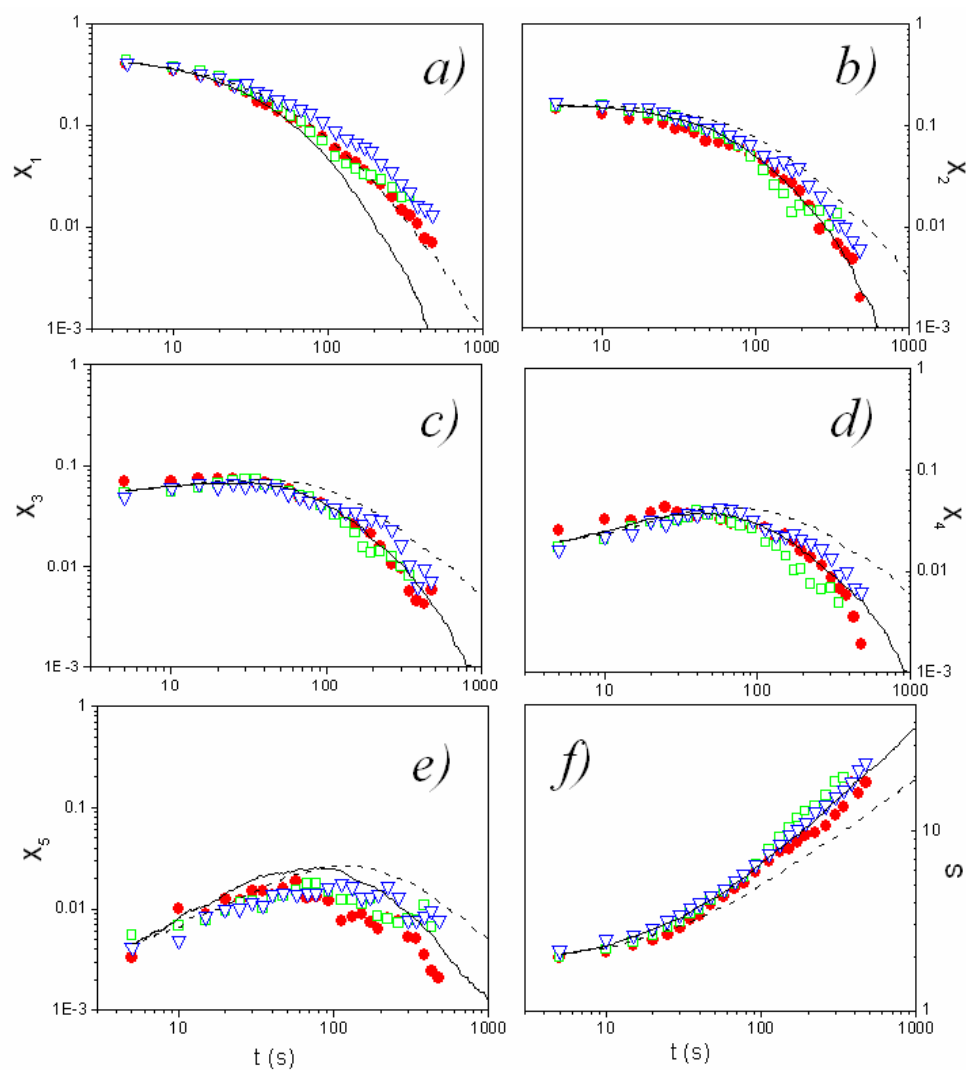


Figure 6.13: Time evolution of the normalized cluster-size distribution. The curves correspond to *a*) monomers, *b*) dimers, *c*) trimers, *d*) tetramers, and *e*) pentamers. The dotted lines show the best fits using the aggregation kernel given by Equation 3.23. The continuous lines show the same fit when differential sedimentation is taken into account. Figure *f*) shows the time evolution of the weight-average chain-length  $S(t)$  as a function of the exposure time to the magnetic field. The experiments were performed at different electrolyte concentrations:  $\bullet$  0 *mM*,  $\square$  0.5 *mM*, and  $\nabla$  1.0 *mM*.

Some authors, however, have argued that the aggregation kinetics of field induced aggregation processes may depend on the volume fraction [7]. During the experiments, typically about 700 particles could be observed in the field of view. A large number of initial monomeric particles is essential for maintaining a reasonable statistics for larger aggregates at long aggregation times. The relatively large depth of field available at low magnification (10x) helped us to keep the particles in focus despite of their random Brownian motion. According to the experimental method described in the Section 5.3.2, we monitored the aggregation processes that were induced in the sample due to the applied external magnetic field at different concentrations of  $KBr$ . Therefore, pictures were captured every 5 seconds during a total time interval of 495 seconds. The field strength of  $3.9 \text{ kA/m}$  employed in this experiment corresponds to  $\lambda = 278$ .

Figure 6.13 (a-e) shows the normalized cluster-size distribution for clusters formed by 1, 2, 3, 4 and 5 monomeric particles in logarithmic scale at different electrolyte concentrations (0.0  $mM$ , 0.5  $mM$  and 1.0  $mM$ ). The data shown in the Figure represent an average over four experiments. They are normalized by the initial number of particles. Errors bars are not included for the sake of clarity. In order to improve the data statistics and to reduce the number of data points to be plotted at longer aggregation times, several consecutive measurements were grouped and averaged accordingly. The number of clusters larger than pentamers became so low that statistical uncertainties and fluctuations prevailed and no meaningful curve could be drawn. For electrolyte concentrations of 0.5  $mM$  and 1.0  $mM$  the results superimpose and follow the curve observed at 0.0  $mM$ . Contrary to the results reported in the previous section, where we observed that the growth behaviour depends strongly on small variations of the electrolyte concentration, in this case the electrolyte does not affect the rate of the process.

Figure 6.13 (f) shows the weight-average chain-length  $S(t)$  as a function of the exposure time to the magnetic field at different electrolyte concentrations. The clusters of all sizes detected on the photos were taken into account for the average. Once more, the growth behaviour does not depend on variations of the electrolyte concentration. In this logarithmic plot,  $S(t)$  shows a clear linear asymptotic behaviour at long aggregation times and so, confirms the typical power law behaviour for the kinetics of aggregation. From the slope at long times, the kinetic exponent  $z$  could be estimated to be  $z = 0.72$ . This value agrees quite well with the value of  $z' = 0.67$  reported previously.

Before comparing the fits with experimental data, we would like to discuss the reason for not having imposed monomeric initial conditions at  $t = 0 \text{ s}$ .

When no magnetic field is present, our superparamagnetic particles diffuse almost without any interaction. Only at relatively short interparticle distances, electrostatic repulsive forces avoid aggregation. Hence, a small fraction of monomeric particles may be so close to each other that they will be located within the attractive zone of the magnetic dipole interaction that appears as soon as the magnetic field is turned on. Due to the strong attractive magnetic forces, these particles will aggregate almost immediately when the field is turned on. An example of the result of such ballistic initial aggregation is shown in Figure 6.14. Since such a transient effect is not described by Smoluchowski's equation, we were forced to impose as boundary conditions for the fits a cluster size distribution that was measured after a sufficiently long time when the aggregation process becomes purely diffusion controlled [36]. Moreover, some small aggregates might initially be present before the magnetic field is applied. Digitalization effects may also play an important role.

In order to fit the experimental results theoretically, we solved Smoluchowski's equation numerically using the aggregation kernel given by Equation 3.23 and we imposed as boundary conditions the cluster-size distribution obtained at  $t = 5$  s. On the other hand, an affine transformation between the time in the simulation  $t_{sim}$  into the experimental one  $t_{exp}$  has been done  $t_{sim} = 60t_{exp}$ . The transformation does not affect the curve shape at all in a log-log plot. It only introduces a horizontal shift of the data set as a whole. Hence, we can conclude that experimental and simulated times are functionally identical [129].

The theoretical results are plotted together with the experimental data in Figure 6.13. The best fits for the experimental data shown in these figures were obtained for an average interaction range of  $\bar{h} = 4.35\mu m$ . This value is about 7.5 times the monomer diameter and is in good agreement with the long range character of the dipolar magnetic interaction. It is, however, much larger than the values ranging from 1.89 to -0.21 times the monomer diameter that were previously reported for the magnetic polystyrene particles. The kinetic exponent obtained for the theoretical curves is  $z = 0.58$  which is very close to the value of  $z = 0.6$  deduced by the model of Miguel et al. [9]. Nevertheless, the theoretical predictions fit the experimental results acceptably well only during the first aggregation stages. After about 20 s, however, the fit and the experimental data start to differ noticeably.

The relatively large range of the interactions observed now could explain why the growth processes do not depend significantly on the electrolyte concentration. The range of the total interaction between the particles may be controlled by varying the electrolyte concentration only when the outreach of

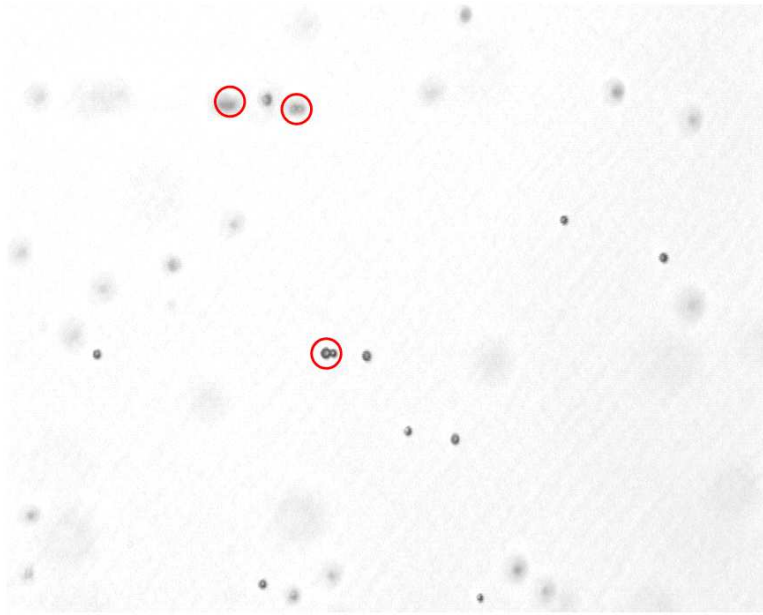


Figure 6.14: High magnification (20x) image taken at 1s after application of the magnetic field. The circled dimers have formed mainly due to immediate ballistic aggregation of two initially close monomers.

the repulsive electrostatic interaction is sufficiently large and overcomes the range of the magnetic interactions substantially. Otherwise, the electrostatic part of the total interaction is negligible at large distances, and an effect of the electrolyte concentration on the aggregation kinetics is not expected. The measured magnetic moments and surface potentials of the particles agree clearly with the latter scenario. The surface potential of the silica particles is approximately 5 times lower than the surface potential of the polystyrene particles. At the employed magnetic field strengths, however, their magnetic moment is approximately 30 times larger than that achieved by the polystyrene particles in the previous Section. Consequently, the corresponding  $\lambda$  value of 278 is much higher compared with the previously reported value of 11.6 [84].

#### 6.4 Sedimentation Effects

For typical practical applications, suspensions of composite magnetic nanoparticles are frequently employed. These particles often contain small grains of

iron oxides which increase their relative density with regard to the dispersion medium. The relatively high particle mass density and the increased size due to chain formation, favour differential sedimentation, i.e. small magnetic particles remain suspended while the large aggregates settle. Therefore, the study of MR fluids in the Earth's gravitational field is not straight forward. In order to overcome this difficulty, some studies have even been performed at the International Space Station (please, see Appendix B). Sedimentation is a serious problem for many manufacturers of technological applications, and gravitational effects must not be omitted for a correct description and modelling of this type of aggregation processes.

In our previous studies we have used small magnetic polystyrene particles of 170 nm in size. Hence, sedimentation was found to be negligible during the experiments due to the relatively small size and low mass density of only  $1.2 \text{ g cm}^{-3}$  of those particles, and the time evolution of the average chain diffusion coefficient at different electrolyte concentrations was successfully described by the aggregation kernel given by Equation 3.23.

However, when we employed silica particles of increased size and mass density, the theoretical predictions fit the experimental results acceptably well only during the first aggregation stages. After about 20 s the fit and the experimental data start to differ noticeably (see Figure 6.13). One possible reason for the mismatch between the theoretical predictions and the experimental results may be the influence of sedimentation. On the sequence of photos, it was clearly observable that the linear aggregates settle the faster the larger they grow (Figure 6.15). This means that the larger aggregates sweep a larger area than the smaller clusters and so, the collision frequency with other clusters is enhanced. During the first aggregation stages, this effect is negligible since there are only individual monomers and some smaller aggregates that settle at a relatively similar low average velocity. At longer aggregation stages, however, the differential sedimentation becomes more and more important.

Since the aggregation kernel given by Equation 3.23 does not account for this effect, it is not surprising that its predictions start to fail as the aggregates become larger. The silica particles will allow us to study coupled field induced aggregation and sedimentation process. Particles of an even higher mass density could have been employed. In this case, however, the Brownian movement would be negligible with respect to the expected sedimentation velocities.

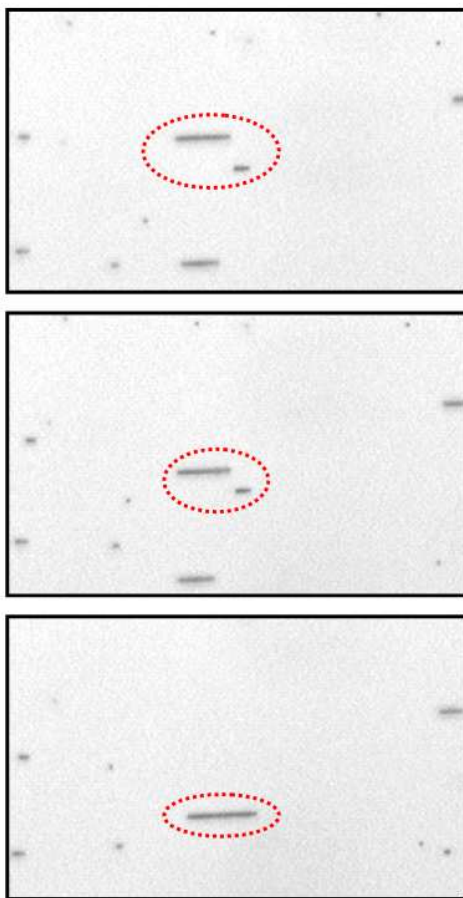


Figure 6.15: Successive images taken after the application of the magnetic field. The circled linear aggregates shown that the larger aggregates sweep a larger area than the smaller clusters and so, the collision frequency with other clusters is enhanced.

In order to account for differential sedimentation, we determined the average settling velocities for monomers and aggregates using video-microscopy and image processing. During the sedimentation velocity measurements, the magnetic field was present in order to maintain the linear structure and orientation of the chains. Figure 6.16 shows the measured average sedimentation velocities  $v_N^s$  as a function of the cluster size  $N$ . As can be seen, the monomer sedimentation velocity was  $v_1^s \approx 0.5 \mu\text{m}/\text{s}$ . This leads to a Péclet number of  $Pe \approx 0.17$ . Since this number quantifies the relative strength of sedimentation

and diffusion effects, we can conclude that thermal diffusion still dominates over sedimentation for the smaller particles. Nevertheless,  $Pe$  is not so small that sedimentation effects even for the monomeric particles may be neglected a priori.

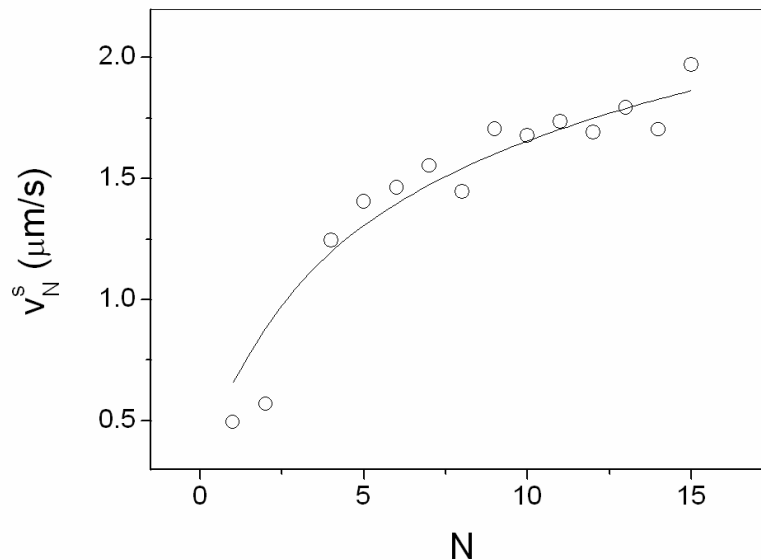


Figure 6.16: Measured sedimentation velocities as a function of the chain length (data points). The continuous line shows the theoretical fit according to Equation 2.62.

We measured the sedimentation velocities of the clusters and compared them with the theoretical predictions given by Equation 2.62:

$$v_N^s = \frac{\ln(N) + \gamma_{\perp}^{end}(N)}{6\eta} a^2 \Delta\rho g.$$

In spite of the fact that all the parameters in the analytic expression for the sedimentation velocity are fixed, we employed the average particle mass density  $\rho_p$  as fitting parameter for the curve shown in Figure 6.16. As can be seen, the theoretical curve fits the data satisfactorily and so, the theoretical expression given by Equation 2.62 may be considered as a valid description for the sedimentation velocities of our chains. The best fit was obtained for  $\rho_p = 4.4g/cm^3$ . This value differs quite significantly from the value of  $\rho_p =$

$3.6g/cm^3$  measured by equilibrium centrifugation in sucrose. Nevertheless, both values lie within the interval defined by the pure silica and iron oxide densities of  $2.2g/cm^3$  and  $5.6g/cm^3$ , respectively. The observed discrepancy, however, could be caused by convective motion and back flow of the water. Previous studies have reported that the liquid induced motion of the particles for a similar geometry is of the order of  $v \approx 1.0\mu m/s$  [14]. Moreover, the fluid flow pattern suffers a distortion due to the presence of the container walls that will also affect the particles. Even when the cell width were large enough to avoid corrections due to wall effects, the sedimentation velocity of the linear aggregates could still be affected significantly due to convection and water back flow effects [14, 76].

For the additional contribution to the aggregation kernel due to differential sedimentation, the expression

$$k_{ij}^{Bdip-s} = k_{ij}^s + k_{ij}^{Bdip}, \quad (6.6)$$

together with the term  $k_{ij}^s = A_{ij}|(v_i^s + v_j^s)|$ , was proposed in Section 3.5.3. Using these expressions as aggregation kernel in Smoluchowski's equation, the cluster size distribution arising in coupled aggregation-sedimentation processes was obtained theoretically.

Also here, the experimental cluster-size distribution measured at  $t = 5$  s was imposed as a boundary condition for the calculations. The sedimentation velocities were determined according to Equation 2.62. The value of the effective range  $\bar{h}$  obtained in the last Section was kept. The calculated theoretical time evolution of the cluster-size distribution is shown in Figure 6.13 (a-e). The weight-average chain-length,  $S(t)$ , was also determined and included in Figure 6.13 (f). As can be seen in the figures, the theoretical fits improve quite substantially when sedimentation effects are considered. Especially the fit for the weight-average chain-length,  $S(t)$ , is now very satisfactory if one takes into account that no additional fitting parameter was introduced.

According to Figure 6.13, the main differences between the fits and the experimental data are observed for the monomer population. Such an under-estimation of the number of monomers was already reported by Fraden et al. [30] for dilute suspensions of micron-diameter particles confined to two dimensions. These authors attributed this effect to the two-dimensional nature of their sample. In this case, larger aggregates partition space and isolate smaller clusters on either side from each other. Hence, there will be more monomers left in the sample than predicted theoretically and a crossover from a two to a one-dimensional behaviour will take place. In our three dimensional exper-



iment, however, a transition of this nature is not expected. The relatively large number of monomers determined experimentally may, however, be due to detection problems since the size of these particles is just of the order of one image pixel. This implies that dust particles or aggregates that are not in the focal plane may erroneously be counted as monomers. Nevertheless, our data make clear that the agreement between the theoretical predictions calculated according to Smoluchowski's theory and the experimental results improve substantially when sedimentation effects are considered. Especially, the asymptotic behaviour of the weight-average chain-length could be reproduced and the theoretically assessed kinetic exponent of  $z = 0.77$  comes quite close to the experimental value of  $z = 0.72$ . This means that higher  $z$  values may be a sign of additional aggregation due to differential sedimentation [84].

## 6.5 Mutual Induction Effects

The relatively large number of monomers that apparently are left behind in the aggregation process seems to indicate that larger chains are more reactive than predicted by theory. One possible effect that could cause such a behaviour is mutual induction between the chain forming particles. At weak field strengths, the degree of magnetization of the particles is proportional to the local field strength and so, the net magnetization of the particles contained within a chain is enhanced by the presence of neighbouring particles. Zhang et al. have shown that mutual induction in the weak field regime may enhance the magnetization of a particle by up to 34% beyond the magnetization that it would have as an isolated single particle [15]. This effect leads to an increased range of the magnetic interaction between the aggregates as they gain in size (see Section 3.5.4).

In order to check the influence that mutual induction may have on the aggregation kinetics, we solved Smoluchowski's equation using the Equation 3.27 for the size dependency of the range of the magnetic dipole interaction

$$\frac{\bar{h}_{ij}}{\bar{h}_{11}} = \frac{1}{\left(1 - \frac{\pi\zeta_j(3)}{3}\right)^{2/3}} \quad j > i$$

As before, the same boundary conditions and aggregation kernel  $k_{ij}^{Bdip-s} = k_{ij}^s + k_{ij}^{Bdip}$  were imposed. The best fits for the experimental data were now obtained for an average interaction range of  $\bar{h} = 2.61\mu m$ . Nevertheless, the fits

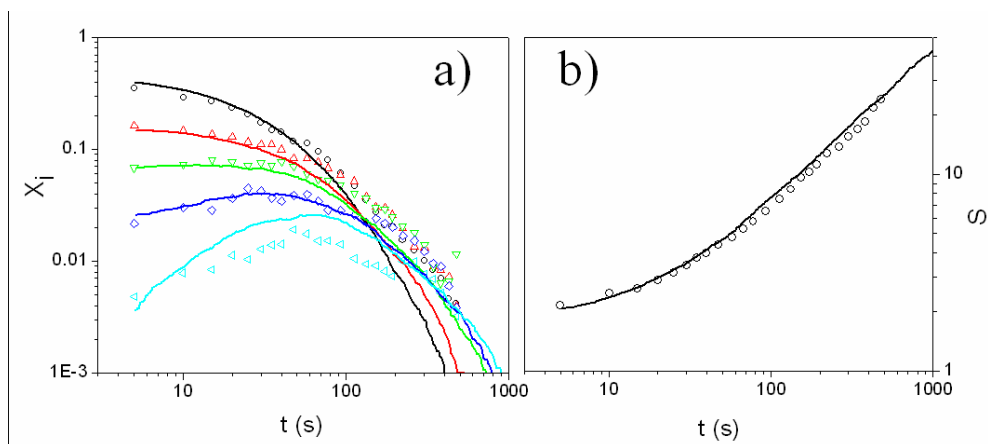


Figure 6.17: *a)* Time evolution of the normalized cluster-size distribution. The data points correspond to ( $\circ$ ) monomers, ( $\triangle$ ) dimers, ( $\nabla$ ) trimers, ( $\diamond$ ) tetramers, and ( $\triangleleft$ ) pentamers at 0 *mM* of electrolyte concentration. The continuous lines show the theoretical fit when both the sedimentation as well as the mutual induction are considered. *b)* Time evolution of the weight-average chain-length as a function of the exposure time to the magnetic field (data points) at 0 *mM* of electrolyte concentration. The continuous lines show the theoretical fit when the sedimentation as well as mutual induction are taken into account.

remain almost unchanged and do not improve significantly with respect to the curves obtained before (see Figure 6.17). This means that mutual induction within the chain-like aggregates increases the average range of the particle interaction with the chain length, but it has no perceptible influence on the aggregation kinetics and cannot explain why such a large number of monomers is left over [84].



## Chapter 7

# Stability and Structure of Magnetic Filaments

In this Chapter we study the morphology and the stability of permanent chains, and focus our attention mainly on the role of the electrolyte concentration. The aim of the research work described in this Chapter was twofold: On the one hand, we wanted to design an accurate experimental protocol that allows the final mean length of the linear aggregates to be controlled by tuning the different interparticle interactions. On the other hand, we tried to show that the final filament size as well as the chain structure may be reliably monitored by light scattering techniques, both when the filaments are either aligned due to the action of the magnetic field, or freely diffusing once the magnetic field is removed. A further purpose of the present Chapter was to calculate the probability that a particle that is caught in a secondary bond escapes to a primary bond and to determine its dependency on the height of the energy barrier between the primary and secondary minima. A suitable system of differential equations for calculating the reaction probability will be proposed. The results obtained for different conditions will be compared with experimental results.

### 7.1 Magnetic Filaments

Field induced aggregation is irreversible as long as the magnetic field is applied. When the field is removed, the linear aggregates break due to the thermal energy, and the magnetic particles return to their original monomeric state. When the magnetic particles are linked together permanently by means of

strong short range attractive interactions, the linear geometry of the aggregates is preserved even in absence of the field. Adhesion may be induced by van der Waals attraction [20], or by adsorbed molecules that form a strong "bridge" between the particles surfaces [20, 22, 69]. There are a variety of linking molecules that have been used to create permanently linked chains. The length of the linear aggregates can be controlled by forming the chains in microchannels of a given height [16]. The chains may be anchored on surfaces to prevent migration in flow processes. Magnetic colloids patterned on a surface can serve as templates for chain growth from the fixed particles [17, 136]. Both Biswal and Gast [19] as well as Goubault et al. [22] employed a variety of optical trapping experiments to measure the flexural rigidity of the magnetic filaments, and to probe bending rigidity at a molecular scale. Both authors agree that the flexibility of the resulting magnetic nanowires is usually controlled by the molecular weight of the linker molecule and their diameter by the bead size. Using similar experimental protocols, more rigid magnetic chains were obtained by other authors [137]. When the synthesis of the magnetic nanoparticles is dominated by aggregation of primary units, an applied magnetic field has been shown to have a dramatic effect on the morphology. In this case extremely rigid rodlike particles may be formed [32]. One dimensional structures have been also obtained for cobalt nanoparticles that undergo a superparamagnetic to ferromagnetic transition, as their size increases during the synthesis process [138]. Magnetic nanowires have also been prepared by electrochemical growth in alumina templates [139].

One-dimensional nanocolloids have received considerable attention over the last years due to their potential for specialized applications. Permanent linear aggregates can be used as micromechanical sensors [20, 22], micromixers [23] and for DNA molecule separation, as obstacles to impede the convective transport of biological species [4]. Linear chains of colloidal magnetic particles linked by DNA and attached to a red blood cell have even been used as flexible artificial flagellum [18].

## 7.2 Formation of Permanent Magnetic Chains

Initially stable samples of monodisperse superparamagnetic polystyrene particles were aggregated in the presence of an external magnetic field and different amounts of electrolyte. The aggregation process was monitored using dynamic light scattering (DLS), as we have discussed in the previous Chapter. When the magnetic field was turned off, a significant change of the effective diffu-

sion coefficient was observed at all electrolyte concentrations. This jump was interpreted in terms of filament break-up and additional rotational diffusive modes. Therefore, the length of the magnetic filaments was determined from the measured average diffusion coefficients applying an adequate theoretical approach. The results prove that the magnetic filaments disassemble completely at low electrolyte concentrations. At intermediate amounts of added electrolyte, a partial cluster break-up is observed. Only at high salt concentrations, the chains withstand the absence of the magnetic field. The results show that the average filament size can be predicted and controlled by tuning the relative strength of the magnetic and electric interactions.

### 7.2.1 Changes in the Mean Diffusion Coefficient

Several series of DLS experiments have been performed at different concentrations of an indifferent 1:1 electrolyte (*KBr*). The final electrolyte concentrations used for reducing the repulsive electrostatic energy barrier were 0.0, 0.10, 0.25, 0.50, 1.0, 2.0, 5.0, 10, 20, 25 and 50 *mM*. The electrolyte was always added to the colloidal dispersion before exposing the samples to the magnetic field. Afterwards, the magnetic field was applied. The strength of the magnetic field was measured to be  $H = 23.9 \text{ kA/m}$  throughout the scattering volume. Figure 7.1 shows the measured mean effective diffusion coefficient  $D_{eff}$  as a function of time for different electrolyte concentrations. During the first 30 minutes of the experiments (zone *I*), the magnetic field was applied. Thereafter, the field was turned off but the DLS measurements were still performed for some additional time (zone *II*). The data shown are always the average of five measurements. The corresponding errors bars are not shown for the sake of clarity. At first glance, two different behaviours can be clearly distinguished.

When the magnetic polystyrene particles are exposed to the magnetic field (zone *I*), a decrease of  $D_{eff}$  is observed in almost all the cases. This means that the average filament size increases with the exposure time to the magnetic field. In presence of an external magnetic field, the filaments are forced to align in the field direction and so, rotational chain diffusion was forbidden. Consequently, only the translational diffusion coefficients  $D_{\perp}$  and  $D_{\parallel}$  have to be considered for the theoretical analysis. In our experimental setup, however, the magnetic field vector is aligned perpendicular to the scattering plane. Due to this geometry, the measurements were only sensitive to the transversal motion of the linear aggregates and so, the measured effective diffusion coefficient corresponds to

$$D_{eff} = D_{\perp} = \frac{\mu_1}{q^2}. \quad (7.1)$$

Evidently, the parallel diffusion coefficient  $D_{\parallel}$  could be neglected [117]. As can be observed in Figure 7.1, for increasing electrolyte concentrations the growth rate rises and reaches a limiting value at about 50 *mM* *KBr*. This interesting kinetic behaviour has been widely extensively in the previous Chapter.

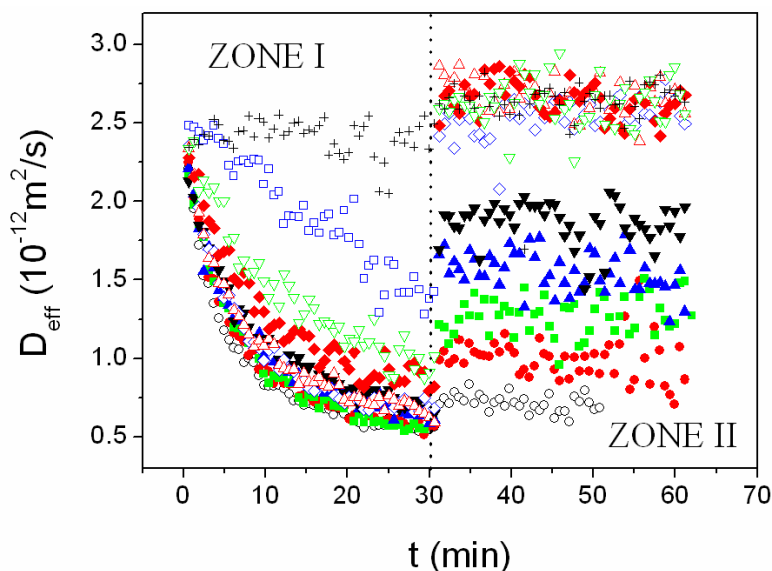


Figure 7.1: Time evolution of the effective diffusion coefficient of the aggregating samples. During the first 30 minutes (zone *I*), the magnetic field was applied. Thereafter, the field was turned off (zone *II*). The electrolyte concentrations were (+) 0.0 *mM*, (□) 0.10 *mM*, (▽) 0.25 *mM*, (◇) 0.50 *mM*, (△) 1.0 *mM*, (◊) 2.0 *mM*, (▼) 5.0 *mM*, (▲) 10 *mM*, (■) 20 *mM*, (●) 25 *mM* and (○) 50 *mM*.

In this Chapter, we will focus our attention on what happens when the magnetic field is turned off. In this case, the effective diffusion coefficient suddenly increases for all electrolyte concentrations and then remains more or less constant. At electrolyte concentrations larger than 2 *mM*, the mean diffusion coefficient does not return to its initial monomeric state. Hence, we can conclude that stable linear aggregates remain in the sample. These aggregates may rearrange and lose their linear morphology once the magnetic field

is turned off. However, chainlike aggregates were observed in videomicroscopy experiments as well as in all TEM images (as an example the Figure 7.2 shows images of different samples aggregated in the presence of an applied magnetic field). This means that the bonds contained in the linear aggregates are strong enough to withstand not only the absence of the magnetic field but also the drying step that was necessary for taking TEM images.

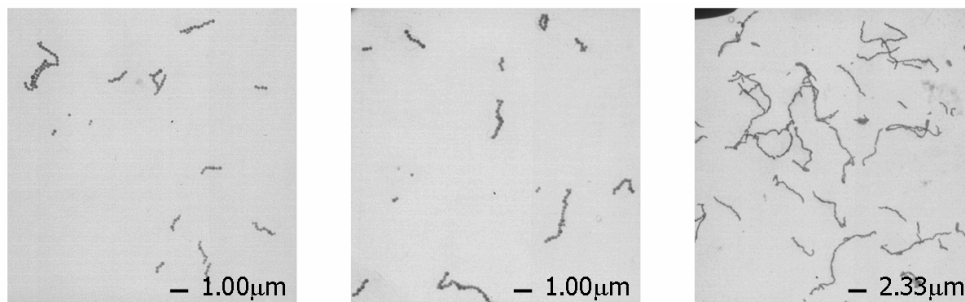


Figure 7.2: Transmission electron microscopy images of different samples aggregated at  $20\text{ mM KBr}$  in the presence of an applied magnetic field. The homogeneous magnetic field was measured to be  $(411 \pm 2)\text{ mT}$ . The images correspond to exposure times of 10 min, 30 min, and 60 min (form left to right).

If we neglect the influence of possible rearrangements of the particles within the clusters, the increment observed in the mean diffusion coefficient could principally be due to two different effects: to a break-up of the magnetic filaments, or to changes in their diffusive behaviour. Filament break-up is expected to depend on the electrolyte concentration. Indeed, our experiments show that the increment of the diffusion coefficient after removing the field becomes smaller for increasing electrolyte concentrations. This means that the degree of filament breaking is less pronounced at high electrolyte concentration. The fact that the observed effective diffusion coefficients do not increase further in time in zone *II* allows us to affirm that most of the magnetic filaments do not suffer any additional rupture. On the other hand, the filaments are forced to align in the field direction and rotational diffusion is not possible as long as the external magnetic field is applied (zone *I*). When the field is turned off rotation is not hindered anymore and hence, give rise to an additional diffusive mode that may be detected as an increase in the assessed effective diffusion coefficient. This ambiguity does not allow any further discussion about the chain growth behaviour at this point. In order to



overcome this uncertainty, it would be very convenient to assess the average chain length in units of particles per chain rather than in terms of an average diffusion coefficient [66].

### 7.2.2 Maeda's Model

Most of the light scattering works for measuring the translational diffusion coefficient  $D_t$  and the rotational diffusion coefficient  $D_r$  of linear scatters employ depolarized dynamic light scattering (DDLS) [13, 91, 92, 93, 94]. This technique, however, presents some drawbacks as we mentioned already in Section 5.3.1. Furthermore, most of these light scattering studies assume the translational diffusion to be isotropic, i.e. , in a reference frame fixed to the molecule, the diffusion coefficients parallel and perpendicular to the long molecule axis are identical,  $D_{\perp} = D_{\parallel} = D_t$ . Hence, the field autocorrelation function is characterized by a depolarized decay rate  $\mu_1 = 2(q^2 D_t + 6D_r)$  (Equations 4.47 and 4.48).

Long rods, however, undergo anisotropic translation, and so a coupling between the translational and rotational modes of their diffusive motion is expected. In this case, a nontrivial coupled diffusion equation has to be resolved (Equation 2.24). As a first approximation, Maeda and Fujime modeled linear aggregates as thin cylinders of length  $L$  (see Sections 4.4.2 and 5.3.1). They derived the following theoretical expression for the effective diffusion coefficient  $D_{eff}$ :

$$\frac{\mu_1}{q^2} = D_{eff} = [\bar{D} - \frac{1}{3}(D_{\parallel} - D_{\perp})] + (\frac{L^2}{12})D_r f_1(K) + (D_{\parallel} - D_{\perp})f_2(K), \quad (7.2)$$

where both  $f_1(K)$  and  $f_2(K)$  are functions depending only on  $K \equiv qL/2$ . (see Figure 4.8). This Equation allows the average chain length  $L$  to be determined directly from the effective diffusion coefficient of the aggregates,  $D_{eff}$ , measured by means of DLS.

We checked the validity of the Maeda-Fujime model for the linear aggregates formed by magnetic polystyrene particles. For this purpose, we measured the autocorrelation function as a function of the scattering angle. Figure 7.3 shows the results obtained, i.e. the effective diffusion coefficient  $D_{eff}$  as a function of the scattering vector  $q$ . Field induced aggregation was achieved by placing the samples in the narrow gap of a toroidal magnet at 20 *mM* of *KBr*. The flux density of the homogeneous magnetic field in the gap was measured to be  $(411 \pm 2)$  *mT*. The samples remained in the magnet during different

time intervals. Afterwards, the samples were removed and placed in the light scattering device. The scattering angle was varied from  $20^\circ$  to  $150^\circ$ . The data were fitted according to the Maeda-Fujime model. The average chain length  $L$  was employed as a fitting parameter and was adjusted such that the diffusion coefficient measured at  $60^\circ$  could be matched. As can be seen in Figure 7.3, the fits reproduce the  $q$  dependence of the effective diffusion coefficient quite satisfactorily, especially at long exposure times. The observed discrepancies may be due to chain polydispersity and to an internal degree of chain flexibility. The best fits were achieved for an average chain length of  $(3.7 \pm 1.3)$ ,  $(9.0 \pm 1.0)$ , and  $(18 \pm 2)$  particles per chain for exposure time of 5 min, 10 min and 20 min, respectively.

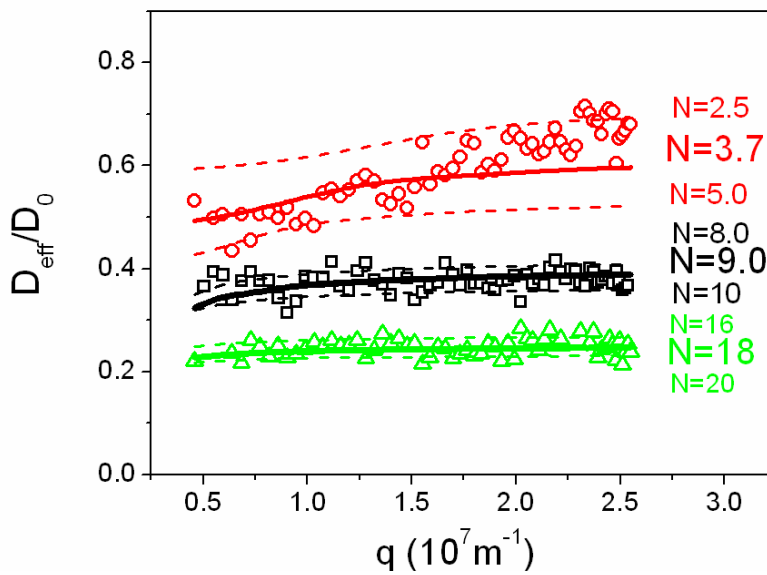


Figure 7.3: Effective diffusion coefficient  $D_{eff}$  normalized by  $D_0$  as a function of the scattering vector  $q$ . The samples were aggregated at  $20 \text{ mM}$ . The exposure times to the magnetic field were 5 min ( $\circ$ ), 10 min ( $\square$ ), and 20 min ( $\triangle$ ). The corresponding average chain lengths  $N$  are indicated in the figure. The continues lines show the best theoretical fits according to the Maeda-Fujime model. The dashed lines indicates the limits of the confidence intervals.

It is also worthwhile to mention that the simple model, in which rotational and translational motions are uncoupled, is not capable of fitting the previous

experimental data. In Figure 7.4 we plot the cumulant  $\mu_1$  as a function of  $q^2$ , measured under the previous experimental conditions. In the uncoupled model the cumulant is given by  $\mu_1 = q^2 D_t + 6D_r$ , and so the slope should give the translational diffusion coefficient,  $D_t$ , and the intercept of the cumulant data provides the rotational diffusion coefficient  $D_r$ . In our experiments, however we obtain  $D_r \approx 0$ , which is an unexpected result when the magnetic field is turned off. Furthermore, if this model were applicable then  $D_{eff}$  was expected to decrease monotonously with increasing scattering vector  $q$ . According to the experimental data, this is definitely not the case (see Figure 7.3). Therefore, translational and rotational diffusions cannot be assumed to be uncoupled. As expected, the chains undergo an anisotropic translation that gives rise to a coupling between translational and rotational modes [67].

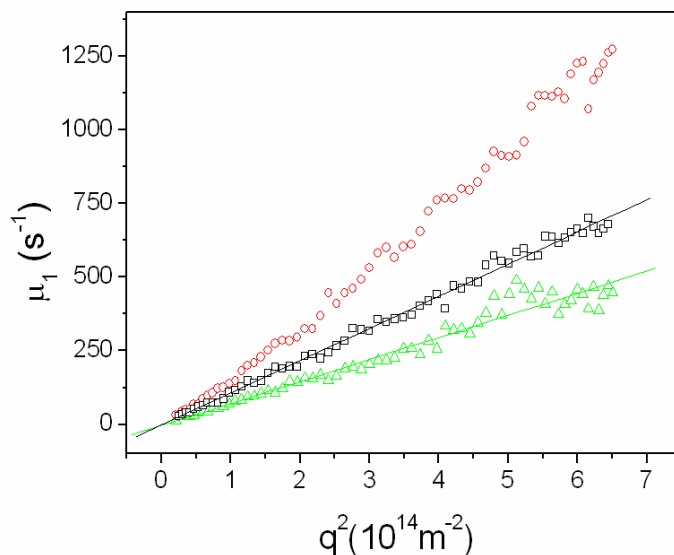


Figure 7.4: The cumulant  $\mu_1$  as a function of the square of the scattering vector  $q$ . The samples were aggregated at 20  $mM$ . The exposure times to the magnetic field were 5 min ( $\circ$ ), 10 min ( $\square$ ), and 20 min ( $\triangle$ ). The solid lines through the data show the corresponding linear fits.

### 7.2.3 Magnetic Chain Rupture

In the previous Section we have shown that the Maeda-Fujime model allows the mean particle chain length  $\langle N \rangle$  to be determined from the experimentally accessible average diffusion coefficient  $D_{eff}$ . Hence, we are now able to measure the filament length quantitatively by means of DLS, and to extract the average filament length, expressed in number of particles per aggregate  $N$ , from the measured effective diffusion coefficients. For this purpose, Equation 7.1 was used for zone *I*, whereas Equation 7.2 was employed for the calculations in zone *II*. Equations 2.37 and 2.38 were employed for the size dependency of the different diffusion coefficients involved  $D_{\perp}$ ,  $D_{\parallel}$ , and  $D_r$ . These equations read:

$$\begin{aligned} D_{\perp}(L) &= \frac{k_B T}{4\pi\eta L} \left( \ln\left(\frac{L}{2a}\right) + \gamma_{\perp}^{end}(L) \right) \\ D_{\parallel}(L) &= \frac{k_B T}{2\pi\eta L} \left( \ln\left(\frac{L}{2a}\right) + \gamma_{\parallel}^{end}(L) \right) \\ D_r(L) &= \frac{3k_B T}{\pi\eta L^3} \left( \ln\left(\frac{L}{2a}\right) + \gamma_r^{end}(L) \right). \end{aligned}$$

The results obtained are shown in Figure 7.5. At first sight, the data seem to resemble the behaviour determined already from Figure 7.1. Nevertheless, this is only correct for zone *I*. There, it can again be observed that the cluster growth rate rises for increasing electrolyte concentrations but now, an almost linear increase with time is observed for the average chain length at all electrolyte concentrations. Only the electrolyte free sample remains stable. In zone *II*, however, three different behaviours may now clearly be distinguished:

1. At electrolyte concentrations of less than 5 *mM*, the linear aggregates formed are not able to survive the absence of the magnetic field. This means that the repulsive electrostatic interactions are strong enough to avoid the formation of permanently bonded filaments. Nevertheless, reversible aggregation may still be possible but only in a shallow energy minimum that disappears once the magnetic field is turned off. Such a breaking behaviour is in good agreement with the super-paramagnetic character of the particles.
2. At intermediate electrolyte concentrations 5, 10, 20 and 25 *mM*, stable aggregates remain in the sample. Nevertheless, the average chain length

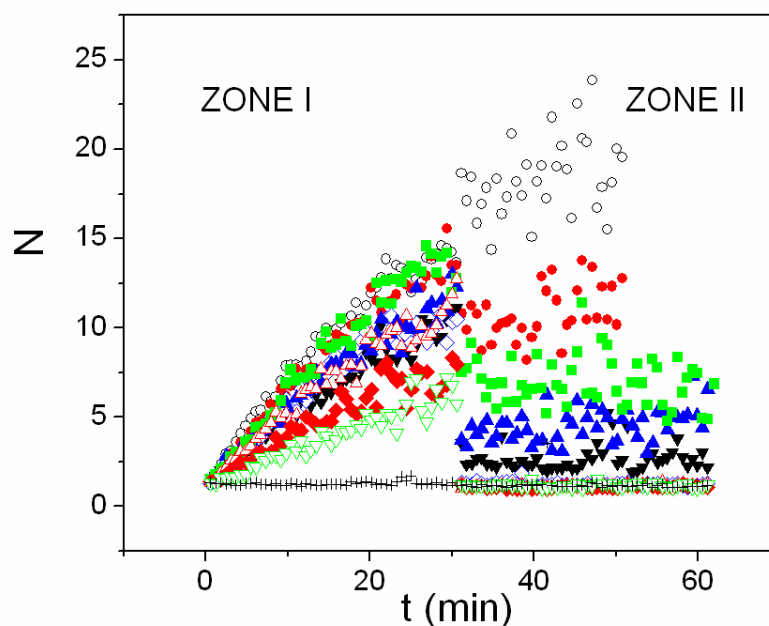


Figure 7.5: Time evolution of the average number of constituent particles per aggregate  $\langle N \rangle$  at electrolyte concentrations of (+) 0.0 mM, ( $\nabla$ ) 0.25 mM, ( $\blacklozenge$ ) 0.50 mM, ( $\blacktriangle$ ) 1.0 mM, ( $\blacklozenge$ ) 2.0 mM, ( $\blacktriangledown$ ) 5.0 mM, ( $\blacktriangle$ ) 10 mM, ( $\blacksquare$ ) 20 mM, ( $\bullet$ ) 25 mM and ( $\circ$ ) 50 mM.

decreases when the magnetic field is turned off. This implies that the chains formed disassemble only partially and so, stable bonds in a deeper primary energy minimum must exist. The theory of colloidal stability, predicts such a deep primary energy minimum at close contact due to attractive short range London-van der Waals forces. Nevertheless, the particles still have to overcome the relatively large energy barrier caused by the electrostatic repulsion before a stable bond is formed. Since the height of the energy barrier decreases for increasing electrolyte concentration, it is not surprising that the average length of the stable aggregates becomes larger at higher salt concentrations.

The coexistence of secondary and primary bonds can be directly observed by means of the Machine Force technique (please, see Section 5.2.3).

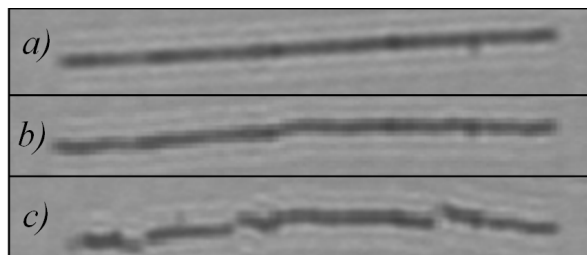


Figure 7.6: (a) Linear aggregates formed may be treated as rigid cylinders when the magnetic field is present. (b) At low magnetic field strengths, however, relative positional particle fluctuations inside the linear aggregates may take place due the competition between Brownian motion and magnetic dipole-dipole interactions. (c) At intermediate electrolyte concentrations some linear aggregates formed are able to survive the absence of the magnetic field. This implies that the chains formed disassemble only partially and so, stable bonds in a deeper primary energy minimum must exist.

As we have seen in Sections 2.7 and 3.7.2, field induced aggregation may occur in a primary minimum of energy, where the particles are in contact with each other, or in a secondary minimum of energy, where the neighbouring particles within the linear aggregates are a short distance apart from each other. In the latter case, the repulsive forces between the colloidal particles are balanced by the attractive magnetic forces. Hence, as soon as the magnetic field is applied, the mean distance between the aligned particles can be assessed by analyzing the Bragg scattering patterns (see Section 4.5.3). Figure 7.7 shows the spectral distribution of the scattered light at 0 *mM* and 20 *mM* *KBr* (Figures *a* and *b*, respectively). The measurements were performed using magnetic silica particles of 180 *nm* in size, synthesized by the Dr. El-Harrak, that were illuminated by a white light source. For 0 *mM* *KBr*, the observed spectral distributions only depicts an outstanding maximum at  $\lambda \approx 500$  *nm* (Figure 7.7 *a*). Hence, according to Equation 4.94

$$d = \frac{\lambda}{n(1 - \cos\theta)},$$

there is a preferential distance  $d$  between neighbouring particles aligned along the field direction which is approximately,  $d \approx 195$  *nm*. At 20

$mM$ , however, two smaller maxima are clearly observed in the spectral distribution (Figure 7.7 *b*). One of them corresponding to  $d \approx 195 \text{ nm}$ , and the other one corresponding to  $d \approx 180 \text{ nm}$ . Since there are two different maxima, there should be two preferential distances. Therefore, at  $20 \text{ mM}$  the field induced aggregation may occur in a primary or in a secondary minimum of energy, where the neighbouring particles are either in close contact or at a short distance, respectively.

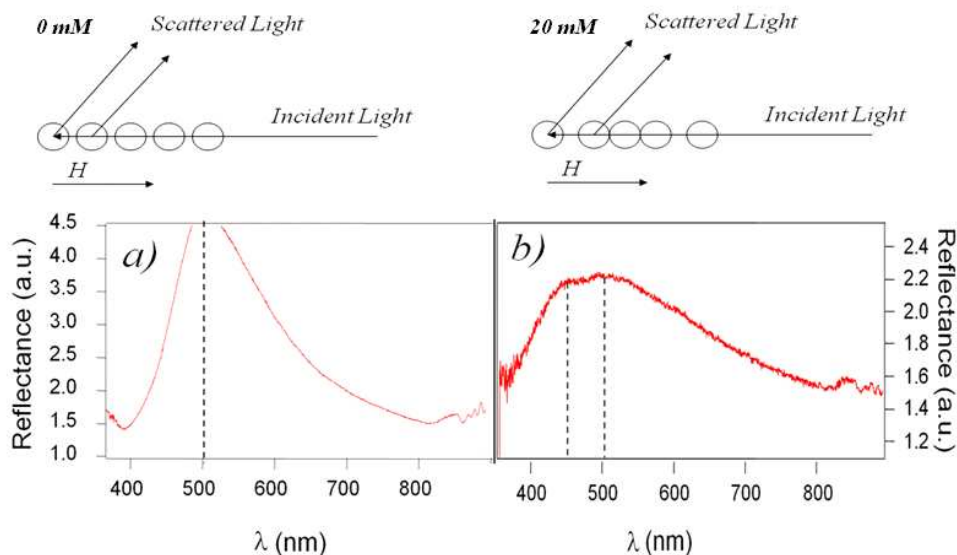


Figure 7.7: The spectral distribution at  $0 \text{ mM}$  (*a*), and at  $20 \text{ mM}$  *KBr* (*b*). The upper scheme shows that field induced aggregation may occur in a primary or in a secondary energy minimum, depending on the electrolyte concentration.

- At electrolyte concentrations of  $50 \text{ mM}$  or above, the magnetic filaments don't disassemble anymore and continue to grow even when the field is turned off. This means that the electrostatic energy barrier that prevented the particles from aggregation in the primary minimum is now almost completely suppressed and all the bonds are stable. It should be noted that linear aggregates will be formed when the field is present. When the field is turned off, however, the magnetic dipole-dipole interactions disappear and so, the linear chains that are already formed are expected to aggregate further following a reaction-diffusion aggregation

scheme. In this case fractal aggregates consisting of chain-like particles are expected (as we will see in Section 7.3.4).

It is quite instructive to point out that the jump observed in time evolution of the average diffusion coefficient at 50  $mM$  (Figure 7.1) is not reproduced in the corresponding cluster size curve shown in Figure 7.5. Hence, it is clear that this can not be caused by cluster break-up. The increased cluster diffusivity must be due to additional rotational diffusion that became possible once the field was turned off. Evidently such a conclusion could not have been drawn directly from the diffusion measurements [66].

Finally, we would like to mention that the linear aggregates formed are of course still quite polydisperse. The Figure 7.8 shows the time evolution of the polydispersity index (p.i.). The polydispersity index is a dimensionless parameter calculated from a cumulants analysis of the measured intensity autocorrelation function (Equation 4.80). It is used to characterize the relative shapes of the cluster-size distributions. For the electrolyte free sample (0  $mM$ ), aggregation is not observed and the polydispersity index remains constant with an average value of 0.08, close to the value measured before for pure monomeric samples. Roughly speaking, the p.i. becomes the larger the larger the mean length of the linear aggregates becomes. At low electrolyte concentrations (0.50  $mM$ ), field induced aggregation is reversible and the mean value of the p.i. returns to its initial value once the magnetic field is turned off.

The degree of monodispersity around a desired average size value might be improved if an accurate separation method could be found. In a not too far future, this could open an experimental way for assembling magnetic filaments of a well determined length by simply adjusting the strength of the magnetic field and the amount of such an added electrolyte. Evidently, further work on this subject is needed before this goal will be achieved [16, 17].

#### 7.2.4 Magnetic Chain Stability

In the former Section, we described how to determine the average chain length  $\langle N(t) \rangle$ . This allows us to monitor  $\langle N \rangle$  as a function of time. Taking into account that the mean number of bonds per chain  $\langle n(t) \rangle$  is given by  $\langle n(t) \rangle = \langle N(t) \rangle - 1$ , we can also assess the time evolution of  $\langle n(t) \rangle$ . If we compare the mean length of the linear aggregates measured just before and after of  $t_{rupture} = 30 \text{ min}$ , i.e. the moment when the magnetic field was turned off, we may also estimate the mean number of secondary bonds per chain that existed at that moment. All the parameters mentioned before are related by the following expression (please, see Figure 7.9)



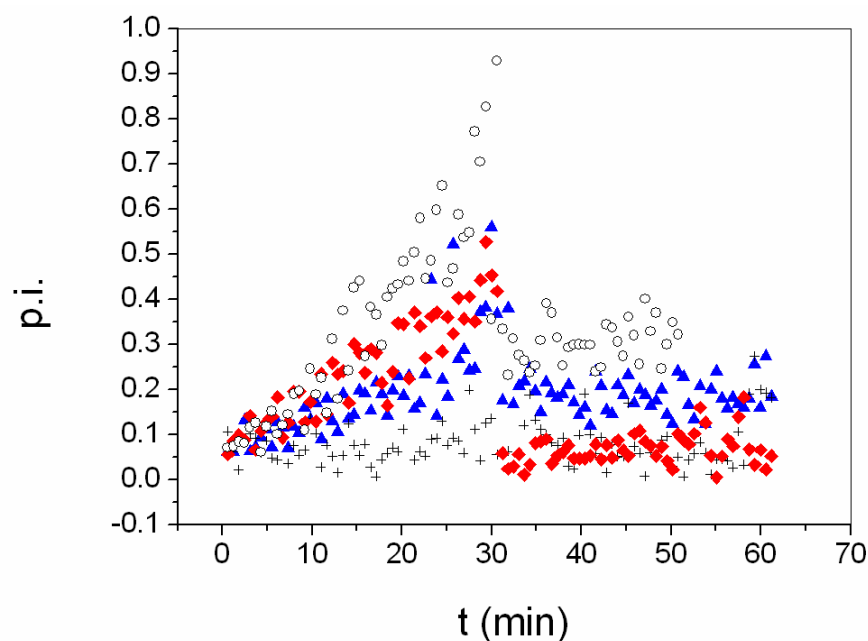


Figure 7.8: Time evolution of the polydispersity index (p.i.) at electrolyte concentrations of (+) 0.0 *mM*, (♦) 0.50 *mM*, (▲) 10 *mM*, and (○) 50 *mM*.

$$\langle N(30^+) \rangle = \frac{\langle N(30^-) \rangle}{\langle n_s(30^-) \rangle + 1}. \quad (7.3)$$

The mean number of particles constituting the linear aggregates just after the removal of the magnetic field,  $\langle N(30^+) \rangle$ , was assessed averaging the mean values measured when the magnetic field was turned off. At 50 *mM*, the chains continue aggregating even after removing the field, and so  $\langle N(30^+) \rangle$  had to be obtained by linear extrapolation of to the expected value at  $t_{rupture}$ . Similarly, the mean value of the number of particles per chain assessed just prior to removing the magnetic field,  $\langle N(30^-) \rangle$ , was calculated by linearly extrapolating from the values measured during the field induced aggregation process to the expected value at  $t_{rupture}$ . The values obtained at the different electrolyte concentrations used for this study are shown in Table 7.1. The table includes the mean number of bonds per chain just before turning off the magnetic field, and the percentage of meta-stable and stable bonds at this time. Figure 7.10 shows the dependence of the latter parameters as a function of the electrolyte concentration.

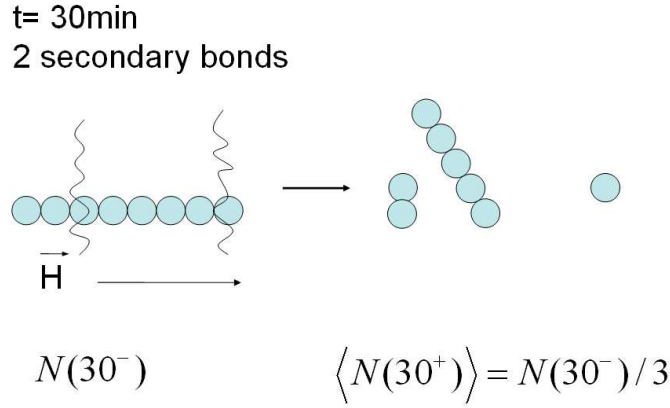


Figure 7.9: The mean length of the linear aggregates measured just prior to  $\langle N(30^-) \rangle$  and after  $\langle N(30^+) \rangle$  removing the magnetic field are directly related to mean number of secondary bonds per chain  $\langle n_s(30^-) \rangle$ .

On the other hand, the mean number of bonds per chain is given by  $\langle n(t) \rangle \approx \frac{n(t)}{N_{aggr}(t)}$ , where  $N_{aggr}(t) \approx \frac{N_0}{\langle N(t) \rangle}$  is the total number of aggregates present in the suspension, and  $N_0$  is the initial number of monomers dispersed throughout the solution. Thus, the total number of bonds is  $n(t) \approx \frac{N_0 \langle n(t) \rangle}{\langle N(t) \rangle} = \frac{N_0(\langle N(t) \rangle - 1)}{\langle N(t) \rangle}$ , and  $\frac{dn(t)}{dt} = -\frac{dn_f(t)}{dt} \approx -N_0 \frac{d\langle N(t) \rangle^{-1}}{dt}$ . Hence, the differential Equations given by 2.59 read:

$$\begin{aligned} \frac{dn_s}{dt} &= -N_0 \frac{d\langle N(t) \rangle^{-1}}{dt} - k_{sp} n_s(t) \\ \frac{dn_p}{dt} &= k_{sp} n_s(t). \end{aligned}$$

Experimentally, we have access to the initial particle concentration  $c_0$ . Hence, we can rewrite the previous Equation in terms of particles and bond concentrations  $[n(t)]$ ,  $[n_s(t)]$ , and  $[n_p(t)]$

$$\begin{aligned} \frac{d[n_s(t)]}{dt} &= -c_0 \frac{d\langle N(t) \rangle^{-1}}{dt} - k_{sp} [n_s(t)] \\ \frac{d[n_p(t)]}{dt} &= k_{sp} [n_s(t)] \end{aligned} \tag{7.4}$$

$[KBr]$	$\langle N(30^-) \rangle$	$\langle N(30^+) \rangle$	$\langle n_s(30^-) \rangle$	% secondary bonds	% primary bonds
50	15.2	16.9	0	0	100
25	14.3	9.7	0.5	3.6	96.4
20	14.1	7.3	0.9	7.1	92.9
10	12.0	3.8	2.2	19.6	80.4
5.0	10.6	2.4	3.3	33.5	66.5
2.0	10.3	1.3	6.9	73.8	26.2
1.0	11.4	1.1	9.7	92.8	7.2
0.50	7.8	1.1	6.5	95.6	5.4
0.25	6.2	0.9	5.9	100	0
0.0	1.3	1.2	0.0	0	0

Table 7.1: Different parameters assessed after 30 min of exposition to the magnetic field as a function of the electrolyte concentration  $KBr$ .

Under our experimental conditions, the concentration of metastable and stable bonds satisfies the boundary conditions  $[n_s(0)] = 0$  and  $[n_p(0)] = 0$  due to the imposed monomeric initial conditions at  $t = 0$  s. Due to the long range of the attractive magnetic forces, the closer magnetic particles may aggregate almost immediately when the field is turned on. However, the initial dimensionless distance between the monomers,  $R_0 = \left(\frac{1}{\phi}\right)^{\frac{1}{3}} = 71$  is bigger than the dimensionless distance  $R_1 = \lambda^{\frac{1}{3}} = 6.5$ , i.e., the average threshold separation within which particle motion ceases to be random [36]. Therefore, the monomeric initial conditions can be ensured. The term  $\frac{d\langle N(t) \rangle^{-1}}{dt}$  has been assessed by fitting an arbitrary exponential decay function  $Ae^{-Bt}$  to the experimental values previously obtained. The fitting process was done for all the electrolyte concentrations employed during the field induced aggregation process, as is shown in Figure 7.11.

Finally, the concentration of primary and secondary mentioned bonds,  $[n_s(30)]$  and  $[n_p(30)]$ , can be calculated by solving the previous differential equations (Equation 7.4). Here the only fitting parameters are the exposure time to the magnetic field  $t$  and the rate constant  $k_{sp}$ . Hence, keeping constant one of the two parameters we can assess the remaining free parameter comparing the theoretical predictions with the experimental results. Firstly, the exposure time to the magnetic field,  $t_{rupture} = 30$  min, is kept constant in our case. From the percentage of the existing secondary and primary bonds

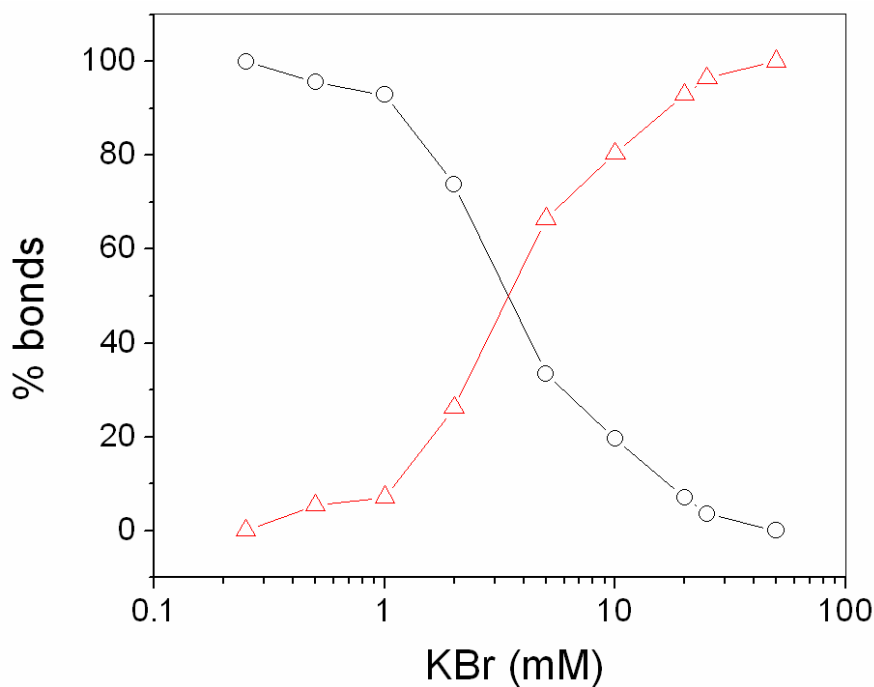


Figure 7.10: Percentage of meta-stable (○) and stable bonds (△) assessed after 30 min of exposition to the magnetic field as function of the electrolyte concentration  $KBr$ .

we can assess the  $k_{sp}$  values at different electrolyte concentrations. The results are shown in Figure 7.12.

In the case of "barrierless" field induced reactions, observed at 50  $mM$ , all the magnetic particles form stable bonds during the aggregation process. Therefore, the stable chains aggregate following a field-induced diffusion-limited scheme, and the time evolution of the stable bonds may be reproduced quite satisfactorily by the corresponding solutions of the Smoluchowski equation<sup>1</sup>. At electrolyte concentrations lower than 0.5  $mM$  the particles disassemble completely. In this case the exposure time to the magnetic field is not long enough to form stable bonds due to the relatively large height of the energy barrier.

The previously estimated rate constants  $k_{sp}$  assess the formation frequency of primary bonds through secondary bonds. They must be independent on

<sup>1</sup>Further details about the Smoluchowski treatment can be found in Chapter 6.

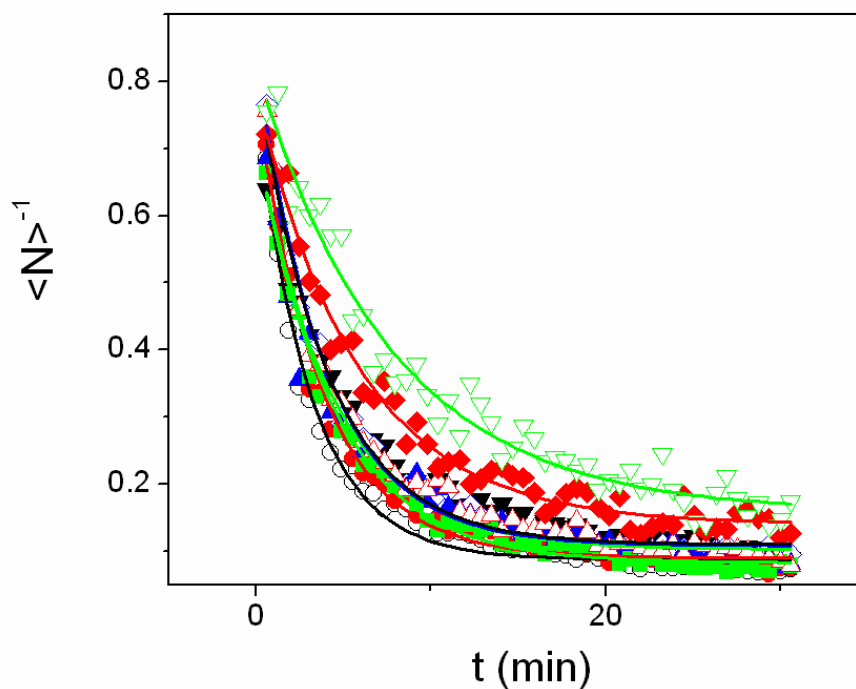


Figure 7.11: Experimental  $\langle N(t) \rangle^{-1}$  fitted by an arbitrary exponential decay function  $Ae^{-Bt}$ . The fitting process was done for all the electrolyte concentrations employed during the field induced aggregation process: (+) 0.0 mM, ( $\nabla$ ) 0.25 mM, ( $\blacklozenge$ ) 0.50 mM, ( $\triangleleft$ ) 1.0 mM, ( $\diamond$ ) 2.0 mM, ( $\blacktriangledown$ ) 5.0 mM, ( $\blacktriangleleft$ ) 10 mM, ( $\blacksquare$ ) 20 mM, ( $\bullet$ ) 25 mM and ( $\circ$ ) 50 mM.

the exposure time to the magnetic field. Hence, we should be able to predict theoretically the degree of rupture at different incubation times if we resolve the differential Equations 7.4 using the previously obtained rate constants. We compared the theoretical predictions with the experimental results by following similar methods to the previously described. We kept the electrolyte concentration constant at 5 mM (corresponding to  $k_{sp} = 7.8 \times 10^{-4} s^{-1}$ ), and varied the exposure times to the external magnetic field. The exposure times to the magnetic field were 10, 20, 30, 40, 50 and 60 min (Figure 7.13). Analogously to the previous calculations, we can assess the time evolution of the mean number of primary and secondary bonds per chain at different exposure times to the magnetic field by comparing the mean size of the chains just after and before the removal of the magnetic field. The theoretical calculations and

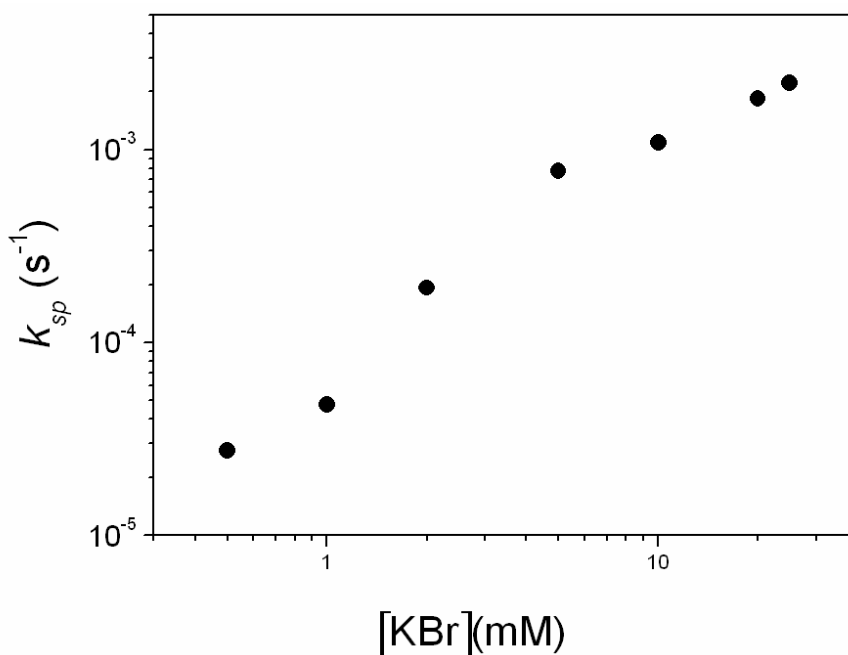


Figure 7.12:  $k_{sp}$  as a function of the electrolyte concentration.

the experimental results are compared and shown in Figure 7.14. The theoretical predictions reproduce the measured time evolution of the percentage of secondary and primary bonds quite satisfactorily. The results prove that, at a given magnetic field strength, electrolyte concentration and exposure time, the mean value of the formed bonds can be predicted. Hence, tuning the relative strength of the magnetic and electric interactions allows the mean length of the linear aggregates be controlled at different exposure times to the magnetic field.

Finally we have assessed the energy barrier  $E_a$  using the Equation 2.60 that reads:

$$k_{sp} = \tau_0^{-1} \exp\left(-\frac{E_a}{k_B T}\right).$$

In the calculations, we have used the attempt frequency  $\tau_0^{-1}$  estimated by Cohen et al.. In their work the attempt frequency was theoretically estimated according to Kramers' theory, and experimentally assessed by studying the de-

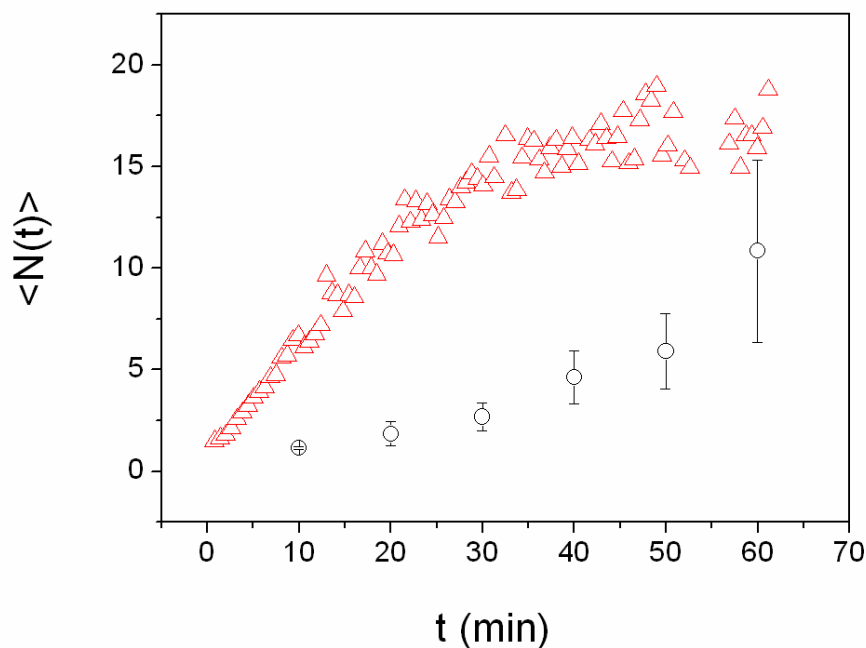


Figure 7.13: Time evolution of the mean number of particles per chain  $\langle N \rangle$  at 5  $mM$  ( $\Delta$ ). The mean chain length  $\langle N \rangle$  was also measured, at different exposure times to the magnetic field, once the field is turned off ( $\circ$ ).

pendence of  $k_{sp}$  with  $T$  [20]. The authors worked with calibrated 800 nm emulsion droplets of an organic ferrofluid in water. They found approximately  $\tau_0^{-1} \approx 10^5 s^{-1}$  as order of magnitude. Figure 7.15 shows how  $E_a$  decreases when the electrolyte concentration increases. If we compare the energy  $E_a$  with the height of the energy predicted by the extended DLVO theory, we find that the latter barriers heights are much higher. Similar discrepancies have been reported by Tannoudji et al. , when these authors studied the van der Waals adhesion of field induced linear aggregates.

### 7.3 Aggregate Morphology

In this Section we will comment on the three dimensional structure of the chainlike aggregates formed by aggregation. Therefore, we measured the aggregate fractal dimension of the samples aggregated. SLS data will be employed to confirm the linear character of filaments and to study chain defor-

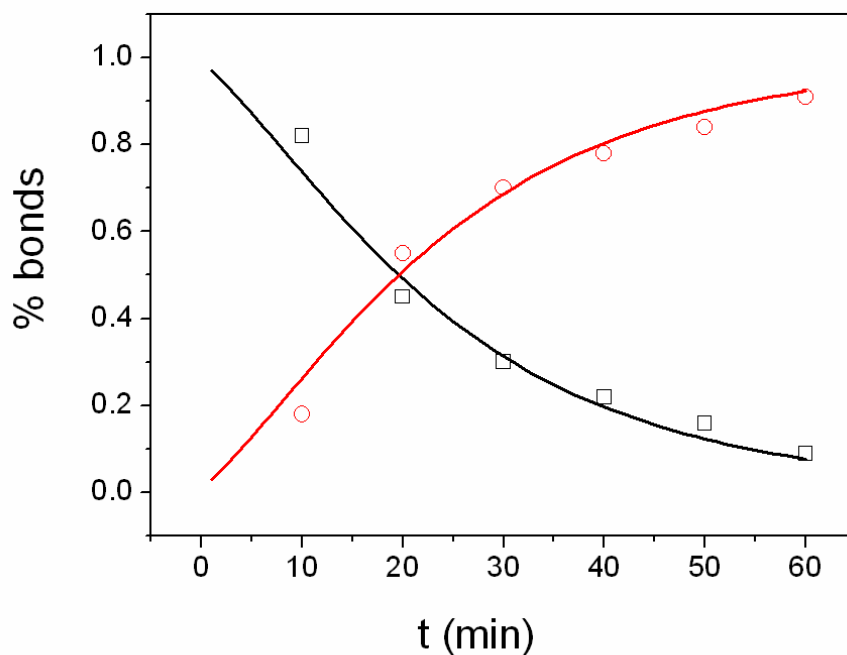


Figure 7.14: Percentage of meta-stable (□) and stable bonds (○) assessed at 5 *mM* *KBr* as a function of the exposure time to the magnetic field.

mation due to the interaction with the surrounding medium. The results will be corroborated by TEM images.

### 7.3.1 Particle Form Factor

Our analysis of the structure of the field induced aggregates starts checking to which extent the mean intensity of the light scattered by our colloidal particles is affected by the increased magnetic permeability and the light adsorption caused by the magnetic grains embedded in the polystyrene matrix. For this purpose, the  $I(q)$  curve was measured for a stable sample. Figure 7.16 shows the obtained results. When the particles are distributed at random this curve gives simply the form factor  $P(q)$  of the individual particles (Equation 4.88).



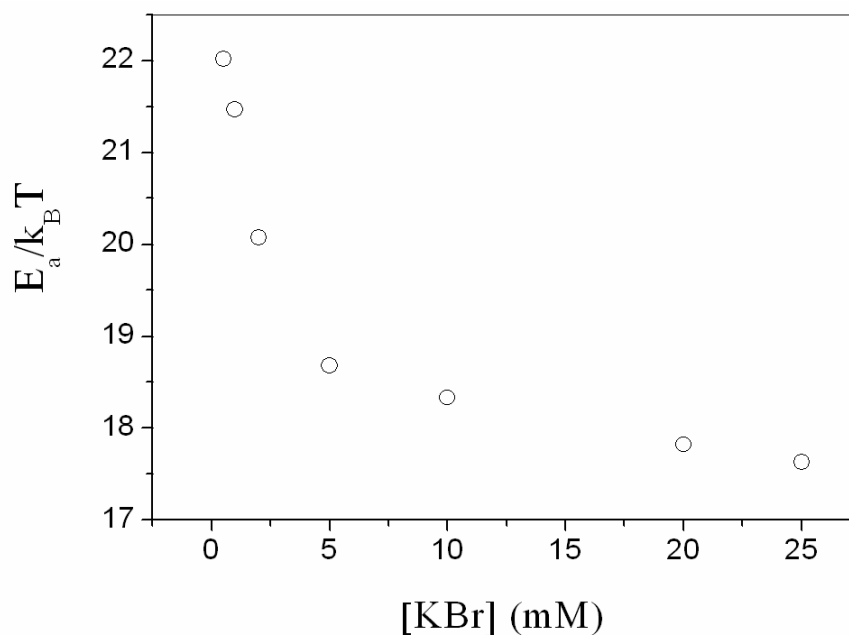


Figure 7.15: Energy barrier height  $E_a$  normalized by the thermal energy as a function of the electrolyte concentration.

The Mie theory has been employed for calculating the theoretical form factor for pure polystyrene latex particles (Equations 4.64-4.69) without any magnetic content. A sphere diameter of  $165 \text{ nm}$ , a relative refractive index of  $n = 1.12$  corresponding to polystyrene in water, and a relative permeability  $\mu = 1.0$  were used for the calculations. Although neither the magnetic character of the particles nor light absorption was considered in the Mie equations the obtained curve agrees quite well with the experimental data for the magnetic polystyrene particles (see Figure 7.16). This suggests that the polydispersity of this sample is low and no evidence of aggregation is found. Furthermore it is possible to assume, at least from an experimental point of view, that light absorption and an increased magnetic permeability do not significantly alter the scattered light intensity at the employed wavelength and particle concentration.

Although the Rayleigh-Gans-Debye scattering theory seems to be of quite limited validity, Equation 4.58 also fit the scattering data of the polystyrene magnetic particles (see Figure 7.16). In this case we used the particle diameter as fitting parameter, obtaining  $d = 170 \text{ nm}$ . The observed result is quite

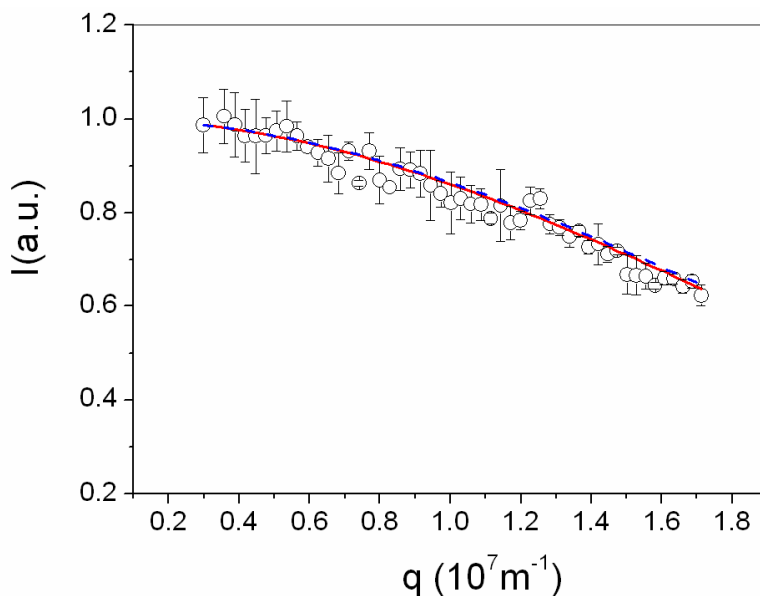


Figure 7.16: Normalized  $I(q)$  curve for a stable sample of super-paramagnetic particle suspension. The experimental data are shown as points (o). The continuous curve (—) was calculated according to Mie's theory for polystyrene particles of the same size without any magnetic content. The dashed line (--) was calculated according to RGD theory.

significant, since the previously employed Maeda's model implicitly assumes the RGD theory to be valid and so, restricts the theory to thin rods<sup>2</sup>.

### 7.3.2 Structure of Electrolyte Induced Aggregates

After having checked that the particles scatter light approximately like model polystyrene particles, we will now prove that neither the magnetic content nor the relatively high density of the particles affect the SLS measurements of the fractal dimensions. For this purpose, we measured the fractal dimension of aggregates formed by pure electrolyte induced aggregation. Figure 7.17 shows the aggregate structure factor  $S(q)$  determined as  $I(q)/P(q)$  for two samples that were aggregated at 1.0 M and 0.1M KBr in the absence of any applied magnetic field. From these curves, the aggregate fractal dimension

<sup>2</sup>The thickness of the rod should be negligible if compared with the wavelength of the incident light (see Section 4.4.2).

was obtained by means of Equation 4.92 that reads

$$S(q) \propto q^{-d_f}.$$

At high electrolyte concentration, a fractal dimension of  $(1.78 \pm 0.05)$  was found. This result is very close to the well-known value of 1.75 that is frequently reported in the literature for freely diffusing sticky particles. The fractal dimension obtained at low electrolyte concentration was  $(2.09 \pm 0.05)$ . A fractal dimension of approximately 2.1 is usually observed when the particles have to overcome a high potential barrier before aggregation [28, 78]. Hence, our magnetic particles behave just like standard latex particles when no magnetic field is applied. At high electrolyte concentration, they aggregate in the well-established aggregation regime of diffusion limited cluster aggregation (DLCA). At lower electrolyte concentrations, they come close to a reaction limited cluster aggregation (RLCA)-like scheme. Consequently, the aggregation behaviour of the particles is completely controlled by the isotropic electrostatic and van der Waals interactions (see Section 3.1). In accordance with the superparamagnetic character of the particles, a possible influence of anisotropic magnetic interactions is not observed in absence of the field. Having shown that our magnetic polystyrene particles behave as standard latex samples when aggregation is induced by surface charge screening, we are now able to investigate their aggregation behaviour when they are exposed to an external magnetic field.

### 7.3.3 TEM Micrographs

Before studying the geometry of the field induced aggregates quantitatively, it will be quite elucidating to discuss some transmission electron microscopy TEM images taken of several aggregated samples. In order to study also the influence of the relative strength of the isotropic electric and the anisotropic magnetic interactions, different electrolyte concentrations were used. Figures 7.2 and 7.18 show TEM micrographs of samples aggregated at a *KBr* concentration of 20 and 0 *mM*, respectively. In both cases, aggregation was induced only by the applied magnetic field since an electrolyte concentration of 20 *mM KBr* or less has proven to be insufficient for destabilizing the samples. The field strength of the homogeneous magnetic field was measured to be  $(411 \pm 2)$  *mT*. As can be seen, chainlike aggregates are observed in all the micrographs. This means that the bonds in these aggregates are strong enough to withstand not only the absence of the magnetic field but also the drying step that

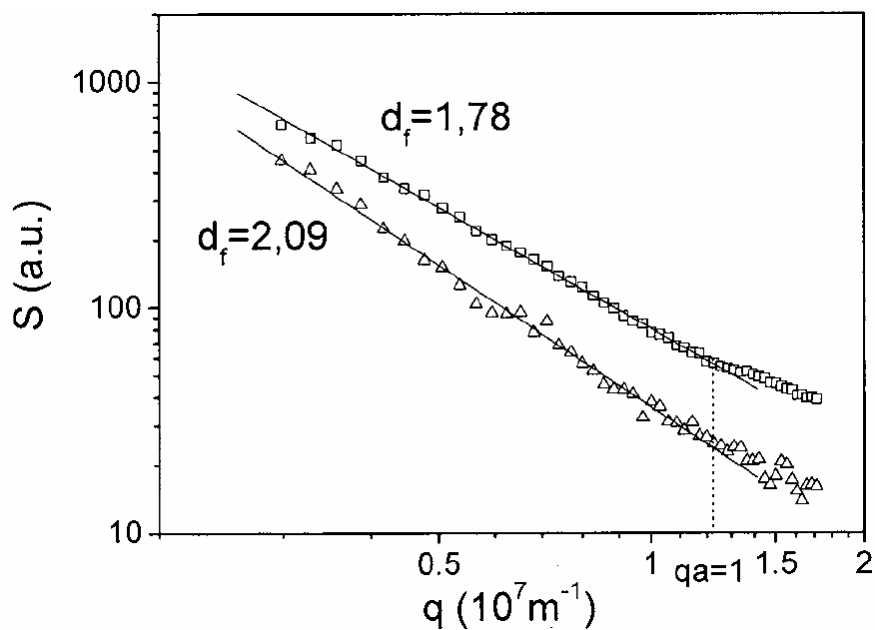


Figure 7.17: Structure factor  $S(q)$  of the samples aggregated at 0.1 M ( $\Delta$ ) and 1.0 M ( $\square$ ) of  $KBr$  electrolyte in absence of applied magnetic field. The continuous lines show the best fits according to Equation 4.92.

is necessary for taking TEM images. The effect of the exposure time to the magnetic field can be observed in the series of micrographs shown in Figure 7.2. As expected, the chains become the larger the longer the samples remain under the influence of the magnetic field. It can also be observed that the smaller aggregates have a relatively straight and linear form, while the larger aggregates seem to be more flexible since they look more bended and twisted.

It is also quite remarkable that a relatively large fraction of free monomeric particles is left over in the electrolyte-free sample, while almost all the particles are forming clusters in the presence of 20 mM  $KBr$ . Hence, electrolyte addition seems to improve chain formation in a sense that it allows a greater fraction of particles to participate in the aggregation process. From here in advance, we will refer to the phenomenon that some particles do take part in the aggregation process while others do not as “selective aggregation.” Hence, an interesting question emerges from these images: why some particles do take part in the aggregation process while others do not? Evidently, selective aggregation can only occur when the particles are not completely identical.

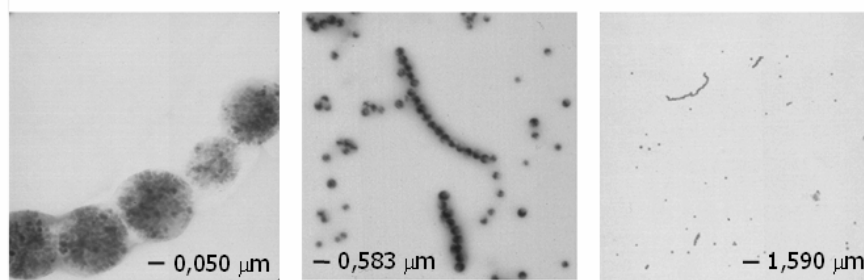


Figure 7.18: Transmission electron microscopy images of different samples aggregated in the presence of an applied magnetic field at 0 *mM* *KBr*.

Figure 7.18 shows the aggregated electrolyte-free sample in a smaller scale in order to check for visible differences between the chain forming particles and the free monomers. Smaller and larger particles with different magnetic contents can be distinguished. Consequently, differences in particle size and magnetic contents can be excluded as a cause for selective aggregate growth in the electrolyte-free sample. Since the degree of selective aggregation was found to depend mainly on the amount of added electrolyte, the origin of selective aggregation seems to be of electric nature [67].

We will try to give an at least qualitative explanation for this behaviour in the frame of the DLVO theory. Therefore, we determined the total particle–particle interaction energy in the presence of an external magnetic field when no electrolyte was added. The magnetic energy produced by interactions between the magnetic dipoles induced in the particles is also included. It is, however, not straightforward to determine the effective magnetic moment of the particles since neither the spatial distribution nor the orientation of the magnetic moments of the ferrite grains contained in the polystyrene particles are known. This problem is usually dealt with by assuming that two particles interact as if their net magnetic moment  $\vec{m}$  were located at the particle centre. The general expression for the effective magnetic moment of the particles is given by  $m = (4/3)^3 M$ . The magnetization,  $M$ , is defined as a function of effective magnetic susceptibility  $M = \chi H$  for not too high field strength. The linear aggregates shown in the TEM pictures were achieved by applying magnetic field is of the order of 400 *mT*. This means that the superparamagnetic particles have also reached their saturation magnetization and the effective magnetic moment of the particles can be calculated using the saturation magnetization given by the magnetization curve (Figure 5.2). The total interaction

energy is calculated supposing that these magnetic moments are located at the particle centre. The obtained energy curve shows a deep primary minimum at short distance and a shallower secondary minimum at further distance separated by an energy barrier. According to the superparamagnetic character of the particles, the secondary minimum will disappear when the field is turned off and the electrostatic repulsion controls the stability of the system, as it can be seen in Figure 7.19.

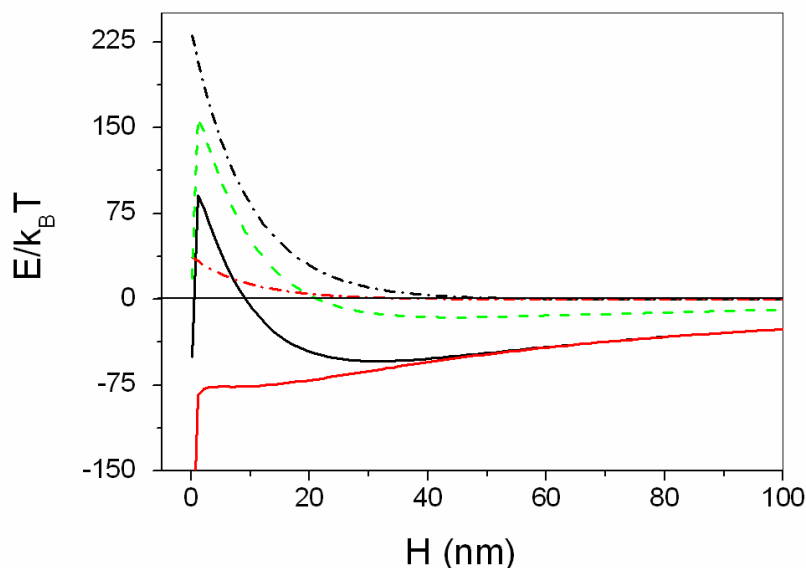


Figure 7.19: Electrostatic repulsion between magnetic particles: when the surface potential of the EDLMP is 50mV (dashed-dotted line  $-\cdot-$ ), when the surface potential of the EDLMP is reduced to 20mV (dashed-dotted line  $-\cdot-$ ). Total particle-particle interaction energy  $E(r)$  for the magnetic polystyrene particles when the magnetic grains are randomly distributed through the particle volume (dashed line  $- -$ ); when the total magnetization is located at the particle centre (continuous line  $-$ ), and the surface potential of the EDLMP is reduced to 20mV (continuous line  $-$ ).

Therefore, the particle chains should break apart if the particles had aggregated in the secondary minimum. However, TEM images show clearly that some of the chains do not break and, so, aggregation in the primary energy

minimum is needed to explain these experimental findings. Only at close contact the short range attractive van der Waals interaction is capable to keep the particles together once the external field has been turned off. Trying to overcome these difficulties, we have developed a more realistic way to calculate the magnetic interaction which uses the direct grain–grain magnetic interactions (Section 2.6.2).

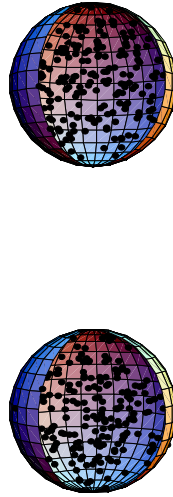


Figure 7.20: Pair of particles containing magnetic grains that are randomly distributed within the spherical particle volumes.

For model calculations we consider the ferrite grains of  $10\text{ nm}$  in size randomly distributed within a spherical particle volume (see Figure 7.20). Due to their small diameter, the grains are magnetic monodomains which have a magnetic moment of  $m = (4/3)\pi a^3 M_s$ . At the employed field strength, the magnetic grains have reached the magnetic saturation. The saturation magnetization of the magnetic grains  $M_s = 312\text{ (kA/m)}$  is lower than the saturation magnetization of bulk magnetite  $M_s = 470\text{ (kA/m)}$  due to surface effects [140]. The small ferrite grains have a superparamagnetic behaviour, and the magnetic moment of each ferrite grain within the polystyrene matrix points along the easy magnetization axis, which is randomly oriented. As an approach which overestimate the magnetic energy of interaction between polystyrene particles, we will assume that all the dipoles of the magnetic grains are aligned along the direction of the external magnetic field, even though their easy magnetization axis were randomly oriented. The employed grain number of  $N \approx 500$

is estimated using the ferrite mass content given by the manufacturer and the former mean grain size. Figure 7.19 shows a typical total interaction energy curve calculated with the proposed method, when a particular random grain distribution is employed. We obtained very similar results when the interaction energy was calculated either by using random distributions of grains inside the particles or when it was calculated supposing that all the grains were placed in the centre of the particles, and similar energy curves are obtained if we change the number of magnetic grains, the mean size of the grains, the particles size, or the value of the magnetic moments. All the obtained energy curves show a deep primary minimum at short distance and a shallower secondary minimum at further distance separated by an energy barrier. The comparison between these energy curves shown in Figure 7.19, and the energy curve which is obtained through the simpler previous model, reveals that the same behaviour is obtained and only a small shift towards a less or a more attractive interaction between the particles is found. The particles aggregate again in the secondary minimum, and the model is not able to explain the presence of the permanent chains. Therefore, considering a homogeneous spatial distribution of the grains in the calculations does not improve the explanation of the experimental findings.

As it is well-known in “classical” colloidal aggregation, the energy barrier between the primary and the secondary minimum is mainly controlled by the electrostatic repulsion. In this way, aggregation in the primary minimum would be found when the surface potential of the particles decreases. Figure 7.19 shows the resulting curve when the Stern potential of the magnetic particles is reduced to 20 *mV*. Clearly, aggregation in the primary minimum is now allowed. So, we have to suppose that in certain cases, the energy barrier between the magnetic particles can be reduced. In order to explain why only some particles participate in the formation of permanent chain-like aggregates as TEM images reveal, we should ask ourselves about the possible causes of the decrease in the electrostatic particle repulsions. The extended DLVO theory justifies, at least qualitatively, the experimental results. However, irreversible aggregation in a primary energy minimum is needed in order to explain the presence of chain-like aggregates once the magnetic field is turned off. The height of the energy barrier between the secondary and primary minima is mainly determined by the electrostatic repulsion. In this way, the selective field induced irreversible aggregation observed in the TEM images can only be explained if some kind of polydispersity in the charge of the particles is considered [68].



### 7.3.4 Structure of Field Induced Aggregates

The fractal dimension of the permanent chains was measured at 20 *mM* by means of SLS. We choose this electrolyte concentration because, as we have shown, there are no free monomeric particles left in the sample at this electrolyte concentration, and so all the scattered light proceeds from aggregates.

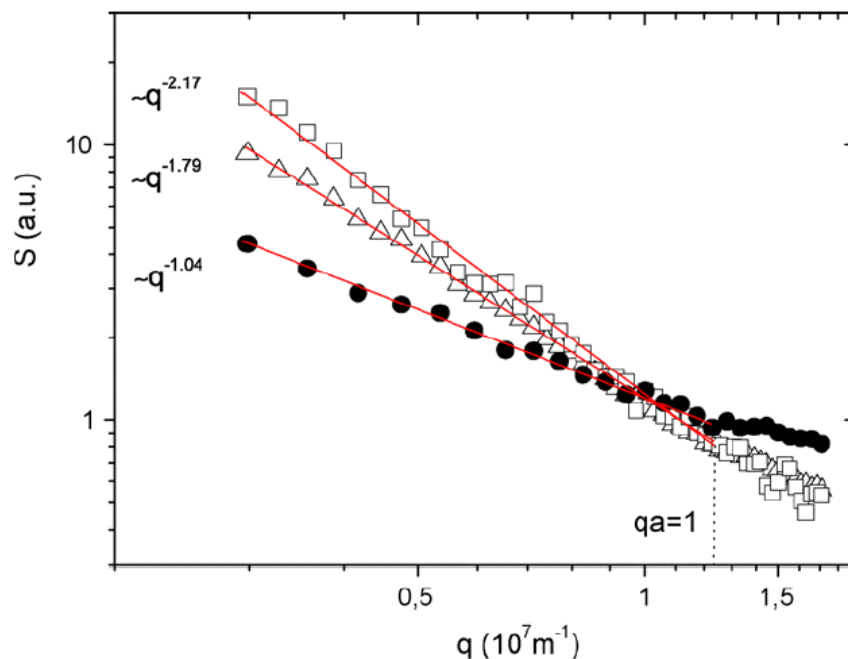


Figure 7.21: Structure factor versus scattering vector for the polystyrene particles aggregated under three different experimental conditions: in the presence of a magnetic field ( $\bullet$ ), in absence of a magnetic field at 0.01 *M NaCl* ( $\square$ ) and at 1.0 *M NaCl* ( $\Delta$ ).

Figure 7.21 shows the  $S(q)$  curves for the polystyrene particles and magnetite aggregated under three different experimental conditions. All the curves exhibit a linear behaviour in the scattering wave vector range  $R_h^{-1} < q < a^{-1}$  (indicated in the plots by a vertical line), and so, the cluster fractal dimension  $d_f$  can be determined from the slope in all cases. The given values are the average of six measurements with a linear regression coefficient of at least 0.99. At high electrolyte concentration, a fractal dimensions of  $(1.79 \pm 0.05)$  was found for the magnetic polystyrene particles. The fractal dimension deter-

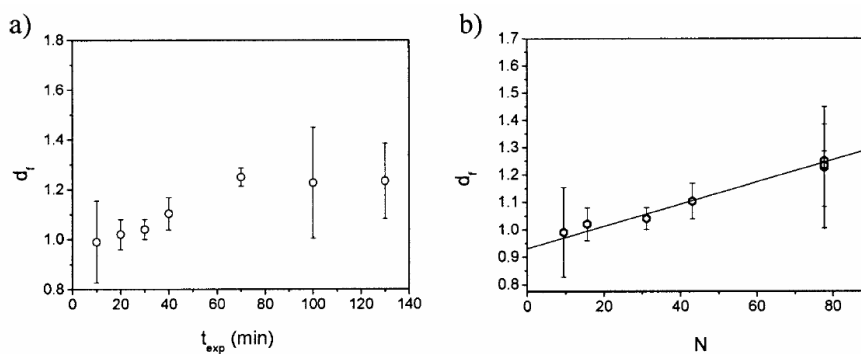


Figure 7.22: (a) Fractal dimension of the aggregates as a function of the exposure time to the magnetic field. The electrolyte concentration in the samples was 20  $mM$  in order to ensure that all the particles participate in the chain formation. (b) The same data plotted as function of the number of particles per aggregate. The continuous line shows the best linear fit.

mined at low electrolyte concentration was  $(2.17 \pm 0.05)$ . The error intervals given are the corresponding standard deviations. In both cases, the aggregation behaviour is controlled by the isotropic electrostatic and van der Waals interactions. However, the main interest of this Section lies in the aggregation taking place under the action of the anisotropic magnetic interaction. Linear aggregates were achieved by applying magnetic field of the order of 400  $mT$ . In this case, a very low fractal dimension of  $(1.04 \pm 0.14)$  has been found for the magnetic polystyrene particles. It should be emphasized that the scattered intensity curves were always measured after the external magnetic fields was applied and once the field was turned off. In this case, some minor spatial reorganization of the particles contained within the chain-like aggregates may be possible.

Figure 7.22 (a) shows the aggregate fractal dimension  $d_f$  as a function of the exposure time to the magnetic field. At short exposure times, fractal dimensions close to unity are observed. This means that the short chains are relatively stiff since they remain linear even when the field is removed. For longer exposure time, however, the fractal dimension increases monotonously and reaches a final value of  $d_f = 1.24 \pm 0.04$ . The slightly higher fractal dimension observed for the larger clusters indicates that these aggregates have lost part of their linear structure after having been taken out of the magnet. According to the results reported in the literature, they should be more flexible

and more susceptible to bending caused by the surrounding fluid [69]. In Figure 7.22 (b), we plot the aggregate fractal dimension as a function of the average chain length. A linear dependence between the chain length and the fractal dimension is observed. The equation of the best linear fit is  $d_f(N) = 0.004N + 0.97$ . It should be emphasized that similar fractal dimensions were reported by other authors for magnetic liposomes [141], magnetite particles coated by two layers of different surfactants [142], and simulations [133, 143]. We interpret the experimentally obtained fractal dimensions close to 1.2 as a result of linear but somewhat bended structures present in the sample [67].

At very high electrolyte concentration, the electrostatic repulsion between the particles is completely overcome by the magnetic interaction when the magnetic field is present (i.e. during the first 30 minutes of the experiments). Therefore, the growth behaviour follows the same tendency already observed for 50 *mM*. At this electrolyte concentration, the system remains almost stable when the linear aggregates are not exposed to the magnetic field. At higher electrolyte concentrations, however, the linear aggregates formed under the action of the external magnetic field continue to aggregate even when the magnetic field is turned off. Due to the super-paramagnetic character of the magnetic colloidal particles, the dipole-dipole interaction between the particles disappears once the magnetic field is turned off. Then, the linear chains formed are expected to aggregate further following a reaction or diffusion limited aggregation scheme. In this case, fractal aggregates made of chain-like aggregates were in fact observed. Figure 7.23 shows the fractal dimension of the clusters as function of the time spent once the magnetic field is switched off. As before, the fractal dimensions were measured by SLS as a function of the time. The electrolyte concentration employed was 1.0 *M*. As can be seen, the linear clusters continue to aggregate forming more and more branched structures.

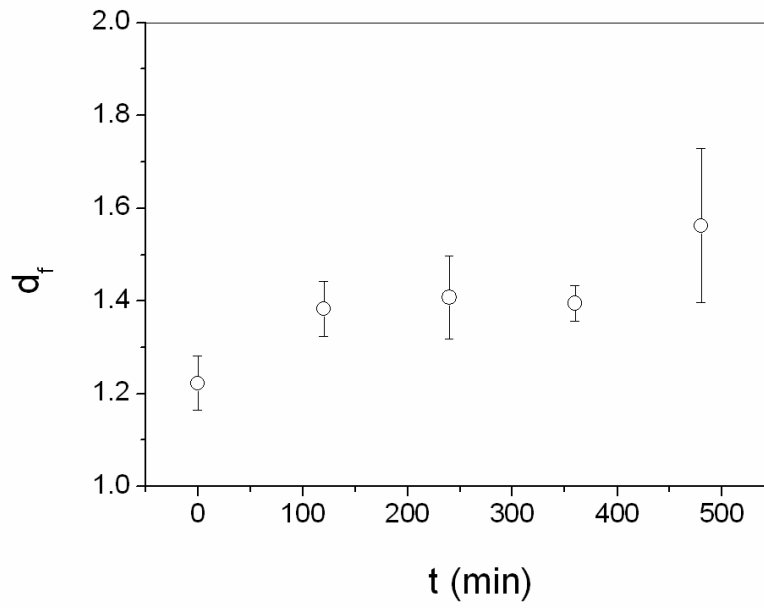


Figure 7.23: Fractal dimension as a function of the time. The linear aggregates continue to aggregate forming more and more branched clusters.



## Chapter 8

# Summary and Conclusions

*Una cosa terrible, contra muchas ventajas, tiene el aumento de la cultura por especialización de la ciencia: que nadie sabe ya lo que se sabe, aunque sepamos todos que de todo hay quien sepa. La conciencia de esto nos obliga al silencio o nos convierte en pedantes, en hombres que hablan, sin saber lo que dicen, de lo que otros saben. Así, la suma de saberes, aunque no sea en totalidad poseída por nadie, aumenta en todos y en cada uno, abrumadoramente, el volumen de la conciencia de la propia ignorancia.*

Antonio Machado, de Juan de Mairena.

Magnetorheological fluids are colloidal dispersions of magnetic particles that present a dipolar interaction when an external magnetic field is applied. The main aim of this Thesis has been to perform an analysis of the aggregation processes arising in these fluids in the presence of a constant and uniaxial magnetic field. Optical videomicroscopy, transmission electron microscopy, and light scattering techniques have been used for studying the morphology, the cluster size distributions, and the average size of the filaments formed. Hence, the influences of different phenomena such as sedimentation effects, electrostatic inter-particle interactions, or the strength of the applied field, have been theoretically studied. For that purpose, we have derived an aggregation kernel which depends explicitly on the average range of the interactions between the

colloidal particles. Finally, the experimental results have been compared with the theoretical predictions.

Usually, the field induced aggregation is reversible, i.e., the magnetic particles return to their original freely monomeric state once the magnetic field is removed. However, if the bonds between the magnetic particles are reinforced by additional linking mechanisms then linear structures able to withstand the field absence are formed. The morphology and the stability of such "permanent" chains were also studied.

## 8.1 Conclusions

### 8.1.1 Light Scattering

In this Thesis, the aggregation behaviour of diluted magnetic fluids has been monitored using non intrusive light scattering techniques. Unlike imaging techniques, light scattering techniques have an improved statistics and are performed faster. These advantages turn light scattering into a highly valuable technique for the development and standardization of materials made from magnetic filaments.

In our experiments the light was scattered by magnetic particles or linear aggregates. Hence, we paid special attention to the influence of the magnetic character of the colloidal particles, the effect of the uniaxial magnetic field, and the linear geometry of the aggregates on the light scattering experiments. All the light scattering results were obtained using small magnetic polystyrene particles of 170 *nm* in size. The main results are:

- In sufficiently dilute magnetic colloidal systems, and modelling the linear aggregates as cylindrical structures, light scattering measurements allow field induced aggregation process to be studied when an uniaxial magnetic field is present. The average filament length can be extracted from experimental DLS data by means of adequate theoretical models. These models account for internal positional fluctuations of the particles contained within the chains.
- Light scattering methods are also suitable for studying the fractal structure and stability of the permanent magnetic filaments. The average filament length can also be extracted from experimental DLS data by means of adequate theoretical models. These models account for the coupling between rotational and translational diffusive modes.

### 8.1.2 Kinetics of Field Induced Aggregation

We monitored the time evolution of the cluster size distribution and the average cluster size arising in aggregating magnetic particle dispersions. The experimental data were used for testing a new proposed aggregation kernel which is based on Smoluchowski's approach

$$k_{ij}^{Bdip} = 4\pi(1 - \cos\varphi_c)(\bar{D}_i + \bar{D}_j)(a_i + a_j + \bar{h}),$$

where  $\varphi_c$  is the aperture angle of the attractive region of the magnetic interactions. The aggregation kernel proposed should be understood as a mean field approximation based on effective quantities such as the effective interaction range  $\bar{h}$  and the effective diffusion coefficients  $\bar{D}_i$  and  $\bar{D}_j$ . It should be noted that the only one freely adjustable parameter is the effective interaction range  $\bar{h}$ . To the best of our knowledge, the previous Equation is the first analytical expression for an aggregation kernel for field induced aggregation process that is explicitly expressed in terms of physically meaningful quantities. Hence, we achieved to describe the effect of the electrostatic interaction between the magnetic particles, the sedimentation of the linear aggregates, or the mutual induction of the chain forming particles, theoretically in terms of an effective interaction range. The main results obtained on this subject were:

#### Kinetics

- The experimental results confirm that the average chain length increases monotonously with the exposure time to the external magnetic field. The time evolution of the average filament size was found to follow a power law with a kinetic parameter of  $z' = 0.66$ .
- Taking into account the anisotropic character of the field induced aggregation processes, we proposed an aggregation kernel that explicitly includes the range of the effective inter-particle interaction as a control parameter and so, depends implicitly on the strength of the applied magnetic field.

#### Magnetic Field Strength

- The strength of the applied magnetic field does not have any noticeable effect on the kinetic parameter  $z'$ . Hence, the aggregation mechanism seems to no depend on the intensity of the dipolar interactions. The



time evolution of the average filament size can be rescaled such that all the curves collapse on a single master curve.

- The cluster growth rates, however, depend on the strength of the magnetic field, i.e. on the range of the net interaction between the particles.
- The solutions of the Smoluchowski equation based on the proposed aggregation kernel, combined with theoretical models for diffusion and light scattering by rigid rods, reproduce the measured time evolution of the average perpendicular aggregate diffusion coefficient quite satisfactorily.

### Electrolyte Concentration

- Added electrolyte does not have any noticeable effect on the kinetic parameters  $z'$  and  $z$ . Hence, the aggregation mechanisms do not seem to depend on the electrolyte concentration. The time evolution of the average filament size can be rescaled such that all the curves collapse on a single master curve.
- The cluster growth rates, however, may depend on the amount of electrolyte added, i.e., on the range of the net interaction between the particles. In this case, the filament growth rate is monotonously related to the amount of electrolyte added.
- The solutions of the Smoluchowski equation based on the proposed aggregation kernel reproduce the experimental results quite satisfactorily.

### Sedimentation

- When we worked with larger magnetic particles the experimental results were fitted by theoretical predictions acceptably well only during the first aggregation stages. Hence, we proposed an additional term to the aggregation kernel that includes also sedimentation effects. In the new aggregation kernel, the effective range of the inter-particle interaction remains as the only control parameter. When sedimentation effects are taken into account, the fits improve especially at long aggregation times. Then, the kinetic exponent obtained from the fits ( $z = 0.77$ ) comes quite close to the experimentally observed value of  $z = 0.72$ .
- A relatively high value of  $z$  may be a sign of additional aggregation due to differential settling.

- The time evolution of the monomer concentration, however, could not be reproduced satisfactorily. A reason for this finding may be the relatively large uncertainties that are introduced when processing images of small particles. Other reasons, however, cannot be excluded.

### Mutual Induction

- The mutual induction within the chain-like aggregates has been theoretically modelled. Our model predicts an increase of the average particle interaction range with the aggregate size. However, this model fails to overcome the discrepancies previously observed between the time evolution of the monomer concentration and the theoretical predictions.

### 8.1.3 Stability of Magnetic Chains

The main aim of this part was twofold: On the one hand, to design an accurate experimental protocol that allows the final mean length of the linear aggregates to be controlled by tuning the different interparticle interactions. On the other hand, to show that the final filament size may be reliably monitored by light scattering techniques, when the filaments are either aligned due to the action of the magnetic field, or when they are freely diffusing. We found:

- At high enough electrolyte concentrations, stable linear aggregates remain in the sample once the magnetic field is turned off.
- Tuning the relative strength of the magnetic and electric interactions allows the mean length of the linear aggregates to be controlled at fixed exposure times to the magnetic field.
- Rate equations are proposed, which allow modeling the time evolution of the mean number of primary and secondary bonds per chain as a function of the exposure time.

### 8.1.4 Structure of Magnetic Chains

The microstructure of magnetorheological fluids plays a significant role for their bulk rheological properties, and evidently, an adequate description of the chain morphology is of practical importance for the control of technological applications. With regard to this topic, we obtained:

- Magnetic particles form standard fractal aggregates when aggregation is induced by surface charge screening only.

- The morphology of the permanent field induced aggregates is characterized by a fractal dimension close to unity. For large linear aggregates, however, the cluster fractal dimension increases to approximately 1.25. This increase is mainly a consequence of the higher degree of internal flexibility of the larger aggregates. These results have been corroborated qualitatively via transmission electron microscopy.
- At high electrolyte concentrations linear aggregates continue to grow when the magnetic field is turned off. More and more branched clusters are formed now.
- TEM images revealed that magnetic polystyrene particles aggregated at low and very low electrolyte concentrations contain a considerable amount of free monomeric particles. The phenomenon that only a fraction of monomeric particles participate in the permanent aggregation process was named "selective aggregation". According to the TEM micrographs, and theoretical energy curves, polydispersities in particle size and magnetic content could be excluded as a possible explanation for this behaviour. The experimental results indicated that the origin for selective aggregation is most likely to be of electric nature. The extended DLVO theory gives a qualitative explanation for the experimental findings.

## Chapter 9

# Resumen y Conclusiones

Los fluidos magneto-reológicos son dispersiones de nano-partículas magnéticas suspendidas en un fluido no magnético. Los momentos magnéticos de las partículas tienden a alinearse en la dirección del campo aplicado. Aparecen entonces fuerzas de naturaleza dipolar, atractivas en la dirección paralela al campo y repulsivas en dirección normal. Debido al carácter anisótropo de la interacción magnética, las partículas tienden a formar agregados lineales, paralelos a la dirección del campo magnético externo. Esto ocurre siempre que la interacción magnética sea lo suficientemente intensa como para superar a las interacciones que regulan la estabilidad de las partículas. Por otro lado, si existen ligaduras entre las partículas que constituyen estos agregados lineales, entonces algunas de estas estructuras lineales son "permanentes", es decir, que mantienen su geometría aun en ausencia del campo magnético externo.

La respuesta al campo externo de las partículas magnéticas, la geometría lineal de los agregados, y la posibilidad de controlar la longitud de los agregados permanentes a través del tiempo de exposición al campo magnético avalan el interés suscitado por estos sistemas y su uso en aplicaciones y en campos muy diferentes como en la separación celular magnética, la conducción de fármacos, sistemas de control sísmico, sistemas ópticos birrefringentes, como instrumentos adecuados para realizar mezclas a escala micrométrica, en el estudio de las propiedades elásticas de ligandos utilizados en el puenteo coloidal, etc. Sin embargo, hasta ahora sólo un número relativamente pequeño de estudios experimentales y de simulaciones se han centrado en el estudio de la formación de estos agregados lineales. Estos trabajos describen la cinética de la formación de agregados inducida por el campo aplicando técnicas de escalado, y casi todos coinciden en reseñar la dependencia potencial del tamaño promedio de los agregados a tiempos largos de agregación. Sin embargo, es

difícil encontrar en ellos un estudio detallado de la cinética del proceso y de la evolución temporal de la distribución del tamaño de los agregados. De este modo, el proceso de agregación de partículas magnéticas inducido por un campo externo sigue siendo a día de hoy un tema abierto de discusión. Aún no se ha descrito adecuadamente el papel que puede desempeñar en estos procesos la interacción electrostática entre las partículas, la inducción mutua entre las partículas, la intensidad del campo magnético externo o los procesos de sedimentación.

El objetivo principal de esta Tesis ha sido el de profundizar en el estudio de la agregación inducida en estos fluidos por un campo magnético uniaxial constante, y mejorar el marco teórico que describe la cinética y la estabilidad de este tipo de procesos. Un mejor entendimiento de la Física que controla la formación de los agregados lineales podría ayudar a optimizar el funcionamiento de nuevas técnicas basadas en la respuesta de estos fluidos a un campo externo.

Durante la tesis se utilizaron principalmente técnicas de videomicroscopía y de dispersión de luz. Estas técnicas permitieron estudiar durante el proceso de agregación las distribuciones de tamaño de los agregados lineales, su tamaño promedio y su morfología. Los resultados experimentales fueron contrastados por las predicciones teóricas.

## 9.1 Conclusiones

### 9.1.1 Dispersión de Luz

Las técnicas de dispersión de luz presentan algunas ventajas con respecto a las técnicas de video-microscopía: la posibilidad de acceder a sistemas de menor tamaño, su inocuidad hacia las suspensiones coloidales durante los procesos de medida, y la obtención de datos con una buena estadística. Durante nuestros experimentos de dispersión de luz prestamos una especial atención a la influencia que diferentes aspectos tales como el carácter magnético de las partículas, la presencia del campo, o la geometría lineal de los agregados, podían tener sobre los experimentos. Los principales resultados obtenidos fueron:

- En una suspensión diluida de partículas magnéticas la dispersión de luz es una técnica adecuada para estudiar tanto la estructura de los agregados como la cinética del proceso de agregación. El estudio de las principales características de los agregados puede hacerse tanto en presencia como en ausencia del campo magnético externo, siempre que se utilicen los marcos teóricos adecuados. Estos modelos han de tener en

cuenta los posibles acoplamientos entre los modos difusivos de rotación y de traslación, la posible fluctuación de las partículas dentro de los agregados, y la orientación del campo aplicado con respecto al plano de dispersión.

### 9.1.2 Cinética de Agregación Inducida por un Campo

En el marco de la ecuación de Smoluchowski se ha propuesto el siguiente kernel de agregación

$$k_{ij}^{Bdip} = 4\pi(1 - \cos\varphi_c)(\bar{D}_i + \bar{D}_j)(a_i + a_j + \bar{h}),$$

en donde  $\varphi_c$  es el ángulo de apertura de la región de atracción de la interacción dipolar magnética. Este kernel de agregación ha de entenderse como una aproximación de campo medio, descrito en función de magnitudes efectivas: el alcance promedio de la interacción  $\bar{h}$ , como único parámetro libre de ajuste, y los coeficientes de difusión efectivos de traslación de los agregados  $\bar{D}_i$  y  $\bar{D}_j$ . La resolución de la ecuación de Smoluchowski permitió comparar las predicciones teóricas con los valores experimentales. Hasta donde nosotros sabemos, no existen trabajos anteriores que contrasten distribuciones de tamaños de los agregados lineales con las predicciones teóricas. Además el anterior es el primer kernel de agregación que describe la formación de agregados inducidos por un campo externo, y que está expresado en términos de magnitudes con significado físico. Los principales resultados han sido:

#### Cinética

- Los datos obtenidos confirman que el tamaño promedio de los agregados lineales crece monótonamente con el tiempo. A tiempos largo la evolución temporal del tamaño promedio de los agregados siguió una ley de potencias con un exponente cinético  $z' = 0.66$ .

#### Intensidad del Campo Magnético y Concentración de Electrolito

- Ni la intensidad del campo externo aplicado ni la concentración de electrolito presentaron ningún efecto apreciable sobre el parámetro cinético  $z'$ . El mecanismo de agregación parece no depender de la intensidad del campo aplicado, ni de la concentración de electrolito añadido. El tiempo de agregación pudo ser escalado de modo que todas las curvas

de evolución temporal del tamaño de los agregados lineales, obtenidas para los diferentes valores del campo aplicado y del electrolito añadido, coincidieran en una única curva maestra.

- El ritmo de crecimiento de los agregados lineales, sin embargo, sí dependió de la intensidad del campo aplicado, es decir, del alcance de la interacción que sufren entre sí las partículas magnéticas.
- Teniendo en cuenta el carácter anisótropo de la interacción dipolar, propusimos un kernel de agregación que incluye explícitamente el alcance efectivo de las interacciones como parámetro de ajuste, y que depende implícitamente de la intensidad del campo aplicado y de la concentración del electrolito. Las correspondientes soluciones de la ecuación de Smoluchowski reprodujeron adecuadamente la evolución temporal del tamaño medio de los agregados lineales obtenido mediante técnicas de dispersión de luz.
- La concentración de electrolito no presentó ningún efecto apreciable sobre el valor del parámetro cinético  $z'$ . De este modo, el mecanismo de agregación pareció no tener ningún efecto sobre el mecanismo de agregación, que a su vez parece estar determinado por la interacción dipolar. El tiempo de agregación pudo ser escalado de modo que todas las curvas de evolución temporal del tamaño promedio de los agregados lineales, obtenidas a diferentes concentraciones de electrolito, colapsaran en una única curva maestra.
- En el caso de las partículas de Sílice, el ritmo de crecimiento de los agregados lineales no dependió de la concentración del electrolito.
- En el caso de las partículas de poliestireno, sin embargo, el ritmo de crecimiento de los agregados lineales dependió de la concentración del electrolito. Para estas partículas, de menor tamaño, la interacción magnética es comparable a la repulsión electrostática. De este modo, la concentración de electrolito afecta al alcance de la interacción neta que sufren entre sí las partículas magnéticas, y el tamaño promedio de las cadenas crece con la concentración de electrolito para un mismo tiempo de exposición al campo magnético.
- Teniendo en cuenta el carácter anisótropo de la interacción dipolar, propusimos un kernel de agregación que incluye explícitamente el alcance efectivo de las interacciones como parámetro de ajuste, por lo

que depende implícitamente de la concentración del electrolito. Las correspondientes soluciones de la ecuación de Smoluchowski reprodujeron adecuadamente la evolución temporal del tamaño medio de los agregados lineales formados por partículas de poliestireno. En el caso de las partículas de sílice, las predicciones teóricas únicamente reprodujeron los valores experimentales durante los primeros estadios del proceso de agregación.

### Sedimentación

- En los experimentos de agregación realizados con las partículas de sílice, el mecanismo de agregación se vio influido por la sedimentación de las partículas y los agregados. Fue entonces necesario introducir un término de agregación adicional que incluyera el efecto que la sedimentación de las partículas tiene sobre el proceso de agregación. El alcance efectivo de la interacción entre las partículas se mantuvo como único parámetro de ajuste.
- Cuando los efectos de la sedimentación en el proceso de agregación fueron incluidos en el kernel de agregación el ajuste teórico a los valores experimentales mejoró apreciablemente, especialmente para tiempos largos de agregación. El exponente cinético  $z = 0.77$  predicho teóricamente se acercó bastante al valor experimental  $z = 0.72$ .
- Un valor elevado del parámetro cinético  $z$  puede ser señal de la influencia del proceso de sedimentación en el mecanismo de agregación inducido por el campo magnético.
- La evolución temporal de la concentración de los monómeros no pudo reproducirse satisfactoriamente por las predicciones teóricas. Pensamos que las dificultades encontradas durante el análisis de las imágenes de videomicroscopía podrían explicar esta discrepancia. Sin embargo otras razones, con un mayor significado físico, no pueden ser descartadas.

### Inducción Mutua

- Finalmente, intentamos reproducir el efecto que la inducción mutua entre las partículas que conforman los agregados lineales pudiera tener sobre el proceso de agregación. La inducción mutua aumenta el alcance de la interacción entre los agregados conforme aumenta el tamaño de los mismos. Sin embargo, el modelo propuesto para incluir esta dependencia



del alcance con el tamaño de los agregados no consiguió explicar las discrepancias anteriormente observadas en la evolución temporal de la población de monómeros.

### 9.1.3 Estabilidad de Cadenas Magnéticas

Recientemente se ha observado que algunos agregados lineales son capaces de soportar la ausencia del campo magnético. La agregación permanente es observada si la agregación inducida por campo tiene lugar en un mínimo primario de energía, donde las fuerzas de van der Waals de corto alcance son responsables de la adhesión irreversible de las partículas que conforman el agregado. Estas estructuras inducidas por un campo externo, y que a partir de ahora denominaremos "cadenas permanentes", también se obtienen cuando la agregación irreversible es debida al puenteo de polímeros absorbidos en la superficie de las partículas. La posibilidad de controlar la geometría y el tamaño de los agregados se presenta como un primer acercamiento hacia la construcción y el control de estructuras y "arquitecturas" coloidales más complejas.

Hasta ahora las características principales de las cadenas permanentes (su geometría, flexibilidad y tamaño) se han estudiado principalmente mediante técnicas de video-microscopía. Sin embargo, es difícil encontrar trabajos en los que estas características sean estudiadas mediante técnicas de dispersión de luz. Se ha comprobado que estas técnicas también permiten caracterizar, en presencia y en ausencia del campo aplicado, tanto la morfología de los agregados formados como el tamaño medio de los mismos.

Otro de los objetivos de la Tesis fue el de diseñar un protocolo experimental que permitiera controlar el tamaño promedio de los agregados sin más que variar la relación entre las diferentes interacciones y el tiempo de exposición al campo. En esta dirección hemos obtenido los resultados siguientes:

- A concentraciones suficientemente elevadas de electrolito, al menos algunos de los agregados lineales formados en presencia del campo fueron capaces de subsistir una vez que el campo magnético desaparece.
- Las cadenas formadas permanecieron unidas aun en ausencia de campo, de modo que pudo controlarse el tamaño de los agregados sin más que variar el tiempo de aplicación del campo magnético. La relación entre las interacciones electrostáticas y magnéticas también influyó en el tamaño medio de los agregados lineales permanentes.
- Se ha propuesto un modelo simple que permite predecir el tamaño de

los agregados lineales permanentes para diferentes tiempos de exposición al campo.

#### 9.1.4 Estructura de Cadenas Magnéticas

Un análisis detallado de la agregación coloidal ha de tener en cuenta no sólo la cinética sino también la morfología de los agregados. La morfología suele describirse por medio de la dimensión fractal, entendiéndose ésta como una medida de cómo llenan las partículas el espacio tridimensional. Las principales conclusiones a destacar fueron:

- Al añadir electrolito, y en ausencia de campo, los agregados formados por las partículas coloidales magnéticas presentaron la clásica geometría fractal ampliamente descrita en la literatura para procesos de agregación controlados por difusión.
- La morfología de los agregados lineales formados en presencia de campo fue caracterizada por una dimensión fractal cercana a la unidad. Para agregados grandes, sin embargo, la dimensión fractal aumentó hasta un valor próximo a 1.2. Este aumento observado es consecuencia del mayor grado de "flexibilidad" observada en los agregados mayores. Esta presunción fue cualitativamente corroborada por las fotos de microscopía electrónica.
- Las imágenes de microscopía electrónica, obtenidas a concentraciones bajas de electrolito, presentaron una cantidad considerable de monómeros libres. Este fenómeno ha sido denominado "agregación selectiva". En las imágenes de TEM no se observó que las partículas que participan en la agregación selectiva sean las más grandes o las de mayor contenido magnético. La influencia de la concentración del electrolito parece señalar que el origen de este fenómeno es de naturaleza eléctrica. La teoría DLVO extendida proporcionó una explicación cualitativa del fenómeno.



## Appendix A

# Table of Magnetic Units

Quantity	Symbol	Gaussian	Conversion factor, C <sup>a</sup>	SI <sup>b</sup>
Magnetic flux	$\phi$	maxwell (Mx)	$10^{-8}$	weber (Wb)
Magnetic flux density	B	gauss (G)	$10^{-4}$	tesla (T)
Magnetic potential difference	U, F	gilbert (Gb)	$10/4\pi$	ampere (A)
Magnetic field strength	H	oersted (Oe)	$10^3/4\pi$	A/m <sup>c</sup>
(Volume) magnetization <sup>d</sup>	M	<i>emu/cm<sup>3e</sup></i>	$10^3$	A/m
(Volume) magnetization	$4\pi M$	G	$10^3/4\pi$	A/m
Magnetic polarization	J	<i>emu/cm<sup>3</sup></i>	$4\pi 10^{-4}$	T
(Mass) magnetization	M	emu/g	1	A·m <sup>2</sup> /kg
Magnetic moment	m	emu	$10^{-3}$	A·m <sup>2</sup>
Magnetic dipole moment	j	emu	$4\pi 10^{-10}$	Wb·m
(Volume) susceptibility	$\chi, \kappa$	dimensionless	$4\pi$	dimensionless
(Mass) susceptibility	$\chi_p, \kappa_p$	<i>cm<sup>3</sup>/g</i>	$4\pi 10^{-3}$	<i>m<sup>3</sup>/kg</i>
(Molar) susceptibility	$\chi_{mol}, \kappa_{mol}$	<i>cm<sup>3</sup>/mol</i>	$4\pi 10^{-6}$	<i>m<sup>3</sup>/mol</i>
Permeability	$\mu$	dimensionless	$4\pi 10^{-7}$	Wb/(A·m)
Relative permeability <sup>f</sup>	$\mu_r$	not defined		dimensionless
(Volume) energy density	W	<i>erg/cm<sup>3</sup></i>	$10^{-1}$	J/m <sup>3</sup>
Demagnetization factor	D, N	dimensionless	$1/4\pi$	dimensionless

<sup>a</sup>Multiply a number in Gaussian units by C to convert it to SI (e.g.  $1G \times 10^{-4}T/G = 10^{-4}T$ ).

<sup>b</sup>SI is based in the definition  $B = \mu_0(H + M)$ , where  $\mu_0 = 4\pi 10^{-7}N/A^2$ .

<sup>c</sup>A/m was often expressed as "ampere-turn per meter" when used field strength

<sup>d</sup>Magnetic moment per unit volume.

<sup>e</sup>The designation emu is not a unit.

<sup>f</sup> $\mu_r = \mu/\mu_0 = 1 + \sigma$ , all in SI

## Appendix B

# INSPACE

InSPACE (acronym for Investigating the Structure of Paramagnetic Aggregates From Colloidal Emulsions) was a microgravity fluid physics experiment operated on the International Space Station (ISS), in the Microgravity Science Glovebox from late March 2003 through early July 2003 (Figure B.1).

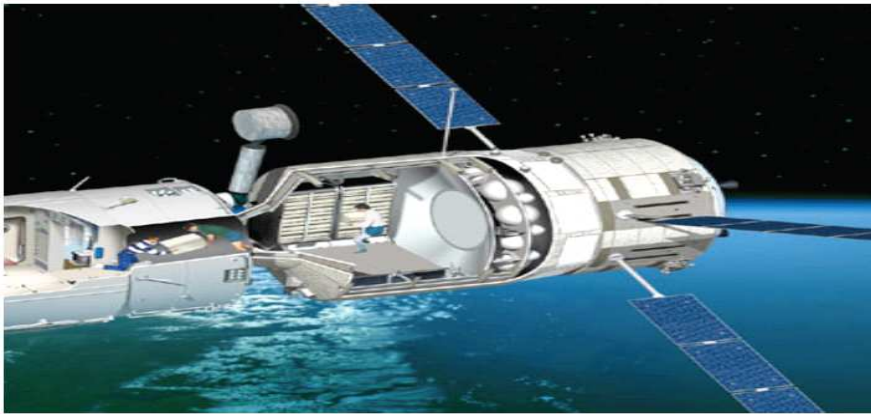


Figure B.1: International Space Station where the InSpace experiments were performed.

InSPACE provided fundamental data for the stability of magnetic fluids. The goal of InSPACE was to determine the three-dimensional structure of a magneto-rheological emulsion in a pulsed magnetic field in absence of sedimentation effects. The crew installed a coil onto an optics assembly that included two cameras for imaging the samples from a straight-on and right-angle view

during test runs. A pulsed magnetic field was used to mimic the forces applied to these fluids in real applications, such as vibration damping systems. A pulsed field also tends to produce thick intricate structures with different properties than structures produced by a constant magnetic field.

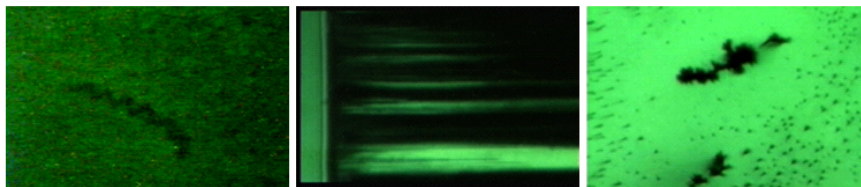


Figure B.2: The experiments, performed in the absence of gravity, show aggregate shapes that are more extended and diverse than those observed on ground.

The experiment were performed using video-microscopy techniques similar to the ones described in the Section 5.2.2. The goal was to study the effect of varying magnetic field strength, pulse frequency, and particle size on the equilibrium microstructures. The video was distributed among the scientists at Massachusetts Institute of Technology and the Telescience Center at NASA's Glenn Research Center in Cleveland, Ohio, so that the scientists and engineers could observe the microstructures as they form and change. The principal investigator for InSPACE was Professor Alice P. Gast of the Massachusetts Institute of Technology (MIT). As a result, Dr. Gast et al. have reported on the formation of aggregate shapes that are more extended and diverse than those observed on the ground (Figure B.2). The data from the experiment should and will be used to test the theoretical models of the structure of suspensions of small particles in applied external fields. As far as we know, however, no results have been published so far<sup>1</sup>.

---

<sup>1</sup>More information can be found in  
<http://spaceflight systems.grc.nasa.gov/Advanced/ISSResearch/MSG/InSPACE/>

## Appendix C

# Magnetotactic Bacteria

*Magnetotactic bacteria* are a special class of bacteria that orient themselves along the magnetic field lines of the Earth's magnetic field. Hence, magnetotactic bacteria tend to move along the geomagnetic field towards favorable habitats. This behaviour is known as *magnetotaxis*. Quite possibly the evolutionary advantage of possessing a system of magnetosomes is related to the ability of efficiently diving within a zone of chemical gradients by simplifying a potential three dimensional search for more favorable conditions to a single dimension. If a bacterium restricts its movement to forwards and backwards directions in its search for nutrient, it will tend to find nutrient rich areas at the same speed or often faster than other bacteria that search both forwards and backwards, to the left and to the right, up-wards and down-wards<sup>1</sup>.

---

<sup>1</sup>More information can be found in [http://en.wikipedia.org/wiki/Magnetotactic\\_bacteria](http://en.wikipedia.org/wiki/Magnetotactic_bacteria)





Figure C.1: Different species of magnetotactic bacteria. The small aligned magnetosomes appear as dark spot in the images.



Figure C.2: Remains of magnetosomes were found in the Martian *meteorite* *ALH84001*. A debate whether this magnetosomes are really fossilized lifeforms is still on going.

The sensitivity of magnetotactic bacteria to the Earth's magnetic field arises from *magnetosomes*, which are magnetic colloidal particles enclosed in a membrane. In most cases magnetotactic bacteria synthesize their magnetic particles forming linear aggregates, as is clearly visible in the microscopic image (Figure C.1). The resulting net magnetic dipole moment of the cell is sufficient to orientate the cell and overcome brownian motion. Individual magnetite crystals in magnetotactic bacteria are of a size between 35 and 120 *nm*, that is, large enough to have a permanent magnetic dipole and at the

same time small enough to remain a single magnetic domain. Bacterial magnetosome particles, unlike those produced chemically, have a consistent shape, a narrow size distribution, and a membrane coating consisting of lipids and proteins [144].

On August 6th, 1996 magnetic bacteria became newsworthy. Even prompting U.S. President Bill Clinton to make a formal televised announcement to mark the event. It was announced that Martian *meteorite ALH84001* might contain traces of magnetotactic bacteria. This was published in an article in *Science* by Dr. David McKay et al. of NASA [145]. Under the scanning electron microscope magnetic structures were revealed that may be the remains of magnetosomes. The magnetosomes found on ALH 84001 are 20-100 *nm* in diameter, similar in size to those usually observed in magnetotactic bacteria (Figure C.2). If the structures were really fossilized lifeforms, they would be the first evidence of the existence of extraterrestrial life. Several tests for organic material have been performed on the meteorite and amino acids and polycyclic aromatic hydrocarbons have been found. However, such claims are being strongly questioned, and the debate whether the organic molecules could have been created by nonbiological processes or are due to contamination from the contact with Antarctic ice is still on going.



# Bibliography

- [1] E.M. Furst and A.P. Gast. Dynamics and lateral interactions of dipolar chains. *Phys. Rev. E*, 62(5):6919, 2000.
- [2] V. Cabuil. *Preparation and properties of magnetic nanoparticles*. Encyclopedia of Surface and Colloid Science, Marcel Dekker, 2002.
- [3] N. Pamme. Magnetism and microfluidics. *Lab on a Chip*, 6:24, 2006.
- [4] P.S. Doyle, J. Bibette, A. Bancaud, and J.L. Viovy. Self-assembled magnetic matrices for DNA separation chips. *Science*, 295(2):2237, 2002.
- [5] M.R. Ibarra. Magnetism: special issue overview. *Europhys. News*, 36(6):209, 2003.
- [6] A. Curtis. Biomedical aspects of magnetic nanoparticles. *Europhys. News*, 36(6):210, 2003.
- [7] J.H.E. Promislow, A.P. Gast, and M. Fermigier. Aggregation kinetics of paramagnetic colloidal particles. *J. Chem. Phys.*, 102(13):5492, 1995.
- [8] S. Miyazima, P. Meakin, and F. Family. Aggregation of oriented anisotropic particles. *Phys. Rev. A*, 36(3):1421, 1987.
- [9] M.C. Miguel and R. Pastor-Satorras. Kinetic growth of field-orientated in dipolar colloidal solutions. *Phys. Rev. E*, 59(1):826, 1999.
- [10] G. Bossis, C. Metayer, and A. Zubarev. Analysis of chining structures in colloidal suspensions subjected to an electric field. *Phys. Rev. E*, 76:041301, 2007.
- [11] C. Tsouris and T.R. Scott. Flocculation of paramagnetic particles in a magnetic field. *J. Colloid Interface Sci.*, 171:319, 1995.

- [12] F.A. Tourinho, A.F.C. Campos, R. Aquino, M.C.F.L. Lara, G.J. da Silva, and J. Depeyrot. Surface charge density determination in electric double layered magnetic fluids. *Braz. J. of Phys.*, 32(2B):501, 2002.
- [13] D. Shon, P.S. Russo, A. Davila, D.S. Poche, and M.L. McLaughlin. Light scattering study of magnetic particles and their interaction with polyelectrolytes. *J. Coll. Int. Sci.*, 177:31, 1996.
- [14] K. Zahn, R. Lenke, and G. Maret. Friction coefficient of rod-like chains of spheres at very low reynolds numbers. *J. Phys. II France*, 4:555, 1994.
- [15] G. Zhang and M. Widom. Field-induced forces in colloidal particle chains. *Phys. Rev. E*, 51(3):2099, 1995.
- [16] E.M. Furst, Suzuki C., Fermigier M., and A.P. Gast. Permanently linked monodisperse paramagnetic chains. *Langmuir*, 14(26):7334, 1998.
- [17] H. Singh, P.E. Laibinis, and T.A. Hatton. Synthesis of flexible magnetic nanowires of permanent linked core-shell magnetic beads tethered to glass surface patterned by microcontact printing. *NanoLetters*, 5(11):2149, 2005.
- [18] R. Dreyfus, J. Baudry, M. Roper, M. L. amd Fermigier, H.A. Stone, and J. Bibette. Microscopic artificial swimmers. *Nature*, 437:862, 2005.
- [19] S.L. Biswal and A. Gast. Rotational dynamics of semiflexible paramagnetic particle chains. *Phys. Rev. E*, 69:041406, 2004.
- [20] L. Cohen-Tannoudji, E. Bertrand, J. Baudry, C. Robic, C. Goubault, M. Pellissier, A. Johner, F. Thalmann, N.K. Lee, C.M. Marques, and J. Bibette. Measuring the kinetics of biomolecular recognition with magnetic colloids. *Phys. Rev. Lett.*, 100:108301, 2008.
- [21] L. Cohen-Tannoudji, E. Bertrand, L. Bressy, C. Goubault, J. Baudry, J. Klein, J.F. Joanny, and J. Bibette. Polymer bridging probed by magnetic colloids. *Phys. Rev. Lett.*, 94:038301, 2005.
- [22] C. Goubault, P. Jop, M. Fermigier, J. Baudry, E. Bertrand, and J. Bibette. Flexible magnetic filaments as micromechanical sensors. *Phys. Rev. Lett.*, 91(26):260802, 2003.
- [23] S.L. Biswal and A. Gast. Micromixing with linked chains of paramagnetic particles. *Anal. Chem*, 76:6448, 2004.

- [24] A. Cebers and I. Javaitis. Dynamic of a flexible magnetic chain in a rotating magnetic field. *Phys. Rev. E.*, 69:021404, 2004.
- [25] E.M. Furst and A.P. Gast. Micromechanics of magnetorheological suspensions. *Phys. Rev. E*, 61(6):6732, 2000.
- [26] J.K.G. Dhont. *An introduction to dynamics of colloids*. Elsevier, 1996.
- [27] Z.M. Saiyed, S.D. Telang, and C.N. Ramchand. Application of magnetic techniques in the fields of drug discovery and biomedicine. *Business Briefing: Future Drug Discovery*, 2004.
- [28] M. Tirado-Miranda. *Agregación de sistemas coloidales modificados superficialmente*. PhD thesis, 2001.
- [29] C. Haro-Pérez, M. Quesada-Pérez, J. Callejas-Fernández, P. Schurtenberger, and R. Hidalgo-Álvarez. Renormalization in charged colloids: non-monotonic behaviour with the surface charge. *J. Phys.: Condens. Matter*, 18(28):363, 2006.
- [30] S. Fraden, A.J. Hurd, and R.B. Meyer. Electric-field association of colloidal particles. *Phys. Rev. Lett.*, 63(21):2373, 1989.
- [31] R.E. Rosenweig. *Ferrohydrodynamics*. Cambridge University Press, 1985.
- [32] F. Vereda, J. de Vicente, and R. Hidalgo-Álvarez. Influence of a magnetic field in the formation of magnetite particles via two precipitation methods. *Langmuir*, 23(7):3581, 2007.
- [33] R. Fernandez-Pacheco, M. Arruebo, C. Marquina, R. Ibarra, J. Arbio, and J. Santamaría. Highly magnetic silica-coated iron nanoparticles prepared by the arc-discharge method. *Nanotech.*, 17:1188, 2006.
- [34] M.T. Klem, M. Young, and T. Douglas. Biomimetic magnetic nanoparticles. *Materials Today*, page 28, 2005.
- [35] S. Lu, J. Ramos, and J. Forcada. Self-stabilized magnetic polymeric composite nanoparticles by emulsifier-free miniemulsion polymerization. *Langmuir*, 23(26):12893, 2007.
- [36] S. Melle, M.A. Rubio, and G.G. Fuller. Time scaling regimes in aggregation of magnetic dipolar particles: scattering dichroism results. *Phys. Rev. Lett.*, 87(11):115501, 2001.

- [37] M. Chaker, N. Breslin, and J. Liu. Influence on rheology of static and dynamic structures in model magnetorheological Fluids. *Int. J. Mod. Phys.*, 15(6):886, 2001.
- [38] I. Hilger, K. Fruhauf, W. Andra, R. Hiergerist, R. Hergt, and W.A. Kaiser. Heating potential of iron oxides for therapeutic purposes in interventional Radiology. *Academic Radiology*, 9(2):198, 2002.
- [39] D.K. Kim, W. Voit, W. Zapka, B. Bjelke, M. Muhammed, and K.V. Rao. Biomedical applications of ferrofluids containing magnetite nanoparticles. *Mat. Res. Soc. Symp.*, 676(8.32):1, 2001.
- [40] J Andreassen. One micron magnetic beads optimised for automated immunoassays. *Immunodiagnostic*, 29(2):22, 2005.
- [41] F. Leal-Calderon, T. Stora, O.M. Monval, P. Poulin, and J. Bibette. Direct measurement of colloidal forces. *Phys. Rev. Lett.*, 72(18):2959, 1994.
- [42] S. Melle, M. Lask, and G.G. Fuller. Pickering emulsions with controllable stability. *Langmuir*, 21(6):2158, 2005.
- [43] P. Tierno, T.H. Johansen, and T.M. Fischer. Magnetically driven colloidal microstirrer. *J. Phys. Chem. B*, 111(12):3077, 2007.
- [44] M. Winklhofer, E. Holtkamp-Rotzler, M. Hanzlik, G. Fleissner, and N. Petersen. Clusters of superparamagnetic magnetite particles in the upper-beak skin of homing pigeons: evidence of magnetoreceptor? *Eur. J. Mineral*, 13:659, 2001.
- [45] S. Johnsen. Magnetoreception in animals. *Phys. Today*, March:29, 2008.
- [46] S. Melle-Hernandez. *Estudio de la dinámica en suspensiones magnetorreológicas sometidas a campos externos mediante el uso de técnicas ópticas*. PhD thesis, 2002.
- [47] A. Einstein. Uber die von der molekularkinetischen theorie der warme geforderte bewegung von in ruhenden flussigkeiten suspendierten teilchen. *Ann. Phys.*, 17:549, 1905.
- [48] W. van Megan, S.M. Underwood, R.H. Ottewill, N.S.J Williams, and P.N. Pusey. Particle diffusion in concentrated dispersions. *Faraday Discuss. Chem. Soc.*, 83:47, 1987.

- [49] D. Chandler. *Introduction to modern statistical mechanics*. Oxford University Press, 1987.
- [50] B.J. Berne and R. Pecora. *Dynamic light scattering*. Dover Publications, 1976.
- [51] M.M. Tirado and J. Garcia de la Torre. Translational friction coefficients of rigid, symmetric top macromolecules. Application to circular cylinders. *J. Chem. Phys.*, 71(6):2581, 1979.
- [52] M.M. Tirado and J. Garcia de la Torre. Rotational dynamics of rigid, symmetric top macromolecules. Application to circular cylinders. *J. Chem. Phys.*, 73(4):1986, 1980.
- [53] S.J. Broersma. Rotational diffusion constant of a cylindrical particle. *J. Chem. Phys.*, 32:1626, 1960.
- [54] S.J. Broersma. Viscous force constant for a closed cylinder. *J. Chem. Phys.*, 32:1632, 1960.
- [55] B.V. Derjaguin and L. Landau. Theory of stability of highly charged lyophobic sols and adhesion of highly charged particles in solutions of electrolytes. *Acta Physicochim. URSS*, 14:633, 1941.
- [56] E.J. Verwey and J.G. Overbeek. *Theory of stability of lyophobic colloids*. 1948.
- [57] Y.C.D. Chan, D. Henderson, J. Barojas, and A.M. Homola. The stability of a colloidal suspension of coated magnetic particles in an aqueous solution. *IBM J. Res. Develop*, 29(1):11, 1985.
- [58] L. Seung-Woo and M.S. Wolfgang. Repulsive van der Waals forces for silica and alumina. *J. Coll. Int. Sci.*, 243(2):365, 2001.
- [59] R. Dreyfus. *Filaments magnétiques: application à la conception de capteurs de forces et de nageurs microscopiques artificiels*. PhD thesis, 2005.
- [60] R.P. Feynman, Leighton R.B., and Sands M. *The Feynman lectures on physics*. Fondo Educativo Interamericano, 1972.
- [61] T.C. Halsey and W. Toor. Structure of electrorheological fluids. *Phys. Rev. Lett.*, 65:2820, 1990.



- [62] J.E. Martin, J. Odinek, and T.C. Halsey. Evolution of structure in a quiescent electrorheological fluid. *Phys. Rev. Lett.*, 69(10):1524, 1992.
- [63] J.E. Martin, K.M. Hill, and C.P. Tigges. Magnetic-field-induced optical transmittance in colloidal suspensions. *Phys. Rev. E*, 59:5676, 1999.
- [64] C.J. Chin, S. Yiacoumi, and C. Tsouris. Probing DLVO forces using interparticle magnetic forces: transition from secondary-minimum to primary-minimum aggregation. *Langmuir*, 17:6065, 2001.
- [65] C.J. Chin, S. Yiacoumi, C. Tsouris, S. Relle, and S.B. Grant. Secondary minimum aggregation of superparamagnetic colloidal particles. *Langmuir*, 16:3641, 2000.
- [66] F. Martínez-Pedrero, M. Tirado-Miranda, A. Schmitt, and J. Callejas-Fernández. Controlling the magnetic filaments length by tuning the particle interactions. *J. Coll. Int. Sci.*, 318(1):23, 2008.
- [67] F. Martínez-Pedrero, M. Tirado-Miranda, A. Schmitt, and J. Callejas-Fernández. Forming chainlike filaments of magnetic colloids: the role of the relative strength of isotropic and anisotropic particle interactions. *J. Chem. Phys.*, 125:084706, 2006.
- [68] F. Martínez-Pedrero, M. Tirado-Miranda, A. Schmitt, and J. Callejas-Fernández. Structure and stability of aggregates formed by electrical double-layered magnetic particles. *Colloids Surf. A*, 306:158, 2007.
- [69] C. Goubault, F. Leal-Calderon, J.L. Viovy, and J. Bibette. Self-assembled magnetic nanowires made irreversible by polymer bridging. *Langmuir*, 21(9):3725, 2005.
- [70] H.A. Krammers. Brownian motion in a field of force and the diffusion model of chemical reaction. *Physica*, 7(4):284, 1940.
- [71] G. Nagele. On the dynamics and structure of charge-stabilized suspensions. *Phys. Report*, 272:215, 1996.
- [72] G.K. Batchelor. Sedimentation in a dilute polydisperse system of interacting spheres. part 2. numerical results. *J. Fluid Mech.*, 124:495, 1982.
- [73] L.N. Donselaar and A.P. Philipse. Interactions between silica colloids with magnetite cores: diffusion, sedimentation and light scattering. *J. Coll. Int. Sci*, 212:14, 1999.

- [74] T. Phenrat, N. Saleh, K. Sirk, R.D. Tilton, and G.V. Lowry. Aggregation and sedimentation of aqueous nanoscale zerovalent iron dispersion. *Environ Sci. Technol.*, 41(1):284, 2007.
- [75] H. Wang and C.S. Wen. Concentration-dependent sedimentation of stable magnetic dispersions. *J. Coll. Int. Sci.*, 213:606, 1999.
- [76] P. Dominguez-García. *Estudio experimental sobre fluidos magnetoreológicos mediante video-microscopía y análisis de imágenes: dinámica, estructura y aplicaciones en microfluidica*. PhD thesis, 2007.
- [77] F. Family and Landau D.P. *Kinetics of aggregation and gelation*. Elsevier, 1984.
- [78] M.L. Broide. *Experimental study of aggregation kinetics: dynamic scaling of measured Cluster-Size Distributions*. PhD thesis, 1981.
- [79] M. von Smoluchowski. *Vertwandtschaftsl. Z. Phys. Chem.*, 92:129, 1917.
- [80] P.G.J. van Dongen and M.H. Ernst. Cluster size distribution in irreversible aggregation at large times. *J. Phys. A*, 18:2779, 1985.
- [81] P.G.J. van Dongen and M.H. Ernst. Dynamic scaling in the kinetics of clustering. *Phys. Rev. Lett.*, 54(13):1396, 1985.
- [82] F. Martínez-Pedrero, M. Tirado-Miranda, A. Schmitt, and J. Callejas-Fernández. Formation of magnetic filaments: A kinetic study. *Phys. Rev. E*, 76:011405, 2007.
- [83] G. Odriozola, R. Leone, A. Moncho-Jorda, A. Schmitt, and R. Hidalgo-Alvarez. Coupled aggregation and sedimentation processes: stochastic mean field theory. *Physica A*, 335:35, 2004.
- [84] F. Martínez-Pedrero, A. El-Harrak, J.C. Fernández-Toledano, M. Tirado-Miranda, J. Baudry, A. Schmitt, J. Bibette, and J. Callejas-Fernández. A kinetic study of coupled field induced aggregation and sedimentation processes arising in magnetic fluids. *Phys. Rev. E*, Accepted 2008.
- [85] J. Cernak, G. Helgesen, and A.T. Skjeltorp. Aggregation dynamics of nonmagnetic particles in a ferrofluid. *Phys. Rev. E.*, 70:031504, 2004.
- [86] B.B. Mandlbrot. *The fractal geometry of nature*. Freeman W.H., 1982.

- [87] T. Vicsek. *Fractal growth phenomena*. World Scientific, 1991.
- [88] F. Hausdorff. Dimension und äusseres mass. *Mathematische Annalen*, 79:157, 1919.
- [89] J.C. Fernández-Toledano. *Interaction, structure and kinetic properties of colloidal monolayers*. PhD thesis, 2008.
- [90] A. Einstein. Theorie der opaleszenz von homogenen flüssigkeiten und flüssigkeitsgemischen in der nähe des kritischen zustandes (theoretical aspects of the opalescence of homogeneous fluids and liquid mixtures near the critical state). *Ann. Phys.*, 33:1275, 1910.
- [91] D. Lehner, H. Lindner, and O. Glatter. Determination of the translational and rotational diffusion coefficients of rod-like particles using depolarized dynamic light scattering. *Langmuir*, 16(4):1689, 2000.
- [92] R. Cush, P.S. Russo, Z. Kucukyavuz, Z. Bu, D. Neau, D. Shih, S. Kucukyavuz, and H. Ricks. Rotational and translational diffusion of a rodlike Virus in random coil polymer solutions. *Macromolecules*, 30(17):4920, 1997.
- [93] B.M.I. van der Zande, J.K.G. Dhont, M.R. Böhmer, and A.P. Philipse. Colloidal dispersions of gold rods characterized by dynamic light scattering and electrophoresis. *Langmuir*, 16(2):459, 2000.
- [94] S. Badaire, P. Philippe, M. Maugey, and C. Zakri. In situ measurements of nanotube dimensions in suspensions of depolarized dynamic light scattering. *Langmuir*, 20(24):10367, 2004.
- [95] J.D. Jackson. *Classical electrodynamics*. Wiley, 1965.
- [96] L.D. Landau and E.M. Lifshitz. *Electrodynamics of continuous media*. Addison Wesley, 1960.
- [97] C. Sinn. Dynamic light scattering by rodlike particles: examination of the vanadium(V)-oxide system. *Eur. Phys. J. B*, 7:599, 1999.
- [98] D. Shon. Kinetic studies of magnetic latex particles self-assembly under applied magnetic field. *J. Magn. Magn. Mat.*, 173:305, 1997.
- [99] M. Kerker. *The scattering of light and other electromagnetic radiation*. Academic Press, 1969.

- [100] H.C. van de Hulst. *Light scattering by small particles*. Dover Publications, 1981.
- [101] S. Asano and G. Yamamoto. Light scattering by spheroidal particle. *Appl. Opt.*, 14:29, 1975.
- [102] A. Dunn and R. Richards-Kortum. Three-dimensional computation of light scattering from cells. *IEEE J. of Select Topics in Quant. Elec.*, 2(4):898, 1996.
- [103] M. Kerker, D.S. Wang, and C.L. Giles. Electromagnetic scattering by magnetic spheres. *J. Opt. Soc. Am.*, 73:765, 1983.
- [104] F.A. Pinheiro, A.S. Martinez, and L.C. Sampaio. Electromagnetic scattering by small magnetic particles. *J. Magn. Magn. Mat.*, 226:1951, 2001.
- [105] B. Hoffman and W. Köhler. Reversible light-induced cluster formation of magnetic colloids. *J. Magn. Magn. Mat.*, 262:289, 2003.
- [106] R.R. Kellner and W. Köhler. Short-time aggregation dynamics of reversible light-induced cluster formation in ferrofluids. *J. Appl. Phys.*, 97:034910, 2005.
- [107] D.E. Koppel. Analysis of macromolecular polydispersity in intensity correlation spectroscopy. *J. Chem. Phys.*, 57:4814, 1972.
- [108] M.Y. Lin, H.M. Lindsay, D.A. Weits, R.C. Ball, R. Klein, and P. Meakin. Universality in colloid aggregation. *Nature*, 339:360, 1989.
- [109] B.J. Frisken. Revisiting the method of cumulants for the analysis of dynamic light scattering data. *Appl. Optics*, 40(24):4087, 2001.
- [110] T. Maeda and S. Fujime. Spectrum of light quasielastically scattered from solutions of very long rods at dilute and semidilute regimes. *Macromolecules*, 17:1157, 1984.
- [111] J. Buitenhuis, J.K.G. Dhont, and H.N.W. Lekkerkerker. Scattering of light for cylindrical particles: coupled dipole method calculations and the range of validity of the rayleigh-gans-debye approximation. *J. Coll. Int. Sci.*, 162:19, 1994.
- [112] H. Yamakawa and M. Fujii. Light scattering from wormlike chains. Determination of the shift factor. *Macromolecules*, 7(5):649, 1974.

- [113] H. Yamakawa and M. Fujii. Translational friction coefficient of wormlike chains. *Macromolecules*, 6(3):407, 1973.
- [114] R. Jullien and R. Botet. *Aggregation and fractal aggregates*. World Scientific, 1987.
- [115] M.Y. Lin, H.M. Lindsay, D.A. Weits, R. Klein, R.C. Ball, and P. Meakin. Universal diffusion-limited colloid aggregation. *J. Phys. Condens. Matter*, 2:3093, 1990.
- [116] W.L. Bragg. The diffraction of short electromagnetic waves by a crystal. *Proc. Cambridge Philosophical Soc.*, 17:43, 1914.
- [117] S. Cutillas and J. Liu. Experimental study on the fluctuations of dipolar chains. *Physical Review E*, 64:011506, 2001.
- [118] S. Melle, O.G. Calderón, G.G. Fuller, and M.A. Rubio. Polarizable particle aggregation under rotating magnetic fields using scattering dichroism. *J. Coll. Int. Sci.*, 247:200, 2002.
- [119] J. Buitenhuis, J.K.G. Dhont, and H.N.W. Lekkerkerker. Static and dynamic light scattering by concentrated colloidal suspensions of polydisperse sterically stabilized boehmite rods. *Macromolecules*, 27(25):7267, 1994.
- [120] S. Sacanna and P. Philpse. Preparation and properties of monodisperse latex spheres with controlled magnetic moment for field-induced colloidal crystallization and (dipolar) chain formation. *Langmuir*, 22(24):10209, 2006.
- [121] S. Gu, J. Onishi, Y. Kobayashi, D. Nagao, and M. Konno. Preparation and colloidal stability of monodisperse magnetic polymer particles. *J. Coll. Int. Sci.*, 289:419, 2005.
- [122] J. Callejas-Fernández, M. Tirado-Miranda, M. Quesada-Perez, G. Odriozola-Prego, and A. Schmitt. *Photon spectroscopy of colloids*. Encyclopedia of Surface and Colloid Science, Marcel Dekker, 2002.
- [123] K. Schätzel, M. Drewel, and S. Stimac. Photon correlation measurements at large lag times: improving statistical accuracy. *J. Mod. Opt.*, 35(4):711, 1988.

- [124] P. Dominguez-García, S. Melle, J.M. Pastor, and M.A. Rubio. Scaling in the aggregation dynamics of a magnetorheological fluid. *Phys. Rev. E*, 76:051403, 2007.
- [125] M. Hagenbuchle and J. Liu. Chain formation and chain dynamics in dilute magnetorheological fluid. *Applied Optics*, 36(30):7664, 1997.
- [126] S. Cutillas and J. Liu. Light scattering of particles dynamics in dipolar magnetic fluids. *Int. J. Mod. Phys. B*, 15(6):803, 2001.
- [127] P. Licinio, A.V. Teixeira, G.A.M. Safar, M.S. Andrade, L.C. Meira-Belo, and U.A. Leitao. Diffusion-limited aggregation of magnetic particles under a field. *J. Magn. Magn. Mat.*, 226, 2001.
- [128] F. Martínez-Pedrero, M. Tirado-Miranda, A. Schmitt, and J. Callejas-Fernández. Aggregation of magnetic polystyrene particles: a light scattering study. *Coll. and Surf. A*, 270, 2005.
- [129] J.M. López-López. *Electrostatic heteroaggregation processes arising in two-Component colloidal dispersions*. PhD thesis, 2006.
- [130] G. Odriozola, A. Schmitt, J. Callejas-Fernández, R. Martínez-García, R. Leone, and R. Hidalgo-Alvarez. Simulated reversible aggregation processes for different interparticle Potentials. *J. Phys. Chem. B*, 107:2180, 2003.
- [131] G. Fermigier and A.P. Gast. Structure evolution in a paramagnetic latex suspension. *J. Colloid Interface Sci.*, 154(2):522, 1992.
- [132] S. Relle, S.B. Grant, and C. Tsouris. Aggregation of oriented anisotropic particles. *Physica A*, 270:427, 1999.
- [133] G. Helgesen, A. T. Skjeltorp, P.M. Mors, R. Botet, and R. Jullien. Aggregation of magnetic microspheres: experiments and simulations. *Phys. Rev. Lett.*, 61(15):1736, 1988.
- [134] S. Relle, B.G. Stanley, and C. Tsouris. Diffusional coagulation of superparamagnetic particles in the presence of an external magnetic field. *Physica A*, 270:427, 1999.
- [135] S.H. Behrens and D.G. Grier. The charge of glass and silica surfaces. *J. Chem. Phys.*, 115:6716, 2001.

- [136] B.F. Lyles, M.S. Terrot, P.T. Hammond, and A.P. Gast. Direct patterned adsorption of magnetic beads on polyelectrolyte multilayers on glass. *Langmuir*, 20(8):3028, 2004.
- [137] H. Singh, P.E. Laibinis, and T.A. Hatton. Rigid, superparamagnetic chains of permanently linked beads coated with magnetic Nanoparticles. Synthesis and rotational dynamics under applied magnetic fields. *Langmuir*, 21(24):11500, 2005.
- [138] V. Salguiriño-Maceira, M.A. Correa-Duarte, A. Hucht, and M. Farle. One-Dimensional assemblies of silica-coated cobalt nanoparticles: magnetic pearl necklaces. *J. Magn. Magn. Mat.*, 303:163, 2006.
- [139] M. Tanase, L.A. Bauer, A. Hulttgren, D.M. Silevitch, L. Sun, D.H. Reich, P.C. Searson, and G.J. Meyer. Magnetic alignment of fluorescent nanowires. *Nano Letters*, 1(3):155, 2000.
- [140] G.A. van Ewijk. *Phase behaviour of mixtures of magnetic colloids and nonabsorbing polymer*. PhD thesis, 2001.
- [141] P. Licinio and F. Frezard. Diffusion limited field induced aggregation of magnetic liposomes. *Braz. J. Phys.*, 31(3):356, 2001.
- [142] L. Shen, A. Stachowiak, S.E.K. Fateen, P.E. Laibinis, and T.A. Hatton. Structure of alkanolic acid stabilized magnetic fluids. A small-angle neutron and light scattering analysis. *Langmuir*, 17:288, 2001.
- [143] R. Pastor-Satorras and J.M. Rubí. Dipolar interactions induced order in assemblies of magnetic particles. *J. Magn. Magn. Mat.*, 221:124, 2000.
- [144] R. Dunin-Borkowski, M.R. McCartney, R.B. Frankel, D.A. Bazylinski, M. Pósfai, and P. Buseck. Magnetic microstructure of magnetic bacteria by electron holography. *Science*, 282:1868, 1998.
- [145] D.S. McKay, E.K. Gibson, K.L. Thomas-Keppta, H. Vali, C.S. Romanek, S.J. Clemett, X.D.F. Chillier, C.R. Maechling, and R.N. Zare. Search for past life on mars: possible relic biogenic activity in martian meteorite alh84001. *Science*, 273:924, 1998.

*En lo de citar en los márgenes los libros y autores de donde sacárades las sentencias y dichos que pusiérades en vuestra historia, no hay más sino hacer, de manera que venga al pelo, algunas sentencias o latines que vos sepáis de memoria, o a lo menos que cuesten poco buscalles... y cuando no sirva de otra cosa, por lo menos servirá aquel largo catálogo de autores a dar de improviso autoridad al libro.*

Miguel de Cervantes, de Don Quijote de la Mancha.



